MODELLING AND OPTIMIZATION OF BIFACIAL PV FARM

POTENTIAL OF E/W VERTICAL FARM CONFIGURATION

Master Thesis

to obtain the degree of Master of Science
at the Delft University of Technology
to be defended on Wednesday August 30, 2023 at 9.00 AM

by

Matteo BARICCHIO

M.Sc. Sustainable Energy Technology
Faculty of Electrical Engineering, Mathematics and Computer Science

Thesis Committee:

Dr. Hesan Ziar	Photovoltaic Materials and Devices, TU Delft
Prof. dr. ir. Arno Smets	Photovoltaic Materials and Devices, TU Delft
Dr. Zian Qin	DC systems, Energy conversion & Storage, TU Delft

TU Delft Delft University of Technology

ABSTRACT

Solar photovoltaic (PV) has seen the most rapid growth among the renewable energy sources in the last decade. The market share of bifacial PV modules is expected to rise up to 70% in 2033. Such technology enables different farm configurations; however, it introduces complexities during the modeling phase, particularly concerning the estimation of incident irradiance on the rear side of the modules. The aim of this thesis is to investigate the potential of E/W vertical bifacial PV farms, in terms of market revenues, with respect to N/S tilted counterparts. A bifacial PV model is developed to estimate the power generated by a large-scale farm. This is based on the view factor concept and a 2D assumption is adopted to enable fast simulations. Such model takes into account the non-uniformity of the incident irradiance as well as the spectral impact. A multi-dimensional matrix approach is implemented to minimize the computational time while performing the calculations for individual cells and wavelength values. The model is validated in collaboration with the company KIPP&ZONEN, focusing on the broadband rear irradiance and its non-uniformity. Overall, the model shows sufficient agreement with the measured data, namely a mean bias deviation of $-1.29\,W/m^2$ (-2.22%) and a RMSE of $12.65\,W/m^2$ (21.69%) are obtained. The validation highlights larger errors in case of higher tilt values, especially during the clear days and at the edge of the modules. Specifically, the error is proportional to the amount of unshaded ground seen by a cell, in alignment with the limitations of the view factor concept. The profitability of vertical modules is studied in relation with various variables, including design parameters, market conditions, curtailment strategies and hybrid vertical/tilted configurations. A global scale is achieved by extending the simulation to 102 locations worldwide. To calculate the revenues of the PV farms, electricity price curves are modelled considering lower noon prices, hence different market conditions are identified by the minimum price and the ratio between morning/evening and noon prices. Whether vertical or tilted configuration is favourable in terms of market revenues is not dependent on the curtailment strategy unless the maximum power is limited to 70% of the nominal value. Combining vertical and tilted modules within a PV farm is found to be advantageous only in case heavy curtailment is applied. Among the design parameters, the row-to-row distance has a higher impact on the market revenues with respect to the modules' elevation. Specifically, larger distances are favourable for both configurations even though such benefit is more evident for vertical modules whereas optimal height values can be identified. A minimum ratio between morning/evening and noon prices is calculated, which represents the lower limit for the higher profitability of E/W vertical modules with respect to the N/S tilted case. Such value is dependent on the specific location and the design parameters. The locations characterized by a low diffuse fraction are recommended to implement vertical PV farms.

ACKNOWLEDGEMENTS

Undertaking this Master's thesis has been an exciting leap in the research world, marked by countless moments of learning, growth, and discovery. This endeavor has kindled an ardent passion for research within me and I am now driven by the aspiration to continue my academic journey, aiming to actively contribute to the energy transition. What began as a mere idea two years ago has now coalesced into a clear direction, empowering me to forge ahead with purpose and determination. In light of this experience, I am deeply grateful to the individuals who have played pivotal roles in facilitating this achievement.

Foremost, my heartfelt gratitude extends to my esteemed supervisor, Hesan, whose guidance throughout this project has been invaluable. I have truly appreciated the perfect equilibrium between his priceless counsel and the autonomy granted, rendering our meetings precious opportunities for both personal and academic growth. His trust in me has provided the liberty to explore preferred directions while embracing and learning from any mistakes encountered along the way.

In addition, I extend sincere thanks to Arno, the second member of the committee, with whom I had the privilege of collaborating as a teaching assistant during this academic year. His vast knowledge has been a profound source of inspiration, ever since I decided to follow his online course on Solar Energy over three years ago. Undoubtedly, that experience has significantly influenced my path, leading me to TU Delft to follow my dreams.

Moreover, I would like to thank Dr. Marc Korevaar and Dr. Pavel Babal from the company Kipp & Zonen for having provided the data adopted during the validation phase.

Lastly, I wish to express heartfelt gratitude to my family and friends for their unwavering support. Their constant love and encouragement have been the bedrock upon which I have built these remarkable achievements.

In conclusion, the completion of this Master's thesis has been a significant milestone, marking not just the culmination of a challenging academic pursuit but also the dawn of a new research journey that I am ardently determined to embrace.

CONTENTS

1

INTRODUCTION

1.1. BACKGROUND AND MOTIVATION

Energy transition is required in the coming years to avoid the drastic consequences of climate change on our society. This involves a radical transformation of the current energy system based on the decarbonization of the energy supply, increasing the share of renewbales in the electricity generation. Among the renewables energy sources, solar photovoltaic (PV) has seen the most rapid growth in the period from 2010 to 2022, reaching a global cumulative installed capacity of 1047 GW at the end of 2022 [1].

Currently, bifacial solar cells represents 65% of the PV market and this share is expected to rise up to 90% in 2033 [2]. This values decreases if PV modules are considered, since bifacial solar cells can be integrated in monofacial modules as well. Therefore, nowadays bifacial PV modules represent only 30% of the market share, but this value will rise up to 70% in the next 10 years according to the estimations [2]. These market trends are summarized in figure 1.1. The peculiarity of bifacial PV modules consists in their property of absorbing the irradiance incident on both the front and the rear side. This can lead to an increase in the generated power up to 30% [3], which increases the energy density of such technology in comparison with monofacial case. On the other hand, the extra energy provided by the bifacial solar cells involves some additional investment costs. In the recent years, a significant decrease in these costs made bifacial PV competitive in terms of levellized cost of energy worldwide [4].

Models that are able to predict the power generated by bifacial PV modules are required to determine the potential and the applicability of this technology. First, optical models are used to determine the radiation that reaches the solar cells. Then, thermoelectrical models are used to translate the irradiance into electrical power. The surplus of irradiance incident on bifacial modules adds complexity in their optical modelling in comparison with monofacial counterpart. On the other hand, the thermoelectrical model follows the same principles in both cases. Besides the front irradiance,

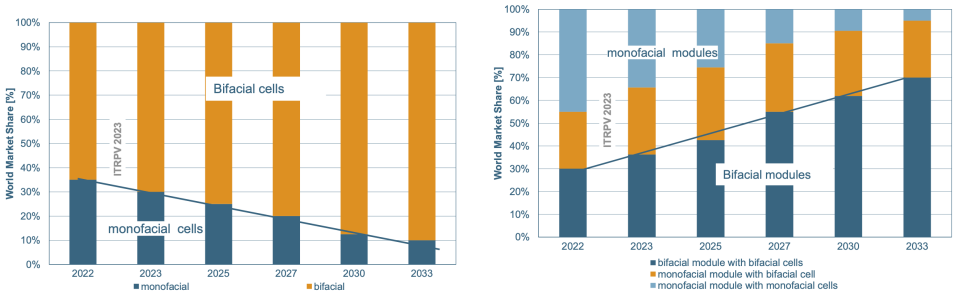

Figure 1.1: Market share of bifacial PV cells and modules [2]

the rear component has to be estimated in order to guarantee an accurate prediction of the power generated by the module. However, the surrounding environment has a higher impact on the rear than the front component of irradiance. Therefore, many effects such as the light reflection of the ground or the shadows due to the mounting structure should be taken into account to obtain an accurate model for the rear irradiance. In the recent years, different models have been developed to estimate the irradiance incident on bifacial PV modules. Various approaches have been explored for this purpose and they can be divided into two categories, depending whether they are based on the concept of view factor or ray-tracing. The former notion is inherited from heat transfer theory and it widely used in the literature due to the low computational time required for the simulations [5]. This is based on the assumption of isotropic scattering of the reflected rays [6]. On the other hand, ray-tracing software like RADIANCE [7] are based on individual sunrays simulations, considering their interaction, i.e. absorption, reflection or transmittance, with every surface [6]. However, in the latter case the increase in precision causes a significant raise in the computational time needed for the simulation [5]. Once decided the main approach, there are other aspects that can be integrated in the models depending on the level of accuracy required. For instance, these include the non-uniformity of the rear irradiance [8], the spectral impact of the incident radiation [9] or the influence of the mounting structure [10]. Usually, such aspects are intrinsic to ray-tracing models whereas they can be considered or neglected in the models based on view factor, depending on the purpose of the study. Therefore, it can be concluded that there are many features which determine the accuracy of bifacial PV models. Due to the trade-off between higher precision and low computational time, the choice of the main approach and whether integrating or neglecting each of mentioned aspects have a significant impact on the final outcome, and they should depend on the objective of the study.

Bifacial PV models are used to predict the power generated by individual bifacial solar cells as well as large-scale power plants. In the latter case, simulations are performed to find the optimal configuration of the farm in terms of modules' tilt, orientation or other design parameters. Various studies have analyzed different configurations to understand the full potential of bifacial PV technology on farm level. These include tilted fixed systems, single-axis and dual-axis tracking systems [4]. The tracking systems en-

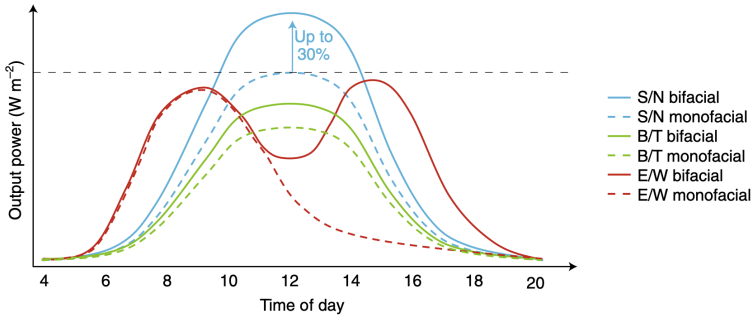

Figure 1.2: Comparison of typical power curves for different bifacial PV configuration [3]. The acronyms S/N, B/T, E/W refer to North/South tilted, East/West vertical and Bottom/Top horizontal configurations.

able an increase of the power produced without affecting the shape of the noon-peak power curve. Moreover, vertical bifacial PV systems are considered as well [11]. These are mounted on the East/West (E/W) orientation to exploit the sun's irradiation during morning and evening in contrast to the conventional North/South (N/S) orientation. Therefore, such configuration is characterized by a two-peaks power curve and a minimum during noon [3]. This is illustrated in the figure 1.2.

Even though the energy yield of E/W vertical configuration is generally lower than the N/S tilted counterpart, there are two main advantages that make such configuration appealing to the market. The first one is related to the physical mounting structure which enables the integration of vertical modules in different applications. Concerning the field of Agrivoltaics, the reduced space occupied by the modules increases the land productivity of the crops [12], [13]. Another application consists in the use of the vertical modules as noise barriers, e.g. close to highways [14]. Moreover, soiling losses decrease due to the lower chance of soil accumulation on a vertical structure, increasing the performance of the system. The second advantage is related to the shape of the power curve produced by this configuration. Such profile could be beneficial in terms of demand-supply matching in case of a load curve characterized by a morning and an evening peak, as happens in the residential sector [15]. This matching would reduce the amount of storage required to guarantee the electricity supply [16], decreasing the total cost of the system. On a larger scale, bifacial vertical configuration improves the stability of the power system by reducing the effect known as duck-curve problem [17]. Finally, vertical bifacial PV could guarantee higher economic revenues than conventional configurations in case the electricity prices are characterized by lower values around noon than the rest of the day. Such condition is usually observed during sunny days when the penetration of PV in the electricity mix of a country becomes relevant. An example of Dutch electricity market is provided in figure 1.3.

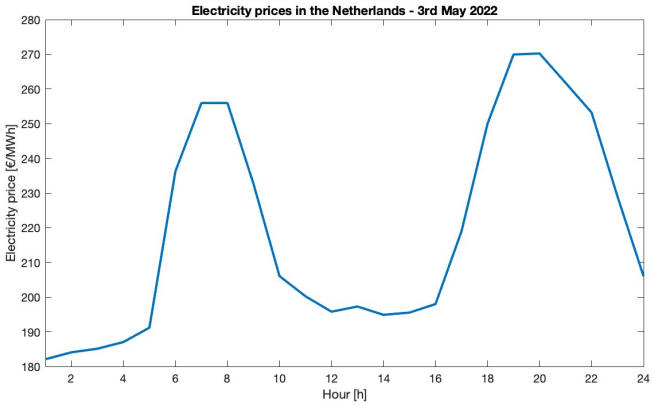

Figure 1.3: Example of electricity prices in the Netherlands (3rd May 2022) [18]

1.2. OBJECTIVE OF THE THESIS AND RESEARCH QUESTION

The objective of this thesis is to develop a model to simulate the performance of a bifacial PV farm, in order to determine the optimal configuration in terms of economic revenues. Such model has to guarantee sufficient accuracy as well as a low computational time of the simulations. The latter requirement arises from the need to extend this analysis on a global scale hence the simulations have to be iterated over multiple locations. This includes the choice of the approach to follow while developing the model, e.g. view factor or ray-tracing, as well as its resolution on different dimensions such as spatial or spectral. Therefore, a first research question can be summarized in the following sentence:

What is the optimal model to simulate the performance of a bifacial PV farm on a global scale?

This model will be adopted to determine the optimal configuration of the bifacial PV farm, identified by design parameters such as tilt, orientation, row-to-row distance or height of the modules. In particular, the benefits of an E/W vertical configuration is investigated in comparison with the N/S tilted conventional counterpart. Therefore, a second research question can be expressed as follows:

What is the potential of E/W vertical bifacial PV modules, in terms of economic revenues, with respect to the N/S tilted counterpart?

The answer to this research question is expected to depend on various factors related to different contexts such as climate conditions, electricity market behaviour and design parameters of the farm. Therefore, from this research question other three subquestions are derived:

1. *What is the impact of the design parameters such as the row-to-row distance and the height of the modules?*

2. *How the electricity market behaviour determines the optimal configuration?*

3. *What are the climate parameters that play a role in selecting appropriate locations for vertical bifacial PV?*

1.3. THESIS OUTLINE

The thesis is structured as follows. A literature review concerning bifacial PV technology and modelling is encompassed in chapter 2. This starts with some background information about bifacial modules. Subsequently, a review of the various modelling approaches and challenges are outlined, along with a classification of the main recent models available in the literature. The methodology is described in chapter 3, where the optical model developed for the scope of the thesis is explained in detail. Then, the thermal and the electrical models are illustrated as well, completing the description of the bifacial PV farm model. This is followed by the outline of the electricity prices modelling and the explanation of the different database used for this analysis. Chapter 4 summarizes the results obtained during this study. First, the outcome of the model's validation is shown, identifying the parameters that have a higher impact on its accuracy. Second, the shape of vertical modules' power curve is studied in relation to various factor, such as the height of the modules or the diffuse fraction. Third, the influence of the design parameters on the energy yield and other relevant metrics is analyzed to obtain a full understanding of the inter-dependency between the design variables and to improve the comparison between the different configurations. The chapter ends with the results concerning the potential of vertical PV modules in terms of economic revenues in relation to multiple variables, such as design parameters, climate conditions and market scenarios. Finally, the main conclusions of the research are outlined in chapter 5, together with some recommendations for future work.

2

LITERATURE REVIEW

This chapter presents a comprehensive literature review that examines the current status of the bifacial PV technology and modelling techniques. It is divided into two main sections. First, the main concepts that distinguish bifacial solar modules from the monofacial counterpart are introduced in section 2.1. This include the explanation of the main metrics, the influence of the design parameters and the different farm configurations. Second, section 2.2 describes the various types of models that can be used to simulate the performance of a bifacial PV farm. This is presented through an outline of the main challenges to tackle as well as a classification of the existing models found in the literature. The aim of this literature review is to select the proper features for a bifacial PV model that are required to fulfill the objective of this study, i.e. a global analysis to compare the potential of different farm configurations.

2.1. BIFACIAL PV TECHNOLOGY

Bifacial solar cells start being conceptualized during the 1980s, when a study from Cuevas et al. [19] mentioned the possibility to obtain a 50% gain power by using bifacial solar cells instead of conventional monofacial ones. The interest in this technology increased over the next decades and new types of solar cells were fabricated following the bifacial concept. The substantial difference with respect to the monofacial cells can be recognized in the rear electrode, which has to enable the solar radiation to be absorbed by the cells as well as in the front case. For this purpose, the backside non-reflective sheet is substituted by a metallic grid, similar to the front side electrode [3]. Figure 2.1 describes schematically this concept for c-Si based solar cells. In the following subsections different aspects about bifacial PV technology are discussed. First, the main metrics are introduced in subsection 2.1.1. Then, the influence of the various parameters on the performance is presented in subsection 2.1.2 whereas the benefits of the vertical configuration for a solar farm are highlighted in subsection 2.1.3.

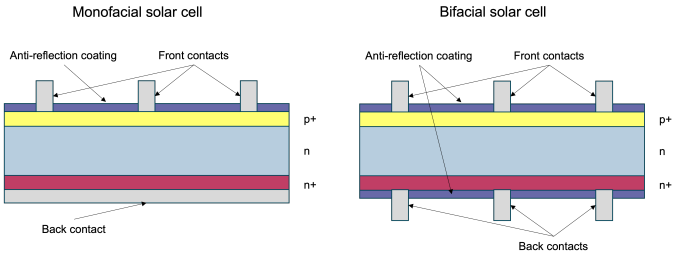

Figure 2.1: Comparison between monofacial and bifacial concept [20]

2.1.1. INTRODUCTION TO THE MAIN METRICS

The bifaciality property of the PV modules is assessed using the bifaciality factor (ϕ_{Bi}), defined as the ratio between the power generated by the rear side and the front side under standard test conditions (STC), as shown in expression 2.1. The values usually range from 60% to 90% in commercial applications [6]. However, bifaciality factor of approximately 92% and 95% can be obtained for Silicon Heterojunction and n-PERT solar cells, respectively [20].

$$\phi_{Bi} = \frac{P_{STC,r}}{P_{STC,f}} \cdot 100 \tag{2.1}$$

The surplus of energy generated by bifacial solar cells with respect to the monofacial is quantified by the bifacial gain (BG), defined in equation 2.2, where the terms EY_{mono} and EY_{bi} refer to the energy yield of monofacial and bifacial cells, respectively. In some studies, the same metric is defined using the instantaneous power instead of the energy yield for the two types, but the concept remains unchanged [3].

$$BG = \frac{EY_{bi} - EY_{mono}}{EY_{mono}} \tag{2.2}$$

This concept can be extended from the cell to the module level. Therefore, various studies have used the bifacial gain to quantify the over-performance of bifacial PV modules with respect to the monofacial. However, the bifacial gain is not a property of the solar cell but depends on the geographic location where the module is installed as well as some design parameters such as the row-to-row distance, the tilt and the height of the modules. Another crucial parameters in this case is the value of the albedo, which determines the ground's property of reflecting the incident radiation. An example performed by Sun et al. [21] of a global analysis concerning bifacial gain calculation is depicted in figure 2.2, where the dependency on the installation conditions is evident.

The development of the bifacial technology in the recent years reduced the gap between bifacial and monofacial modules' cost in most of the regions worldwide. Such affirmation can be confirmed and quantified through a comparison between the levellized cost of electricity (LCOE) of the two technologies. Similarly to the bifacial gain concept, the LCOE depends on the installation conditions of the modules, hence design parameters or ground's type can affect significantly the outcome of the analysis. This occurs

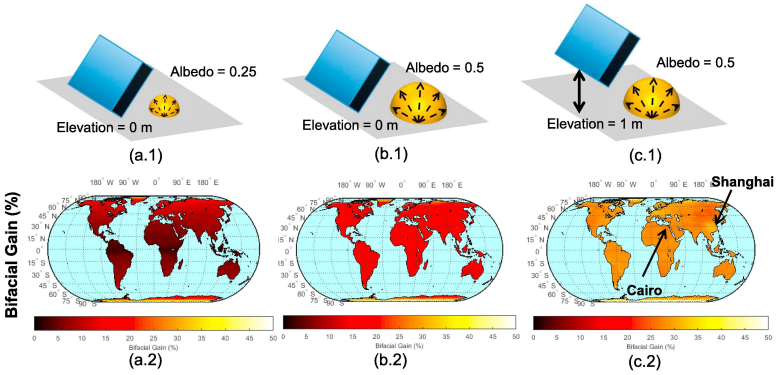

Figure 2.2: Example of bifacial gain calculation for different installation conditions and albedo values [21]

due to the higher sensitivity of bifacial performance on such conditions with respect the monofacial case. The results obtained by Rodríguez-Gallegos et al. [11] show that the cost-effectiveness of bifacial over monofacial modules is guaranteed over a certain latitude, approximately around 40°. On the other hand, lower latitudes require minimum value of albedo between 0.12 and 0.30 to achieve such condition. However, this trend is expected to increase further due to the cost reductions concerning bifacial technologies' manufacturing that are expected in the coming years [3].

2.1.2. EFFECT OF DIFFERENT PARAMETERS ON THE PERFORMANCE

As anticipated in the previous paragraphs where the main metrics have been discussed, the performance of bifacial PV modules are highly dependent on the installation parameters. In case of monofacial modules, the optimization of the design parameters is limited to two main aspects. First, the tilt and the orientation of the modules are optimized in order to maximize the energy yield. An approximate rule of thumb recommends to use tilt values close to the latitude whereas the orientation has to be set to North or South depending on the hemisphere. Second, the row-to-row distance of the farm is chosen to avoid mutual shading during a certain time window. On the other hand, the bifacial nature of the modules involves new challenges since the irradiance incident on the rear side is the results of multiple reflections that depend on the interplay of various parameters. These include the values of albedo, tilt, distance and height of the modules [22]. Moreover, the interdependence between these parameters adds complexity to the design phase [23].

The performance of a bifacial PV module are highly dependent on the albedo value, which determines the fraction of the radiation that is reflected by the ground. In general, a high value of albedo is beneficial for PV modules, since it increases the incident irradiance. However, such benefit is significantly more evident in case of bifacial modules with respect to the monofacial counterpart, since in the former type the amount of the ground reflected component is substantially larger than for the latter. Therefore, both the bifacial gain and the energy are highly sensitive to the albedo. In particular, Asgharzadeh et

al. [23] have mentioned the presence of a linear relation between the albedo and the bifacial gain in their study. Moreover, in real outdoor conditions the albedo of the ground is not constant along the year due to seasonal variations which can therefore affect the energy yield. However, such effect have been quantified by Patel et al. [24] and its limited influence on the energy yield has been proved, concluding that a time-constant albedo value is sufficiently accurate.

Another parameter that affects the performance of the bifacial PV modules within a farm is the row-to-row distance. The influence of such variable is related both to the mutual shading between different rows and the amount of ground that is seen by the modules, especially from the rear side. From the technical perspective, many studies have highlighted that the increasing of the row-to-row distance leads to an increase of the energy yield [22]. However, the increase of the farm's surface is related to higher land cost, which affects the LCOE of the system. Therefore, the optimal trade-off between the technical constraints and the economical implications has to be found, as analyzed in several studies [4], [25], [26].

The elevation of the modules has a relevant impact on the energy yield of bifacial PV farms since it affects the irradiance incident on the rear side. Unlike the other parameters, in literature there is not a complete agreement concerning the influence of the height on the performance. Asgharzadeh et al. [23] have mentioned that higher values of elevation are beneficial in terms of bifacial gain, hence increasing the energy yield, up to a certain saturation value, equal to 1 m in their case. Therefore, it is stated that increasing the height beyond that limit has no effect on the performance [27]. On the other hand, Yusufoglu et al. [22] have shown the presence of optimal height values that maximise the energy yield in their simulation for Cairo (Egypt) and Oslo (Norway). In this study, an initial increasing in the energy yield is registered in agreement with the other works whereas a decreasing trend is observed instead of saturation behaviour. The authors justify such behaviour as a consequence of the trade-off between the self-shading and utilization of the reflective surface, determined by its view factor. However, there is not a general rule for the optimal height value since it is dependent on the location and the other parameters.

Similarly to the monofacial case, calculating of the optimal tilt that maximize the energy is crucial during the design phase. However, in case of bifacial modules the interdependence between multiple variables requires a detailed sensitivity analysis [22]. In particular, a positive correlation is observed between the optimal tilt and the albedo value [21]. This occurs since higher tilt values enable the module's surfaces to see a larger portion of the ground hence increasing the fraction of ground reflected irradiance. Such rule is valid both for monofacial and bifacial modules, but in latter case the impact is higher [23]. The same trend is followed when considering the row-to-row distance: low reflective areas lead to lower optimal tilt values [22], [28]. On the other hand, a negative correlation is registered with respect to the module's height [21], [22]. Moreover, the optimal tilt changes also when considering large farm instead of stand-alone PV modules [23]. Figure 2.3 summarizes the dependence of the optimal tilt on the albedo and the

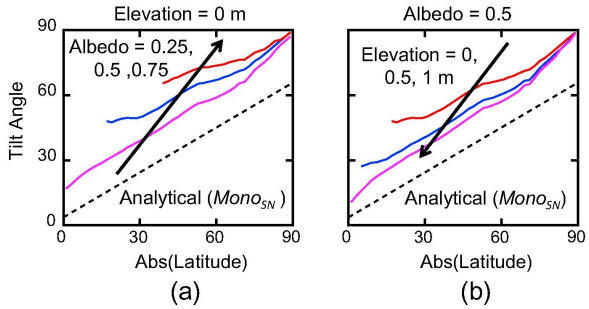

Figure 2.3: Example of optimal tilt for various locations, (a) and (b) highlight respectively the trend with the albedo and the elevation [21]

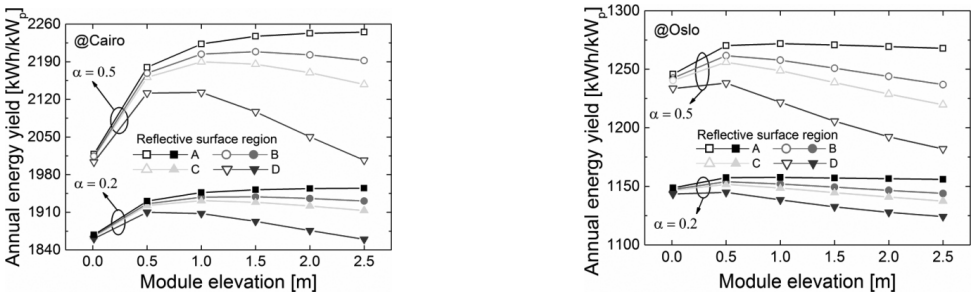

Figure 2.4: Summary of the interdependence of the design parameters on the energy yield of bifacial PV modules. The simulations refer to Cairo (left) and Oslo (right).[22]

modules' elevation.

The main takeaway of this section is that the bifacial nature of the PV modules causes an interdependence between the various design parameters and installation conditions. Therefore, an analysis on this technology requires a careful sensitivity analysis to guarantee a complete overview of the matter. An example of such interdependence is shown in figure 2.4, which is limited to two different locations [22]. However, the impact of these parameters is mainly studied for PV modules mounted at their optimal tilt. There are only few studies that highlight such concepts for vertical PV farms but a comparison of the influence of the installation conditions between different configurations is missing in the literature.

2.1.3. POTENTIAL OF VERTICAL PV MODULES

Bifacial PV modules enables multiple configurations for a solar farm with respect to the monofacial technology. Besides the N/S conventional tilted configuration aimed to maximize the energy yield, also the E/W vertical modules have been analyzed in many studies [11], [14], [16], [17], [21], [29]–[34]. The advantages of such configuration have been introduced in chapter 1, mentioning both the benefits related to the physical structure and the power curve characterized by two peaks.

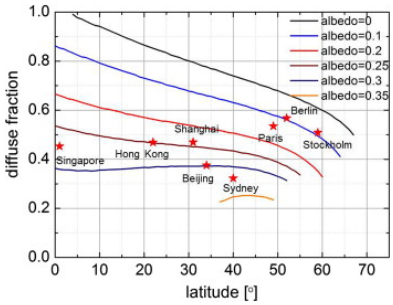

Figure 2.5: Diffuse fraction value for which bifacial vertical PV modules receive more irradiation than tilted monofacial counterpart, depending on the latitude. This is shown for different albedo values [31]

The performance of vertical modules are highly affected by the climate conditions of the analyzed locations. In particular, the diffuse fraction plays a significant role. Guo et al. [31] have shown that a high diffuse fraction is beneficial for vertical modules in terms of total energy generated. This is shown in figure 2.5, where the diffuse fraction for which vertical modules receives more irradiation than the monofacial tilted configuration is highlighted for different albedo values. However, this study is limited to the analysis of the influence of the diffuse fraction on the total energy yield. Therefore, it is neglected the effect of this climate variable on the different periods of the daily power curve, whose shape determines the advantages of the vertical configuration.

To estimate the potential of vertical PV modules, various authors have proposed different metrics. Most of the studies still focus on the LCOE for the comparison with conventional installations. However, the vertical configuration presents a higher LCOE with respect to the conventional one [30], with the exception of some latitudes close to the poles and very high albedo values [11]. This metric is not able to capture the advantages of such technology since it only depends on the energy yield, which is usually lower for vertical farms. Therefore, there is a need of a metric that is able to show the advantage related to the shape of the power curve instead of only considering its integral. Chudinzow et al. [30] have adopted the value factor, defined in equation 2.3, to understand the potential of the vertical configuration in terms economic revenues. This metric weights the power produced by a power plant depending on the market price. In their case study, they have focused on Germany, where the high PV penetration leads to a minimum in the daily price curve around noon. Therefore, vertical PV are characterized by a higher value factor than the conventional tilted configuration, highlighting the economical superiority of the former over the latter. However, the value factor is able to show only the capability of capturing high electricity prices, without considering the total amount of revenues earned. In conclusion, this limitation prevents the use of the value factor to state the absolute economical superiority of one configuration among the others.

$$value\ factor = \frac{Specific\ revenues\ of\ a\ power\ plant\left[\frac{€}{MWh}\right]}{Average\ market\ price\left[\frac{€}{MWh}\right]} \tag{2.3}$$

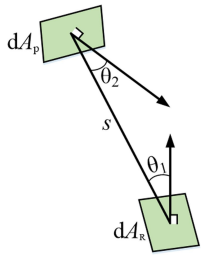

Figure 2.6: View factor concept [36]

2.2. MODELLING OF BIFACIAL PV FARM

The modelling of bifacial PV solar cells is essential to predict the power generated by one single module up to utility-scale farms. In this section the main approaches and the critical challenges for bifacial PV modelling are described. First, subsection 2.2.1 describes the difference between the optical modelling methods based on view factor and ray-tracing concept, highlighting their advantages and disadvantages. Then, the main challenges of bifacial PV optical modelling are presented in subsections 2.2.2 and 2.2.3, respectively. Subsection 2.2.4 focuses on a classification of the existing optical models present in literature. Subsequently, the main thermo-electrical models adopted for bifacial PV are described in subsection 2.2.5. Lastly, subsection 2.2.6 summarizes the conclusions of the literature review on bifacial PV modelling and outlines the approach that is followed in this study.

2.2.1. VIEW FACTOR VS RAY-TRACING

Estimating the amount of irradiance incident on the rear side of a bifacial PV module represents the the main challenge of the modelling of this technology. Different approaches can be adopted for this purpose and they can be divided into methods based on either view factor or ray-tracing principles. Such techniques are explained in detail in the following paragraphs.

The concept of view factor, also known as configuration factor in literature, is defined as the fraction of radiation that leaves a surface A_P and is received by a surface A_R. These surfaces are assumed to be opaque, isothermal and diffuse [35]. Such concept is inherited from the heat transfer theory and it has been widely used to determine the radiation exchange between two surfaces. It is a purely geometric factor, i.e. its value is independent on the amount of radiation involved as well as the temperature of the objects. Mathematically, the view factor is defined as expressed in equation 2.4. A_R, A_P and dA_R, dA_P are the considered surfaces and their differential elements whereas θ_1 and θ_2 are the angles between these infinitesimal surfaces and their distance s.

$$F_{A_R \rightarrow A_P} = \frac{1}{A_R} \iint_{A_R A_P} \frac{\cos\theta_1 \cos\theta_2}{\pi s^2} dA_R \, dA_P \tag{2.4}$$

The view factor approach to estimate the radiation incident on the different surfaces is based on the solution of the integral shown in equation 2.4. However, it can be solved

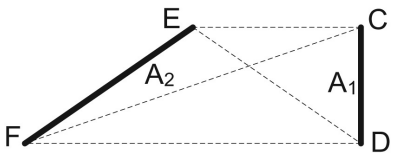

Figure 2.7: Hottel's cross string rule [40]

analytically only for a limited number of simple cases. Therefore, either a computational approach is followed or analytical approximations are made. Several methods have been developed for this purpose [37], including direct integration, unit spheres, Hottel's crossed strings, matrix and Monte Carlo methods.

Direct integration provides an exact analytical solution to the problem but it is only applicable in case of simple geometries. Unit spheres method has been developed by Nusselt in 1928 [38], who simplified the problem from a double to a single integration introducing a large distance assumption. In this method, the surface A_P is projected onto a hemisphere built over the plane of the surface A_R. Then, the view factor is calculated as the fraction of the circle, i.e. the base of the hemisphere, determined by the orthogonal projections of the surface projected onto the hemisphere. Nevertheless, this method is limited by the large-distance assumption and requires a computational time higher than the previous one. Hottel's cross string method consists in a simplification of the view factor calculation applicable for 2D cases irrespective of the shape of the surfaces, e.g. flat, convex or concave [39]. A schematic representation is illustrated in figure 2.7 whereas the view factor is calculated according to the formula 2.5 [40]. The advantage of this technique is the low computational time required to complete the calculations with respect to the other methods. Another technique that can be applied for this purpose is the Monte Carlo method, which is based on a statistical characterization of the phenomenon and it is also applicable for complex surfaces. However, a high computational time is required to obtain the final solution of the problem, which is an approximation subjected to statistical fluctuation [41]. Finally, a matrix approach be adopted for view factor calculation. It is based on the property stating that, in case of enclosed geometry, the sum of the view factors between a particular surface and all the other surfaces visible from that surface is equal to unity.

$$F_{A_1 \to A_2} = \frac{CF + DE - CE - DF}{2 \cdot CD} \tag{2.5}$$

Concerning the objective of this study, i.e. the modelling of a bifacial PV farm, only few of the mentioned methods can be adopted. Direct integration requires numerical integration since the application of the view factor formula cannot be solved analytically for two rectangles in an arbitrary position of 3D space. An example regarding two perpendicular rectangles is reported by Abishek et al. [42], where the analytical calculations are developed until the extent possible and then approximated formulas are provided. Such concept have been applied by Alam et al. [35], where the ground view factor of the rear cells is calculated under six different design variables and both uniform and non-

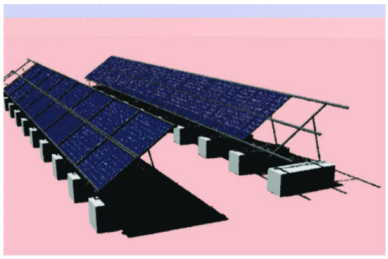

Figure 2.8: Example of a rendered image obtained using RADIANCE simulation software [46]

uniform grounds are tested. Nusselt's method cannot be applied in this case since the interaction between the ground and the modules does not satisfy the large distance hypothesis. On the other hand, Hottel's cross string rule could be applied for the view factor calculations required for this study only in case of 2D approximation. Such assumption entails considering a farm characterized by infinitely-long modules' rows, i.e. large-scale PV farms. In other terms, this 2D assumption neglects the "edge effect" (EE) [6], namely the increase of the irradiation received by the modules at the edge of the rows due to the presence of less obstacles. This parameter is defined in equation 2.6 in relation to the bifacial gain, according to Pelaez et al. [6]. Monte Carlo method represents a viable solution in case of high accuracy requirements and absence of computational time restrictions. Finally, the matrix technique seems not to be suitable for the modelling of a bifacial PV farm since the enclosed geometry requirement cannot be easily satisfied unless a large number of surfaces are considered, increasing the complexity of the problem.

$$EE = \frac{BG(\#\,rows, \#\,modules\,per\,row)}{BG(\infty\,rows, \infty\,modules\,per\,row)} \tag{2.6}$$

Another approach for the optical modelling of a bifacial PV farm consists in the use of ray-tracing algorithms. The principle consists in the simulation of individual rays' path to obtain a an illumination mapping through a rendering process. RADIANCE [7] is a widely used open-source software adopted for PV modelling purposes [43]. Moreover, NREL developed a version of this software called bifacial_radiance [44] specifically for bifacial PV applications. This is based on backward ray-tracing, i.e. the rays are traced from the object to the source [45]. It enables the modelling of 3D complex environments, capturing the edge effects, the influence of the racking system and the non-uniformity on the spatial dimension [46]. The accuracy of the results obtained by using this approach depends on the resolution of the rendering image. In general, more accurate results can be obtained in comparison to view factor based techniques. However, such method requires a significantly higher computational time, up to order of $10^4 - 10^5$ higher with respect to 2D view factor methods [46].

To provide a complete overview of bifacial PV modelling, the presence of empirical models has to be mentioned. Such models are characterized by equations with coefficients obtained from a combination of the results from real measurements and simulations. The advantage of these methods consists in a low computational time in com-

parison to the other cases. However, the results are usually limited to certain aspects, e.g. the calculation of bifacial gain, and the level of accuracy is generally low. For instance, two empirical models have been developed by SolarWorld [47] and PrismSolar [48], where the bifacial energy gain is calculated as a function of the design parameters and the albedo value.

Various studies from different authors have compared the performance of widely used models based on view factor or ray-tracing [6], [46], highlighting the advantages and disadvantages on both techniques. A summary of these works is present in table 2.1, where the most popular models have been selected.

Table 2.1: Comparison of the existing models adopted for bifacial PV modelling [6], [46]

	Approach	Computational time	Edge effect
SolarWorld [47]	Empirical	Very low	Neglected
PrismSolar [48]	Empirical	Very low	Neglected
pvfactors [49]	2D VF (Matrix)	Low	Neglected
NREL VF [5]	2D VF (Hottel)	Low	Neglected
PVSyst [50]	2D VF	Low	Neglected
bifacial_radiance [44]	Ray-tracing	High	Considered

The analysis highlights the ability of ray-tracing model to capture the edge effects whereas the other methods ensure a lower computational time. This latter parameter depends on the resource available and discrepancies are present among different studies in literature. For instance, the computational time of the ray-tracing method is mentioned to be from 6 [6] up to $10^4 - 10^5$ [46] time higher with respect to view factor methods. Such variety of results is probably caused by the dependency of the time required for one simulation on the dimensions of the simulated PV farm in case of ray-tracing. On the other hand, most of the analyzed view factor models are not sensitive to this feature due to their infinite length's assumption. The accuracy of the various approaches can be determined by observing the results of this comparison, which are depicted in figures 2.9, 2.10 and 2.11.

Pelaez et al. [6] concluded that the edge effect start becoming significant above a certain elevation of the modules, hence ray-tracing methods are required to obtain an accurate estimation of the irradiance in that case. In general, figures 2.9 and 2.10 show sufficient agreement between view factor and ray-tracing models with the measured data, where the former approach seems to be more conservative. In particular, the error on the bifacial gain is within 2%. The study of Asgharzadeh et al. [46] confirms that ray-tracing guarantees the most accurate estimation of the rear irradiance, as shown in figure 2.11. This work proves that the main gain in accuracy is obtained by considering the influence of the racking structure whereas the edge effect is limited in case of large farms. Moreover, even though angle of incidence (AOI) losses have a marginal effect within the model's outcome, it is recommended to include them in a bifacial PV model. Lastly, it is concluded that 2D models are accurate enough in terms of annual energy yield estima-

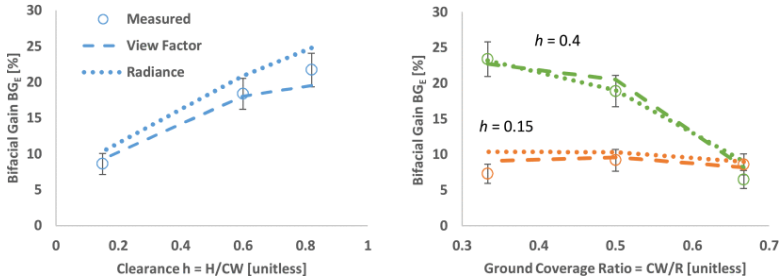

Figure 2.9: Comparison between the accuracy of ray-tracing and view factor models in predicting bifacial gain in relation to the height and row-to-row distance of the modules, which are normalized through the clearance and the ground coverage ratio [6]

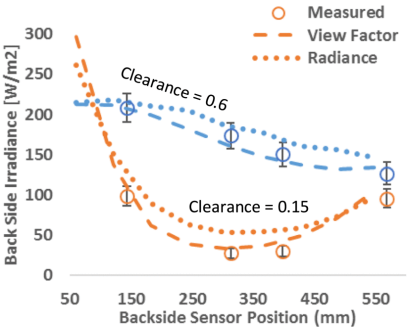

Figure 2.10: Comparison between the accuracy of ray-tracing and view factor models in predicting backside irradiance in relation to the position of the cell along the module [6]. The clearance value refers to the normalized height of the modules.

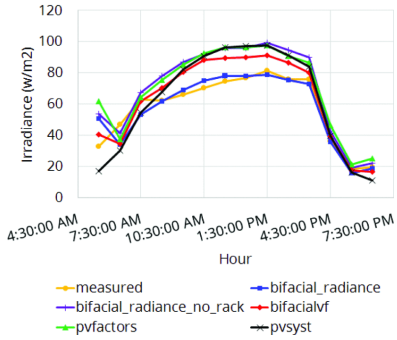

Figure 2.11: Comparison between the accuracy of the models presented in table 2.1 [46]. Empirical models are omitted whereas bifacial_radiance is tested also neglecting the racking structure.

tion despite the higher resolution ensured by 3D models.

2.2.2. NON-UNIFORMITY OF REAR IRRADIANCE

One of the main drawbacks in bifacial PV technology is the non-uniformity of the irradiance incident on the rear side of the module, which causes mismatch losses (MM_{loss}) that limit the total generated power. Such losses can be defined as shown in equation 2.7, which quantifies the decrease in the power output of the PV array with respect to the value of the individual cells [51]. In general, the interconnection between the solar cells is such that a non-uniform rear irradiance leads to a deviation of the point of operation from the maximum power point (MPP). Therefore, the output current is usually limited by the solar cell that receives the lowest amount of radiation. Such non-uniformity arises from various effect. The configuration of a farm leads to an alternating pattern of shaded and unshaded ground portions that depend on the position of the sun along the day. Furthermore, the ground's field of view of a rear cell, i.e. the angular fraction of ground seen by a cell, varies along the module's length. Moreover, the ground below

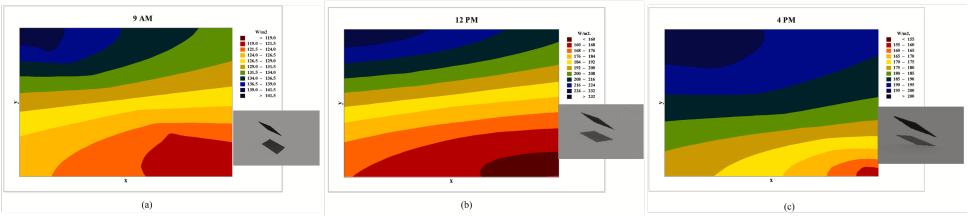

Figure 2.12: Example of ray-tracing simulation that highlights the non-uniformity of rear irradiance [8]

the PV modules is not homogeneous due to the exposure on the outdoor climate. Therefore, these effects lead to a ground reflected irradiance that is not uniform on the rear side of the module, as depicted in figure 2.12. Such behaviour is not present on the front side, since the albedo irradiance component represents only a limited fraction of the incoming radiation, dominated by sky irradiance. The non-uniformity of the rear irradiance is enhanced by the presence of the mounting structure, which causes additional shading and reflections. These operational conditions could lead to an increase in the degradation of the solar cells besides the power losses. Therefore, the minimization of the non-uniformity has to be considered carefully during the design phase of a bifacial PV farm.

$$MM_{loss} = \left(1 - \frac{P_{array}}{\sum P_{cells}}\right) \cdot 100\% \tag{2.7}$$

Unlike the non-uniformity experienced on the front side cells, the heterogeneity of the rear irradiance is not sufficient to activate the bypass diodes and avoid that the least illuminated cell limits the performance of the module. This occurs since the difference in rear irradiance is modest when considering the total radiation, i.e. sum of front and rear components. Therefore, it is not sufficient to activate the bypass diodes [51]. However, alternative configurations of bypass diodes have been proposed by Faturrochman et al. [14] that can reduce the mismatch losses from 13.3% to 10.7%. In particular, a novel L-shaped configuration has been introduced, as depicted in figure 2.13. However, such study is limited to the application of vertical bifacial PV modules, hence limited installation conditions have been tested.

Various metrics are used in the literature to quantify the non uniformity of the rear irradiance. The most popular is the GNU defined in equation 2.8, where the normalized difference between the maximum and the minimum irradiance is calculated [52]. To evaluate the effect on the overall performance of the module, the parameter INU is introduced, as shown in equation 2.9 [52], which weights the non-uniformity on the rear side with the front irradiance value. G_{max} and G_{min} indicate the maximum and minimum values of rear irradiance, respectively, whereas G_{front} is the (average) front irradiance.

$$GNU = \frac{G_{max} - G_{min}}{G_{max} + G_{min}} \tag{2.8}$$

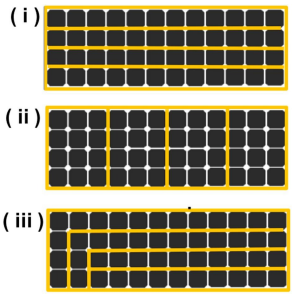

Figure 2.13: Alternative configuration of bypass diodes to reduce the mismatch losses: i) 1 diode per row, ii) 1 diode per 4 rows, iii) L-shaped [14]

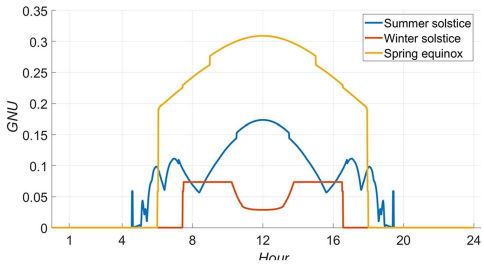

Figure 2.14: Example of GNU profile along the day for a bifacial PV module located in Madrid [52]

$$INU = \frac{\phi_{Bi} \cdot (G_{max} - G_{min})}{2 \cdot G_{front} + \phi_{Bi} \cdot (G_{max} + G_{min})} \tag{2.9}$$

According to Raina and Sinha [8], the value of GNU can be used to estimate the the mismatch losses through the fitting equation 2.10, characterized by $R^2 = 98.1\%$, as stated in their study. GNU varies instantaneously depending on the sun's position and the intensity of the solar irradiation. Figure 2.14 reports an example of a simulated GNU daily profile in Madrid [52]. Moreover, GNU values are extremely sensitive to the design parameters of the modules, namely the height, the row-to-row distance and the tilt values. The interplay between these parameters complicates the full understanding of the behaviour. However, the GNU seems to decrease when the height of the modules is increased, and presents a maximum while the tilt changes [8]. Moreover, high albedo environments cause an increase in GNU whereas its value is not very sensitive on the orientation of the modules [8].

$$MM_{loss}[\%] = 1.16 + 0.12 \cdot GNU[\%] \tag{2.10}$$

Other metrics are adopted to quantify the non-uniformity of the rear irradiance. The choice of these metrics is led by the necessity of obtaining a relation with the mismatch losses. Deline et al. [51] proposed the mean standard deviation ($\sigma_{G_{rear}}$) and the mean absolute difference ($\Delta_{G_{rear}}$) due to their high correlation with MM_{loss}. They have developed three empirical relations that relate these variables to the mismatch losses.

Equations 2.11 and 2.12 express MM_{loss} as a function of $\sigma_{G_{rear}}$ and are characterized by $R^2 = 0.977$ and $R^2 = 0.983$, respectively. The accuracy increases up to $R^2 = 0.995$ when $\Delta_{G_{rear}}$ is used, as shown in equation 2.13.

$$MM_{loss}[\%] = \exp\left(1.57 \cdot \ln\left(\sigma_{G_rear}[\%]\right) - 2\right) \tag{2.11}$$

$$MM_{loss}[\%] = 0.15 \cdot \left(\sigma_{G_rear}[\%]\right) + 0.027 \cdot \left(\sigma_{G_rear}[\%]\right)^2 \tag{2.12}$$

$$MM_{loss}[\%] = 0.142 \cdot \left(\Delta_{G_rear}[\%]\right) + 0.032 \cdot \left(\Delta_{G_rear}[\%]\right)^2 \tag{2.13}$$

The modelling of the non-uniformity of the rear irradiance is therefore essential to avoid the overestimation of the power output. This means that the spatial resolution of the model with respect to the PV modules has to be higher in comparison to previous monofacial models, hence the incident irradiance has to be estimated for each cell instead using an average value for the whole surface. Alternatively, empirical relations can be used to estimate the mismatch losses induced by the non-uniformity of the rear irradiance. They can be beneficial when the computational time required for the simulation is very low and can limit the error up to 0.1% on yearly basis [51].

Since the heterogeneity of the irradiance is caused by the interplay of multiple effects, some limitations have to be taken during the modelling phase. Therefore, it is important to select the most relevant phenomena when computational time constraints are present. For instance, the influence of the mounting structure can affect significantly the distribution of the irradiance incident on the rear side of the modules, therefore a proper design of such components is required. A study of Pelaez et al. [6] analyzed the influence of the torque tube in a 1-axis tracking system and concluded that neglecting the mismatch losses could lead to an underestimation of the DC power losses of approximately 1%.

The concept of "decisive solar cell" has been introduced by Berrian and Libal [45]. This is used to identify the cell that receives the lowest irradiance hence limiting the total current of the module. Since the decisive solar cell changes in time, the frequency is reported to understand which cells are responsible for the highest mismatch losses. From figure 2.15 it is evident that the lowest irradiance occurs in the central area of the module. Furthermore, it is mentioned that both view factor and ray-tracing models are able to estimate accurately the irradiance of the decisive solar cell, leading to a slight underestimation in most of the cases. Surprisingly, lower relative deviations have been found for view factor models but values up to ±2% have been obtained in both cases.

2.2.3. SPECTRAL INFLUENCE

Solar cells are spectrally-sensitive devices, hence the power generated is dependent on the spectrum of the incoming radiation, whose shape depends on several factors, including the air mass (AM), aerosol optical depth (AOD) and precipitable water (PW) [53]. In case of bifacial PV modules, the presence of different incident spectral irradiance on the front and the rear side increases the complexity of spectral influence on the performance

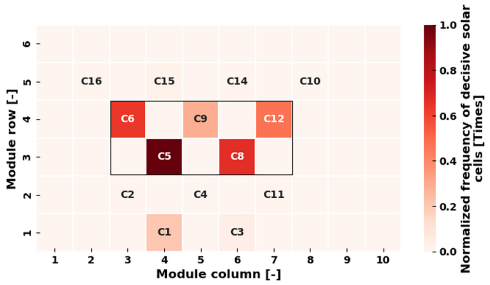

(A) Measured.

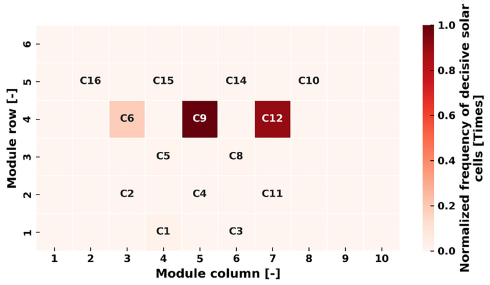

(B) Modeled.

Figure 2.15: Example of decisive solar cell identification, including both modelled and measured values [45]

[9]. For tilted installations, the irradiance incident on the rear side mainly consists in ground reflected component, whose spectrum is determined by the interaction with the ground. Therefore, several studies recommend to consider the spectral effect while developing bifacial PV models [9], [54]–[56] since the use of a constant scalar albedo could lead to relative error in bifacial gain calculations up to 19.5% [56].

Depending on the ground type, different regions of the spectrum are absorbed whereas others are reflected. Such effects can be captured by a bifacial PV model using a spectral curve for the albedo instead of a constant scalar value, increasing the accuracy of the rear irradiance estimation. An example of such curves for four different ground types is reported in figure 2.16, where also the typical Silicon spectral response is illustrated [9].

The shape of the spectra can be expressed through the average photon energy (APE) values, defined in equation 2.14 [57], [58], which indicates the chromatic distribution. In the equation, E_R is ground-reflected spectrum and Φ_R is the photon flux, both dependent on the wavelength (λ), whereas q is the conversion factor from eV to J. In particular, a red-shifted spectrum is characterized by a low APE value whereas high values of APE are obtained for spectra shifted towards the ultra-violet regions [9]. Table 2.2 reports the APE values of the four ground types illustrated in figure 2.16, where for instance the blueish profile of white sand spectrum is shown. Another metric used to quantify the shape of a spectrum is the normalized difference vegetation index ($NDVI$), which expresses whether the spectrum is shifted towards red or blue regions as well [55].

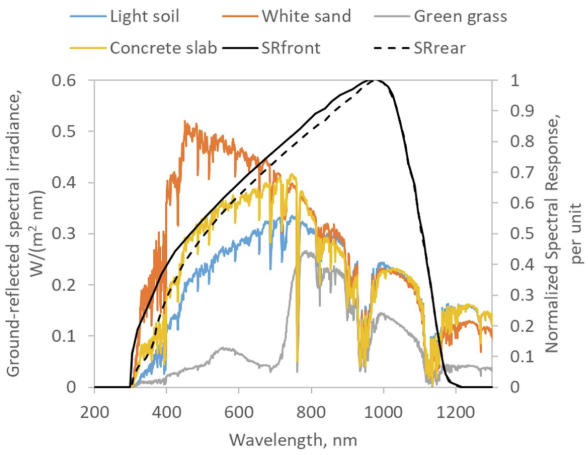

Figure 2.16: Spectral albedo curves for four different surfaces obtained through SMARTS software [9]

$$APE = \frac{\int_{\lambda_{min}}^{\lambda_{max}} E_R(\lambda)\, d\lambda}{q \cdot \int_{\lambda_{min}}^{\lambda_{max}} \Phi_R(\lambda)\, d\lambda} \tag{2.14}$$

Table 2.2: APE values of four selected ground types [9]

	Light soil	White sand	Green grass	Concrete slab
Ground-reflected APE [eV]	1.622	1.809	1.454	1.696

There are several metrics that can be used to quantify the impact of the spectrum in the estimation the power generated by a solar cell. They calculate the error with respect to the adoption of a reference spectrum, which in the simplest case is constant for each wavelength. The introduction of such metrics is also related to the instantaneous changes in the spectrum's shape due to the variation of the external conditions. A widely used metric is the spectral factor (SF) [59], which can be defined as shown in equations 2.15 and 2.16 for the front and the rear side, respectively. $SR(\lambda)$ is the spectral response of the device whereas $E_{front/rear}(\lambda)$ and $E_{front/rear,ref}(\lambda)$ indicate the actual and the reference spectral irradiance, respectively. Similarly, $G_{front/rear}$ and $G_{front/rear,ref}$ refer to their integrated values. A value of spectral factor equal to 1 means that there is no difference between reference or actual spectrum. On the other hand, spectral gains and losses occur when it is higher or lower than 1, respectively. In literature, the concept of spectral impact (SI) is introduced to estimate the effect of the spectral factor over the time and it consists in its average value weighted by the broadband irradiance [55].

$$SF_{front} = \frac{\int_{\lambda_{min}}^{\lambda_{max}} SR_{front}(\lambda) \cdot E_{front}(\lambda) \cdot d\lambda}{\int_{\lambda_{min}}^{\lambda_{max}} SR_{front}(\lambda) \cdot E_{front,ref}(\lambda) \cdot d\lambda} \cdot \frac{G_{front,ref}}{G_{front}} \tag{2.15}$$

$$SF_{rear} = \frac{\int_{\lambda_{min}}^{\lambda_{max}} SR_{rear}(\lambda) \cdot E_{rear}(\lambda) \cdot d\lambda}{\int_{\lambda_{min}}^{\lambda_{max}} SR_{rear}(\lambda) \cdot E_{rear,ref}(\lambda) \cdot d\lambda} \cdot \frac{G_{rear,ref}}{G_{rear}} \tag{2.16}$$

To combine the spectral effect of both front and rear side, Mouhib et al. [9] proposed a metric called bifacial spectral factor (BSF), defined in equation 2.17, where the coefficient $MM_{spectral}$ quantifies the mismatch between the two reference spectrum. Such metric can be used as a spectral correction while estimating the power generated by a bifacial PV module. The results of their studies show the high dependence of the SF_{rear} and BSF on the ground type and annual values of BSF up to 1.65% have been found in case of green grass. These results are in agreement with the study of Riedel-Lyngskær et al. [55], who have obtained values of SF_{rear} up to 25% for green grass, namely approximately 2% when translated in BSF. Seasonal variations of SF_{rear} have been proved as well as on daily basis [55]. The dependence on the sun's zenith has been highlighted [55], obtaining a U-shaped profile during the day [9]. Such dependence is evident during sunny days whereas becomes poor during cloudy conditions [55]. Furthermore, the correlation between SF_{rear} and other parameters has been investigated by several studies. Absence of correlation between SF_{rear} and APE has been proved, whereas higher values have been found for $NDVI$.

$$BSF = \frac{G_{front} \cdot SF_{front} + \phi_{Bi} \cdot G_{rear} \cdot MM_{spectral} \cdot SF_{rear}}{G_{front} + \phi_{Bi} \cdot G_{rear}} \tag{2.17}$$

$$MM_{spectral} = \frac{\int_{\lambda_{min}}^{\lambda_{max}} SR_{rear}(\lambda) \cdot E_{rear,ref}(\lambda) \cdot d\lambda}{\int_{\lambda_{min}}^{\lambda_{max}} SR_{front}(\lambda) \cdot E_{front,ref}(\lambda) \cdot d\lambda} \cdot \frac{G_{front,ref}}{G_{rear,ref}} \tag{2.18}$$

To capture the spectral variations throughout the day, various approaches can be followed. Rodríguez-Gallegos et al. [11] included in their model a factor f_1 which is multiplied to the power output to take into account this effect. It is defined through an empirical relation based on the absolute air mass (AM_a) [60] as shown in equation 2.19, obtained through a fourth order regression with the coefficients a_0, a_1, a_2, a_3, a_4 [61], [62].

$$f_1(AM_a) = a_0 + a_1 \cdot AM_a + a_2 \cdot (AM_a)^2 + a_3 \cdot (AM_a)^3 + a_4 \cdot (AM_a)^4 \tag{2.19}$$

In conclusion, the spectral influence of the rear irradiance should be considered as a non-negligible second order effect due to high fraction of irradiance incident to the front side with respect to the total [9]. Russell et al. [63] have estimated that a wavelength-independent albedo could lead in an underestimation of power output up to 3.1% and 5.2% for the green grass and the white sand, respectively. However, the use of spectral albedo and irradiance increases the complexity of bifacial PV models, decreasing the performance in terms of computational time. In particular, the resolution of the spectral data has a significant impact and high values are not required to obtain sufficiently accurate results [55].

2.2.4. CLASSIFICATION OF THE CURRENT OPTICAL MODELS

The trade-off between accuracy of the results and computational time leads to various choices of optical models among the studies present in literature. The purpose of the next paragraphs is to classify the existing optical models for bifacial PV and to investigate their use throughout different studies present in literature.

The first step of the classification consists in dividing the models depending whether they are based on the view factor or ray-tracing concept. Concerning the former, most of the studies have developed their own model, where the implementation of certain aspects, e.g. the spectral impact, AOI corrections or geometrical constraints, depends on the individual case. However, many works uses the popular model created by Marion et al. [5] as the starting point for their analysis. On the other hand, the studies based on ray-tracing concept usually refer to the RADIANCE simulation open-source software [7]. In particular, the adapted version named bifacial_radiance [44] developed exclusively for bifacial PV applications is gaining popularity.

Figure 2.17 classifies the studies analyzed during this literature review depending on the approach adopted for the development of the optical model, which are grouped in four different categories. First, view factor models are distinguished from ray-tracing. Moreover, studies that discuss and compare both approaches are included as well as research that are based on alternative methods, e.g. empirical approaches. It is evident from figure 2.17 that the use of view factor models is preferred with respect to ray-tracing, especially when multiple locations are analyzed for a time period of one year. Concerning view factor models, the number of spatial dimensions considered, i.e. 2D or 3D, is also included in the visualization. The 3D view factor models are still limited due to the complex geometrical implications that require numerical integration. These affect significantly the computational time, hence 3D models are only used to estimate targeted behaviours where high accuracy is needed. Lastly, the colours in figure 2.17 are used to understand which of these studies has validated the model with experimental data. To quantify the ability of the model to predict the incident irradiance, the root mean square error ($RMSE$) and the mean bias deviation (MBD) between modelled and measured data are usually adopted, both in terms of absolute [W/m^2] and relative [%] error [5]. Moreover, the agreement between measurements and modelled data is often shown considering the sum of the front and the rear components [5]. Lower errors are obtained in this case since the rear irradiance represents only a limited fraction of the total incident irradiance.

The second step of this classification consists in understanding whether the studies present in literature have considered or neglected two main challenges of bifacial PV modelling: non-uniformity of rear irradiance and the spectral influence. In the subsections 2.2.2 and 2.2.3, the impact of these challenges in relation with the accuracy of the models have been discussed along with their advantages and disadvantages. Figure 2.18 shows how these aspects have been tackled by the studies available in the literature, highlighting the number of locations considered for the simulations. It can be observed that less features are considered when a high number of locations is examined, due to

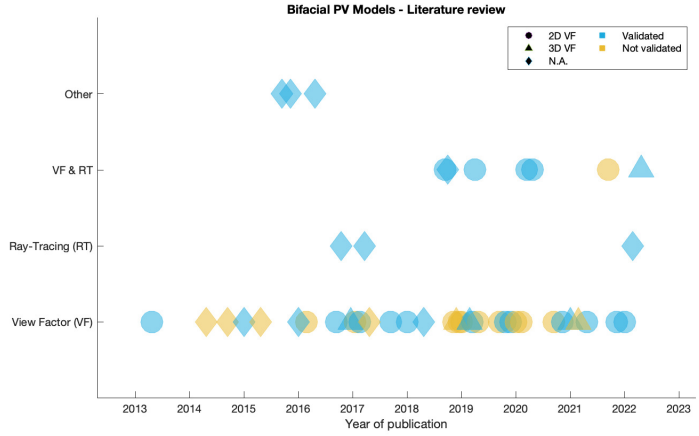

Figure 2.17: Classification of the models adopted in the studies available in literature concerning the main approach used for the irradiance estimation

the implications on the computational time that additional spatial and spectral dimensions involve. In particular, there is an absence of global analysis that take into account both the non-uniformity of the rear irradiance and the spectral impact simultaneously.

In conclusion, the literature review on optical models shows that their characteristics are highly dependent on the objective of the individual study, especially in terms of number of locations considered and time interval of the simulation. Concerning the approach to use, the accuracy increases from 2D view factor to ray-tracing models. However, the difference is marginal in case large-scale farms are considered. On the other hand, non-uniformity of rear irradiance and spectral impact are crucial aspects in bifacial PV modelling, therefore the optimal trade-off considering the computational time has to be found.

2.2.5. THERMO-ELECTRICAL MODEL

The objective bifacial PV models is to estimate the electrical power output of the device depending on the external conditions. Whereas the optical model provides the irradiance incident on the surfaces of the modules, a thermo-electrical model is needed to convert such information into generated power. It consists in two submodels: an electrical submodel that simulates the behaviour of the electrical components and a thermal submodel that takes into account the effect of the temperature on the performance. In contrast to the optical modelling, the changes with respect to the monofacial counterpart are limited concerning the thermo-electrical part. Therefore, there is an extensive literature that can be consulted to find the most appropriate model depending on the scope of the analysis, since the development of such models is rather mature as it started with monofacial PV research. In the next paragraph the main approaches adopted for the thermo-electrical modelling of bifacial PV are described.

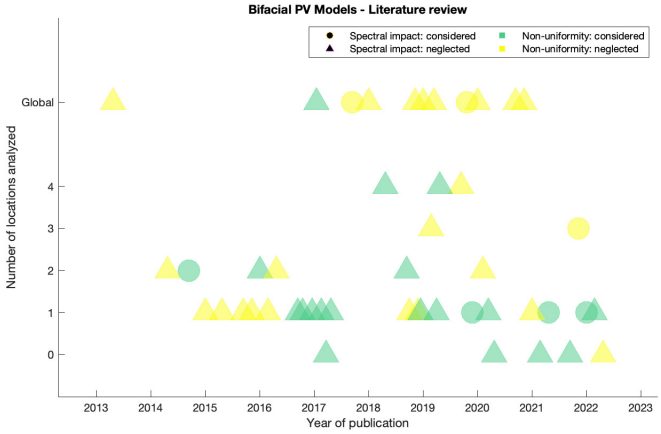

Figure 2.18: Classification of the models adopted in the studies available in literature concerning the non-uniformity of the rear irradiance and the spectral impact

The most popular electrical model in the literature is the 1-diode approximation, which is based on the equivalent circuit depicted in figure 2.19. The $I-V$ characteristics of each solar cell is determined by the equation 2.20 [8], where I_{ph} and I_0 indicate the photogenerated current and the reverse saturation current, respectively. N_s is the number of cells connected in series whereas n is the ideality factor. The thermal voltage is defined as $V_t = kT/q$, hence it depends on the absolute temperature T, the Boltzmann constant k and the elementary charge q. Finally, R_S and R_{SH} represent the series and the shunt resistance of the circuit. Therefore, there are five parameters that need to be extracted to simulate the behaviour of the solar cell: I_0, I_{ph} n, R_S R_{SH}. However, only four equations are available that relate these parameters, hence approximations are needed, as described by Raina and Sinha [8]. The main difference with monofacial modules regards the calculation of the photogenerated current, which consists in the sum of the front and the rear irradiance components, as highlighted in equation 2.21. In particular, the front ad the rear side are assumed to be in parallel.

$$I = I_{ph} - I_0 \cdot \left[\exp\left(\frac{V + IR_S}{N_s n V_t} \right) - 1 \right] - \frac{V + IR_S}{R_{SH}} \tag{2.20}$$

$$I_{ph} = I_{ph,front} + I_{ph,rear} \tag{2.21}$$

The 1-diode approximation is versatile in terms of applicability. Depending on the photogenerated current, it can be adopted from individual cell to module level. The former approach enables the consideration of the non-uniformity of rear irradiance, leading to higher accuracy. On the other hand, the spectral information can be included while calculating the photogenerated current by considering the spectral response of the module. Moreover, bypass diodes can be introduced by limiting the current of each cell

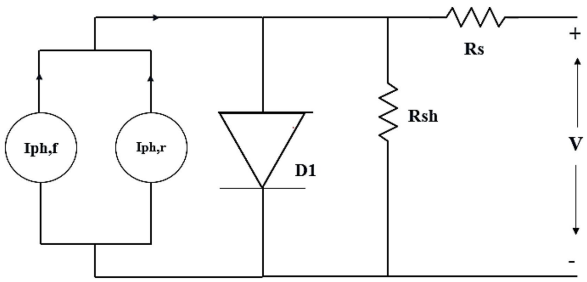

Figure 2.19: 1-diode equivalent circuit of a solar cell [8]

depending on the power optimizer configuration. These characteristics justify the large use of this method among different studies present in literature. Nevertheless, such approach could be limited by computational time constraints since the maximum power point has to be extracted from the $I-V$ characteristic using a numerical method, which can affect the accuracy of the results.

Another model that is used as electrical equivalent circuit of a solar cell is the 2-diodes approximation [14], [64]. In this case, additional parameters are included to obtain a $I-V$ characteristics which simulates better the non-ideality of the solar cell. This method follows the same principle of the 1-diode approximation, presenting the same advantages and disadvantages. In principle, its higher level of complexity leads to more accurate results.

Besides the electrical models that are based on the equivalent circuit of a solar cell, other methods with a lower degree of complexity are widely used in the literature. Such models are suggested in case of global analysis due to the limited computational time involved. For instance, Rodríguez-Gallegos et al. [11] have adopted a model which uses a constant efficiency value to convert the incident irradiance into electrical power. This model also includes corrective coefficients to take into account other effects like degradation, spectral impact and temperature, following the principle of Skoplaki and Palyvos [65]. Similalry, Sun et al. [21] have used two different values of efficiencies for the front and the rear side, including the concept of bifaciality factor. Lastly, Ledesma et al. [52] adopted an irradiance-dependent efficiency to develop their bifacial PV model.

The electrical performance of the PV modules are highly influenced by the operating temperature of the solar cells, i.e. high temperatures limit the electrical power by affecting the $I-V$ characteristic [64]. First, Lamers et al. [66] address the question whether bifacial modules operate at higher temperatures with respect to the monofacial counterpart. Such inquiry arises from two opposite effects: the higher total irradiance increases the module's temperature whereas the higher transmission of infrared spectral region decreases it [67]. Their study has shown that the temperature is higher for bifacial modules only when the rear irradiance is higher than 15% of the front one. Therefore, such situation depends on the installation conditions, in particular on the the albedo value.

However, a positive bifacial gain is always guaranteed also in the most negative temperature scenarios.

Complementary to the electrical ones, thermal models are required for the calculation of solar cells' temperature. A wide variety of options is present in literature, which differ in terms of accuracy and computational time. Similarly to the previous case, the choice of the model is based on the objective of the study and its boundaries in terms of number of locations and time interval considered. A first option consists in the INOCT (Installed Nominal Operating Cell Temperature) model that estimates the cell temperature depending on the installation type, distinguishing direct mounted, stand-off and rack mounted structures [68]. The formula used in this case is expressed in the equation 2.23 [69]. This approach has been implemented in many studies thanks to the low computational time required and the limited number of variables needed [4], [11], [22], [52]. Such conditions are favorable especially in case of global analysis, where many locations have to be simulated and the input data can be less accurate or missing.

$$G_{tot} = G_{front} + G_{rear} \tag{2.22}$$

$$T_{cell} = T_{amb} + \frac{G_{tot}}{G_{NOCT}} \cdot \left(T_{INOCT} - 20^{\circ}C\right) \tag{2.23}$$

Other models have been developed to take into account additional parameters that have an influence on the cell's temperature, e.g. wind speed (ws). In case of Sandia model [62], ws is correlated to the T_{cell} using two empirical variables a and b as shown in equation 2.24. On the other hand, Faiman [70] introduced the variables U_0 and U_1 which represent the conductive and the convective heat transfer components, respectively. This is illustrated in the equation 2.25. A similar model has been introduced by Janssen et al. [71] adapting for bifacial modules the one used in PVSyst. It includes the module's conductivity U_L and the reflection coefficient α_r, as described in equation 2.26.

$$T_{cell} = T_{amb} + G_{tot} \cdot \exp\left(a + b \cdot ws\right) \tag{2.24}$$

$$T_{cell} = T_{amb} + \frac{G_{tot}}{U_0 + U_1 \cdot ws} \tag{2.25}$$

$$T_{cell} = T_{amb} + \frac{\alpha_r \cdot G_{tot} \cdot \left(1 - \eta\right)}{U_L} \tag{2.26}$$

Further complex models can be obtained by taking into account additional variables such as the efficiency value, the transmittance and the absorption coefficient, as proposed by Duffie and Beckman [72] and implemented by Skoplaki and Palyvos [65]. A generalization of this model is recommended by Patel et al. [73] to take into account the sub-bandgap absorption, being more relevant for bifacial modules with respect to the monofacial case. Lastly, complex fluid-dynamics models are also used in thermal modeling of bifacial PV modules [14], [16], [74], which are based on the heat transfer equations [64], [75]. Such models involve a large number of variables and investigate the thermal behaviour of each layer of the solar cell, requiring a significant computational

time.

In conclusion, the studies concerning bifacial PV modeles available in the literature present a large variety of thermal models. Similarly to the optical models, the choice is determined by its application's purpose, in particular by scale of the simulation, e.g. number of locations. Therefore, global analysis prefer fast thermal model such as the INOCT whereas there are studies limited to few locations that have implemented detailed heat transfer models for their simulations.

2.2.6. CHARACTERISTICS OF THE MODEL IMPLEMENTED FOR THIS STUDY

The literature review concerning the main bifacial PV models available in literature have highlighted the main directions that can be taken depending on the specific application. Since the objective of this study is to perform a global analysis to understand the optimal farm configuration, a low computational time is the main requirement.

Concerning the approach to follow while developing the optical model, 2D view factor method represents the only feasible solution to perform a global analysis, i.e. iterating the simulations over a large number of locations. Even though 3D view factor and ray-tracing techniques can lead to more accurate results, the high computational time involved prevents their application in this analysis. However, the large-scale of the PV farms considered in this study decreases the influence of the edge effects on the overall performance, limiting the effect of the 2D assumption. On the other hand, the influence of the racking structure cannot be capture by view factor models. In conclusion, 2D view factor approach seems to be the optimal solution in terms of accuracy and computational time.

In the previous subsection, the effect on the modelling accuracy caused by the non-uniformity of the rear irradiance and the use of spectral data have been discussed. Prior analysis available in literature have highlighted the importance of integrating such aspects in bifacial PV models. Nevertheless, their implementation is limited to small-scale studies, where the simulations are performed only over few locations. This can be noticed in the classification shown in figure 2.18, where the selected global analysis take into account up to one of these two aspects [4], [11], [21], [25], [73], [76]. In particular, their models usually consider the irradiance incident in the middle of the module as representative for the entire surface and the spectral impact is either included through a corrective coefficient or neglected. These limitations arises from the necessity to have a low computational time that enables a worldwide analysis. On the other hand, including such aspects entails extending the dimensions over the problem from one to three, since in addition to the time dimension, a spatial and a spectral dimension should be added. This means that besides calculating the incident irradiance for every hour (time dimension), such calculation should be iterated for every cell along the module's surface (spatial dimension) and for every wavelength of the spectrum (spectral dimension). The challenge of this work consists in integrating such aspects while limiting their effect on the computational time. A multi-dimensional matrix approach will be introduced to achieve this goal by taking advantage of the matrix nature of MATLAB software.

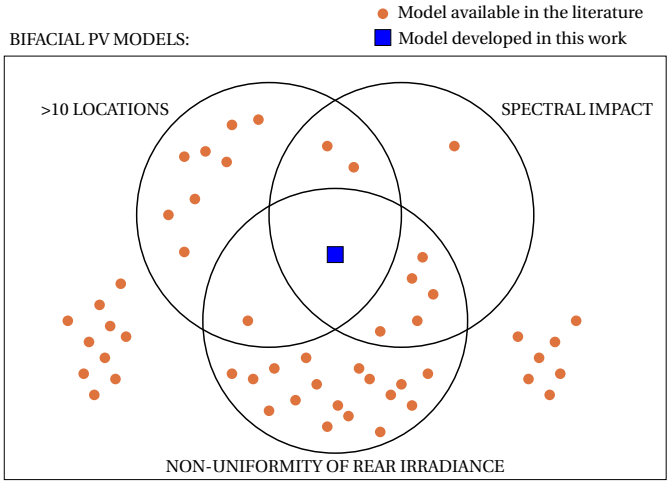

Figure 2.20: Venn diagram of the bifacial PV models available in literature

The previous discussion is summarized by the Venn diagram in figure 2.20, where the gap concerning existing bifacial PV models is evident. Therefore, the purpose of this study is to create a model positioned in the middle of the diagram, which considers both the effect of the non-uniformity of rear irradiance and the spectral impact while performing a global analysis.

Another peculiarity of the model that will be developed during this study is the possibility of selecting different design parameters for every row of the PV farm, i.e. tilt, height and row-to-row distance. The purpose of this feature is to enable the simulation of PV farm with unconventional configurations, which can be either the outcome of forced restrictions during the design phase or an experimental test to obtain beneficial effects on the power curve of the PV farm. However, such additional feature requires the extension of the problem to a fourth spatial dimension, since the irradiance calculation would also be iterated along the different rows of the farm. As described in the previous paragraph, the aim of this work is to develop a multi-dimensional matrix approach, hence the additional dimension should not impact the performance of the model significantly.

Concerning the choice of the thermo-electrical model, different possibilities will be tested in order to find the optimal solution. The choice will be led by two different criteria. The first criterion concerns the availability of the data required for the simulations whereas the second criterion is related to the computational time, which should not exceed the order of magnitude of the optical model.

3

METHODOLOGY

This chapter describes the methodology adopted in this work to answer the research questions introduced in chapter 1, which concern the development a model to simulate a bifacial PV farm and to investigate the optimal configuration. In particular, in this chapter the modelling phase is explained in detail. Section 3.1 focuses on the optical model, whose purpose is to estimate the irradiance incident on both sides of the modules. Subsequently, the thermo-electrical model that converts the irradiance information into electrical power is outlined in section 3.2. Then, an elementary model for the electricity market is developed to compare different farm configurations not only in terms of energy yield but also under an economical perspective. This is described in section 3.3. In conclusion, the selection of the appropriate database for gathering input data used in the simulations is discussed in section 3.4.

3.1. OPTICAL MODEL

This section describes of the optical model that estimates the irradiance incident on the modules of a bifacial PV farm, appointed also as irradiance model. It has been implemented in MATLAB and the various choices and assumptions arises from the literature review of different studies outlined in chapter 2. This section is organized as follows. First, subsections 3.1.1 and 3.1.2 outline the main characteristics of the model and its structure, which assure the optimal trade-off between the computational performance and the accuracy of the output. In the subsection 3.1.3, the method used to calculate the irradiance components is explained, whereas subsection 3.1.4 describes the algorithm developed to identify the portions of shaded ground below the modules. Subsection 3.1.5 explains the process used to recognize the different elements seen by a PV cell within its angular view. Lastly, subsections 3.1.6, 3.1.7 and 3.1.8 describe the methods adopted to calculate the sky irradiance, the irradiance reflected by the ground and by the neighbouring modules, respectively.

3.1.1. MAIN CHARACTERISTICS AND ASSUMPTIONS

The main characteristics of the model have already been introduced in subsection 2.2.6 and are summarized in the following list:

- 2D view factor approach
- Calculation of the incident irradiance on cell level
- Spectral irradiance is considered

Concerning the approach to adopt for the optical model, view factor and ray-tracing have been considered. The literature review presented in subsection 2.2.1 has shown that the increase in accuracy obtained by the latter technique requires a significant computational time, hence it is not applicable for a global analysis where many simulations are performed. On the other hand, the former method neglects the influence of elements such as the racking structure. The view factor approach is also limited to the 2D approximation, increasing the speed of the algorithm by neglecting the edge effects. However, the impact of such simplification decreases when considering large-scale farms, which aligns with the objective of this research.

The other two characteristics, i.e. the calculation of irradiance on cell level and the use of spectral values, are implemented to take into account the effect of the non-uniformity of rear irradiance and the spectral impact, respectively. In the literature review it has been shown that such effects have a significant impact on the accuracy of the model, hence their neglect would decrease the reliability of the outcome of this analysis. As mentioned in subsection 2.2.6, this involves an increase in the dimension of the problem, which is tackled using the MATLAB functionalities for matrix calculation.

As introduced in subsection 2.2.6, this model allows to test unconventional configurations enabling different design parameters at each row. Unlike most of the models found in literature, where the irradiance incident on a module's row is multiplied for the total number of rows to obtain the total farm values, the process is iterated for each row individually. Such feature allows the user to select different tilt, height and distance values at each row. The challenge consists in performing such iteration through matrix calculations without limiting the performance of the model in terms of computational time.

3.1.2. STRUCTURE OF THE MODEL

In this section, the main structure of the irradiance model is outlined, focusing on the input required to calculate the irradiance on each solar cell, which is the output of the model. Flowcharts are used to understand the operating logic of the algorithm and the strategy implemented to achieve efficient computational performance is mentioned.

INPUT

The input of the irradiance model can be distinguished in the following categories:

- Specifications of the PV modules: the length of the modules (l) and the cells (c) are used as input as well as the reflectivity (r) of the PV modules.

- Design parameters of the PV farm: these include for each row of modules the tilt angle (θ), the orientation angle (A_m), the elevation from the ground (h) and the distance (d) between each row.
- Ground segmentation parameters: the length (g) of the ground segments and the extension (ext) that defines the boundaries of the considered ground determine the accuracy of the calculations. Further details about these variables are included in subsection 3.1.4.
- Meteorological and location-specific parameters: both the information about the irradiance intensity, namely direct normal irradiance (DNI) and diffuse horizontal irradiance (DHI), and the sun's position, i.e. sun's altitude (a_s) and sun's azimuth (A_s), are required as input for the model. Furthermore, the atmospheric pressure (p) and the day of the year (doy) are necessary to calculate the different irradiance components. Lastly, the ground albedo (ρ) is the location-specific key parameter that determines the ground reflected irradiance, which ensures the higher irradiance for bifacial modules with respect to their monofacial counterpart. For the ground albedo values, as well as for DNI and DHI, the model enables the use of spectral values to increase the accuracy of the output.

Table 3.1 summarizes the input required by the optical model.

OUTPUT

The output of the optical model consists in the incident irradiance on the PV modules emitted or reflected by different sources:

- Sky irradiance
- Irradiance reflected by the ground
- Irradiance reflected by the neighbouring modules

These irradiance values are calculated for the front side as well as for the rear side of the PV modules. Moreover, the spatial resolution of the output is on cell level, i.e. different values of irradiance are obtained for each solar cell that constitute the modules, highlighting the non-uniformity typical of rear irradiance of bifacial PV modules. In case spectral values are used as input for DNI, DHI and ground albedo, these output values are given for the provided spectral range. Table 3.2 summarizes the output that can be calculated through this optical model.

FLOWCHART

The structure of algorithm developed in MATLAB to implement the irradiance model is outlined in figure 3.1. As depicted in the figure, the main model can be divided into three different sections. First, the irradiance components are calculated using the Perez model [77], as it will be discussed in subsection 3.1.3. Second, a segmentation of the ground is performed, calculating the sky view factor of each ground segment, also identified as

Table 3.1: Input of the optical model

Category of input	Input parameter	Symbol	Unit	Comments
PV modules' specifications	Module's length	l	$[m]$	
	Cell's length	c	$[m]$	
	Module's reflectivity	r	$[-]$	
Design parameters of the PV farm	Orientation	A_m	$[°]$	Only one value can be used for the whole farm
	Tilt	θ	$[°]$	Different values can be assigned to each row
	Row-to-row distance	d	$[m]$	Different values can be assigned to each row
	Height	h	$[m]$	Different values can be assigned to each row
Ground segmentation parameters	Length of ground segment	g	$[m]$	
	Ground extension	ext	$[m]$	
Meteorological and location-specific parameters	Direct normal irradiance	DNI	$[W/m^2]$, $[W/m^2nm]$	Spectral data are supported
	Diffuse horizontal irradiance	DHI	$[W/m^2]$, $[W/m^2nm]$	Spectral data are supported
	Sun's azimuth	A_s	$[°]$	
	Sun's altitude	a_s	$[°]$	
	Day of the year	doy	$[day]$	
	Atmospheric pressure	p	$[Pa]$	
	Ground albedo	ρ	$[-]$	Spectral data are supported

Table 3.2: Output of the optical model

Output parameter	Symbol	Unit	Comments
Sky irradiance incident on the front cells	$I_{front,sky}$	$[W/m^2]$, $[W/m^2nm]$	Spectral values are supported
Sky irradiance incident on the rear cells	$I_{rear,sky}$	$[W/m^2]$, $[W/m^2nm]$	Spectral values are supported
Ground reflected irradiance incident on the front cells	$I_{front,ground}$	$[W/m^2]$, $[W/m^2nm]$	Spectral values are supported
Ground reflected irradiance incident on the rear cells	$I_{rear,ground}$	$[W/m^2]$, $[W/m^2nm]$	Spectral values are supported
Irradiance incident on the front cells reflected by neighbouring modules	$I_{front,mod}$	$[W/m^2]$, $[W/m^2nm]$	Spectral values are supported
Irradiance incident on the rear cells reflected by neighbouring modules	$I_{rear,mod}$	$[W/m^2]$, $[W/m^2nm]$	Spectral values are supported

shaded or unshaded. A detailed description of this step is present in subsection 3.1.4. Lastly, the different incident irradiance components are calculated. This part can be divided into two separate sub-models and their flowcharts are depicted in figures 3.2 and 3.3, respectively. Both sub-models begin with the identification of the field of view of the solar cells to the different elements, i.e. sky, ground and neighbouring modules, which is explained in subsection 3.1.5. Subsequently, the first sub-model calculates the incident sky irradiance and ground reflected irradiance, as described in subsections 3.1.6 and 3.1.7. On the other hand, the second sub-module uses these values to estimate the incident irradiance on each cell due to the reflections from the neighbouring modules. This is further described in subsection 3.1.8.

MULTI-DIMENSIONAL MATRIX APPROACH AND DECOUPLING

As anticipated in the previous sections, the challenge concerning the trade-off between accuracy and computational time is tackled through a multi-dimensional matrix approach. This is based on the MATLAB feature that facilitates matrix calculations. Therefore, the strategy adopted in this model consists in the use a four-dimensional matrix as a base unit to perform the calculations: the first dimension represents the modules' row within the farm, the second dimension refers to the position of the cell within the module, then multiple time periods are considered simultaneously along the third dimension, and lastly the fourth dimension represents the wavelength of the spectrum.

Such method involves calculations between matrices up to the sixth dimension, for instance when the segmentation of the ground and different angular sectors add two additional dimensions to the operations. This method increases the complexity of the algorithm, e.g. if-statements and loops are replaced by logical matrices or other operations. However, the computational speed is increased up to 20 times for a 4-rows farm and the benefits of this approach are expected to be even more evident in case of larger farms' simulations.

Despite the significant increase in the performance, preliminary tests have shown that the computational time required for a global simulation was still substantial and therefore improvements were needed. For this purpose, a new version of the algorithm have been developed which is based on the decoupling of the different dimensions. In particular, such decoupling regards the spectral dimension and it is achieved by assuming that the shape of the spectrum of the different irradiance components is not dependent on time. This methods aligns with the input data available which will be extensively described in section 3.4. The main difference while implementing this modification consists in the output of the optical model. These are integrated values that are used in the thermo-electrical model not only to obtain the broadband value of incident irradiance, but also as weights to find the proper shape of the spectrum.

3.1.3. IRRADIANCE COMPONENTS

The purpose of this section is to outline the procedure adopted to calculate the different components of the irradiance incident on the elements of the PV farm. This method is based on the work of Perez et al. [77] and described in [78], widely known as Perez Sky

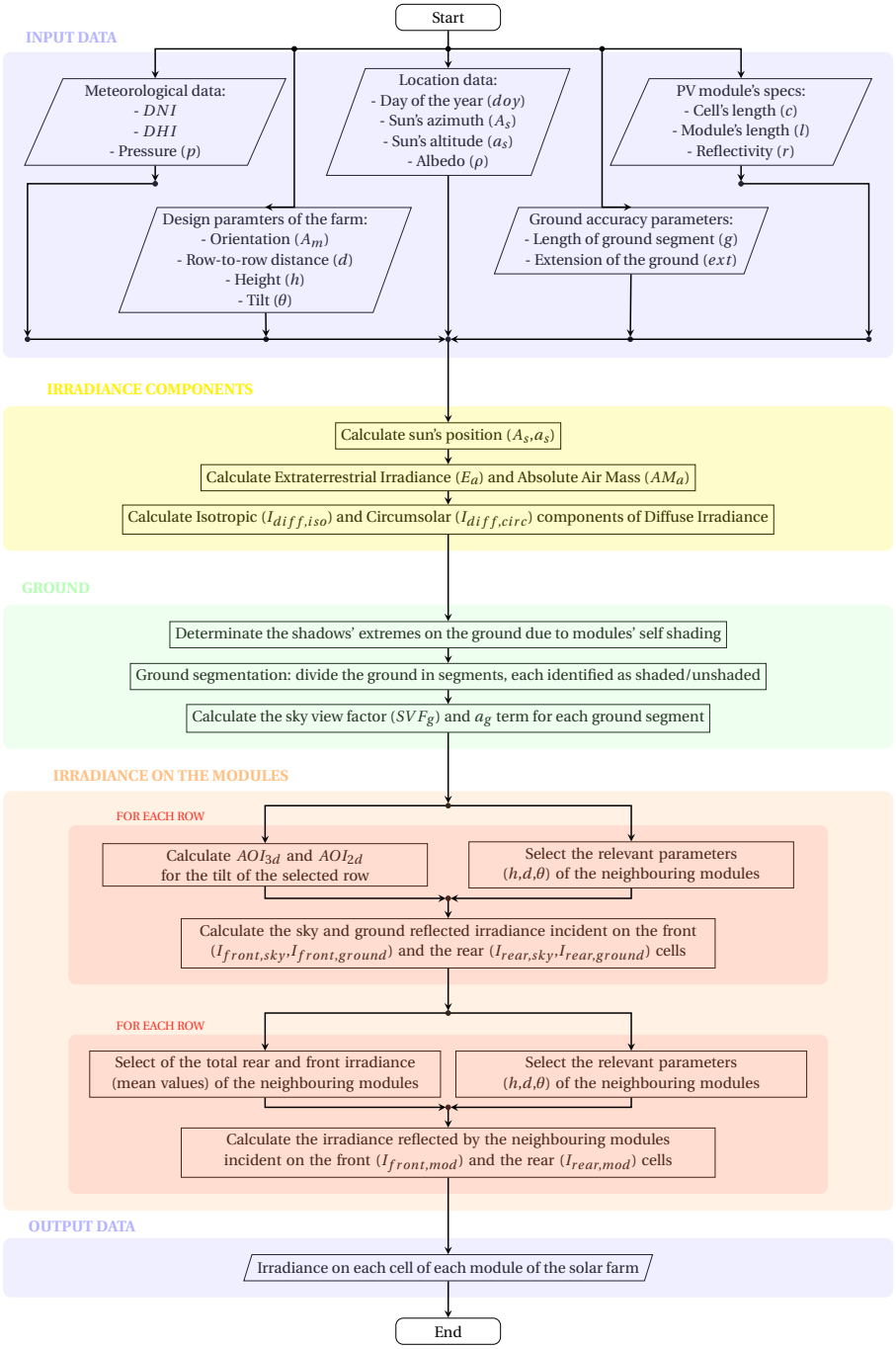

Figure 3.1: Flowchart of the optical model

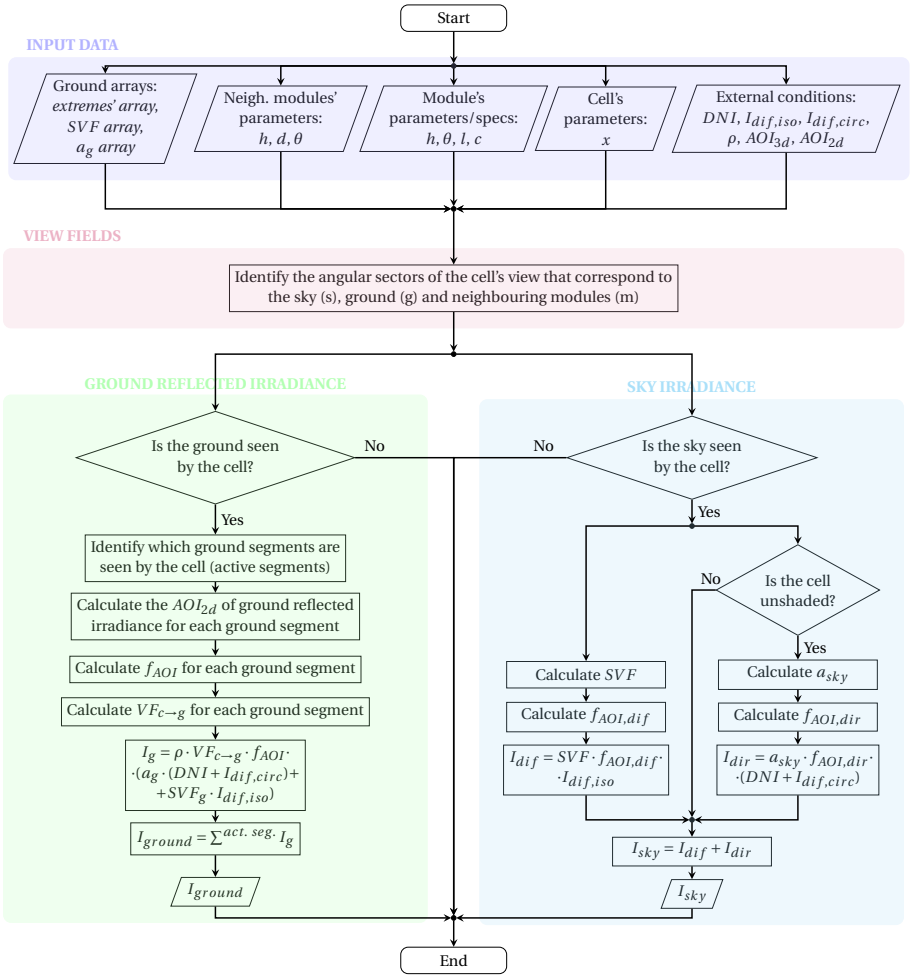

Figure 3.2: Flowchart of the sub-model to calculate sky and ground irradiance

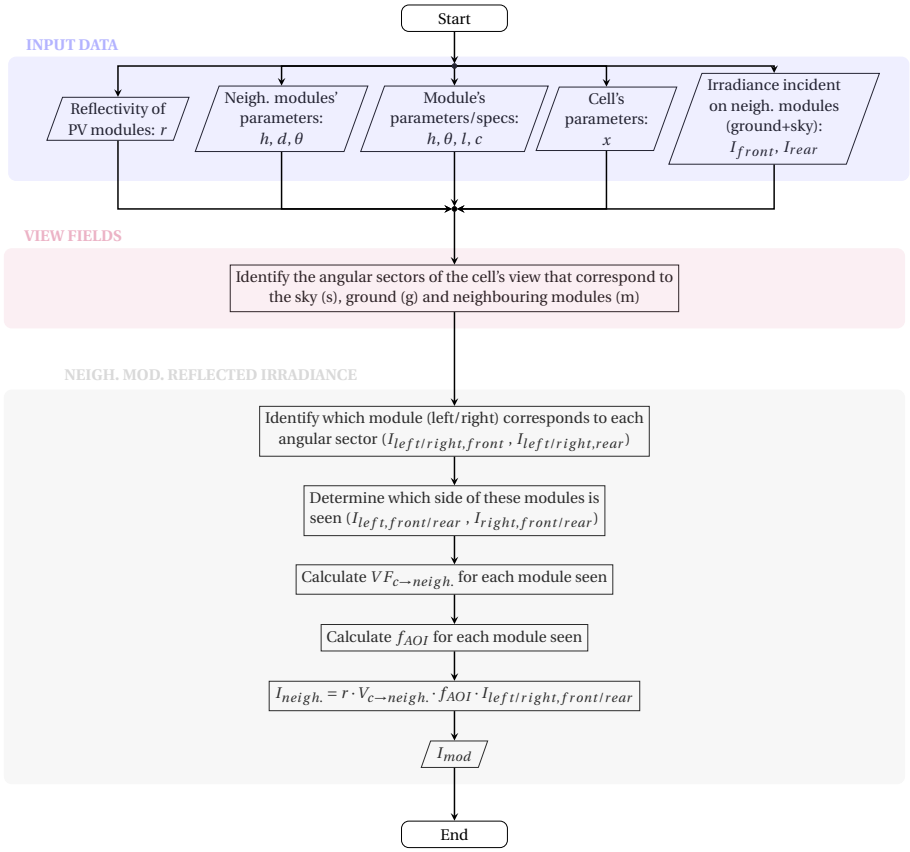

Figure 3.3: Flowchart of the sub-model to calculate the irradiance reflected by the neighbouring modules

Diffuse Model. This allows the distinction between three different components of diffuse irradiance, namely isotropic ($I_{dif,iso}$), circumsolar ($I_{dif,circ}$) and horizon ($I_{dif,hor}$), which are described in equations 3.1, 3.2 and 3.3, respectively. Unlike the expressions described in [78], these parameters are defined for a surface perpendicular to the direct irradiance direction ($\cos(AOI) = 1$) characterized by a sky view factor equal to 1. The information concerning the angle of incidence and the sky view factor will be included separately for each element.

$$I_{dif,iso} = DHI \cdot (1 - F_1) \tag{3.1}$$

$$I_{dif,circ} = DHI \cdot F_1 \cdot \left(\frac{1}{b}\right) \tag{3.2}$$

$$I_{dif,hor} = DHI \cdot F_2 \cdot \sin(\theta) \tag{3.3}$$

The coefficients b, F_1 and F_2 have been calculated using the formulas provided by [78], which depend on the sun's altitude (a_s), the extraterrestrial radiation (E_a) and the absolute air mass (AM_a). The latter parameters require the atmospheric pressure (p) and the day of the year (doy) to be calculated.

3.1.4. GROUND

The presence of PV arrays prevents part of irradiance to reach the ground, causing a shadows' pattern that depends on the configurations of the farm and its geometrical parameters. This subsection aims to identify each portion of the ground as shaded or unshaded and to calculate its sky view factor. In this model, a horizontal ground surface is considered and the shadows created by the mounting structure of the modules are neglected.

IDENTIFICATION OF THE SHADOWS ON THE GROUND

Considering the 2D model introduced in the previous sections, the first step consists in the calculation of the projections of the direct sun rays to the ground surface, in order to determine the extremes of the different shadows. These are calculated for each module of the farm, using the equations 3.4, and 3.5.

$$y_1 = \frac{h - \frac{l}{2}\sin(\theta)}{\tan(\phi_s)} - \frac{l}{2}\cos(\theta) \tag{3.4}$$

$$y_2 = \frac{h + \frac{l}{2}\sin(\theta)}{\tan(\phi_s)} + \frac{l}{2}\cos(\theta) \tag{3.5}$$

These formulas refer to the a reference system centered on the middle point of the array, hence the extremes are then shifted accordingly. Due to the 2D geometric assumption of the model, ϕ_s is the projected angle of the sun's rays that depends on a_s and A_s through the relation 3.6.

$$\phi_s = \max\left[0, \arctan\left(\frac{\tan(a_s)}{\cos(A_m - A_s)}\right)\right] \tag{3.6}$$

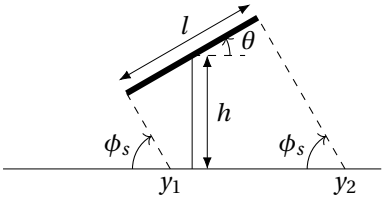

Figure 3.4: Extremes of the shadow on the ground

SEGMENTATION OF THE GROUND

By applying the procedure explained in the previous section, an array of segments containing the binary information shaded/unshaded is obtained. The length of such segments is relatively large, i.e. they have the same order of magnitude of the PV modules' length. Such information is used to determine whether each ground portion receives both direct and diffuse irradiance or only the latter component.

To quantify the diffuse irradiance incident on the ground, the sky view factor (SVF_g) has to be calculated, which defines the portion of the sky seen by the ground. Unlike the shadows' information, SVF_g is a continuous function along the spatial coordinate that depends on the geometrical configuration of the PV farm, hence adopting a single value for each shaded or unshaded ground's section would decrease significantly the accuracy of the results. For this purpose, a segmentation of the ground is performed. This means that the ground below the PV farm is divided into small segments characterized by a length g, which is an input parameter of the model that determines the accuracy of the results. In this model, it is assumed that a segment is considered shaded only if completely included in the boundaries of shadows caused by the PV arrays. However, the error caused by this assumption is negligible until g is kept sufficiently small.

Another parameter that defines the accuracy of the model at this stage is the extent (ext) of the ground that is considered at the boundaries of the PV farm. This is given as input to the model and determines the extremes (y_{start}, y_{end}) of the ground that is divided into segments with a length g, as described in the equations 3.7. $y_{1,1}$ and $y_{2,n}$ indicate the first extreme of the shadow caused by the first row and the second extreme of the shadow caused by the last row, respectively.

$$y_{start} = y_{1,1} - ext \qquad y_{end} = y_{2,n} + ext \tag{3.7}$$

For all these segments the SVF_g is calculated as explained in the next section. Moreover, two semi-infinite segments are added at the beginning and at the end of the array, which are characterized by $SVF_g = 1$ and considered unshaded. This means that the farm is assumed not to be surrounded by other shading objects.

SKY VIEW FACTOR OF GROUND'S SEGMENTS

As introduced in the previous subsection, the diffuse light does not penetrate uniformly to the ground below the PV array since the portion of the sky seen differs for each ground

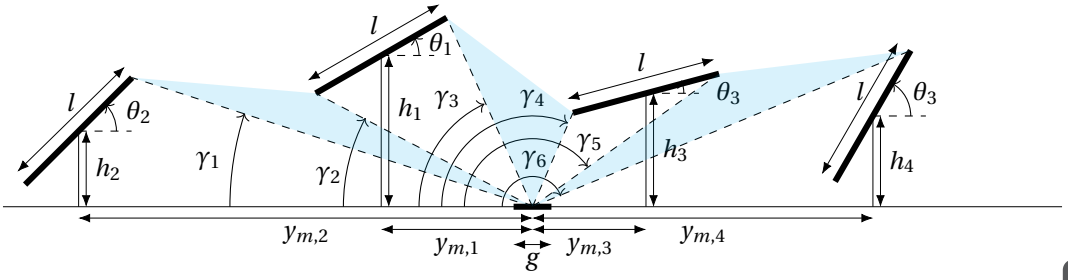

Figure 3.5: Sky view factor of a ground segment

segment. This information is expressed through the SVF_g, which is therefore calculated for each ground segment. In this model it is assumed that every ground segment can see the sky only through the three gaps between the four nearest modules' row, as described in figure 3.5.

First, the angles between the mid-point of the ground segment and the extremes of the four relevant modules are determined. These angles $\gamma_1 - \gamma_6$ are highlighted in figure 3.5 and can be determined from the geometrical parameters of the farm through the expressions included in the Appendix B. As depicted in figure 3.5, the model allows unconventional configurations where different modules' height, tilt angles and distances can be used within the same PV farm. The SVF_g is determined using the expression 3.8, which is based on Hottel's cross string rule and considers the three angular sectors mentioned in the previous paragraph.

$$SVF_g = \frac{\cos(\gamma_1) - \cos(\gamma_2)}{2} + \frac{\cos(\gamma_3) - \cos(\gamma_4)}{2} + \frac{\cos(\gamma_5) - \cos(\gamma_6)}{2} \tag{3.8}$$

SHADED/UNSHADED INFORMATION FOR GROUND'S SEGMENTS

In addition to the SVF_g that is used to determine the contribution of isotropic diffuse components, a_g is calculated for each ground's segment, as shown in equation 3.9. This coefficient is used to quantify the amount of direct and circumsolar diffuse irradiance components incident on the ground segments.

$$a_g = \begin{cases} 0 & \text{if the segment is shaded} \\ \max\left(0, \cos(AOI_g)\right) & \text{if the segment is unshaded} \end{cases} \tag{3.9}$$

AOI_g is the angle of incidence of the solar radiation on the ground segment. Since a horizontal surface is assumed, the expression for $\cos(AOI_g)$ simplifies as described in equation 3.10.

$$\cos(AOI_g) = \sin(a_s) \tag{3.10}$$

3.1.5. FIELD OF VIEW OF THE SOLAR CELLS

The estimation of the irradiance received by each cell on both sides of a PV module requires an accurate calculation of the "field-of-view" of each solar cell. This means that all the elements seen by each cell have to be identified in order to calculate the view factors correspondent to each element, which are discussed in the next sections separately. In this model such elements are limited to the sky, the ground and the neighbouring modules, since it is assumed that there are not other surrounding objects that influence the performance of the PV farm. Furthermore, to limit complexity of the model, only the two neighbouring modules are considered while determining the field-of-view, i.e. one module on the left and one module on the right with respect to the module that is examined. Due to the two-dimensional assumption of the model, the view of a solar cell is limited to 180° and each element seen by the cell can be identified through an angular sector within this range. Therefore, the objective of this section is to obtain such 180° field of view for each cell of the farm, where the angular range of each element seen by the cell is specified. An example is provided for a front cell and a rear cell in figures 3.6 and 3.7, respectively.

The procedure to calculate the field of view can be summarized as follows. First, the angles between the cell and each of the relevant neighbouring modules are determined. They depend on the geometrical parameters of the PV farm, namely the height (h_1, h_2, h_3) and the tilt angles $(\theta_1, \theta_2, \theta_3)$ of the neighbouring modules that are considered, as well as the row-to-row distances (d_1, d_2), the position of the cell (x) and its length (c). These relations are described in the equations B.11-B.18 provided in the Appendix B, which refer to the cases depicted in the figures 3.6 and 3.7. In case of unconventional configurations, the algorithm sorts the angles appropriately and limit their values in the range $[0° - 180°]$. Lastly, the angular sectors indicating the boundaries of the elements within the view range of the cell are calculated. Each of these angular sectors is associated to its correspondent element (sky, ground or neighbouring modules).

3.1.6. SKY IRRADIANCE

In this subsection the method used to calculated the sky irradiance is explained. From the field-of-view obtained in the previous step, the algorithm individuates for each cell the angular sector that corresponds to the sky, irrespective it belongs to the front or the rear side. Such information is used to determine whether the cell is shaded or unshaded. For this purpose, the projection of the angle of incidence (AOI_{2d}) is calculated, as shown in equations 3.11 and 3.12, which refer to a front and a rear cell, respectively. As it can be observed in these equations, the reference system is chosen in order to match the definition of the field-of-view, which differ from the traditional definition of the three-dimensional AOI mentioned in other sections. In case such angle lies in the sky angular sector, the cell is considered unshaded, otherwise it is marked as shaded. In the latter situation, only the isotropic diffuse irradiance is received by the cell otherwise also the direct component and the circumsolar component of diffuse irradiance are considered.

$$AOI_{2d,f} = \arctan\left(\frac{\sin(a_s)}{\cos(a_s)\cdot\cos(A_s - A_m)}\right) + \theta \tag{3.11}$$

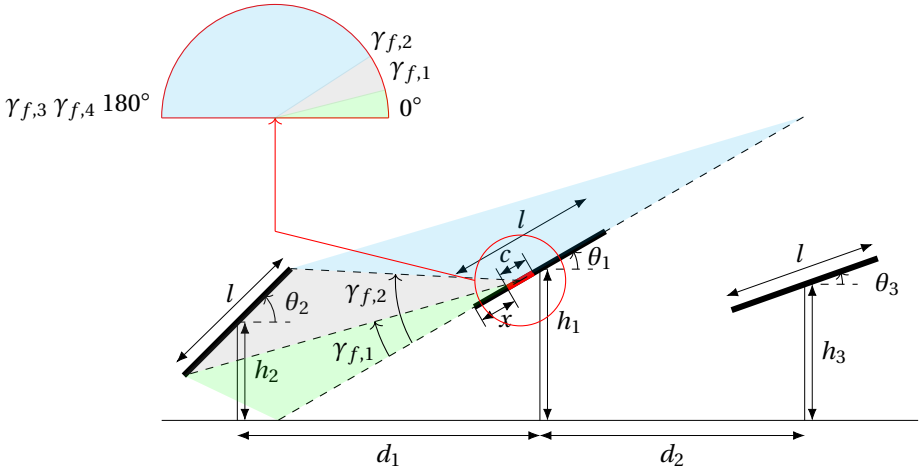

Figure 3.6: Field of view: example of front cell

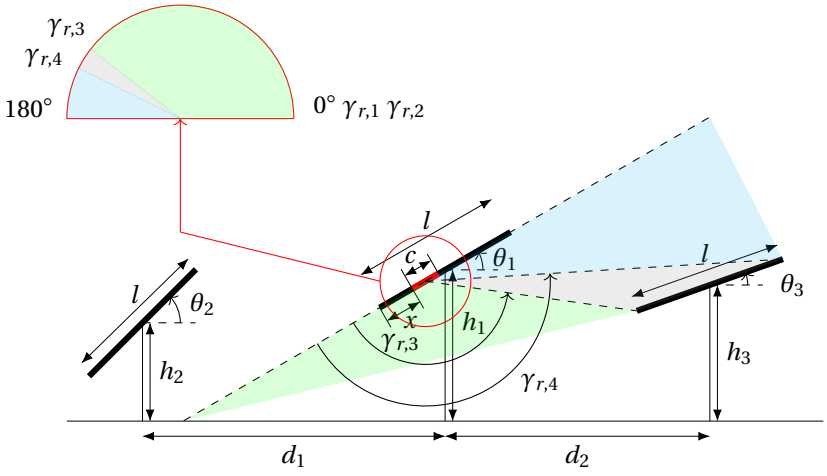

Figure 3.7: Field of view: example of rear cell

$$AOI_{2d,r} = -\arctan\left(\frac{\sin(a_s)}{\cos(a_s)\cdot\cos(A_s - A_m)}\right) - \theta \tag{3.12}$$

The total sky irradiance incident on a cell is calculated using equation 3.13. The term $I_{dif,hor}$ is not included in this expression since it is neglected due to its limited contribution, similarly to [5].

$$I_{sky} = a_{sky}\cdot f_{AOI,dir}\cdot(DNI + I_{dif,circ}) + SVF\cdot f_{AOI,dif}\cdot I_{dif,iso} \tag{3.13}$$

The a_{sky} factor includes the information about the angle of incidence and whether the cell is shaded or unshaded. This is shown in equation 3.14, where AOI refers to the widely defined angle of incidence, defined in 3.15 and 3.16 for a front and a rear cell, respectively.

$$a_{sky} = \begin{cases} \cos(AOI) & \text{if the cell is unshaded} \\ 0 & \text{if the cell is shaded} \end{cases} \tag{3.14}$$

$$\cos(AOI_f) = \sin(\theta)\cdot\cos(a_s)\cdot(A_m - A_s) + \cos(\theta)\cdot\sin(a_s) \tag{3.15}$$

$$AOI_r = \pi - AOI_f \tag{3.16}$$

The terms $f_{AOI,dir}$ and $f_{AOI,dif}$ are the AOI correction factors for the direct and the diffuse irradiance. These are based on the theory of Martin and Ruiz [79] hence the formula 3.17 is used. The AOI_{2d} follows the reference system mentioned previously. The coefficient a_r is set equal to 0.155, referring to a technology's configuration Air/glass/SiO/Si. Unlike to $f_{AOI,dir}$ where the angle of incidence is used, $f_{AOI,dif}$ refers to the entire angular sector of the sky within the field-of-view of the cell. Therefore, the average between the f_{AOI} of a one-degree-resolution series of angles within the extremes of the angular sector is adopted. An example of the dependence of f_{AOI} on the angle of incidence is shown in figure 3.8.

$$f_{AOI} = \frac{1 - \exp\frac{-\sin(AOI_{2d})}{a_r}}{1 - \exp\frac{-1}{a_r}} \tag{3.17}$$

Lastly, the SVF is calculated using the angles that defines the sky angular sector of the field-of-view, indicated in equation 3.18 as γ_1 and γ_2.

$$SVF = \frac{\cos(\gamma_1) - \cos(\gamma_2)}{2} \tag{3.18}$$

3.1.7. GROUND-REFLECTED IRRADIANCE

The irradiance incident on the ground and reflected to the PV modules represents a significant component in bifacial modules, giving the highest contribution for the rear side irradiance in conventional configuration. Therefore, an accurate estimation of the ground reflected irradiance is essential to calculate the total irradiance incident on bifacial PV modules.

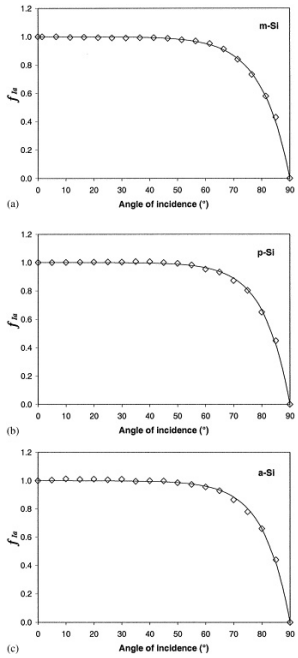

Figure 3.8: AOI corrective factor for various technologies [79]

As explained in section 3.1.4, a ground segmentation has been performed and the factors a_g and SVF_g have been calculated for every ground segment, which determine the amount of direct and diffuse component of incident irradiance. Depending on the geometrical configuration of the PV farm, the view of each cell is limited to certain number of ground segments. Therefore, to calculate the total ground reflected irradiance that is incident on a specific solar cell, the segments seen by such cell are selected. These segments are appointed as "active segments". They can be obtained from the field-of-view of each cell, considering the angular sector that corresponds to the ground, as described in subsection 3.1.5. From such angular sector, the extremes that delimit the active segments are obtained, irrespective of the fact that the cell belongs to the front or the rear side of the module. An example is shown in figure 3.9. The algorithm recognizes as active only the cells that are completely enclosed in ground view of the cell, hence a segment that is crossed by the projection of the view is considered inactive. The ground reflected irradiance incident on a cell is calculated using the equation 3.19, where the contribution of all the active segments is summed.

$$I_{ground} = \rho \cdot \sum_{\substack{\text{active} \\ \text{segments}}} f_{AOI} \cdot VF_{c \to g} \cdot \left(a_g \cdot (DNI + I_{dif,circ}) + SVF_g \cdot I_{diff,iso} \right) \tag{3.19}$$

The factor f_{AOI} indicates the AOI correction calculated using equation 3.17, where the angle of incident depends on the positions of the segment and the cell. For this purpose, the middle points of the cell and the ground segment are considered. SVF_g and a_g

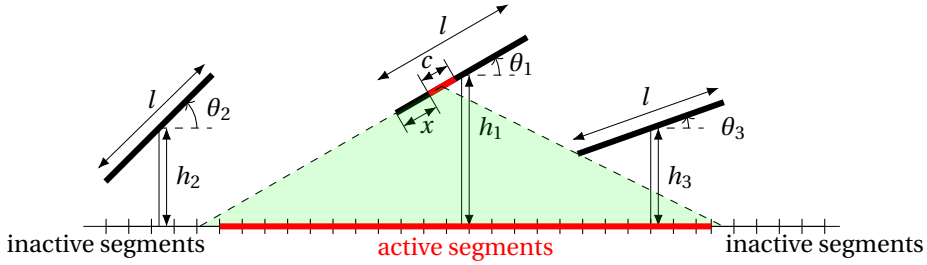

Figure 3.9: Ground active segments

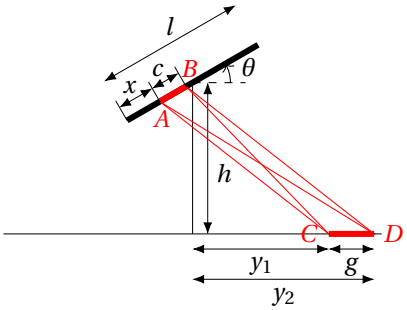

Figure 3.10: View factor between a cell and a ground segment

determine the amount of irradiance received by each segment and they are calculated using the expressions 3.8 and 3.9, as discussed in subsection 3.1.4. Lastly, $VF_{c\to g}$ is the view factor between the cell and the ground segment considered. It is calculated using Hottel's cross strings rule, as shown in equations 3.20-3.24 and described in figure 3.10.

$$AC = \sqrt{\left(h + \left(x - \frac{l}{2}\right)\cdot\sin(\theta)\right)^2 + \left(y_1 - \left(x - \frac{l}{2}\right)\cdot\cos(\theta)\right)^2} \tag{3.20}$$

$$AD = \sqrt{\left(h + \left(x - \frac{l}{2}\right)\cdot\sin(\theta)\right)^2 + \left(y_2 - \left(x - \frac{l}{2}\right)\cdot\cos(\theta)\right)^2} \tag{3.21}$$

$$BC = \sqrt{\left(h + \left(x - \frac{l}{2} + c\right)\cdot\sin(\theta)\right)^2 + \left(y_1 - \left(x - \frac{l}{2} + c\right)\cdot\cos(\theta)\right)^2} \tag{3.22}$$

$$BD = \sqrt{\left(h + \left(x - \frac{l}{2} + c\right)\cdot\sin(\theta)\right)^2 + \left(y_2 - \left(x - \frac{l}{2} + c\right)\cdot\cos(\theta)\right)^2} \tag{3.23}$$

$$VF_{c\to g} = \frac{BC - AC + AD - BD}{2\cdot c} \tag{3.24}$$

3.1.8. IRRADIANCE REFLECTED BY THE NEIGHBOURING MODULES

Not all the light that is incident on the PV modules is effectively absorbed since a limited fraction is transmitted or reflected. Although the contribution of the latter is marginal, it has to be considered for an accurate estimation of the irradiance. This section aims to model the irradiance reflected by the neighbouring modules that affects the total irradiance incident on a cell.

First, the modules seen by the specific cell have to be identified from its field of view. In particular, the angular sectors of the field of view that correspond to a neighbouring module are recognized by the algorithm. The position of these modules with respect to the considered cell is determined from their geometric parameters. Only two neighbouring modules are considered to limit the complexity of the model, i.e. one module on the left and one on the right. This assumption is inherited from the definition of the field of view in subsection 3.1.5. Furthermore, the algorithm associates each of these modules to the side (front or rear) seen by the cell. This step is trivial for conventional configurations of PV farms whereas it requires a procedure that depends on the geometric parameters in case of unconventional cases, which are allowed by this model. The identification of the neighbouring modules and their sides seen by the cell is required to quantify the irradiance incident on them that is reflected to the considered cell. Such irradiance is the sum between the sky and the ground reflected irradiance calculated in subsections 3.1.6 and 3.1.7 for each cell of every module of the farm. Although different spatial values have been calculated for each module, an average incident irradiance is considered to limit the complexity of the problem. This is indicated as $I_{incident\ neigh\ mod}$ in equation 3.25, where the irradiance reflected by the neighbouring modules that is incident on a solar cell is calculated. This expression also includes the view factor between the cell and the neighbouring module ($VF_{c\rightarrow m}$) and the AOI correction factor (f_{AOI}), defined in equation 3.17. The latter parameter is calculated similarly to the isotropic diffuse sky component since such irradiance is coming from an angular sector instead of a specific angle.

$$I_{mod} = r \cdot VF_{c\rightarrow m} \cdot f_{AOI} \cdot I_{incident\ neigh\ mod} \tag{3.25}$$

The parameter r is the reflectivity of the PV modules, which depends on the specific PV technology. In this research it is assumed to be equal to 0.1 and it can be considered representative of each technology since its influence to the total irradiance estimation is marginal. Moreover, in case of spectral data the value of r is assumed to be constant for every wavelength.

The calculation of $VF_{c\rightarrow m}$ is based on Hottel's cross string rule. The expression used for this purpose depends on the few cases based on the geometric configuration of the farm, for instance whether the module on the right or the module on the left is seen by the cell. The complexity is increased by allowing the possibility that the view of the neighbouring module can be limited due to the tilt of cell. Therefore, equations 3.26-3.29 refer to the conventional case depicted in figure 3.11 and define the coordinates of the points used to calculate $VF_{c\rightarrow m}$. Symbols ξ_1 and ξ_2 in equations 3.28 and 3.29 indicate the angles between the lines that connect the extremes of the cell and the neighbouring

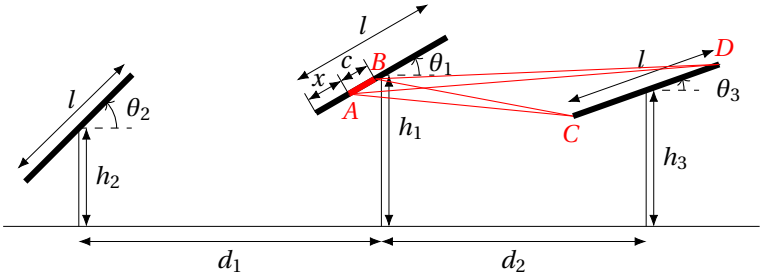

Figure 3.11: View factor between a cell and the neighbouring module

modules with the vertical direction.

$$\begin{cases} x_a = (x - \frac{l}{2}) \cdot \cos(\theta_1) \\ y_a = h_1 + (x - \frac{l}{2}) \cdot \sin(\theta_1); \end{cases} \tag{3.26}$$

$$\begin{cases} x_b = (x - \frac{l}{2} + c) \cdot \cos(\theta_1) \\ y_b = h_1 + (x - \frac{l}{2} + c) \cdot \sin(\theta_1); \end{cases} \tag{3.27}$$

$$\begin{cases} x_c = \frac{-\tan(\xi_1 - \frac{\pi}{2}) \cdot x_a + y_a + \tan(\theta_2) \cdot d_2 - h_3}{\tan(\theta_2) - \tan(\xi_1 - \frac{\pi}{2})} \\ y_c = \tan(\theta_3) \cdot (x_c - d_2) + h_3 \end{cases} \tag{3.28}$$

$$\begin{cases} x_d = \frac{-\tan(\xi_2 - \frac{\pi}{2}) \cdot x_b + y_b + \tan(\theta_3) \cdot d_2 - h_3}{\tan(\theta_3) - \tan(\xi_2 - \frac{\pi}{2})} \\ y_d = \tan(\theta_3) \cdot (x_d - d_2) + h_3 \end{cases} \tag{3.29}$$

From these equations, the length of the segments AC, AD, BC, BD can be easily obtained and $VF_{c \to m}$ is calculated using the expression 3.30.

$$VF_{c \to m} = \frac{BC + AD - AC - BC}{2 \cdot c} \tag{3.30}$$

Lastly, the algorithm also allows configurations where both neighbouring modules, i.e. on the left and on the right, are seen by the same solar cell. This situation could occur for unconventional configurations where the rear cell of a horizontal module has a higher height with respect to the neighbouring modules.

3.2. THERMO-ELECTRICAL MODEL

This section explains the thermo-electrical model used to convert the incident irradiance calculated by the optical model into electrical power. As mentioned during the literature review outlined in subsection 2.2.5, the thermo-electrical model for bifacial PV modules is based on the same principle of the monofacial case, hence no relevant modifications have been added to conventional models widely used so far. However, to take advantage of the method adopted in the optical model, a multi-dimensional matrix approach is implemented also in this case. This section is organized as follows. First, the model chosen to calculate the temperature of the solar cells is explained in subsection

3.2.1. Second, the implementation of two different approaches for the electrical model are described in subsections 3.2.2 and 3.2.3.

3.2.1. TEMPERATURE MODEL

In the literature review phase described in subsection 2.2.5 various thermal models have been analyzed, highlighting their advantages and disadvantages in terms of the trade-off between the computational time and their accuracy. Given these considerations, two criteria have been used to choose the proper thermal model for this analysis. First, the computational time required for the simulations has to be in the same order of magnitude the optical model. Otherwise, the advantages of using a fast matrix-approach-based optical model would be useless. Such criteria excludes all the thermal models that require an iteration between the thermal and the electrical parts to converge towards the solution. Second, the other criteria consists in selecting the methods that involve only variables that are available in the database adopted for this study, which will be explained in section 3.4. Therefore, the most appropriate method is the INOCT concept considering both criteria, which ensures a very fast simulation and the minimum number of variables. On the other hand, the accuracy of this method is supposed to be the lowest among the options presented in subsection 2.2.5, but is sufficient for the scope of the study.

Using INOCT model, the cell temperature is calculated according to the equations 3.31 and 3.32 [68], since a rack mounting configuration is considered. T_{NOCT} is a parameter of the PV module that can be found in the specification sheet whereas G_{NOCT} is equal to 800 W/m^2 from the standards.

$$T_{INOCT} = T_{NOCT} - 3 \tag{3.31}$$

$$T_{cell} = T_{amb} + \frac{G_{tot}}{G_{NOCT}} \cdot \left(T_{INOCT} - 20°C\right) \tag{3.32}$$

G_{tot} is the total irradiance incident on a solar cell and it is calculated by integrating the spectral profile. Due to the bifaciality of the solar cells, both sides have to be considered and the values are summed. This step is described by the equations 3.33, 3.34 and 3.35. The extremes of integration λ_1 and λ_2 are ideally 0 and $+\infty$ but they are usually limited within a certain range that depends on the input spectral data.

$$G_{front} = \int_{\lambda_1}^{\lambda_2} \left[I_{front,sky}(\lambda) + I_{front,ground}(\lambda) + I_{front,mod}(\lambda)\right] d\lambda \tag{3.33}$$

$$G_{rear} = \int_{\lambda_1}^{\lambda_2} \left[I_{rear,sky}(\lambda) + I_{rear,ground}(\lambda) + I_{rear,mod}(\lambda)\right] d\lambda \tag{3.34}$$

$$G_{tot} = G_{front} + G_{rear} \tag{3.35}$$

In case of decoupling of the spectral dimension, the equations to calculate the irradiance follow the same principle but they appear slightly different in practice, since the complete spectrum is created as an intermediate step from the output weights of the optical model.

3.2.2. 1-DIODE ELECTRICAL MODEL

The 1-diode electrical model represents the most popular choice among the studies on PV modules performance, thanks to its optimal trade-off between accuracy and computational time. These are indeed the reasons that have led the choice of following this method.

The first step of this model consists in the calculation of the short-circuit current density (J_{sc}) and the open-circuit voltage (V_{oc}) for each cell of the PV module. These are calculated in the equations 3.36, 3.37, 3.38 and 3.39, where it is assumed a parallel circuit between the front and the rear side.

$$J_{sc,front} = \frac{q}{hc} \cdot \left(1 + k_{J_{sc}} \cdot (T_{cell} - 25°C)\right) \cdot \int_{\lambda_1}^{\lambda_2} I_{front}(\lambda) \cdot EQE_{front}(\lambda)\, d\lambda \tag{3.36}$$

$$J_{sc,rear} = \frac{q}{hc} \cdot \left(1 + k_{J_{sc}} \cdot (T_{cell} - 25°C)\right) \cdot \int_{\lambda_1}^{\lambda_2} I_{rear}(\lambda) \cdot EQE_{rear}(\lambda)\, d\lambda \tag{3.37}$$

$$J_{sc} = J_{sc,front} + J_{sc,rear} \tag{3.38}$$

$$V_{oc} = \left[\frac{V_{oc,specs}}{N_s} + \frac{nk \cdot (T_{cell} + 273\,K)}{q} \cdot \log\left(\frac{G_{tot}}{G_{STC}}\right)\right] \cdot \left(1 + k_{V_{oc}} \cdot (T_{cell} - 25°C)\right) \tag{3.39}$$

In the equations above several terms are present. First, the constants q, h, c, k are the elementary charge, the Planck's constant, the light's speed and the Boltzmann constant, respectively. $k_{J_{sc}}$ and $k_{V_{oc}}$ indicate the current and the voltage temperature coefficients, which can be found on the module's specs, as well as the number of cells connected in series (N_s) and the module's open-circuit voltage ($V_{oc,specs}$). Then, n is the ideality factor, G_{STC} is the irradiance at STC equal to $1000\,W/m^2$ and G_{tot} is the total integrated irradiance calculated in equation 3.35. Lastly, $EQE(\lambda)$ is the external quantum efficiency of the modules, and two different curves for the front and the rear side can be used.

Subsequently, the short-circuit current (I_{sc}) of every cell can be calculated from the dimensions of the cell as shown in equation 3.40. Moreover, the saturation current (I_0) is determined using the equation 3.41.

$$I_{sc} = J_{sc} \cdot l^2 \tag{3.40}$$

$$I_0 = \frac{I_{sc}}{\exp\left(\frac{qV_{oc}}{nk \cdot (T_{cell} + 273\,K)}\right) - 1} \tag{3.41}$$

Even though the short-circuit current is calculated for every cell, the total string current is limited by the cell that receives the lowest irradiance. An imbalance of the incident irradiance among the different cells can be caused by partial shading or non-uniformity

of the rear component and it is tackled by adopting bypass diodes. In this models, three bypass diodes have been implemented for each module, each of them connecting strings of cells whose direction is perpendicular to the plane of interest of the 2D approximation. In other words, the line that represent the PV module in the plane of interest is divided into three different regions, each of them connected to a different bypass diode. Such choice is related to the assumption that the modules are mounted in the landscape configuration, due to the typical connection of bypass diodes in the products available in the market. The implementation of such aspects in the model consists in considering seven different combinations for which the three bypass diodes can be active or inactive. The number of combination is determined as follows: $2^3 - 1$. The number 2 represent the possible status of the bypass diodes, i.e. active or inactive, whereas the 3 is the number of bypass diodes present in one module. Lastly, the result is decreased by one unit since the combination when all the bypass diodes are active is neglected. For each of these seven different combinations the short-circuit current of each cell is recalculated considering the limiting effect of the least illuminated cell in the string, extending the dimension of the problem. The size of this additional dimension is equal to the number of the combinations, namely 7.

The next step consists in the computation of the $I-V$ curve in the model for each cell, considering the different possible combinations of the bypass diodes. The resolution of the $I-V$ curve is a crucial aspect that significantly affects the performance of the model in terms of computational time, since the dimension of the problem is extended once more and the resolution determines the size of such dimension. For the simulation performed in this analysis the resolution is set equal to $0.1\,A$. This means that for each cell the $I-V$ curve is determined by current values (I) from $0\,A$ to I_{sc} value with steps of $0.1\,A$. The correspondent voltage V is calculated as shown in equation 3.42.

$$V = \frac{kn \cdot (T_{cell} + 273\,K)}{q} \cdot \log\left(\frac{I_{sc} - I}{I_0} + 1\right) \tag{3.42}$$

Once the $I-V$ curve is computed for each solar cell, the $P-V$ curve on module level is computed by summing the effects of the different cells. The maximum power point is then found for each module and the most beneficial configuration of bypass diodes is selected. These steps are implemented through the extraction of the maximum power value along the dimensions of interest, assuming that a power optimizer is placed on module level. In conclusion, through the multi-dimensional matrix approach of the algorithm, the power produced by the entire PV farm is calculated by summing the values obtained for the individual modules.

3.2.3. FILL FACTOR APPROXIMATION

After some preliminary tests, it has been observed that the 1-diode electrical model requires a computational time which is at least one order of magnitude higher than the optical model to complete a simulation. The reason mainly lies in the increase in the problem's dimensions when computing the $I-V$ curve since a high RAM capacity is required to operate with these matrices. The imbalance would limit significantly the ad-

vantages of the approach adopted to calculate the incident irradiance, preventing the global scale of the analysis. Therefore, it is chosen to develop an alternative approximated model that could achieve high computational performance, slightly decreasing the accuracy of the results.

This alternative method has to avoid the extension of the dimension caused by the creation of the $I-V$ curve for every cell. This means that the maximum power point at which the different cells operate has to be obtained using a different strategy. The solution adopted in this model is based on the approximation of the fill factor (FF) using the expression introduced by Green [80] shown in equations 3.43 and 3.44.

$$FF = \frac{v_{oc} - \log\left(v_{oc} + c_{ff}\right)}{v_{oc} + 1} \tag{3.43}$$

$$v_{oc} = \frac{qV_{oc}}{k(T_{cell} + 273\,K)} \tag{3.44}$$

The constant c_{ff} is appropriately tuned to minimize the error with respect to the 1-diode configuration. In particular, an optimization technique based on the gradient method has been used to find the optimal c_{ff}. It is based on the minimization of the root mean square error ($RMSE$) between the power generated through this approximated method and the 1-diode model during a yearly simulation for a given location. Such process is iterated for 31 locations while the design parameters (tilt, orientation, distance, height) are kept constant. Therefore, an optimal value of c_{ff} is calculated for each location but for simplicity the average is used for the analysis shown in this study.

The average value of c_{ff} obtained through is method is approximately 200. This is highlighted in figure 3.12, where it is compared with all the values obtained for the different locations. Moreover, figure 3.13 shows that the error caused by this approach is below 0.7% in annual energy yield with respect to the 1-diode model. Lastly, it can be observed that the value obtained for c_{ff} is significantly larger in comparison to factor used by Green [80] in his study. The discrepancy can be attributed to the fact that the fill factor refers to the entire module in this case since the resistance caused by the interconnection between the different cells is not modelled. On the other hand, Green's formula refers to an individual solar cell, for which higher fill factor is obtained.

3.3. MODELLING OF THE ELECTRICITY PRICES

The purpose of this analysis includes the study of the optimal configuration for a bifacial PV farm in relation to the economic revenues that can be achieved, which depend on the electricity market. Therefore, the instantaneous electricity prices have to be known for the time period of the simulation. However, the purpose of this study is to provide an answer to the main research question outlined in chapter 1 by considering different market scenarios, hence simulating various prices' behaviours. For this purpose, a model that estimates the a yearly price curve has been developed in this study and it is described in this section.

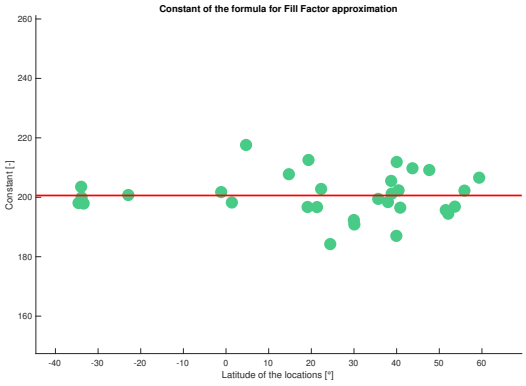

Figure 3.12: Value of c_{ff} obtained for the analyzed locations

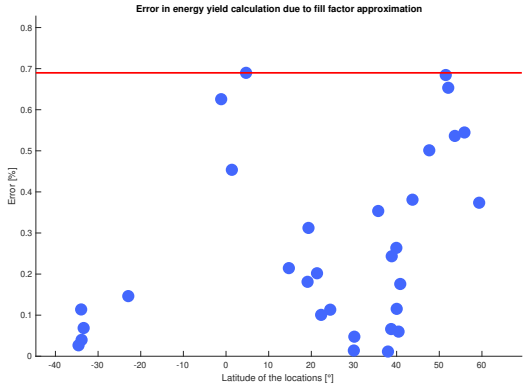

Figure 3.13: Error in yearly energy yield calculation caused by fill factor approximation method

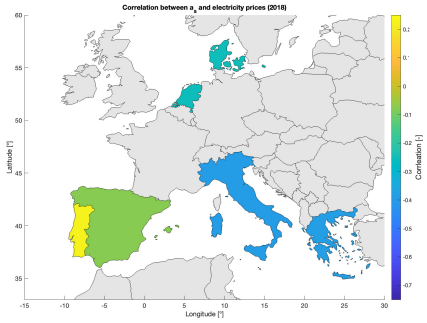

Figure 3.14: Correlation between electricity prices in 2018 and a_s for few selected countries in Europe

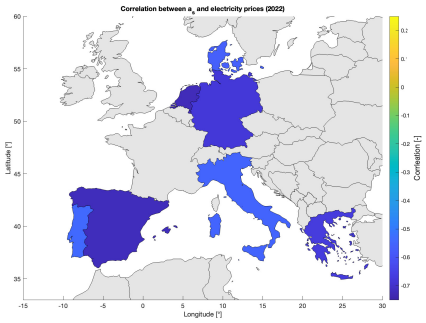

Figure 3.15: Correlation between electricity prices in 2022 and a_s for few selected countries in Europe

In the introduction presented in chapter 1, it has been shown how different PV farm configurations are characterized by dissimilar daily power curves. Therefore, the purpose of this modelling phase is to capture the electricity prices' behaviour on daily basis. In particular, a clear correlation has been observed between the sun's altitude (a_s) and the electricity prices. To avoid the impact of the seasonal effects, this investigation is performed on daily basis. Such correlation has negative values, which means that lower electricity prices occur during noon, as expected. Moreover, it can be noticed from figures 3.14 and 3.15 that such correlation has increased (in absolute value) from 2018 to 2022, due to the increase of the PV penetration in the electricity mix of the nations taken into account. These considerations are based on the electricity prices available in [18].

The relation between the electricity prices and the sun's altitude is the principle adopted to model the evolution of the prices in time. The idea consists in defining two different values: a "noon-price" and a "morning/evening price". The criteria used to assign the price to a specific timespan is based on a_s value instead of the hour of the day. Therefore, proper a_s values are chosen to make the transition for the two price values. Unlike a method based on the hour of the day, this enables to take into account the availability of the solar energy source in locations characterized by different latitudes. Moreover, this approach implicitly incorporates a seasonal effect while creating the annual price curve, and it is illustrated with the following example. Imagine that a particular a_s' value has been selected as threshold to make the transition between high and low prices. For instance, in the Netherlands, during the summer the number of hours within a day for which $a_s > a_s'$ is higher with respect to the winter. Therefore longer period with higher prices are present in the winter with respect to the summer in the Netherlands according to this model.

The modelling of the electricity prices is based on five parameters, which are used as input to generate an annual price curve together with an a_s time-series:

- Price ratio (p_{ratio})

- Minimum price (p_{min})
- Minimum a_s ($a_{s,min}$)
- Maximum a_s ($a_{s,max}$)
- Shape factor (f_{shape})

Being linked to the a_s values, the resolution of the price curve depends on the a_s input array, e.g. hourly input values lead to a hourly price curve. The latter oscillates between the minimum "noon price" identified by p_{min} and the maximum "morning/ evening price" calculated as $p_{min} \cdot p_{ratio}$. Once the higher and the lower boundaries are defined, such curve could assume in principle various behaviours, for instance sinusoidal, rectangular or triangular. Therefore, the remaining three parameters are used to determine the shape of the electricity price curve, which is assumed to be trapezoidal in this study. In particular, $a_{s,min}$, $a_{s,max}$ and f_{shape} defines the transition between the maximum and the minimum price. First, a_s values that satisfy the condition $a_s < a_{s,min}$ are associated to the maximum price whereas the minimum price is assigned to a_s values such that $a_s > a_{s,max}$. Subsequently, f_{shape} is an integer number that determines the presence of intermediate prices between the maximum and the minimum values. In particular, it is defined as the number of possible prices that can be assumed by the price curve. For instance, $f_{shape} = 2$ leads to a rectangular curve that oscillates only between the maximum and the minimum. On the other hand, increasing f_{shape} by one unit adds one intermediate price during the transition. However, since the electricity price is determined only by a_s value, transitional prices are linked only to intermediate a_s values, hence such transitional behaviour could not be observed in case of a sharp transition between a high to a low a_s, especially when a low time resolution is adopted, e.g. hourly.

These five parameters adopted to model the shape of the electricity price curve have been tuned using real data, namely annual hourly prices of 8 different European countries. Moreover different years have been taken into account, i.e. 2018 and 2022, obtaining a total of 16 cases. Therefore, the five optimal values that minimize the RMSE between the real and the approximated prices are calculated for each location. For this purpose, two different approaches have been tested. In the first approach, an entire year of prices' timeseries is given as input to the optimization function. On the other hand, in the second approach the yearly optimization problem was divided into daily sub-problems and the optimal values are determined by the averaging 365 values. In both approaches, the cases when $a_s < 0$ have been filtered out, i.e. night values have been removed. Due to the high impact of the seasonal effects, the latter approach has been used for the further analysis. Moreover, this choice is justified by the fact that the main purpose of this study is to draw conclusions related to the shape of the power curve on daily basis. This means that average p_{ratio}, p_{min}, $a_{s,min}$, $a_{s,max}$, f_{shape} are assumed to be representative for the whole year. Lastly, the definitive five parameters used for the further analysis are obtained through an average between the 16 cases that have been used for the tuning.

Table 3.3: Constant values of the parameters used to model the electricity prices. These are the result of the tuning based on 16 real cases, as explained in section 3.3.

Parameter	Value
$a_{s,min}$	5.4°
$a_{s,max}$	32.5°
f_{shape}	4

In this study various market conditions will be simulated by changing some of these parameters. In particular, since the focus of the analysis is the price difference between the time periods of the day, different p_{min} and p_{ratio} will be tested. On the other hand, $a_{s,min}$, $a_{s,max}$ and f_{shape} will be kept constant and their values are presented in table 3.3.

The process of creation of the electricity price curve can be summarized with the example shown in figure 3.16. The transitions between each sub-figure represent a relevant step in this procedure, and they can be described as follows:

1. Observation: correlation (negative) between the a_s values and the electricity prices.
2. First approximation of the electricity prices: tuning of the five parameters on daily basis.
3. Second approximation of the electricity prices: assuming that the averages of the daily values for the five parameters are representative for the whole year.

The main limitation of this model used to estimate the electricity prices consists in considering only the availability of the solar energy source as factor that has an influence on the prices, neglecting for instance the impact of other renewable sources, like wind energy. Moreover, high penetration of PV in the electricity mix is assumed worldwide, since a limited amount solar power plants would not have a significant impact on the price curve.

3.4. DATA USED FOR THE SIMULATIONS

In this section, the input data used for the simulations performed in this study are outlined. Various databases have been adopted to gather different types of data, for instance the climate conditions of some selected locations or the spectral albedo curve of a chosen ground type.

102 locations worldwide have been selected for this analysis, following the criteria of covering the most populated areas of the world. The climate conditions for each of these location have been obtained using the software METEONORM. The variables that have been used for each location are summarized in table 3.4 and consist in yearly timeseries with hourly resolution. Unfortunately, only data from 01/01/2005 to 31/12/2005 were available, therefore the input data refer to the year 2005. In principle, this can affect the results of the study since the magnitude of the irradiance has been impacted by the climate change in the recent years [81]. However, such issue is not expected to influence

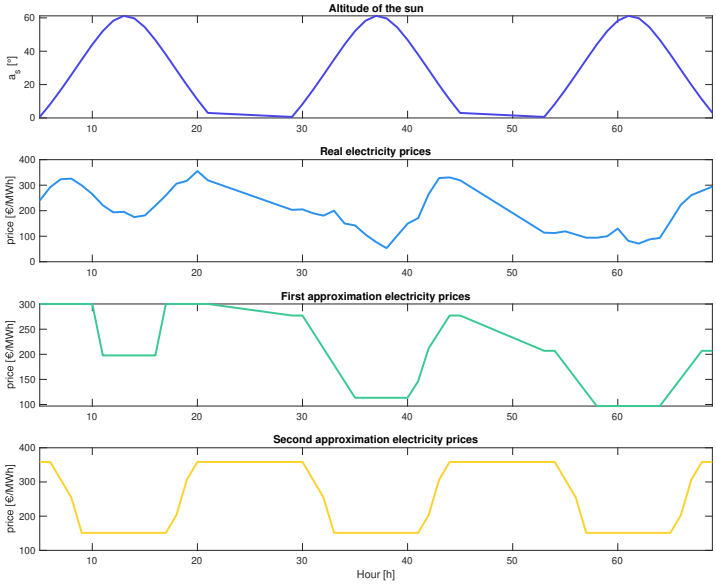

Figure 3.16: Main steps in the modelling of the electricity prices. This example refers to the period 16-18 June 2022 of the Netherlands.

Table 3.4: Data obtained from METEONORM for the 102 selected locations.

Parameter	Symbol
Date and time	-
Sun's altitude	a_s
Sun's azimuth	A_s
Direct normal irradiance	DNI
Diffuse horizontal irradiance	DHI
Atmospheric pressure	p
Ambient temperature	T_{amb}

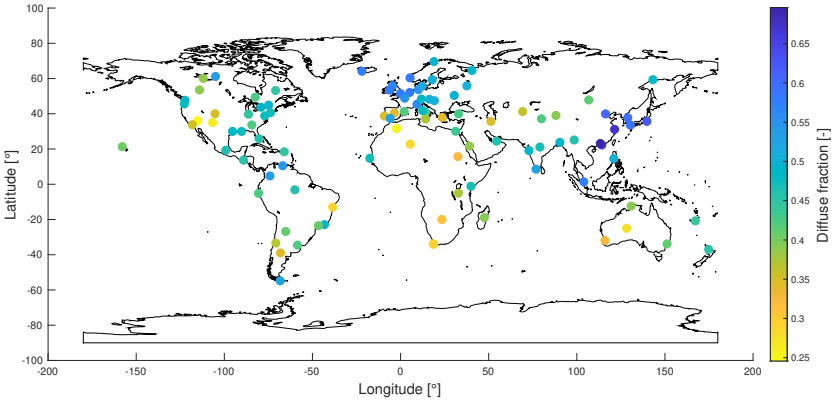

Figure 3.17: Locations selected for this research and their GHI-weighted average diffuse fraction

significantly the outcome of the analysis, which focuses on the comparison of different farm configurations.

The locations analyzed in this research can be visualized in the map present in figure 3.17. To classify such locations depending on their climate conditions, their diffuse fraction has been calculated. However, a weighted-average value is used to avoid the time-dependence of the variable, where the weighting factor is the GHI value.

The spectral albedo curve used in this study refers to the light soil and it is obtained from the software SMARTS. The wavelength resolution of this curve is set to $5\,nm$, in accordance with Riedel-Lyngskær et al. [55], who highlight that a high resolution is not required to achieve sufficiently accurate results. Moreover, the spectral range is limited from $280\,nm$ to $1200\,nm$ since higher wavelengths are not absorbed by the PV module

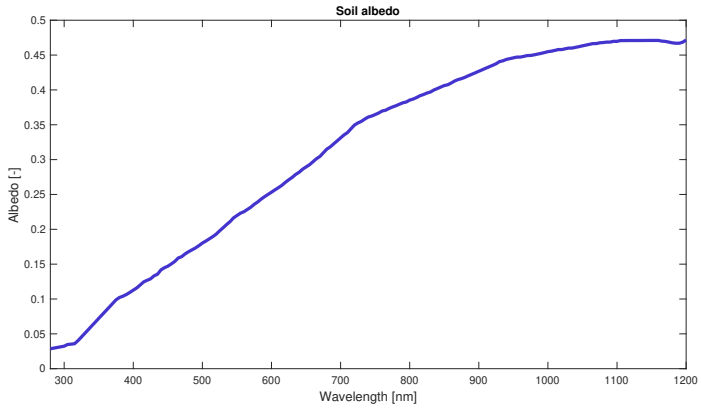

Figure 3.18: Spectral albedo for light soil obtained from SMARTS software

based on c-Si, hence they are neglected to reduce the computational time of the simulations. Figure 3.18 shows the albedo curve of the light soil, where higher reflection can be observed for larger wavelengths.

As anticipated in subsection 3.1.2, in this research an average normalized spectrum has been used for both direct and diffuse component of the irradiance. Therefore, through the integrated DNI and DHI values obtained from METEONORM, the spectral irradiance can be reconstructed for each hour of the year. This technique enables the decoupling of the spectral dimension, reducing significantly the computational time of the simulations. Such spectra are calculated through an irradiance-weighted average of the time-varying spectral irradiance. Subsequently, they have been normalized in order to contain only the information regarding their shape. These data have been obtained from a global database with a resolution of one degree of latitude and longitude [82]. Therefore, the correspondent spectrum is associated to each of the selected location by choosing the nearest point in the database.

Table 3.5 shows the parameters of the modules considered for the PV farm simulated in this study. They are based on the specification sheet of the product LG400N2T-A5. As shown in the table, six cells are present along the short dimension, which corresponds to the length of the modules in the landscape configuration, according to the 2D approximation of the model. Therefore the dimension of cell (c) is assumed to be $c = l/6 = 0.1707m$, neglecting the inactive area of the module. Moreover, the ideality factor (n) and the reflectivity of the modules (r) are assumed to be equal to 2 and 10%, respectively. Such values can be considered representative for the main technologies and a detailed study on such choice is out of the scope of this research, since they have a limited impact on the outcome of this work.

To take advantage of the spectral characterization of the model, two different EQE

Table 3.5: PV modules' specifications adopted in this study, based on the product LG400N2T-A5.

Parameter	Value
Dimensions of the module ($w \cdot l$)	$2.064 \times 1.024\,m$
Cells configuration	6×12
Bypass diodes	3
Cell's length (c)	$0.1707\,m$
Rated power (P_{rated})	$440\,Wp$
Short-circuit current ($I_{sc,STC}$)	$11.24\,A$
Open-circuit voltage ($V_{oc,STC}$)	$49.7\,V$
Series-connected cells (N_s)	72
Parallel-connected cells (N_p)	1
NOCT Temperature (T_{NOCT})	$45°C$
Temperature coefficient for I_{sc} ($k_{I_{sc}}$)	$0.03\,\%/C$
Temperature coefficient for V_{oc} ($k_{V_{oc}}$)	$-0.27\,\%/C$
Ideality factor (n)	2
Reflectivity (r)	10%

Table 3.6: Ground parameters that determine the accuracy of the ground-reflected irradiance

Parameter	Value
Length of ground's segments (g)	$0.2\,m$
Extension of ground's segmentation (ext)	$4\,m$

curves have been used for the front and the rear side, as anticipated in subsection 3.2.2. These have been obtained from the work of Carolus et al. [83] and are visualized in figure 3.19. In this case, the same spectral resolution of the albedo curve is considered. These two EQE curves allows the calculation of the bifaciality factor, as shown in equation 3.45. In this case, it amounts to 65.14%, which is relatively low with respect to the values mentioned in literature.

$$\phi_{Bi} = \frac{J_{sc,rear}}{J_{sc,front}} = \frac{\int_{\lambda_1}^{\lambda_2} EQE_{rear}(\lambda)}{\int_{\lambda_1}^{\lambda_2} EQE_{front}(\lambda)} \tag{3.45}$$

Lastly, the ground's parameters that determine the accuracy of the ground-reflected irradiance have to be decided. These are the length of the ground's segments (g) and the extension (ext) of the ground's segmentation at the boundaries of the farm. Their values are included in table 3.6. Moreover, figure 3.20 shows the sensitivity analysis for different g and ext values with respect to the annual energy yield calculation. The values selected for the simulations are indicated with the circle, which have been chosen by taking into account the trade-off between the accuracy of the results and the computational time.

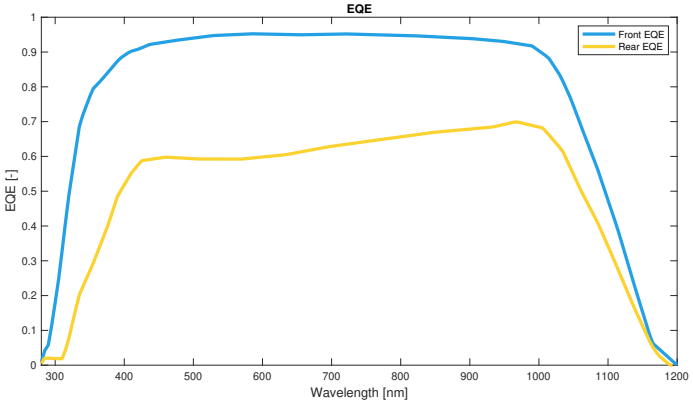

Figure 3.19: EQE curves for front and rear side of the PV module

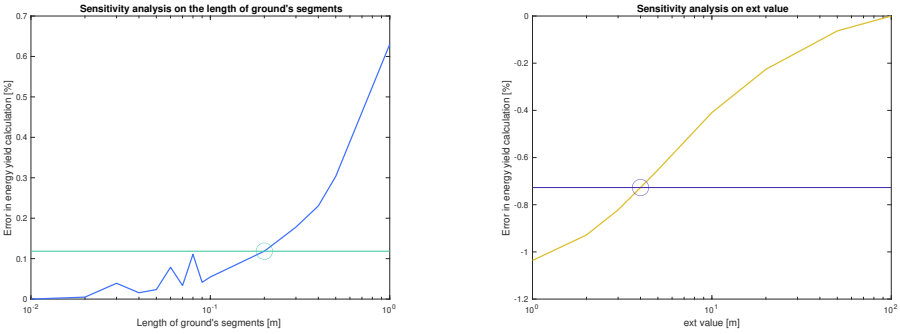

Figure 3.20: Sensitivity analysis on g and ext values with respect to the energy yield. The simulation refers to optimally tilted modules in Utrecht ($h = 1.5\,m$ and $d = 4\,m$).

4

RESULTS AND DISCUSSION

This chapter describes the results that have been found during this study, providing an answer to the research questions presented in 1. First, the outcome of the model's validation is described in section 4.1, analyzing the factors that have a larger impact on the the accuracy of the model. The focus will then move to the comparison of different farm configurations, namely tilted and vertical options. Section 4.2 analyzes the effect of various parameters on the power curve of bifacial PV farms, including climate conditions as well as installation choices. The effect of the design parameters on the energy yield is studied in detail in section 4.3, focusing on the influence of the modules' elevation and the row-to-row distance. Lastly, the economic potential of vertical bifacial PV farms in comparison to the tilted counterpart is studied in section 4.4.

4.1. VALIDATION OF THE MODEL

The validation of the model is limited to the rear irradiance, hence only the ability of the model to estimate such component is tested. The validation of the other features of the bifacial PV model has not been considered in this study, since the methods adopted in that case refer to widely used models adopted for the monofacial modules as well [5]. This validation has been conducted in collaboration with the company KIPP&ZONEN which has performed a series of measurements of the irradiance incident on the rear side of bifacial PV modules, using their sensors. This section is organized as follows. First, the experimental setup is described in subsection 4.1.1. Second, the selection of the data and their processing is discussed in subsection 4.1.2. Subsequently, subsection 4.1.3 illustrates the main results of the validation in terms of precision of the estimations. Lastly, the influence of installation and meteorological conditions on the model's performance is analyzed in subsection 4.1.4.

4.1.1. EXPERIMENTAL SETUP

The measurements used for the validation took place in Delft $(52.0°N, 4.4°E)$ between July and September 2020. The experimental setup consists in three bifacial PV modules

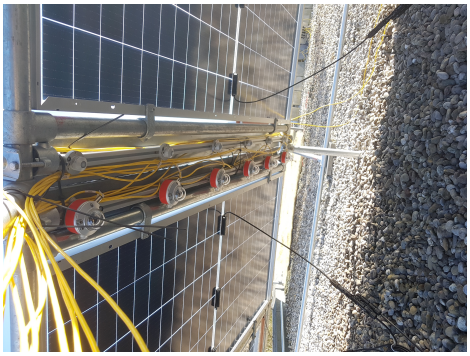

Figure 4.1: Experimental setup implemented by KIPP&ZONEN

equipped with different sensors used to measure the incident irradiance. Moreover, additional structures or monofacial modules have been placed next to the bifacial modules as well as in front and behind this modules' row. This is implemented to simulate an environment typical of a PV farm instead of a stand-alone module, as depicted in figure 4.1. During the measurements, the tilt of the modules and their elevation with respect to the ground has been modified to provide diversified data that can add wider generalization to this validation phase. Moreover, different ground types have been tested, in order to gather data concerning various albedo values. On the other hand, the row-to-row distance is kept constant and equal to 4.3 m between the first and the second row and to 4.8 m in other case. Furthermore, the wall behind the last row is covered using black sheets to avoid reflections that can alter the measurements. Its distance from the last row is equal to 5 m. The row of interest, i.e. containing the bifacial modules and the sensors, has a length of 2.14 m whereas it amounts to 1.77 m for the additional rows. However, a length of 2.14 m is assumed for all the rows, due to the limitations of the model. Conversely, the model allows different row-to-row distance values since such design parameters can be assigned to each row of the farm individually. Lastly, the orientation of the modules has been set to 187°, namely 7° to West.

Various sensors have been used by KIPP&ZONEN to gather data from this experimental setup. Such devices have been mounted for a limited time duration and the measurements have been affected by periods of maintenance, especially when the installation parameters or the ground type have been changed. These sensors are summarized in the following list:

- A *RaZON* sensor is mounted on the roof and used to measure DNI, DHI and GHI. It consists in two integrated pyranometer and pyrheliometer.
- Six *SP Lite* pyranometers are mounted on the rear side of the bifacial modules of interest, distributed along the module's length.
- Six *CMP11* pyranometers are mounted on the rear side of the bifacial modules of interest, distributed along the module's length.

- A *SP Lite* pyranometer is mounted on the front side of the bifacial modules to measure the plane-of-array front irradiance.
- A *CMP11* pyranometer is mounted on the front side of the bifacial modules to measure the plane-of-array front irradiance.
- Five *CMP11* pyranometers are mounted on the rear side of the bifacial modules of interest, distributed along the module's length.
- An albedometer is used to measure the instantaneous albedo.

Using these sensors, broadband irradiance values have been registered. Therefore, the spectral influence is neglected during the validation process, limiting the outcome of the analysis.

4.1.2. SELECTION AND PROCESSING OF THE DATA

The criteria adopted to select the data to use in the validation from the raw measurements' database are explained in this paragraph. First, the measurement performed by the six *SP Lite* sensors have been chosen to create the rear irradiance measured profile due to the completeness of the data with respect to the other sensors. Second, these data have been filtered by considering only the cases when the information about the meteorological conditions were available, namely DNI and DHI values from the *RaZON* sensor. Lastly, the periods of maintenance or equipment's mounting have been discarded, as suggested in a detailed logbook provided by company. After this filtering process, 12 days have been selected and used for the validation purposes, which are shown in table 4.1.

For most of the selected time periods, also the measurements concerning the plane-of-array front irradiance were available: Therefore, they have been used to test the model also considering the sum of both front and rear irradiance, following the validation steps performed by Marion et al. [5]. On the other hand, the availability of the data gathered by the albedometer were limited to few time periods. Therefore, time-independent values of albedo have been used. Such values have been determined using the average of the albedometer signal when a relevant amount of data was present for a specific day. On the other hand, if no sufficient data from the albedometer were present for a day, the value of albedo is assumed following the recommendations of the company's logbook. These are specified in table 4.1.

Different time resolutions were present among the data measured by the different sensors. Therefore, a time-averaging process has been accomplished to match the time resolution of the different signals. In particular, a 15-minutes resolution is adopted to solve slight misalignment observed in high time-resolution data, in accordance to the approach of Marion et al. [5].

Table 4.1: Time periods selected for the model's validation and the correspondent installation conditions. The height value refers to the distance between the ground and the bottom extreme of the module.

Time period	Weather	Ground type	Albedo	Height	Tilt
28 July 2020 15.30-18.15	Cloudy	White fleece	0.53	0.5 m	30°
29 July 2020 10.00-18.00	Cloudy	White fleece	0.53	0.5 m	30°
30 July 2020 11.00-18.00	Sunny	White fleece	0.53	0.5 m	30°
31 July 2020 11.30-15.30	Sunny	Grass	0.13	0.5 m	30°
1 August 2020 10.00-18.00	Cloudy	Stones	0.19	0.5 m	30°
2 August 2020 10.00-18.00	Sunny	Stones	0.19	0.5 m	30°
3 August 2020 10.00-18.00	Rainy	Stones	0.15	0.5 m	30°
4 August 2020 10.00-18.00	Sunny	Stones	0.19	0.5 m	45°
1 Sep 2020 14.00-18.00	Cloudy	White fleece	0.50	0.5 m	52°
6 Sep 2020 9.00-19.00	N.A.	White fleece	0.45	0.5 m	52°
7 Sep 2020 12.30-19.00	Cloudy	White fleece	0.50	0.5 m	52°
13 Sep 2020 9.00-19.00	Sunny	Stones	0.18	0.5 m	52°

4.1.3. RESULTS: RMSE AND MBD

To validate the model, a simulation for the days selected in table 4.1 has been performed, using the design parameters described in the previous paragraphs. Therefore, a high-spatial-resolution curve of simulated rear irradiance is obtained for each timespan of the selected days. The values that correspond to the position of the sensors are compared to the measurements, calculating the root mean square error (RMSE) and the mean bias deviation (MBD). Considering all the analyzed data for the rear irradiance, the MBD and RMSE values amount to $-1.29\,W/m^2$ (-2.22%) and $12.65\,W/m^2$ (21.69%). Such values are in accordance to other studies based on a view factor approach, e.g. [5]. A complete overview of RSME and MBD values calculated for each day can be found in Appendix C. Figures 4.2 and 4.3 show the scatter plots containing all the data analyzed, where the red line indicates the perfect agreement between the modelled and the measured data. Comparing the figures 4.2 and 4.3, it can be observed that the error on the rear irradiance becomes less evident in case the front component is added.

4.1.4. INFLUENCE OF VARIOUS PARAMETERS ON MODEL'S PERFORMANCE

This subsection aims to identify which parameters have the highest impact on the model's performance, in order to determine the conditions in which the model implemented for this study ensures sufficient accuracy.

Figure 4.4 shows the relative error on the rear irradiance estimation with respect to the hour of the day. Moreover, the dependence on the albedo and tilt values is included through the shape and the colour of the scattered data, respectively. A slight trend with respect to the hour of the day can be observed, where higher errors have been obtained during morning and evening periods. A possible reason to explain this behaviour could be that the sun rays approaching the PV modules during those periods of the day are more influenced by the surrounding structure, due the lower sun's altitude. This is justified by the picture 4.1, where the presence of obstacles is evident. However, the clearest

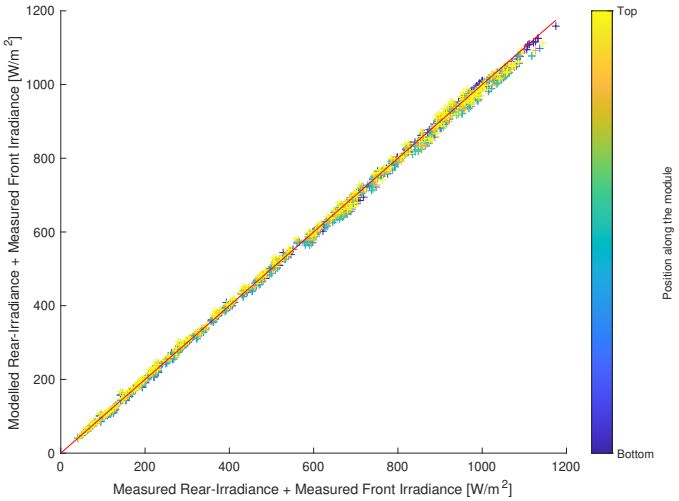

Figure 4.2: Accuracy of the rear irradiance estimations with respect to the measured data. In this case, the measured front irradiance is summed to the rear component to show the limited impact of the deviations.

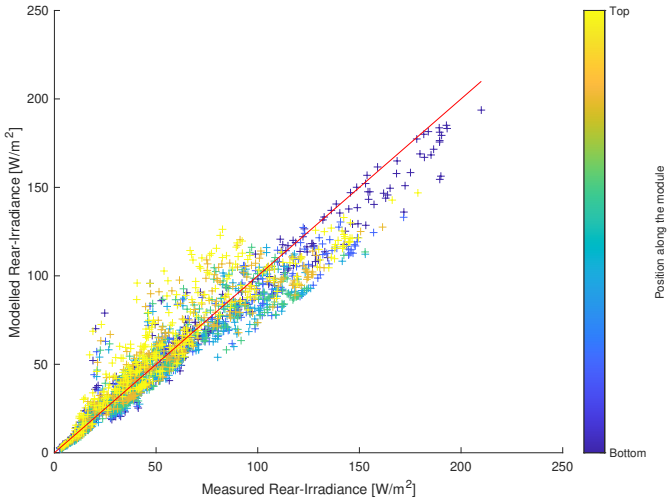

Figure 4.3: Accuracy of the rear irradiance estimations with respect to the measured data. In this case, only the rear component is shown to highlight the errors of the model.

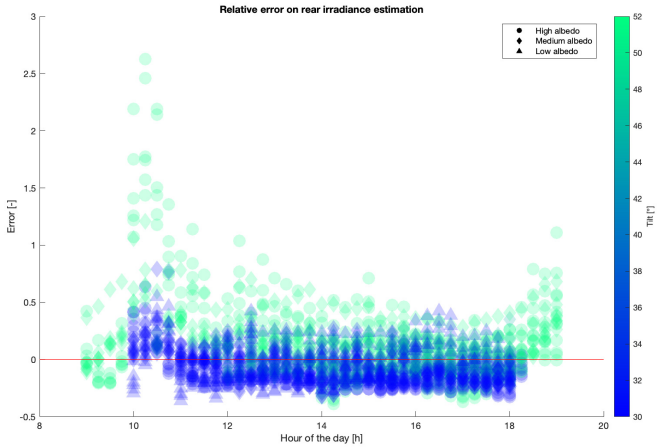

Figure 4.4: Relative error on rear irradiance estimation with respect to the real measurements. The dependence on the hour of the day, tilt and albedo values is highlighted.

trend visible in figure 4.4 concerns the tilt values: high tilts lead to an overestimation of the irradiance whereas an underestimation is registered in case of low values. In general, it is observed that higher tilt values also cause larger errors in the estimation. Such behaviour can be explained by taking into account the limitations of the view factor approach, which assumes a diffuse reflection of the incident light. Therefore, the largest errors occur in case of higher tilts, for which a larger portion of unshaded ground is visible by the rear cells. For these ground segments, the hypothesis of diffuse surfaces is indeed quite inadequate. Lastly, a trend associated to the albedo cannot be detected from figure 4.4. However, the absence of this relation can be caused by the lack of the data in terms of variety of albedo values, hence it requires further investigation.

The relation between the error in the estimation of the rear irradiance and the tilt value is confirmed by the analysis depicted in figure 4.5. In this graph the relative error is shown with respect to the position of the cell along the module, distinguishing six different values from the top to the bottom. Similarly to the previous figure, the dependence with the tilt and the diffuse fraction is highlighted using different colors and shapes. It can be noticed that the higher errors occur at the edges of the module for low values of diffuse fraction. This result is in agreement with the previous justification concerning the portion of unshaded ground seen by each cell. The top and the bottom cells are indeed the areas characterized by the largest view factor wit respect to the unshaded segments. Moreover, the fact that low diffuse fraction values lead to highest errors proves that view factor theory fails in case of direct reflection.

Lastly, the influence of the hour of the day, albedo and tilt is investigated for rear GNU estimation. Such metric has been introduced in subsection 2.2.2 and quantifies the non-uniformity of the rear irradiance. From figure 4.6, the absence of trend with albedo or

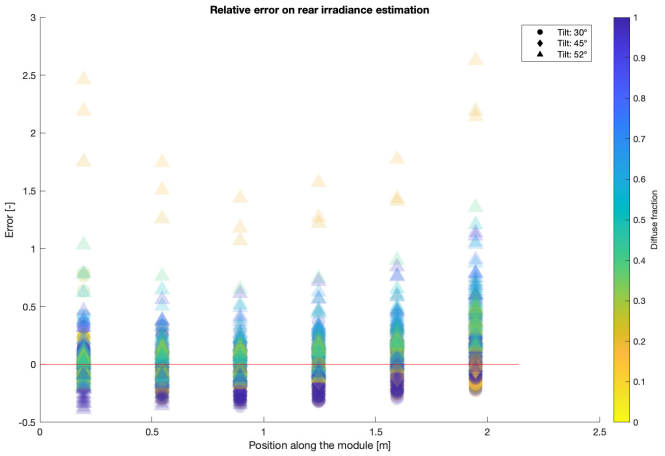

Figure 4.5: Relative error on rear irradiance estimation with respect to the real measurements. The dependence on the position along the module, tilt and diffuse fraction is highlighted.

diffuse fraction can be observed. On the other hand, it is clear that an underestimation of GNU occurs for high tilt values whereas lower tilts lead to an overestimation of the non-uniformity. This is a consequence of the reasons explained in the previous paragraphs, since the GNU error arises from the spatial distribution of the error in predicting the irradiance along the module, and the tilt has been demonstrated to be a key factor in this sense.

In conclusion, it has been shown that the tilt is the parameter that has the highest impact on the model's accuracy, which decreases in case of high values. The reason that has been identified to explain this relation lies in the limitations of the view factor approach, for which the surfaces are assumed to be diffuse emitters.

4.2. TILTED VS VERTICAL: DAILY POWER CURVE

In this section the impact of the farm configuration on the daily power curve is analyzed. As introduced in chapter 1, this study focuses on the comparison between the conventional tilted case and farms where the modules are installed vertically. Concerning the former configuration, the modules are tilted at the optimal angle, namely the value that maximizes the energy yield along the year. Such value is appointed as optimal tilt in this study.

4.2.1. OPTIMAL TILT CONFIGURATION

The technique used to calculate the optimal tilt is based on the gradient method, hence multiple annual simulations are performed until the value that maximizes the energy yield is found. In particular, the *StepTolerance* and the initial value have been set to 10^{-3} and 0°, respectively. Such constraints arises from the limited computational resources

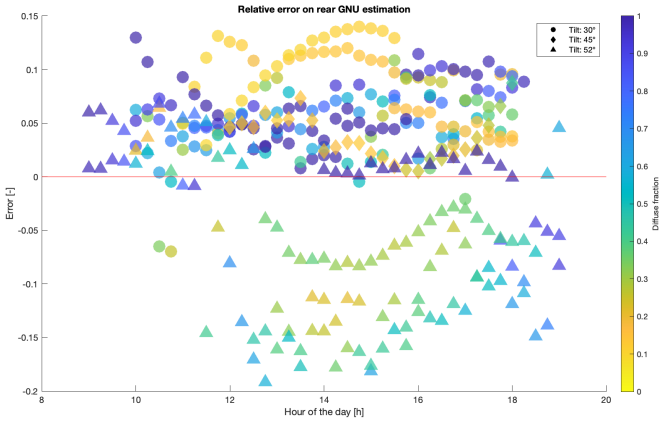

Figure 4.6: Relative error on rear GNU estimation with respect to the real measurements. The dependence on the hour of the day, tilt and diffuse fraction is highlighted.

available for this study. Moreover, an alternative approach based on genetic algorithm has been tested with the scope of increasing the accuracy of the results. However, it resulted to be not feasible in terms of computational time while extending the analysis to a global scale.

Unlike monofacial PV modules, the optimal tilt value is highly sensitive on the installation conditions in case of bifacial PV, as illustrated in subsection 2.1.2. Therefore, it is essential to discuss the dependence of the optimal tilt on the design parameters before continuing with the analysis. The parameter that has the highest impact on the optimal tilt is the albedo, since a higher albedo leads to higher ground-reflected irradiance and higher tilt values are suggested. However, this study is limited to the use of light soil as ground type, therefore the impact of such variable is not considered. On the other hand, the impact of design parameters such as the height of the modules and the row-to-row distance is one of the objective of this research. For this reason, the optimal tilt has been calculated for different h and d values and the results are shown in figure 4.7 for two locations, as example. First, the difference between monofacial and bifacial modules can be observed. In case of lower latitudes, for low height values the optimal tilt for bifacial is higher than for monofacial ($\theta_{opt,bi} > \theta_{opt,mono}$) whereas the opposite occurs for high heights ($\theta_{opt,bi} < \theta_{opt,mono}$). However, the transitional height value is dependent on the row-to-row distance of the farm. On the other hand, higher optimal tilt values for bifacial modules are registered in most of the cases when considering higher latitudes. Moreover, both bifacial and monofacial modules show an increasing trend with respect to the row-to-row distance, as highlighted by the colors in figure 4.7. Such trend occurs with the exception of low row-to-row distance values, for which bifacial modules are characterized by an irregular behaviour. On the other hand, the dependence on the height values is only present for bifacial modules, where higher tilts are observed for low heights, confirming the trend described in subsection 2.1.2. In general, similar values

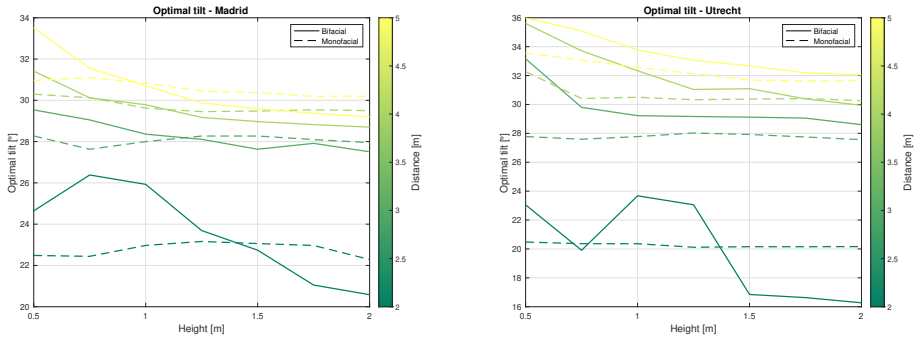

Figure 4.7: Example of optimal tilt dependence on the design parameters (h, d) for Madrid (left) and Utrecht (right).

of optimal tilt are observed for both bifacial and monofacial modules. This occurs due to the low albedo value of the light soil ground. However, the difference is expected to be more evident in case of higher albedo values, for which higher tilts are suggested for bifacial PV due to the higher impact of the ground-reflected irradiance.

For simplicity, the optimal tilt values adopted for this study for bifacial PV modules are limited to the case obtained considering a row-to-row distance equal to 3 m and a modules' height of 1.5 m. This choice is justified by the minimal impact of the design parameters on the optimal tilt value above a certain limit. These optimal tilt values are depicted in the global map presented in figure 4.8. This map has been obtained from the simulation over the 102 locations mentioned in section 3.4. However, the coloured areas have been obtained from the coordinates presented in figure 3.17 by assigning each point of a 1-degree resolution grid to the nearest analyzed location. Uncoloured regions arises from a maximum distance over which no locations are assigned, in this case set to 10°.

4.2.2. INFLUENCE OF THE DIFFUSE FRACTION ON THE POWER CURVE

This subsection aims to study the effect of the diffuse fraction on the daily power curve of the two configurations analyzed. In particular, the purpose is not to draw general conclusion but only to understand with intuitive examples the relation between the different variables involved. The diffuse fraction has been found to be the climate parameter that mostly influence the comparison between vertical and tilted farms. Therefore, a daily power curve that is representative for the entire year has been created by averaging the power produced during the each hour of the day. In this case, different diffuse fraction values are imposed by tuning appropriately the value of DNI and DHI while keeping the actual GHI. The result is depicted in figure 4.9, where two locations are analyzed, namely Madrid and Utrecht. It can be observed that a lower diffuse fraction is beneficial for the tilted configuration, as expected. This occurs also for the vertical modules during the morning and evening hours. On the other hand, vertical modules prefer a high diffuse fraction in the middle hours of the day. This can be explained by considering

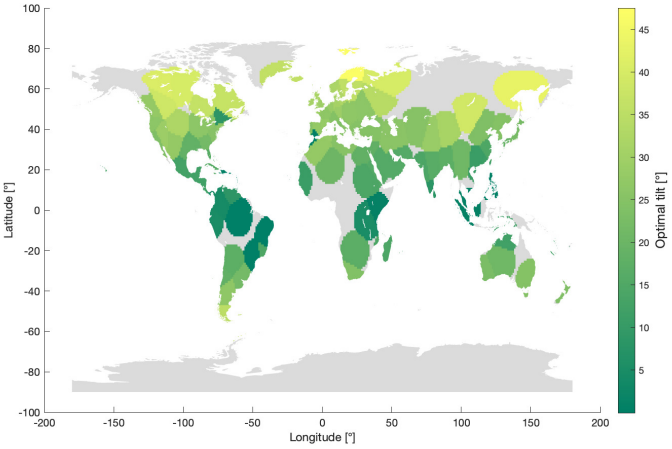

Figure 4.8: Optimal tilt for bifacial PV modules obtained from the simulation of 102 location, where d and h have been set to 3 m and 1.5 m, respectively.

that around noon the sun is not directed towards the faces of the modules, hence diffuse radiation is preferred. Therefore, the most beneficial condition for vertical farms is to experience low diffuse fraction in the morning/evening and high values during noon. However, such condition does not usually occur in most of the locations.

4.2.3. INFLUENCE OF THE DISTANCE ON THE POWER CURVE

The same process is performed to investigate the influence of the row-to-row distance on the daily power curve of vertical and tilted modules. In this case, the actual values of DNI and DHI are used and the representative daily behaviour is obtained through the same averaging method adopted for the diffuse fraction. The result is shown in figure

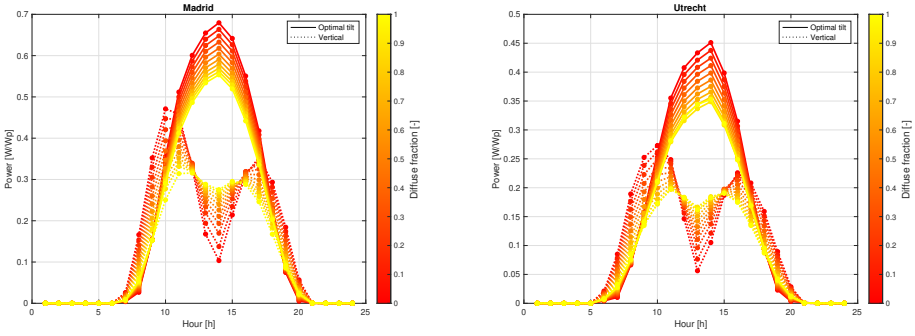

Figure 4.9: Representative daily power curves for Madrid and Utrecht obtained for different diffuse fraction values

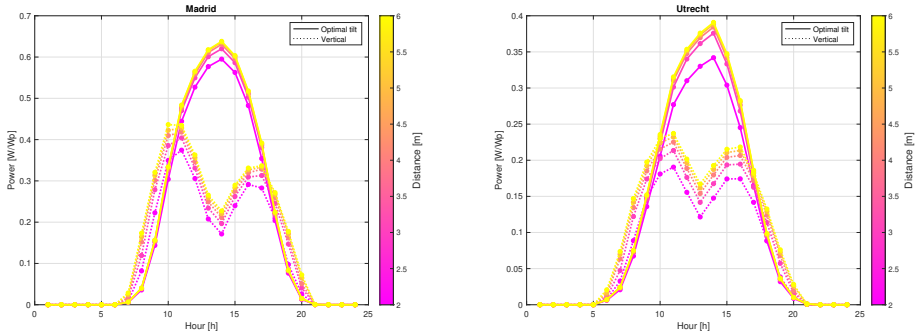

Figure 4.10: Representative daily power curves for Madrid and Utrecht obtained for different distance values

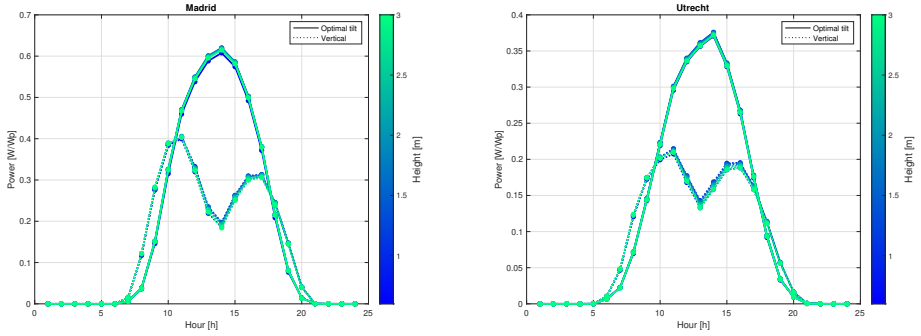

Figure 4.11: Representative daily power curves for Madrid and Utrecht obtained for different height values

4.10, where both the cases of Madrid and Utrecht are depicted. Concerning the row-to-row distance, both configurations follow the same trend, i.e. the curve shifts upwards as the distance increases almost uniformly along the day. However, such trend is more evident for the vertical configuration, proving the higher sensitivity of the power generated by this configuration to this parameter with respect to the tilted case. Moreover, a saturation behaviour can be noticed for both configurations.

4.2.4. INFLUENCE OF THE HEIGHT ON THE POWER CURVE

Figure 4.11 analyzes the effect of the elevation of the modules on the daily power curve, which has been obtained as described in the previous case. In contrast to the influence of the row-to-row distance, it can be observed that the effect of the height on the power curve seems negligible. Therefore, it can be concluded that it represents a second order effect which requires further investigation since no particular trend can be detected from this analysis.

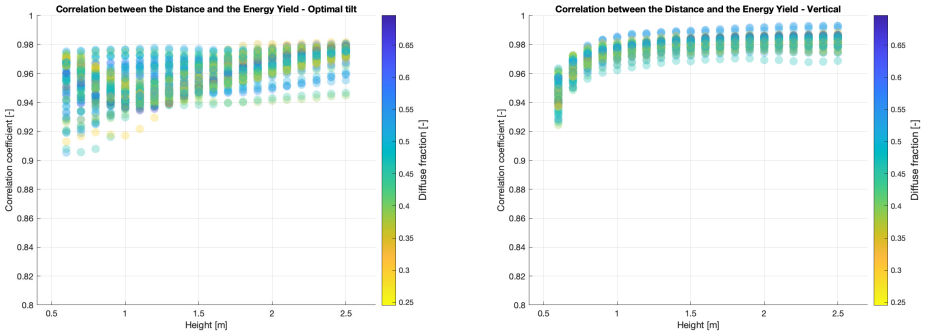

Figure 4.12: Correlation between the energy yield and the row-to-row distance for both optimally-tilted (on the left) and vertical (on the right) configurations

4.3. TILTED VS VERTICAL: ENERGY YIELD

This section aims to analyze the impact of design parameters such as row-to-row distance and height of the modules on the energy yield of the PV farm for the two configurations analyzed in this study, namely optimally-tilted and vertical PV modules. First, the effect of the row-to-row distance and the height is investigated in subsections 4.3.1 and 4.3.2, respectively. Subsequently, subsection 4.3.3 focuses on the relation between these design parameters and some individual aspects that determine the energy yield of the farm, like the unshaded ground portion or the occurrence of mutual shading. The purpose is to provide a better understanding of the impact of the different design parameters on the energy yield, in order to make the findings of this research more intuitive.

4.3.1. INFLUENCE OF THE ROW-TO-ROW DISTANCE ON THE ENERGY YIELD

The analysis on the sensitivity of the energy yield on the row-to-row distance starts by calculating the correlation between these two variables. The results are depicted in figure 4.12, where both tilted and vertical PV are considered. These results have been obtained from multiple global simulations where also the value of height has been varied. The locations are identified through their diffuse fraction, which is indicated using different colors in figure 4.12. It can be observed that not only the correlation between energy yield and distance is dependent on the specific location, but it also depends on the height of the modules. This occurs both for tilted and vertical configurations. However, a general trend can be clearly recognized since high positive values of correlation have been obtained in every case. This means that increasing the row-to-row distance in a PV farm is always beneficial in terms of energy yield. The difference between the two configurations is minimal since a slight increasing trend of the correlation with the height can be observed in both types, despite the higher values obtained for vertical modules. On the other hand, a trend with the diffuse fraction is absent.

To investigate deeper the effect of the row-to-row distance on the energy generated by a PV farm, the derivative of the energy yield with respect to this design parameter is calculated. This is expressed as percentage of increase in the energy yield value for an

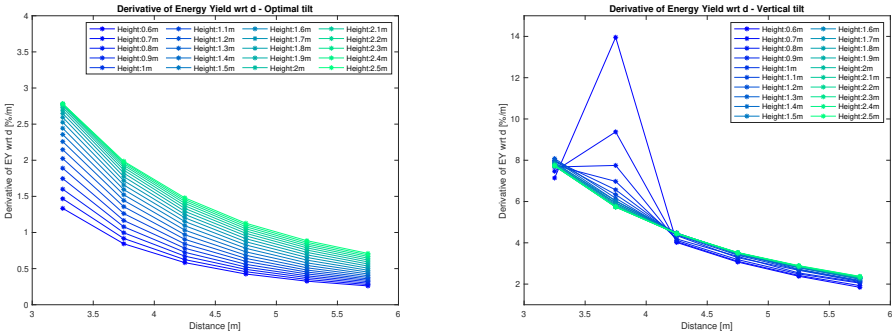

Figure 4.13: Derivative of the energy yield with respect to the row-to-row distance. An average value of all the locations is presented for both tilted (on the left) and vertical (on the right) configuration.

increment of distance by 1 m. Similarly to the correlation, in figure 4.13 the results are shown for different height values but are averaged among the different locations. The derivative is always positive, as expected from the analysis concerning the correlation. However, higher values are registered for the vertical configuration with respect to the optimal tilt case, highlighting that such design parameter has more impact in case a vertical PV farm is considered. In general, both configurations show a decreasing trend of the derivative while increasing the distance value, proving a saturation behaviour. Therefore, after a certain limit, an increase in the row-to-row distance leads to a limited improvement in terms of energy yield. An exception is registered for ground-mounted vertical PV modules, where a maximum in the derivative is obtained for a certain height value. Even though for optimally-tilted modules is more evident, both configurations exhibit the same trend with respect to the height value, namely the derivative of the energy yield is proportional to the elevation of the modules. It can be concluded that for modules characterized by a higher height value, the benefits in terms of energy yield of a larger distance are more evident.

The dependence of the derivative of the energy yield on the different locations is shown in figure 4.14, which refers to the height of 1 m. Similarly to figure 4.12, the different locations are identified through their diffuse fraction. It can be observed that the value of the derivative is location-dependent but the general trend discussed in the previous paragraph is confirmed. Moreover, a trend with the diffuse fraction cannot be detected in this case as well. The global overview is clearer when these values are shown on a world map as depicted in figure 4.15, where regional trends can be recognized.

4.3.2. INFLUENCE OF THE HEIGHT ON THE ENERGY YIELD

The same procedure adopted in subsection 4.3.1 is followed to investigate the influence of the elevation of the modules on the energy yield of a PV farm. Figure 4.16 shows the correlation between the energy yield and the height for the different locations. Similarly to the previous case, the correlation depends on the row-to-row distance, proving the high inter-dependence between these two design parameters. In case of optimal tilt

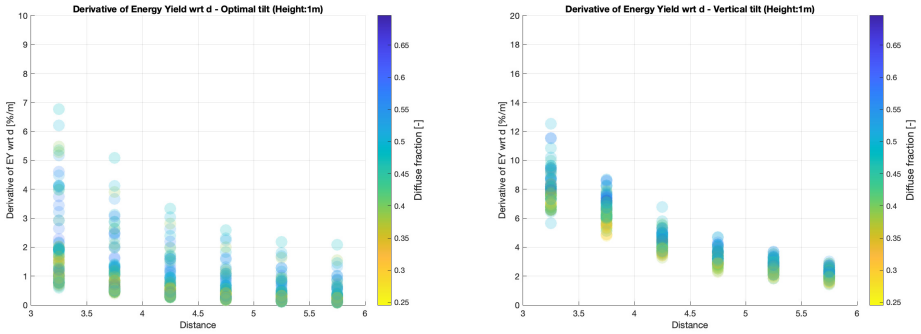

Figure 4.14: Derivative of the energy yield with respect to the row-to-row distance. Values of different locations are presented for both tilted (on the left) and vertical (on the right) configuration. A height of 1 m is considered.

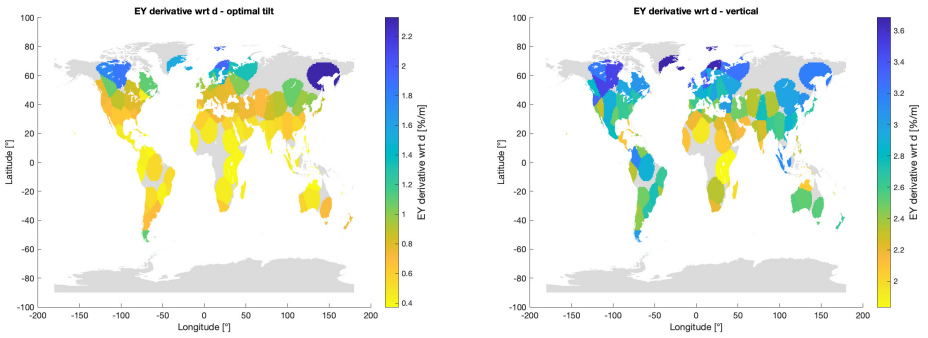

Figure 4.15: Derivative of the energy yield with respect to the row-to-row distance. Values of different locations are presented on a global map for both tilted (on the left) and vertical (on the right) configuration. A height of 2 m and 1 m are selected for tilted and vertical farms, respectively, whereas the distance is set to 5 m for both cases.

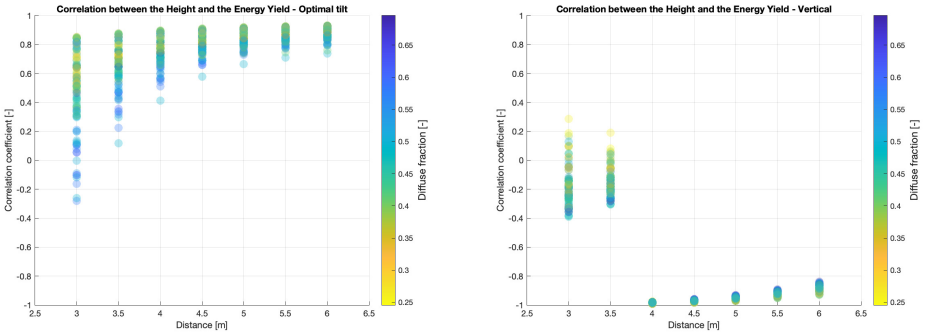

Figure 4.16: Correlation between the energy yield and the height for both optimally-tilted (on the left) and vertical (on the right) configurations

configuration, in most of the cases the correlation is positive hence an increase in the height value leads to a beneficial effect on the energy yield. However, this trend is not as clear as for the distance and varies significantly for each location. The situation is completely different in case of vertical modules where the correlation oscillates between positive and negative values for low distances depending on the location. On the other hand, larger values of distance lead to negative correlations. Therefore, a detailed analysis on the magnitude of such effect is necessary to draw general conclusions, which is performed by studying the derivative of the energy yield, similarly to subsection 4.3.1.

The derivative of the energy yield with respect to the height is visualized in figure 4.17, where the average for all the locations is calculated for different distance values. First, a saturating behaviour is clearly visible for both configurations, as highlighted by the red lines. In contrast to the distance's influence, negative values of the derivative are registered after a certain height in this case. This suggests the presence of an optimal height that maximizes the energy yield, which depends on the distance value. This confirms the results showed by Yusufoglu et al. [22]. Such value is identified by the intersection between the curves and the continuous red line in figure 4.17. However, once the optimal height value is reached, a further increase leads to minimal penalization in the energy yield. Therefore, the optimal height can be appointed as a saturation limit as well. In this case, significant differences between the optimal tilt and vertical modules are evident. The former configurations exhibit higher optimal height values with respect to the latter. Moreover, for tilted modules there is a clear trend with the distance, i.e. higher distances involve higher optimal heights, which is not evident for the vertical case. Nevertheless, this analysis is limited to the average values among all the locations considered hence further investigation is required to increase the validity the conclusion.

Figure 4.18 highlights the dependence of the derivative of the energy yield with respect to the height for the different locations. In particular, it can be observed that the optimal height depends not only on the distance value but it is also very sensitive to the

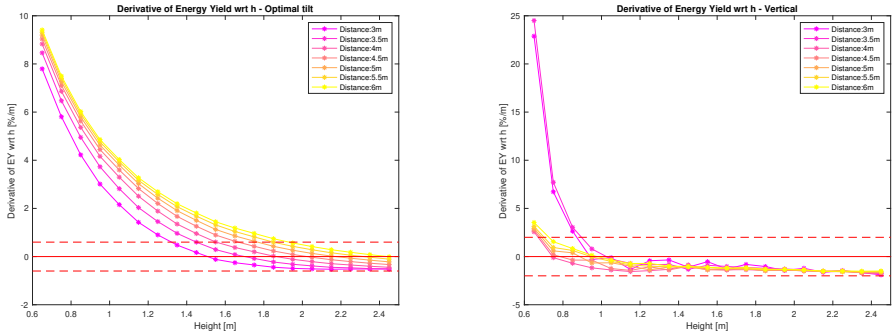

Figure 4.17: Derivative of the energy yield with respect to the height. An average value of all the locations is presented for both tilted (on the left) and vertical (on the right) configuration.

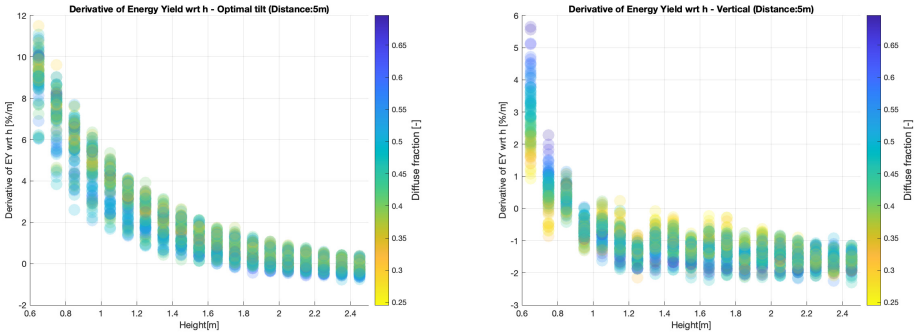

Figure 4.18: Derivative of the energy yield with respect to the height. Values of different locations are presented for both tilted (on the left) and vertical (on the right) configuration. A row-to-row distance of 5 m is considered.

location. Therefore, the trend mentioned in the previous paragraph is confirmed by this analysis. Similarly to the case illustrated in subsection 4.3.1, no trend with the diffuse fraction can be detected and the results are illustrated through a global map in figure 4.19 as well. From this figure, it can be observed that the magnitude of the derivative of the energy yield is significantly lower with respect to distance case, shown in figure 4.15.

4.3.3. EFFECT OF DESIGN PARAMETERS ON INDIVIDUAL ASPECTS

The findings described in the subsections 4.3.1 and 4.3.2 can be summarized in the two following statements:

1. Increasing the row-to-row distance of a bifacial PV farm is beneficial for the energy yield irrespective of the configuration.

2. An optimal height value that maximizes the energy yield can be calculated depending on the location and the other design parameters.

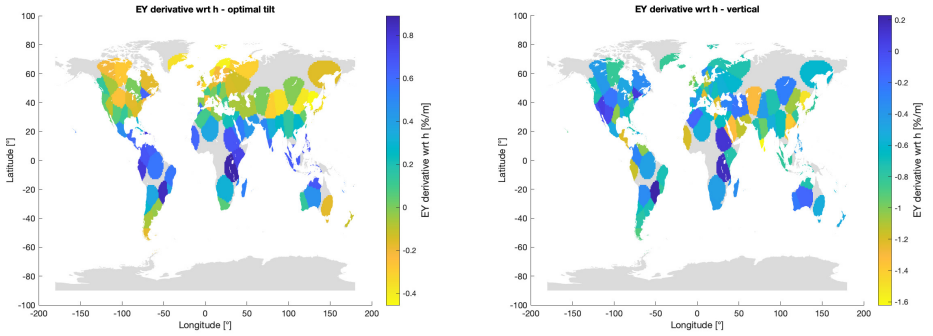

Figure 4.19: Derivative of the energy yield with respect to the height. Values of different locations are presented on a global map for both tilted (on the left) and vertical (on the right) configuration. A height of 2 m and 1 m are selected for tilted and vertical farms, respectively, whereas the distance is set to 5 m for both cases.

Even though the first statement can be easily intuitive, the dependence on the height is not trivial. This is confirmed by the contrast of the results analyzed during the literature review in subsection 2.1.2. Therefore, in the next paragraphs the influence of the design parameters is studied in relation to individual aspects that determine the energy yield of PV farm. These include concepts such as ground sky view factor, unshaded ground fraction, mutual shading and non-uniformity of the irradiance.

GROUND SKY VIEW FACTOR

The first parameter that is analyzed in this subsection is the ground sky view factor (SVF_g), which determines the amount of light that is incident on the ground and then reflected towards the PV modules. Therefore, a high SVF_g is beneficial for the energy yield of a PV farm. SVF_g is dependent only on the design parameters of the farm, i.e. it is constant over time. It is calculated as explained in subsection 3.1.4 and it is a function of the ground's coordinate. The dependence on the design parameters is shown in figure 4.20, both for tilted and vertical farms. It can be observed that for both configurations larger distances increase the SVF_g in the middle ground regions between two neighboring modules whereas the benefit on the extremes is limited. On the other hand, lower heights increase the spatial non-uniformity of SVF_g values but higher SVF_g are obtained in the middle ground region. Therefore, it seems that lower heights could be beneficial in terms of SVF_g. In conclusion, larger row-to-row distances increase SVF_g values whereas lower heights seem to guarantee higher SVF_g. However, the effect of the latter parameters is not evident from this analysis.

UNSHADED GROUND FRACTION

Another aspect that influence the performance of a bifacial PV farm is the unshaded ground fraction. This is defined as the ratio between the length of the unshaded ground visible to the rear of a PV module (g_{unsh}) and the total ground's length (g_{tot}) that is seen by the such side. Obliviously, the former parameter can be determined as the difference between g_{tot} and the shaded ground's length (g_{sh}). A higher amount of unshaded ground is beneficial for the modules since the DNI contribution increases the

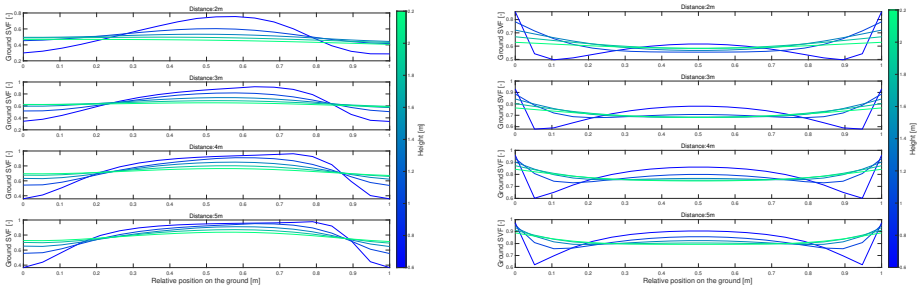

Figure 4.20: Influence of the design parameters d and h on SVF_g. The results are shown for both optimally-tilted (on the left) and vertical modules (on the right). The optimal tilt value refers to Utrecht. The values 0 and 1 correspond to the positions of two neighbouring modules.

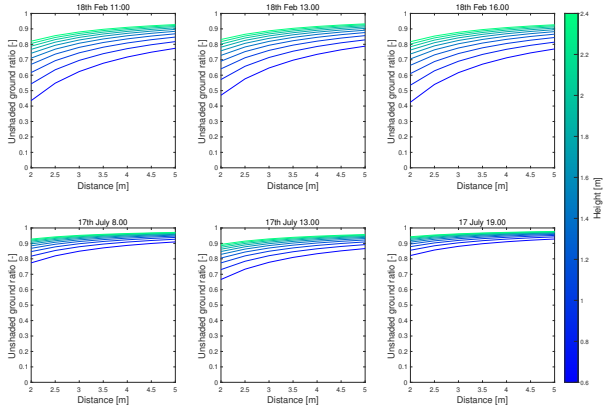

Figure 4.21: Dependence of the unshaded ground fraction on the design parameters. Six relevant time periods are shown for an optimally-tilted farm located in Utrecht

ground-reflected irradiance. Unlike SVF_g, the g_{sh} is time-dependent since the shadows produced by the modules are determined by the position of the sun (a_s, A_s) and the tilt angle. However, It can be highlighted that g_{sh} is not dependent on d and h, i.e. $g_{sh} = f(\theta, a_s, A_s)$. On the other hand, g_{tot} is proportional to both d and h, as illustrated in equation 4.1. Therefore, it can be concluded that higher d and h are beneficial for the PV farm in terms of unshaded ground fraction, since g_{tot} increases while g_{sh} remains unchanged. This is illustrated in figures 4.21 and 4.22, where six relevant time periods are shown referring to Utrecht as location.

$$g_{tot} = \frac{h \cdot d}{l \cdot \sin(\theta)} + \frac{d}{2} \tag{4.1}$$

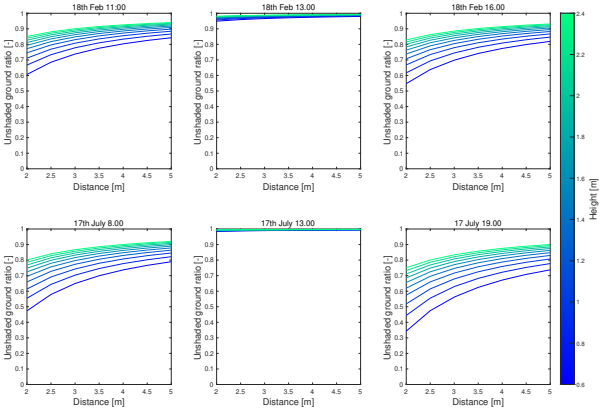

Figure 4.22: Dependence of the unshaded ground fraction on the design parameters. Six relevant time periods are shown for a vertical farm located in Utrecht

MUTUAL SHADING

The mutual shading affects significantly the performances of a bifacial PV farm, therefore it is essential to limit this effect by properly increasing the row-to-row distance of a PV farm. Equations 4.2 and 4.3 show the shadow-free distance required to avoid mutual shading on the front and the rear side of the modules, respectively. As it can be observed from the equations, the shadow-free distance depends on the sun's position (a_s, A_s), hence usually a shadow-free time window is considered depending on the location. Figure 4.23 illustrates the shadow-free distance for the locations analyzed during this study, in relation to their latitude. a_s filters have been used to determine the shadow-free time window, since the more common hourly filters would have been affected by the heterogeneity of the locations. However, the zig-zag appearance of the curve is caused by the low (hourly) resolution of the data. The results highlight the latitude dependence of the shadow-free distance in case of optimally-tilted modules whereas such effect is not present for the vertical configuration. In conclusion, it can be stated that increasing the distance is beneficial to avoid mutual shading whereas the height has no influence on this effect.

$$\frac{d}{l} \geq \cos(\theta) + \sin(\theta) \cdot \frac{\cos(A_M - A_s)}{\tan(a_s)} \tag{4.2}$$

$$\frac{d}{l} \geq \frac{1}{\tan(\theta)} - \frac{\cos(A_M - A_s)}{\tan(a_s)} \tag{4.3}$$

NON-UNIFORMITY OF INCIDENT IRRADIANCE

As described in subsection 2.2.2, the non-uniformity of the rear irradiance is one of the main challenges in bifacial PV since it affects significantly the power output. Therefore, it is necessary to study the impact of the design parameters on such effect to have a complete understanding of the interplay between d and h on the energy yield. To quantify

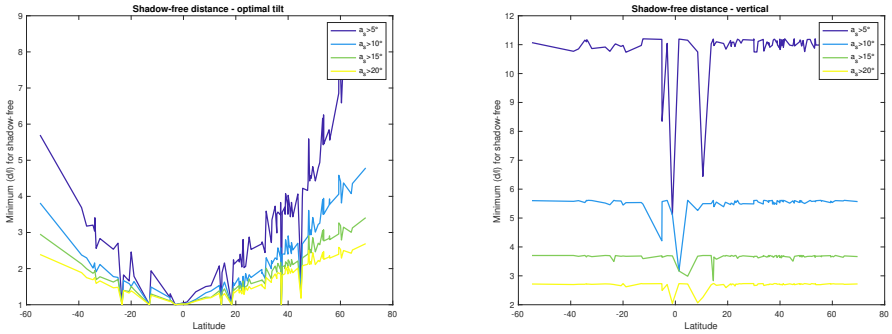

Figure 4.23: Mutual-shadow-free distances for optimally-tilted (on the left) and vertical (on the right) configurations

the non-uniformity of the irradiance, the metric *GNU* introduced in subsection 2.2.2 is calculated for both the front and the rear side, since for the vertical configuration the distinction of the two module's faces is less relevant. *GNU* depends on various factors, including the sun's position hence it is a time-dependent variable. However, in this analysis the weighted average *GNU* value is considered for every location, where the incident irradiance is adopted as weight. Therefore, a yearly value of *GNU* is obtained for both the front and the rear side and the results are shown in figures 4.24, 4.25 and 4.26 where the impact of θ, d and h is highlighted, referring to Utrecht as example location. As expected, for tilted modules the non-uniformity of the rear irradiance on the front side is not dependent on their height, since it is mainly caused by mutual shading. Therefore, a sufficient row-to-row distance is needed to avoid high *GNU* values on the front side, as illustrated in figure 4.24. Moreover, the effect is more evident when higher tilts are considered. In figure 4.25 the same trend with d and θ can be observed for the rear side. However, in this case the influence of the height is evident. For low tilts, a higher height is necessary to avoid high *GNU* values. On the other hand, increasing the tilt, a minimum value of *GNU* can be identified for an optimal height. Such height-dependence is even more evident in case of vertical configuration, as depicted in figure 4.26. The analysis has been extended to multiple locations to verify the outcome illustrated for the Utrecht case, and the same trends have been obtained. Further visualizations can be found in Appendix D.

FINAL OVERVIEW

The influence of the distance and the height on the individual aspects analyzed in this section can be summarized in table 4.2. It shows whether higher, lower or optimal values are beneficial for the energy yield concerning each of these aspects.

It can be concluded that the influence of d and h on the energy yield is the result of the interplay of various aspects. Table 4.2 shows that increasing the row-to-row distance is always beneficial in terms on energy yield. On the other hand, the influence of the modules' elevation is a consequence of the conflicting effects that determine the

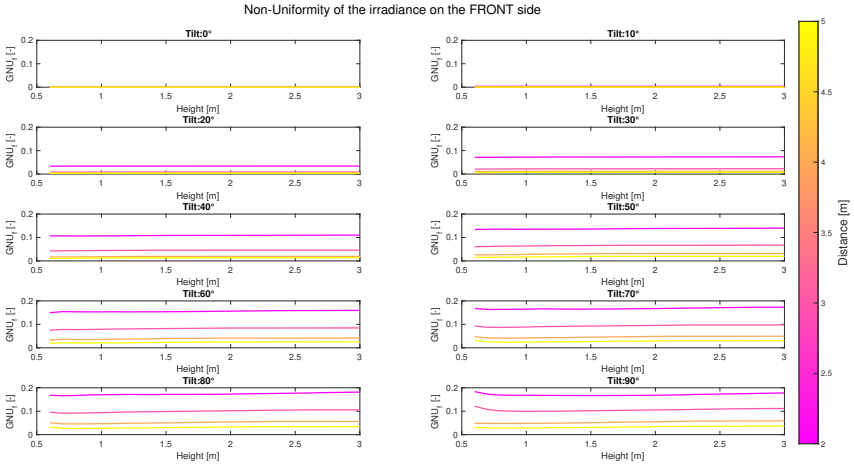

Figure 4.24: Influence of the design parameters on the weighted-average *GNU* of the front side for an optimally-tilted PV farm located in Utrecht.

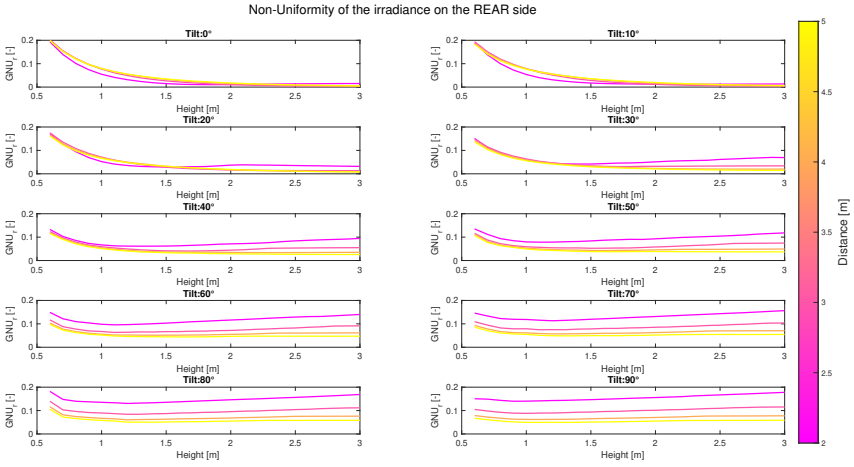

Figure 4.25: Influence of the design parameters on the weighted-average *GNU* of the rear side for an optimally-tilted PV farm located in Utrecht.

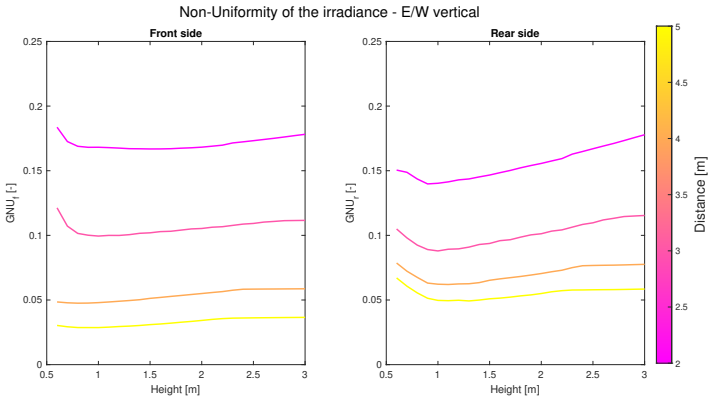

Figure 4.26: Influence of the design parameters on the weighted-average *GNU* of both sides for a vertical PV farm located in Utrecht.

Table 4.2: Influence of d and h on individual aspects of bifacial PV farms that determine the total energy yield. It is indicated whether high, low or optimal values are beneficial for the energy yield concerning the aspect mentioned in each column.

	Ground SVF	Unshaded ground fraction	Mutual shading	GNU
Distance	High	High	High	High
Height	Low	High	No influence	Optimal

presence of an optimal height value that maximizes the energy yield.

4.4. TILTED VS VERTICAL: ECONOMIC POTENTIAL

This section aims to answer the research question of this study concerning the economic potential of the vertical configuration for a bifacial PV farm. First, the relevant variables are introduced in subsection 4.4.1. Subsequently, the concept of "gain region" for vertical modules is explained through some examples in subsection 4.4.2. Subsection 4.4.3 extends such results to a global scale. Lastly, the correlation between the economic potential of the vertical configuration and the diffuse fraction is analyzed in subsection 4.4.4.

4.4.1. INTRODUCTION TO THE RELEVANT VARIABLES

The introduction presented in chapter 1 has mentioned the matching between the shape of the daily power curve of E/W vertical PV installations and the electricity prices' behaviour. However, the previous sections have demonstrated that the power generated by the bifacial PV modules is highly influenced by the design parameters. On the other hand, the electricity prices can assume different profiles, which determine the revenues of the power plant. Moreover, there are other factors that can influence the choice of the optimal farm configuration, for instance a curtailment strategy. Therefore, whether a vertical or a tilted PV farm ensures higher revenues does not have a binary answer. The

purpose of this subsection is to list and describe the variables that are crucial while determining the most profitable farm configuration analyzed.

Section 4.3 has highlighted the impact of the row-to-row distance and the height on the energy yield, which directly affects the revenues of a PV farm. Moreover, section 4.2 has shown how different d and h influence the shape and the magnitude of the daily power curve for the two different configurations. Therefore, a sensitivity analysis on d and h is required to provide a complete understating of the issue.

Another aspect that has to be taken into account while studying the most profitable configuration is the curtailment strategy. To decrease the cost of the grid connection, in some cases it can be favourable to limit the maximum power of the plant to a fraction of the total rated power. This choice is justified by the fact that the periods when the PV farm operates at nominal power are very limited in most of the locations worldwide. Therefore, the energy lost due to a curtailment strategy could be minimal while the total cost of the system could significantly be reduced. This aspect is considered in this study through a variable named maximum power fraction ($n_{max,power}$), which is defined as the ratio between the maximum power allowed and the nominal power of a plant, as shown in equation 4.4. Undoubtedly, the value of $n_{max,power}$ has to be close to the unit otherwise a significant amount of energy is curtailed, leading to a non-profitable strategy.

$$n_{max,power} = \frac{P_{max}}{P_{nominal}} \tag{4.4}$$

To combine the advantages of both optimally-tilted and vertical configurations, "hybrid" PV farms are considered. In this study, such term is used to refer to PV farms composed by both E/W vertical and N/S tilted modules. The aim is to create a power curve characterized by a rectangular shape: "gaining" power during the morning and the evening from the vertical modules, without "losing" excessive power during noon thanks to the presence of tilted modules. Such possibility is included through the variable n_{vert}, which is defined as the ratio between the number of vertical and total modules in the farm, hence ranging from 0 (only tilted modules) to 1 (only vertical modules).

$$n_{vert} = \frac{\#\text{vertical modules}}{\#\text{total modules}} \tag{4.5}$$

The electricity price scenario is identified by the minimum noon price (p_{min}) and the price ratio (p_{ratio}) between such price and the price that occurs during the morning/evening period, as described in section 3.3. The following list summarizes the variables considered in this study, for which a sensitivity analysis to understand the most profitable configuration is performed.

- Max power fraction ($n_{max,power}$)
- Ratio vertical/total modules (n_{vert})
- Row-to-row distance (d)

- Elevation of the modules (h)
- Minimum noon price (p_{min})
- Price ratio (p_{ratio})

Lastly, to quantify the economic potential of a PV farm configuration the difference in the revenues is calculated in comparison to a conventional tilted installation. This is expressed through the revenues' gain (R_{gain}), defined as shown in equation 4.6. In contrast to other studies presented in subsection 2.1.3, this metric is preferred to the "value factor" thanks to its ability to capture the economical benefits in absolute terms.

$$R_{gain} = \frac{R_{\text{new configuration}} - R_{\text{optimal tilt}}}{R_{\text{optimal tilt}}} \cdot 100\% \tag{4.6}$$

4.4.2. "GAIN REGION" FOR VERTICAL CONFIGURATION

A preliminary assessment of the economic potential of the vertical configuration can be performed by identifying the combination of $n_{max,power}$ and n_{vert} that achieve a positive revenues' gain ($R_{gain} > 0\%$). The results can be visualized with contour plots, as illustrated in figure 4.27, which reports the examples of Utrecht and Madrid. The graphs are characterized by n_{vert} on the x-axis and $n_{max,power}$ on the y-axis whereas the contour lines refer to the energy yield and the R_{gain} depending on the color scale. Therefore, the axis describe the characterization of a hybrid PV farm and the curtailment strategy, respectively. The value of R_{gain} compares a hybrid PV farm with the optimally-tilted counterpart characterized by the same $n_{max,power}$. As expected, the highest energy yield is found at the top-left corner, which refers to an optimally-tilted PV farm where curtailment is not applied. It can be observed that decreasing $n_{max,power}$, the energy yield remains almost unchanged up to a certain limit of n_{vert} in both locations. In alternative terms, the presence of a fraction of vertical modules does not limit the energy yield of a PV farm in case partial curtailment is applied. However, the main focus of these graphs is to study the presence of regions in the plot where the condition $R_{gain} > 0\%$ occurs. Such regions are appointed as "gain regions" and define the condition in terms of $n_{max,power}$ and n_{vert} for which it is more profitable to use the hybrid (or vertical in case $n_{vert} = 1$) farm configuration than the conventional optimally-tilted counterpart. In the case depicted in figure 4.27, it can be observed that such condition never occurs in Utrecht, i.e. the presence of vertical modules is never favourable irrespective of any $n_{max,power}$ and n_{vert} conditions. On the other hand, in Madrid hybrid PV farms are more profitable in case of low $n_{max,power}$ since the bottom region of the graph is characterized by $R_{gain} > 0\%$. Nevertheless, these results are sensible to the other variables, which in this example have been set as follows: $d = 3\,m$, $h = 1\,m$, $p_{min} = 200\,€/MWh$ and $p_{ratio} = 2$.

Figure 4.28 shows the same contour plots analyzed in the previous paragraph for a higher value of row-to-row distance. It can be observed that a gain region appears at the bottom of the Utrecht contour plot whereas the number of possible combinations of $n_{max,power}$ and n_{vert} that guarantees a positive revenues' gain is larger for the Madrid

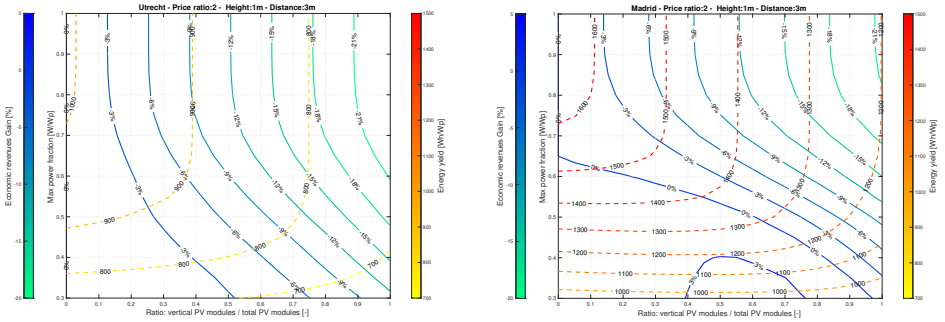

Figure 4.27: Contour plots that show the energy yield and the revenues' gain for different $n_{max,power}$ and n_{vert} values. The examples of Utrecht (on the left) and Madrid (on the right) are presented. The other variables are set as follows: $d = 3\,m$, $h = 1\,m$, $p_{min} = 200€/MWh$, $p_{ratio} = 2$

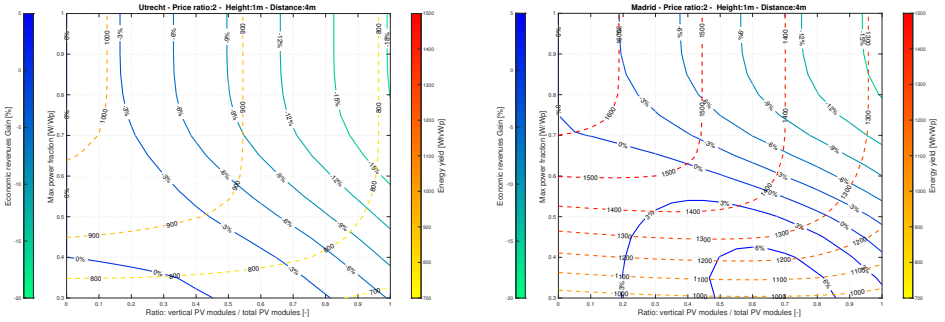

Figure 4.28: Contour plots that show the energy yield and the revenues' gain for different $n_{max,power}$ and n_{vert} values. The examples of Utrecht (on the left) and Madrid (on the right) are presented. The other variables are set as follows: $d = 4\,m$, $h = 1\,m$, $p_{min} = 200€/MWh$, $p_{ratio} = 2$

example. This confirms the observation of the previous section for which the row-to-row distance value has more beneficial impact for the vertical than the tilted configuration. Moreover, in figure 4.29 the analysis is repeated by increasing the value of price ratio, increasing the benefits of the vertical PV power curve. As a consequence, in both cases the gain region enlarges, covering most of the graph's surface in the Madrid example.

Overall, in the conditions shown in these examples vertical or hybrid PV farms appear to be favourable only in case a low power fraction is considered, which it is not realistic due to the excessive energy curtailed. Therefore, further analysis is required to understand the profitability of these alternative configurations. Specifically, the results have to be extended to a global scale as well as in terms of variables, i.e. considering different combinations of the parameters introduced in 4.4.1.

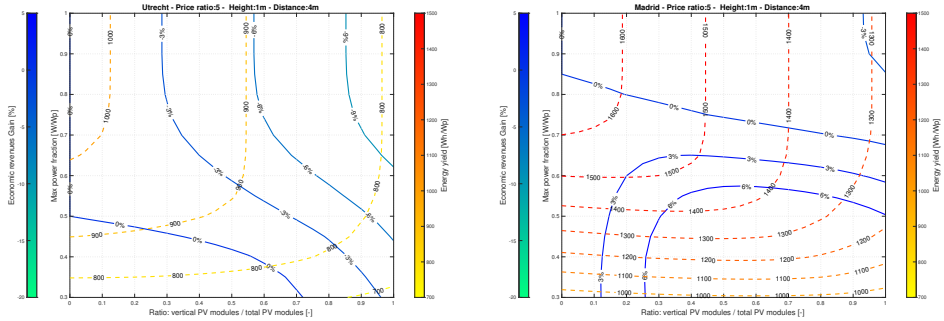

Figure 4.29: Contour plots that show the energy yield and the revenues' gain for different $n_{max,power}$ and n_{vert} values. The examples of Utrecht (on the left) and Madrid (on the right) are presented. The other variables are set as follows: $d = 4\,m$, $h = 1\,m$, $p_{min} = 200\,€/MWh$, $p_{ratio} = 5$

4

4.4.3. GLOBAL ANALYSIS

In this subsection, the profitability of vertical PV farms is analyzed on a global perspective. Specifically, to understand whether E/W vertical or N/S tilted modules are favourable, the focus is shifted to the following question:

What is the minimum price ratio required to achieve more revenues using E/W vertical instead of N/S tilted PV modules?

In alternative terms, the aim is to identify the minimum p_{ratio} to achieve the condition $R_{gain} > 0$. In particular, the purpose of the next paragraphs is to provide an answer to this question with respect to the variables introduced in subsection 4.4.1 for each location analyzed in this study. This is achieved by using scatter plots characterized by p_{ratio} on the y-axis and the examined feature on the x-axis, i.e. $n_{max,power}$, n_{vert}, d, h or p_{min}. The size of each data point is proportional to the number of locations that satisfy the condition $R_{gain} > 0$ for a specific p_{ratio} and feature's value. Moreover, a color scale is used to identify the diffuse fraction (weighted-averaged yearly value) of each location. In case a data point represents more than one location, i.e. is larger in size, the color refers to the average diffuse fraction of these locations. Price ratios between 1 and 10 are considered in the analysis. Furthermore, the maximum value on the y-axis indicates the locations for which the condition of $R_{gain} > 0\%$ is never achieved for these p_{ratio} values. In simple terms, the larger the size of the dots at the bottom of the graphs, the higher is the profitability of the vertical/hybrid farm with respect to the conventional tilted configuration.

CURTAILMENT STRATEGY

As introduced in subsection 4.4.1, the curtailment strategy of a PV farm is identified by the variable $n_{max,power}$, which assumes the value of 1 in case no curtailment is applied. The influence of $n_{max,power}$ on the minimum price ratio required to achieve revenues' gain is depicted in figure 4.30. In the left figure the possibility of hybrid farms is excluded, therefore it is limited to the comparison between completely E/W vertical or N/S tilted

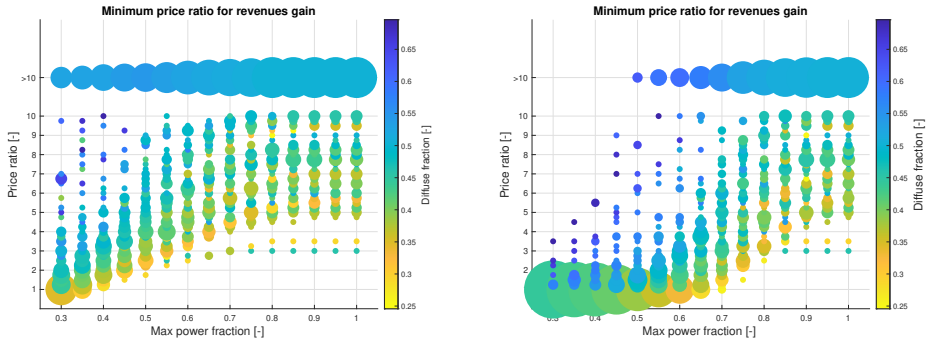

Figure 4.30: Influence of $n_{max,power}$ on the minimum price ratio required to achieve revenues' gain, where both $n_{vert} = 1$ (on the left) and $n_{vert} = var$ (on the right) are considered. The other variables are set as follows: $d = 4\,m$, $h = 1\,m$, $p_{min} = 100\,€/MWh$

farms, i.e. n_{vert} is constant and equal to 1. It can be observed that the profitability of the vertical configuration increases as the $n_{max,power}$ value decreases, as expected. However, such trend is only evident for $n_{max,power} < 0.7$ which entails significant power losses due to curtailment. On the other hand, the figure on the right allows the possibility of hybrid PV farms, i.e. the dots refer to the value of n_{vert} that maximizes R_{gain}. It is evident that hybrid PV farms are highly beneficial for low values of $n_{max,power}$ since the noon peak generated by the tilted configuration is affected by the curtailment. Nevertheless, such advantages are limited to minimal values of $n_{max,power}$, similarly as for the previous case. Moreover, figures 4.30 show that no relevant differences can be detected for both $n_{vert} = 1$ and variable n_{vert} cases when $n_{max,power}$ is close to 1. Therefore, hybrid farms seem not to be favorable in case of high $n_{max,power}$ values. In conclusion, the influence of the curtailment strategy on configurations' profitability is evident only for values of $n_{max,power}$ lower than approximately 0.7, which are considered not reasonable for the purpose of this research.

"HYBRID" PV FARM

To confirm the preliminary observation concerning the benefits of hybrid PV farms, further investigation is needed about the influence of n_{vert} on the minimum price ratio required to achieve $R_{gain} > 0$. Therefore, the same methodology of the curtailment strategy is applied, using n_{vert} as examined feature. This is depicted in figure 4.31, where the cases $n_{max,power} = 0.7$ and $n_{max,power} = 1$ are shown. When no curtailment is applied, it can be observed that n_{vert} has no influence on the condition concerning p_{ratio}. In alternative terms, either completely E/W vertical or N/S tilted configuration is favourable depending on the location and the market condition. On other hand, for $n_{max,power} = 0.7$, hybrid vertical/tilted installations can be advantageous. Therefore, the conclusion of the previous paragraph has been confirmed.

ROW-TO-ROW DISTANCE

The impact of the row-to-row distance on the energy yield has been studied extensively in subsection 4.3.1, where it has been demonstrated that larger d values increase the

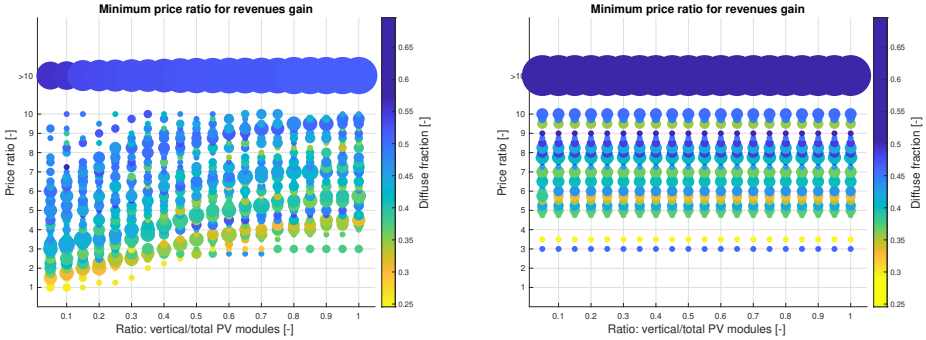

Figure 4.31: Influence of n_{vert} on the minimum price ratio required to achieve revenues' gain, where both $n_{max,power} = 0.7$ (on the left) and $n_{max,power} = 1$ (on the right) are considered. The other variables are set as follows: $d = 4\,m$, $h = 1\,m$, $p_{min} = 100\,€/MWh$

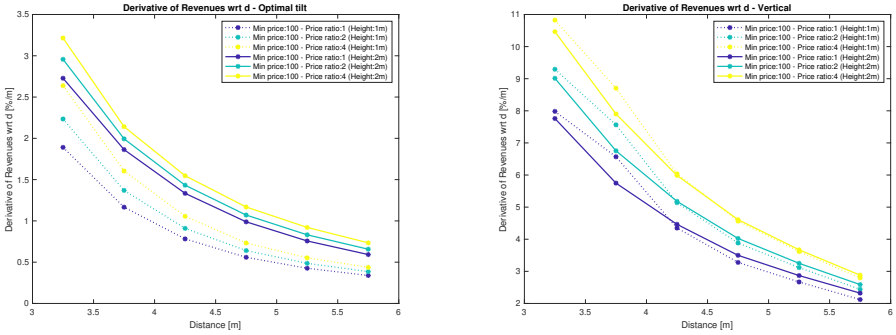

Figure 4.32: Derivative of the revenues with respect to the distance. An average value of all the locations is presented for both tilted (on the left) and vertical (on the right) configuration.

power production of the farms. As depicted in figure 4.32, this trend is confirmed also for the revenues, where the same saturation behaviour is visible. Specifically, it can be observed that the derivative of the revenues, expressed in $[\%/m]$, is affected more by the height than the market conditions. Moreover, higher derivative values for vertical modules are obtained concerning the revenues, similarly as for the energy yield. Therefore, an increase in the row-to-row distance is expected to have more beneficial impact on the revenues of vertical than tilted farms. This is confirmed by the results depicted in figure 4.33, where larger dots for low p_{min} are found while increasing the row-to-row distance. Therefore, larger d values foster the profitability of vertical PV modules. This outcome is limited to case where no curtailment strategy or hybrid farms are considered, on the basis of the conclusions drawn in the previous paragraphs.

ELEVATION OF THE MODULES

A similar analysis is performed to study the impact of the height on the revenues. The results depicted in figure 4.34 show that the interplay between d and h is dominant with

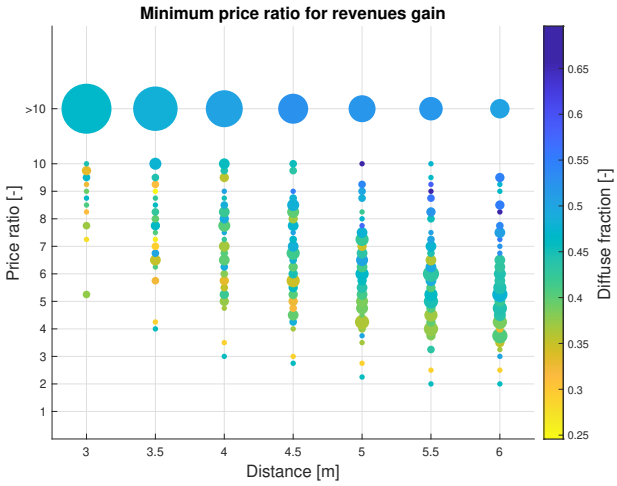

Figure 4.33: Influence of d on the minimum price ratio required to achieve revenues' gain. The other variables are set as follows: $h = 1\,m$, $p_{min} = 100€/MWh$, $n_{vert} = 1$, $n_{max,power} = 1$

respect to the market condition, analogously to what has been observed for the row-to-row distance. Therefore, the presence of an optimal height that maximizes the revenues is confirmed, and it is approximately equal to the value that ensures the highest energy yield. However, the impact of h is expected to be lower due to the limited derivative values obtained in this case. This is indeed observed in figure 4.35 where no evident influence of h is detected above a certain value. On the other hand, lower h seem to slightly foster vertical modules among the tilted installations.

PRICE SCENARIO

Lastly, the impact of the price scenario is investigated. Since the influence on the price ratio is the objective of the study, this analysis is limited to the effect of the minimum price. Therefore, the minimum p_{ratio} to satisfy the condition $R_{gain} > 0$ is calculated for different values of p_{min} and the results are shown in figure 4.36. Two main conclusions can be drawn from this visualization. First, vertical PV modules are always favourable in case of negative minimum prices. This is a consequence of the revenues' losses caused by the energy produced around noon, which is higher for N/S tilted configuration, since curtailment is not considered in this case. Second, different values of positive p_{min} do not affect the minimum price ratio to achieve revenues' gain. Therefore, R_{gain} is independent on the magnitude of the variable p_{min}, but it only depends on its sign. This arises from the definition of R_{gain}, which is expressed in percentage. The minimum price indeed influences the revenues gain in absolute terms but has no impact when relative metrics are adopted, as explained through the following example.

Let's consider two different electricity price curves $e_1(t)$ and $e_2(t)$ modelled as described in section 3.3. Suppose that $e_1(t)$ and $e_2(t)$ are characterized by the same price ratio ($p_{ratio,1} = p_{ratio,2}$) but two different (positive) minimum noon prices ($p_{min,1} \neq$

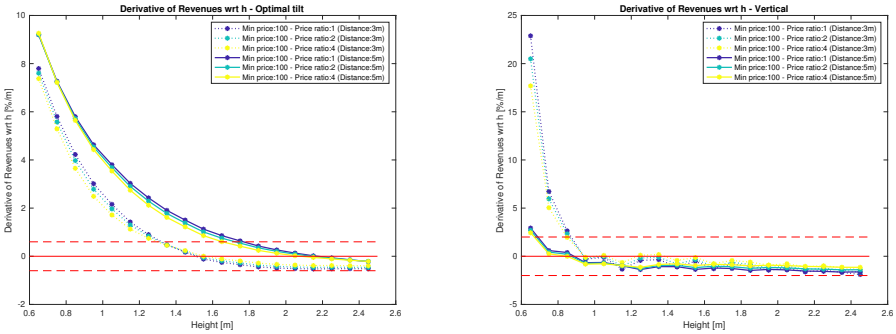

Figure 4.34: Derivative of the revenues with respect to the height. An average value of all the locations is presented for both tilted (on the left) and vertical (on the right) configuration. The red lines highlight the saturation behaviour.

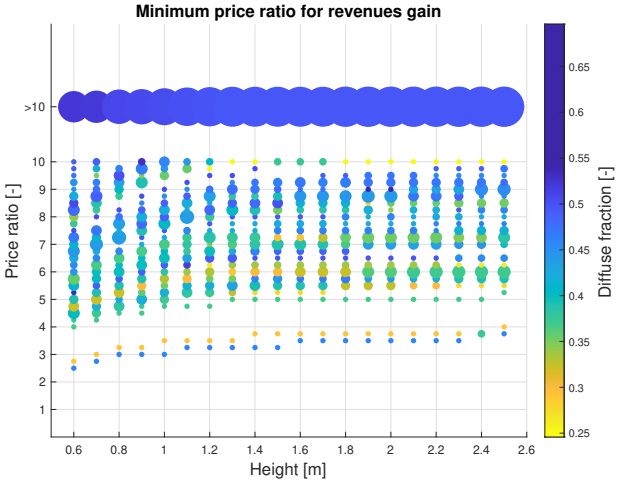

Figure 4.35: Influence of h on the minimum price ratio required to achieve revenues' gain. The other variables are set as follows: $d = 4\,m$, $p_{min} = 100 €/MWh$, $n_{vert} = 1$, $n_{max,power} = 1$

$p_{min,2}$). According to their definition, the relation between $e_1(t)$ and $e_2(t)$ expressed in equation 4.7 is valid.

$$e_1(t) = \frac{p_{min,1}}{p_{min,2}} \cdot e_2(t) \tag{4.7}$$

The revenues of the vertical and the tilted configuration obtained for the market conditions described by $e_1(t)$ are indicated with $R_{v,1}$ and $R_{t,1}$. Similarly, $R_{v,2}$ and $R_{t,2}$ refer to $e_2(t)$ electricity price curve. The revenues' gain can be obtained as shown in the expressions 4.8 and 4.9, where $P_v(t)$ and $P_t(t)$ are the power curves of the vertical and tilted farm during the time period $[t_1, t_2]$.

$$R_{gain,1} = \frac{R_{v,1} - R_{t,1}}{R_{t,1}} = \frac{\int_{t_1}^{t_2} e_1(t)P_v(t)dt - \int_{t_1}^{t_2} e_1(t)P_t(t)dt}{\int_{t_1}^{t_2} e_1(t)P_t(t)dt} = \frac{\int_{t_1}^{t_2} e_1(t)P_v(t)dt}{\int_{t_1}^{t_2} e_1(t)P_t(t)dt} - 1 \tag{4.8}$$

$$R_{gain,2} = \frac{R_{v,2} - R_{t,2}}{R_{t,2}} = \frac{\int_{t_1}^{t_2} e_2(t)P_v(t)dt - \int_{t_1}^{t_2} e_2(t)P_t(t)dt}{\int_{t_1}^{t_2} e_2(t)P_t(t)dt} = \frac{\int_{t_1}^{t_2} e_2(t)P_v(t)dt}{\int_{t_1}^{t_2} e_2(t)P_t(t)dt} - 1 \tag{4.9}$$

Therefore, combining the relations 4.7, 4.8 and 4.9, the condition illustrated in equation 4.10 can be obtained, proving the validity of the results shown in figure 4.36.

$$\begin{aligned} R_{gain,1} = \frac{\int_{t_1}^{t_2} e_1(t)P_v(t)dt}{\int_{t_1}^{t_2} e_1(t)P_t(t)dt} - 1 = \frac{\int_{t_1}^{t_2} \left[\frac{p_{min,1}}{p_{min,2}} \cdot e_2(t)\right] P_v(t)dt}{\int_{t_1}^{t_2} \left[\frac{p_{min,1}}{p_{min,2}} \cdot e_2(t)\right] P_t(t)dt} - 1 = \\ = \frac{\cancel{\frac{p_{min,1}}{p_{min,2}}} \cdot \int_{t_1}^{t_2} e_2(t)P_v(t)dt}{\cancel{\frac{p_{min,1}}{p_{min,2}}} \cdot \int_{t_1}^{t_2} e_2(t)P_t(t)dt} - 1 = \frac{\int_{t_1}^{t_2} e_2(t)P_v(t)dt}{\int_{t_1}^{t_2} e_2(t)P_t(t)dt} - 1 = R_{gain,2} \end{aligned} \tag{4.10}$$

SUMMARY

Table 4.3 summarizes the findings of the previous paragraphs. It can be concluded that the row-to-row distance is the variable that mostly influence the choice of the optimal configuration within the boundaries set by this study. Lastly, figure 4.37 depicts the minimum price ratio for which E/W vertical modules should be preferred to the N/S tilted counterpart for the different locations analyzed in this case. Additional visualizations are included in the appendix E.

4.4.4. DIFFUSE FRACTION CORRELATION

In the previous section the impact of the design parameters and the market conditions on the configurations' choice has been analyzed for various locations. As shown by figure 4.37, the spatial diversification of the results suggests that the performance of bifacial PV modules are strictly dependent on the local climate. However, a slight trend between the diffuse fraction and the results presented in subsection 4.4.3 can be recognized, where

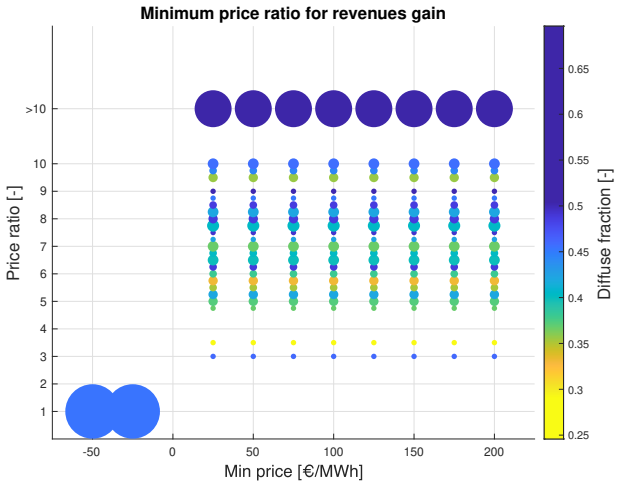

Figure 4.36: Influence of p_{min} on the minimum price ratio required to achieve revenues' gain. The other variables are set as follows: $d = 4\,m$, $h = 1\,m$, $n_{vert} = 1$, $n_{max,power} = 1$

low diffuse fraction seems to be favourable for the vertical configuration. As mentioned multiple times during this research, the GHI-weighted average diffuse fraction is used as a representative yearly value for each location. To investigate such behaviour, the correlation between the diffuse fraction and R_{gain} is studied, and the results are depicted in figure 4.38. As expected, a negative correlation can be observed, i.e. it is more advantageous to adopt the E/W vertical configuration when the location is characterized by a low diffuse fraction. Figure 4.38 also highlights that this behaviour is not affected by d or h values whereas higher (absolute) values of correlation are obtained for high price ratios.

The influence of the diffuse fraction is confirmed by analyzing its correlation with respect to the minimum p_{ratio} needed by vertical modules to overcome the tilted installations in terms of revenues. Figure 4.39 indeed shows positive values of correlation, i.e. the lower the diffuse fraction the less strict is the market condition to satisfy $R_{gain} > 0$. However, in this case a dependence with the design parameters can be recognized, especially while considering the row-to-row distance.

Lastly, the influence of the diffuse fraction daily profile is investigated. The concern arises from two different observations. First, the U-shape of the electricity price curve entails that the R_{gain} mainly depends on the magnitude of the power peaks during morning and evening for the vertical configuration. Second, the analysis on the influence of diffuse fraction on the shape of the power curve presented in 4.2 shows that a low diffuse fraction is beneficial during morning and evenings. Therefore, the idea consists in investigating if the correlation between the diffuse fraction and R_{gain} increases (in absolute value) when only morning and evening periods are considered. First, for each

Table 4.3: Summary of the findings concerning the influence of different variables on the minimum price ratio required to achieve revenues' gain while using vertical instead of tilted configuration

Variable	**Influence**
Max power fraction ($n_{max,power}$)	The influence of the curtailment strategy is significant only in case of low $n_{max,power}$ values, which are not considered relevant for large-scale PV farms
Ratio vertical/total modules (n_{vert})	Hybrid PV farms are favourable only in case of low $n_{max,power}$, hence they are not relevant for this study
Row-to-row distance (d)	Large d values increase the profitability of the vertical configuration over the tilted modules
Elevation of the modules (h)	h values have a limited impact on the revenues, but lower values increase the profitability of vertical modules with respect to the tilted counterpart
Minimum noon price (p_{min})	Only the sign of the minimum price is relevant to decide the optimal configuration and vertical modules are always preferred in case of a negative p_{min}

location the GHI-weighted average diffuse fraction is calculated for each hour of the day, in order to obtain a hourly profile of the diffuse fraction that is representative for the entire year. To establish the boundaries of morning and evening periods, a method based on a_s value is adopted, similarly to the modelling of the electricity prices described in section 3.3. Specifically, an a_s value has to be associated to each diffuse fraction, hence GHI-weighted average a_s are calculated for each hour of the day as well, iterating this process for each location. The correlation is now studied while filtering out the values of diffuse fraction around noon, which satisfy the condition $a_s > a'_s$. The results are illustrated in figure 4.40, where the correlation is calculated for different a'_s values shown on the x-axis. Therefore the left region of the graph refers to cases where only morning and evening data are considered whereas the right part takes into account the whole day. Moreover, after some preliminary test it has been decided to filter out the values of diffuse fraction for which $a_s < 5°$ since the high diffuse fraction that characterizes periods when $a_s \approx 0°$ compromises the trend highlighted in figure 4.40.

It can be observed that the hypothesis that a low diffuse fraction during the morning/evening periods fosters vertical PV profitability over tilted configuration is partially confirmed. The expected trend occurs indeed for values of price ratio up to 6. In these cases the correlation between the diffuse fraction and R_{gain} increases in absolute value when the daily time window is restricted by filtering out the noon values, i.e. increasing a'_s. However, for higher values of p_{ratio} the correlation stabilizes or a slight opposite trend is observed.

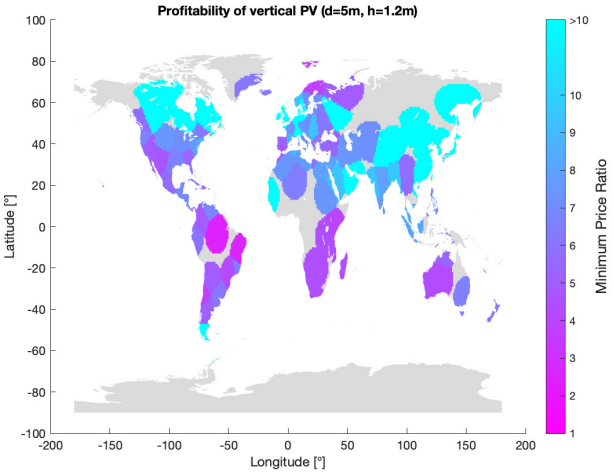

Figure 4.37: Global map of the minimum price ratio for which vertical modules are more profitable than the tilted counterpart. The relevant variables are set as follows: $d = 5\,m$, $h = 1.2\,m$, $p_{min} = 100€/MWh$, $n_{vert} = 1$, $n_{max,power} = 1$

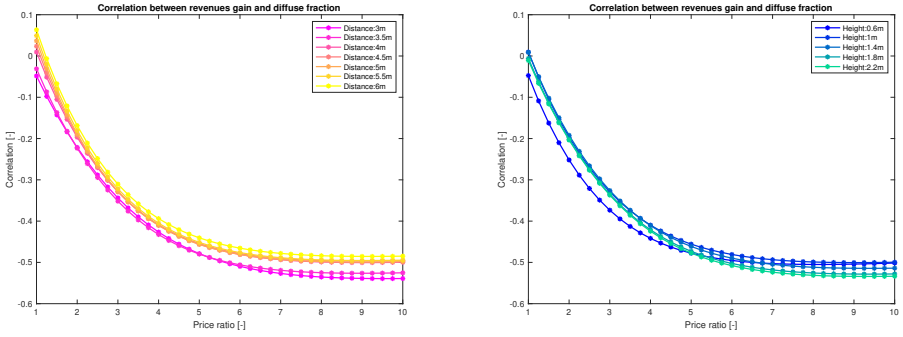

Figure 4.38: Correlation between the diffuse fraction (GHI-weighted average) and R_{gain}. The influence of d, h and p_{ratio} is highlighted. Unless specified in the legend, the other variables are set as follows: $d = 4\,m$, $h = 1\,m$, $n_{vert} = 1$, $n_{max,power} = 1$

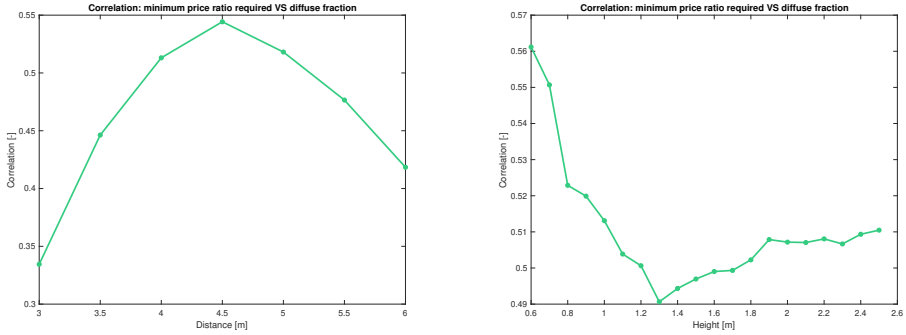

Figure 4.39: Correlation between the diffuse fraction (GHI-weighted average) and the minimum p_{ratio} for which $R_{gain} > 0$ is satisfied. The influence of d and h is highlighted. Unless specified in the axis, the other variables are set as follows: $d = 4\,m$, $h = 1\,m$, $n_{vert} = 1$, $n_{max,power} = 1$

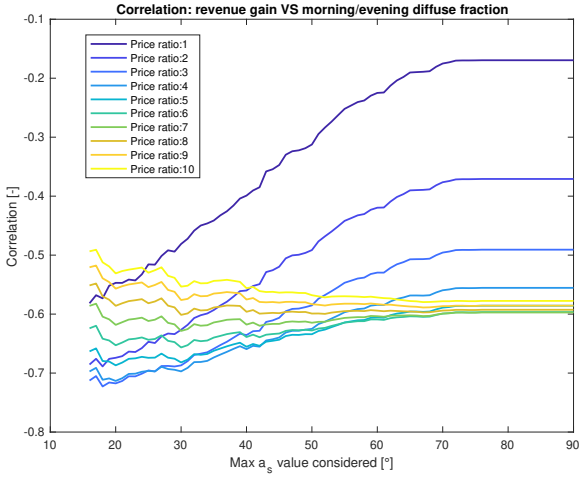

Figure 4.40: Correlation between GHI-weighted average diffuse fraction and R_{gain} while considering only morning/evening periods. The relevant variables are set as follows: $d = 4\,m$, $h = 1\,m$, $p_{min} = 100\,€/MWh$, $n_{vert} = 1$, $n_{max,power} = 1$

5

Conclusion and Recommendations

This concluding chapter summarizes the findings of this study and illustrates the recommendations for future research that could improve and extend the outcome of this work.

5.1. Conclusion

The aim of this thesis was to investigate the potential of E/W vertical bifacial PV farm in terms of market revenues. To ensure a sufficient generalization of the topic, the benefits of such configuration have been studied in comparison to the N/S conventional tilted counterpart for multiple locations. This is achieved through the development of a bifacial PV model that estimates the power generated by a PV farm. Various market scenarios and installation conditions have been tested while simulating PV farms' operation using this model, in order to understand which parameters are relevant while determining the optimal configuration.

An extensive literature review has been performed to understand the features and the limitations of the existing models used for bifacial PV modules. View factor and ray-tracing have been identified as the two main possible approaches. Specifically, the former ensures lower computational time whereas the latter provides higher accuracy. Due to the global scale of the analysis, view factor has been selected as the optimal method and the 2D assumption is adopted. Furthermore, the models implemented by the previous studies have been classified depending on the methods used to tackle two main challenges of bifacial modelling, namely the non-uniformity of rear irradiance and the spectral impact. It was observed that these aspects are crucial to guarantee a sufficient accuracy and a gap in the literature was highlighted concerning models that simultaneously take into account both aspects while performing a global analysis. Therefore, an algorithm based on a multi-dimensional matrix approach has been developed in this

study to model bifacial PV farms. The functionalities of MATLAB has been used to execute calculations along multiple dimensions, from spectral to spatial, e.g. modules' rows or cells. Moreover, such model enables the simulation of farms characterized by unconventional configurations since the design parameters can be set at each row rather than for the entire farm. For instance, this includes the possibility of selecting different tilt, elevation and row-to-row distance values for each modules' row individually. These aspects constitute the optical submodel, which is coupled with the thermo-electrical part to convert the information about the incident irradiance into electrical power. In particular, INOCT concept is adopted to estimate cells' temperature whereas the electrical submodel is based on a fill factor approximation to achieve sufficient computational speed.

The model has been validated in collaboration with the company KIPP&ZONEN, which has provided the data of measurements on bifacial PV modules that took place in Delft (Netherlands) between July and September 2020. Different tilt values and ground types have been tested to investigate the accuracy of the model under multiple installation conditions. This validation is limited to the irradiance incident on the rear side of the modules, since the submodels adopted to predict the front irradiance and to estimate the electrical power are inherited from the monofacial technologies hence the accuracy of such methods has been widely tested. Therefore, measurements from six pyranometers located along the module's back surface have been compared with the model's output, in order to investigate the effect of the non-uniformity of rear irradiance. Unfortunately, this validation process is limited to broadband irradiance values due to the unavailability of spectral measurements. In general, sufficient agreement between modelled and measured data has been obtained, which is quantified by a mean bias deviation of $-1.29\,W/m^2$ (-2.22%) and a root mean square error of $12.65\,W/m^2$ (21.69%) for the rear irradiance. Such values are aligned with most of models based on view factor concept found in literature. Moreover, it has been observed that the design parameter that mostly affect the model's performance is the tilt, i.e. higher tilts increase the errors. Specifically, overestimation of irradiance usually occurs for higher tilts whereas underestimation is registered for values close to the horizontal inclination. Moreover, the error increases at the edges of the modules, especially during clear days. Therefore, it has been concluded that the accuracy of the model decreases as the amount of unshaded ground seen by the specific cell increases, proving the limitations of view factor concept, which assumes all surfaces to be diffuse emitters.

The influence of the climate conditions and the design parameters on the daily power curve has been investigated for vertical and tilted bifacial PV farms. It has been shown that the diffuse fraction affects significantly the shape of such curve for vertical modules, i.e. low diffuse fraction during morning/evening periods is beneficial. On the other hand, larger row-to-row distance shifts up the power curve for both configurations whereas the effect of the modules' elevation is less relevant. This has been confirmed by analyzing the sensitivity of the energy yield on these parameters. Specifically, the presence of an optimal height that maximizes the energy yield has been proved. However, such optimal value is dependent on the specific location and a strong interdependence

with the row-to-row distance has been proved.

The economic potential of the E/W vertical configuration with respect to the N/S tilted counterpart has evaluated by considering a modelled electricity price curve, which is characterized by lower prices during noon and higher values for the morning/evening time periods. The choice of the optimal configuration has been discussed with respect to various variables, including design parameters, market conditions, curtailment strategies and hybrid farm configurations. The results have shown that hybrid PV farms guarantees an increase in the economic revenues only in case a heavy curtailment strategy is adopted, namely the maximum power fraction has to be lower than 70% of the nominal value. Otherwise, either completely vertical or entirely optimally tilted PV modules have to be preferred depending on the other parameters. Moreover, the maximum power fraction has an influence concerning the profitability of vertical in comparison to tilted farms only in case the value is sufficiently low (<70%), which has been considered as not suitable due to the significant amount of power losses.

If the variation in the profitability of vertical among tilted modules is calculated through a revenues' gain expressed as percentage, the dependence on the market conditions is determined only by the ratio between noon and morning/evening price, not on the minimum noon value. Specifically, a minimum price ratio that guarantees the economical superiority of the E/W vertical configuration can be identified. However, it is highly dependent on the specific location and other design parameters. In broad terms, the increase of the row-to-row distance is beneficial in terms of revenues up to a certain saturation value. Such behaviour is registered for both vertical and tilted farms, even though the impact is higher for the latter case. As a consequence, larger distances lead to lower minimum price ratios required to ensure the higher profitability of the vertical configuration. The second-order effect of the height observed for the energy yield remains unchanged while considering the market revenues hence an optimal value can be found depending on the individual location and other design parameters. Lastly, a trend with the diffuse fraction has been recognized in the results, i.e. a negative correlation between the revenues' gain and such climate condition has been found. Specifically, lower diffuse fraction enhances the profitability of the vertical configuration, requiring a lower minimum price ratio to become superior in terms of market revenues. Such effect becomes more evident if the analysis is limited to the morning/evening hours, when the market revenues of vertical modules are boosted by a low diffuse fraction whereas the impact is limited for the tilted case. In conclusion, for the locations characterized by a low diffuse fraction, especially during the morning and evening periods, less stringent market conditions are required to ensure higher profitability for E/W vertical bifacial PV farms with respect to the conventional N/S tilted configuration.

5.2. RECOMMENDATIONS

This report has proposed a validated model to simulate the performance of bifacial PV farms on a global scale, in order to draw conclusions concerning the profitability of E/W vertical modules with respect to the tilted counterpart. However, the exhaustiveness of this work is constrained by time limitations and the computational resources available,

preventing further investigation on the topic. In this section some guidelines for future studies are presented, aiming to outline the possible research pathways concerning the field of bifacial PV modelling and the economic potential of different farm configurations.

A first recommendation concerns possible improvements for the model developed in this study. Even though the main limitations are intrinsic to the view factor concept, the use of corrective coefficients to include the effect of the mounting structure could be considered, in order to increase the accuracy of the rear irradiance estimation. This could be achieved by comparing the model's results with ray-tracing simulations or real data. Moreover, the validation process of the model should be based on measurements performed in an environment characterized by long modules' row and free horizon, simulating the operation of a large farm. Such approach would increase the reliability of the results.

The computational speed of the algorithm is one the main requirement to perform a detailed global analysis when various installation conditions are tested. The multi-dimensional matrix approach presented in this thesis reduces significantly the time required for the simulations. However, large matrices characterized by multiple dimensions require sufficient RAM capacity and involve operations that limit the speed of the process. Therefore, the dimensions of the problem could be decreased by introducing some approximations. For instance, the information concerning the non-uniformity of the rear irradiance contained along the cells' spatial dimension could be replaced by the adoption of corrective coefficients, that should depend on the design parameters (e.g. tilt, height, distance) and the meteorological conditions. For this purpose, various machine learning techniques could be used to quantify the dependence of the non-uniformity on these variables, since this study has been limited to qualitative consideration about this issue. A significant decrease of the computational time of the algorithm developed in this work would broaden its applicability. Specifically, the possibility of testing unconventional farm configurations by changing the design parameters on row level could be investigated. For instance, depending on the market prices' behaviour, the differentiation of the tilt for of each farm's row could be beneficial in terms of revenues. However, the use of optimization methods based on gradient methods have shown limitations during some preliminary tests on this aspect. Therefore, genetic algorithm should be preferred, which requires higher computational resources/time or a simplified model.

A third recommendation regards a different research direction that could be investigated using the model presented during this study. In this research, the potential of E/W vertical configuration is studied only in relation with the electricity market prices. Therefore, the coupling with storage technologies is neglected as well as the matching of vertical PV power curve with load profiles typical of different sectors/applications. For instance, the dual-peaks profile could lead to a decrease in the battery capacity of a stand-alone PV system or other benefits when net-metering is present. Such concepts gain importance especially when lower scale plants are considered, e.g. residential cases.

Therefore, it is suggested to study further the potential of E/W vertical modules in relation to these aspects, in order to achieve a 360 degrees overview of the advantages this configuration.

BIBLIOGRAPHY

[1] IRENA, *World Energy Transitions Outlook 2023: 1.5°C Pathway, Volume 1*. Abu Dhabi: International Renewable Energy Agency, 2023. [Online]. Available: https://mc-cd8320d4-36a1-40ac-83cc-3389-cdn-endpoint.azureedge.net/-/media/Files/IRENA/Agency/Publication/2023/Jun/IRENA_World_energy_transitions_outlook_v_1_2023.pdf?rev=b1d4be858ad549a9a750921d0f2b5d53.

[2] M. Fischer, M. Woodhouse, P. Baliozian, and J. Trube, *International technology roadmap for photovoltaics (ITRPV) 14th edition: 2022 results*, 2023.

[3] R. Kopecek and J. Libal, "Towards large-scale deployment of bifacial photovoltaics," *Nat Energy*, vol. 3, pp. 443–446, 2018. DOI: 10.1038/s41560-018-0178-0. [Online]. Available: https://doi.org/10.1038/s41560-018-0178-0.

[4] C. D. Rodríguez-Gallegos, H. Liu, O. Gandhi, *et al.*, "Global techno-economic performance of bifacial and tracking photovoltaic systems," *Joule*, vol. 4, no. 7, pp. 1514–1541, 2020, ISSN: 2542-4351. DOI: https://doi.org/10.1016/j.joule.2020.05.005. [Online]. Available: https://www.sciencedirect.com/science/article/pii/S2542435120301884.

[5] B. Marion, S. MacAlpine, C. Deline, *et al.*, "A practical irradiance model for bifacial pv modules," pp. 1537–1542, 2017. DOI: 10.1109/PVSC.2017.8366263.

[6] S. A. Pelaez, C. Deline, S. M. MacAlpine, B. Marion, J. S. Stein, and R. K. Kostuk, "Comparison of bifacial solar irradiance model predictions with field validation," *IEEE Journal of Photovoltaics*, vol. 9, no. 1, pp. 82–88, 2019. DOI: 10.1109/JPHOTOV.2018.2877000.

[7] G. J. Ward, *The RADIANCE Lighting Simulation and Rendering System*. New York, NY, USA: Association for Computing Machinery, 1994, pp. 459–472, ISBN: 0897916670. DOI: 10.1145/192161.192286. [Online]. Available: https://doi.org/10.1145/192161.192286.

[8] G. Raina and S. Sinha, "A comprehensive assessment of electrical performance and mismatch losses in bifacial pv module under different front and rear side shading scenarios," *Energy Conversion and Management*, vol. 261, p. 115 668, 2022, ISSN: 0196-8904. DOI: https://doi.org/10.1016/j.enconman.2022.115668. [Online]. Available: https://www.sciencedirect.com/science/article/pii/S0196890422004642.

[9] E. Mouhib, P. M. Rodrigo, L. Micheli, E. F. Fernández, and F. Almonacid, "Quantifying the rear and front long-term spectral impact on bifacial photovoltaic modules," *Solar Energy*, vol. 247, pp. 202–213, 2022, ISSN: 0038-092X. DOI: https://doi.org/10.1016/j.solener.2022.10.035. [Online]. Available: https://www.sciencedirect.com/science/article/pii/S0038092X2200768X.

[10] S. Ayala Pelaez, C. Deline, J. S. Stein, B. Marion, K. Anderson, and M. Muller, "Effect of torque-tube parameters on rear-irradiance and rear-shading loss for bifacial pv performance on single-axis tracking systems," Oct. 2020. DOI: 10.1109/PVSC40753.2019.9198975. [Online]. Available: https://www.osti.gov/biblio/1726058.

[11] C. D. Rodríguez-Gallegos, M. Bieri, O. Gandhi, J. P. Singh, T. Reindl, and S. Panda, "Monofacial vs bifacial si-based pv modules: Which one is more cost-effective?" *Solar Energy*, vol. 176, pp. 412–438, 2018, ISSN: 0038-092X. DOI: https://doi.org/10.1016/j.solener.2018.10.012. [Online]. Available: https://www.sciencedirect.com/science/article/pii/S0038092X18309915.

[12] O. A. Katsikogiannis, H. Ziar, and O. Isabella, "Integration of bifacial photovoltaics in agrivoltaic systems: A synergistic design approach," *Applied Energy*, vol. 309, p. 118 475, 2022, ISSN: 0306-2619. DOI: https://doi.org/10.1016/j.apenergy.2021.118475. [Online]. Available: https://www.sciencedirect.com/science/article/pii/S0306261921016986.

[13] H. Alam, M. A. Alam, and N. Z. Butt, "Techno economic modeling for agrivoltaics: Can agrivoltaics be more profitable than ground mounted pv?" *IEEE Journal of Photovoltaics*, vol. 13, no. 1, pp. 174–186, 2023. DOI: 10.1109/JPHOTOV.2022.3215087.

[14] G. Faturrochman, M. de Jong, R. Santbergen, W. Folkerts, M. Zeman, and A. Smets, "Maximizing annual yield of bifacial photovoltaic noise barriers," *Solar Energy*, vol. 162, pp. 300–305, 2018, ISSN: 0038-092X. DOI: https://doi.org/10.1016/j.solener.2018.01.001. [Online]. Available: https://www.sciencedirect.com/science/article/pii/S0038092X1830001X.

[15] J. Dickert and P. Schegner, "A time series probabilistic synthetic load curve model for residential customers," pp. 1–6, 2011. DOI: 10.1109/PTC.2011.6019365.

[16] S. Obara, D. Konno, Y. Utsugi, and J. Morel, "Analysis of output power and capacity reduction in electrical storage facilities by peak shift control of pv system with bifacial modules," *Applied Energy*, vol. 128, pp. 35–48, 2014, ISSN: 0306-2619. DOI: https://doi.org/10.1016/j.apenergy.2014.04.053. [Online]. Available: https://www.sciencedirect.com/science/article/pii/S0306261914004061.

[17] R. Shigenobu, M. Ito, and H. Taoka, "Optimal design of bifacial pv system to mitigate duck-curve problem of power system with the uc problem," *Energy Reports*, vol. 7, pp. 7004–7014, 2021, ISSN: 2352-4847. DOI: https://doi.org/10.1016/j.egyr.2021.10.060. [Online]. Available: https://www.sciencedirect.com/science/article/pii/S2352484721010775.

[18] *ENTSO-E Transparency Platform*, https://transparency.entsoe.eu/, Accessed on May 15, 2023.

[19] A. Cuevas, A. Luque, J. Eguren, and J. del Alamo, "50 per cent more output power from an albedo-collecting flat panel using bifacial solar cells," *Solar Energy*, vol. 29, no. 5, pp. 419–420, 1982, ISSN: 0038-092X. DOI: https://doi.org/10.1016/0038-092X(82)90078-0. [Online]. Available: https://www.sciencedirect.com/science/article/pii/0038092X82900780.

[20] G. Raina and S. Sinha, "A holistic review approach of design considerations, modelling, challenges and future applications for bifacial photovoltaics," *Energy Conversion and Management*, vol. 271, p. 116 290, 2022, ISSN: 0196-8904. DOI: https://doi.org/10.1016/j.enconman.2022.116290. [Online]. Available: https://www.sciencedirect.com/science/article/pii/S0196890422010676.

[21] X. Sun, M. R. Khan, C. Deline, and M. A. Alam, "Optimization and performance of bifacial solar modules: A global perspective," *Applied Energy*, vol. 212, pp. 1601–1610, 2018, ISSN: 0306-2619. DOI: https://doi.org/10.1016/j.apenergy.2017.12.041. [Online]. Available: https://www.sciencedirect.com/science/article/pii/S0306261917317567.

[22] U. A. Yusufoglu, T. M. Pletzer, L. J. Koduvelikulathu, C. Comparotto, R. Kopecek, and H. Kurz, "Analysis of the annual performance of bifacial modules and optimization methods," *IEEE Journal of Photovoltaics*, vol. 5, no. 1, pp. 320–328, 2015. DOI: 10.1109/JPHOTOV.2014.2364406.

[23] A. Asgharzadeh, B. Marion, C. Deline, C. Hansen, J. S. Stein, and F. Toor, "A sensitivity study of the impact of installation parameters and system configuration on the performance of bifacial pv arrays," *IEEE Journal of Photovoltaics*, vol. 8, no. 3, pp. 798–805, 2018. DOI: 10.1109/JPHOTOV.2018.2819676.

[24] M. T. Patel, M. Ryyan Khan, A. Alnuaimi, O. Albadwawwi, J. J. John, and M. A. Alam, "Implications of seasonal and spatial albedo variation on the energy output of bifacial solar farms: A global perspective," pp. 2264–2267, 2019. DOI: 10.1109/PVSC40753.2019.8981163.

[25] M. T. Patel, M. R. Khan, X. Sun, and M. A. Alam, "A worldwide cost-based design and optimization of tilted bifacial solar farms," *Applied Energy*, vol. 247, pp. 467–479, 2019, ISSN: 0306-2619. DOI: https://doi.org/10.1016/j.apenergy.2019.03.150. [Online]. Available: https://www.sciencedirect.com/science/article/pii/S0306261919305604.

[26] P. Tillmann, K. Jäger, and C. Becker, "Minimising the levelised cost of electricity for bifacial solar panel arrays using bayesian optimisation," *Sustainable Energy Fuels*, vol. 4, pp. 254–264, 1 2020. DOI: 10.1039/C9SE00750D. [Online]. Available: http://dx.doi.org/10.1039/C9SE00750D.

[27] S. Wang, O. Wilkie, J. Lam, *et al.*, "Bifacial photovoltaic systems energy yield modelling," *Energy Procedia*, vol. 77, pp. 428–433, 2015, 5th International Conference on Silicon Photovoltaics, SiliconPV 2015, ISSN: 1876-6102. DOI: https://doi.org/10.1016/j.egypro.2015.07.060. [Online]. Available: https://www.sciencedirect.com/science/article/pii/S1876610215008280.

[28] V. Durković and Ž. Đurišić, "Extended model for irradiation suitable for large bifacial pv power plants," *Solar Energy*, vol. 191, pp. 272–290, 2019, ISSN: 0038-092X. DOI: https://doi.org/10.1016/j.solener.2019.08.064. [Online]. Available: https://www.sciencedirect.com/science/article/pii/S0038092X19308448.

[29] J. Appelbaum, "Bifacial photovoltaic panels field," *Renewable Energy*, vol. 85, pp. 338–343, 2016, ISSN: 0960-1481. DOI: https://doi.org/10.1016/j.renene.2015.06.050. [Online]. Available: https://www.sciencedirect.com/science/article/pii/S0960148115300732.

[30] D. Chudinzow, S. Nagel, J. Güsewell, and L. Eltrop, "Vertical bifacial photovoltaics – a complementary technology for the european electricity supply?" *Applied Energy*, vol. 264, p. 114 782, 2020, ISSN: 0306-2619. DOI: https://doi.org/10.1016/j.apenergy.2020.114782. [Online]. Available: https://www.sciencedirect.com/science/article/pii/S0306261920302944.

[31] S. Guo, T. M. Walsh, and M. Peters, "Vertically mounted bifacial photovoltaic modules: A global analysis," *Energy*, vol. 61, pp. 447–454, 2013, ISSN: 0360-5442. DOI: https://doi.org/10.1016/j.energy.2013.08.040. [Online]. Available: https://www.sciencedirect.com/science/article/pii/S0360544213007275.

[32] J. S. Stein, D. Riley, M. Lave, C. Hansen, C. Deline, and F. Toor, "Outdoor field performance from bifacial photovoltaic modules and systems," pp. 3184–3189, 2017. DOI: 10.1109/PVSC.2017.8366042.

[33] M. R. Khan, E. Sakr, X. Sun, P. Bermel, and M. A. Alam, "Ground sculpting to enhance energy yield of vertical bifacial solar farms," *Applied Energy*, vol. 241, pp. 592–598, 2019, ISSN: 0306-2619. DOI: https://doi.org/10.1016/j.apenergy.2019.01.168. [Online]. Available: https://www.sciencedirect.com/science/article/pii/S0306261919301278.

[34] M. R. Khan, A. Hanna, X. Sun, and M. A. Alam, "Vertical bifacial solar farms: Physics, design, and global optimization," *Applied Energy*, vol. 206, pp. 240–248, 2017, ISSN: 0306-2619. DOI: https://doi.org/10.1016/j.apenergy.2017.08.042. [Online]. Available: https://www.sciencedirect.com/science/article/pii/S0306261917310589.

[35] M. Alam, M. S. Gul, and T. Muneer, "Ground view factor computation model for bifacial photovoltaic collector field: Uniform and non-uniform surfaces," *Energy Reports*, vol. 7, pp. 9133–9149, 2021, ISSN: 2352-4847. DOI: https://doi.org/10.1016/j.egyr.2021.11.206. [Online]. Available: https://www.sciencedirect.com/science/article/pii/S2352484721013457.

[36] Y. Zhang, J. Q. Gao, Y. Yu, Q. Shi, and Z. Liu, "Influence of incidence angle effects on the performance of bifacial photovoltaic modules considering rear-side reflection," *Solar Energy*, vol. 245, pp. 404–409, 2022, ISSN: 0038-092X. DOI: https://doi.org/10.1016/j.solener.2022.08.027. [Online]. Available: https://www.sciencedirect.com/science/article/pii/S0038092X22005771.

[37] M. K. Gupta, K. J. Bumtariya, H. Shukla, P. Patel, and Z. Khan, "Methods for evaluation of radiation view factor: A review," *Materials Today: Proceedings*, vol. 4, no. 2, Part A, pp. 1236–1243, 2017, 5th International Conference of Materials Processing and Characterization (ICMPC 2016), ISSN: 2214-7853. DOI: https://doi.org/10.1016/j.matpr.2017.01.143. [Online]. Available: https://www.sciencedirect.com/science/article/pii/S2214785317301438.

[38] W. Nusselt, *Graphische Bestimmung der Winkelverhaltwisses beider Warmestrahlang*. 1928, vol. 72, p. 673.

[39] H. C. Hottel and A. F. Sarofin, *Radiative Transfer*. New York: McGraw Hill, 1967, pp. 31–39.

[40] J. Appelbaum, "The role of view factors in solar photovoltaic fields," *Renewable and Sustainable Energy Reviews*, vol. 81, pp. 161–171, 2018, ISSN: 1364-0321. DOI: https://doi.org/10.1016/j.rser.2017.07.026. [Online]. Available: https://www.sciencedirect.com/science/article/pii/S1364032117310924.

[41] M. Mirhosseini and A. Saboonchi, "View factor calculation using the monte carlo method for a 3d strip element to circular cylinder," *International Communications in Heat and Mass Transfer*, vol. 38, no. 6, pp. 821–826, 2011, ISSN: 0735-1933. DOI: https://doi.org/10.1016/j.icheatmasstransfer.2011.03.022. [Online]. Available: https://www.sciencedirect.com/science/article/pii/S0735193311000674.

[42] S.Abishek, S. R. Kannan, and S. Katte, "View factors between disk/rectangle and rectangle in parallel and perpendicular planes," *Journal of Thermophysics and Heat Transfer*, vol. 21, pp. 236–239, Jan. 2007. DOI: 10.2514/1.26851.

[43] C. Deline, S. MacAlpine, B. Marion, F. Toor, A. Asgharzadeh, and J. S. Stein, "Assessment of bifacial photovoltaic module power rating methodologies—inside and out," *IEEE Journal of Photovoltaics*, vol. 7, no. 2, pp. 575–580, 2017. DOI: 10.1109/JPHOTOV.2017.2650565.

[44] S. A. Pelaez and C. Deline, "Bifacial_radiance: A python package for modeling bifacial solar photovoltaic systems," *Journal of Open Source Software*, vol. 5, no. 50, p. 1865, 2020. DOI: 10.21105/joss.01865. [Online]. Available: https://doi.org/10.21105/joss.01865.

[45] D. Berrian and J. Libal, "A comparison of ray tracing and view factor simulations of locally resolved rear irradiance with the experimental values," *Progress in Photovoltaics: Research and Applications*, vol. 28, no. 6, pp. 609–620, 2020. DOI: https://doi.org/10.1002/pip.3261. [Online]. Available: https://onlinelibrary.wiley.com/doi/abs/10.1002/pip.3261.

[46] A. Asgharzadeh, M. A. Anoma, A. Hoffman, *et al.*, "A benchmark and validation of bifacial pv irradiance models," pp. 3281–3287, 2019. DOI: 10.1109/PVSC40753.2019.8981272.

[47] M. Kutzer, A. Fülle, A. Jahnke, *et al.*, "Ertragssteigerung durch bifaciale modultechnologie," Mar. 2016.

[48] J. E. Castillo-Aguilella and P. S. Hauser, "Multi-variable bifacial photovoltaic module test results and best-fit annual bifacial energy yield model," *IEEE Access*, vol. 4, pp. 498–506, 2016. DOI: 10.1109/ACCESS.2016.2518399.

[49] M. A. Anoma, D. Jacob, B. C. Bourne, J. A. Scholl, D. M. Riley, and C. W. Hansen, "View factor model and validation for bifacial pv and diffuse shade on single-axis trackers," pp. 1549–1554, 2017. DOI: 10.1109/PVSC.2017.8366704.

[50] A. Mermoud and B. Wittmer, "Bifacial Shed Simulations with PVsyst," in *Bifacial Workshop 2017*, Konstanz, Germany, 2017.

[51] C. Deline, S. Ayala Pelaez, S. MacAlpine, and C. Olalla, "Estimating and parameterizing mismatch power loss in bifacial photovoltaic systems," *Progress in Photovoltaics: Research and Applications*, vol. 28, no. 7, pp. 691–703, 2020. DOI: https://doi.org/10.1002/pip.3259. [Online]. Available: https://onlinelibrary.wiley.com/doi/abs/10.1002/pip.3259.

[52] J. Ledesma, R. Almeida, F. Martinez-Moreno, *et al.*, "A simulation model of the irradiation and energy yield of large bifacial photovoltaic plants," *Solar Energy*, vol. 206, pp. 522–538, 2020, ISSN: 0038-092X. DOI: https://doi.org/10.1016/j.solener.2020.05.108. [Online]. Available: https://www.sciencedirect.com/science/article/pii/S0038092X20306071.

[53] M. Theristis, E. F. Fernández, F. Almonacid, and P. Pérez-Higueras, "Spectral corrections based on air mass, aerosol optical depth, and precipitable water for cpv performance modeling," *IEEE Journal of Photovoltaics*, vol. 6, no. 6, pp. 1598–1604, 2016. DOI: 10.1109/JPHOTOV.2016.2606702.

[54] N. Riedel-Lyngskær, M. Ribaconka, M. Pó, *et al.*, "Spectral albedo in bifacial photovoltaic modeling: What can be learned from onsite measurements?," pp. 0942–0949, 2021. DOI: 10.1109/PVSC43889.2021.9519085.

[55] N. Riedel-Lyngskær, M. Ribaconka, M. Pó, *et al.*, "The effect of spectral albedo in bifacial photovoltaic performance," *Solar Energy*, vol. 231, pp. 921–935, 2022, ISSN: 0038-092X. DOI: https://doi.org/10.1016/j.solener.2021.12.023. [Online]. Available: https://www.sciencedirect.com/science/article/pii/S0038092X21010720.

[56] M. R. Vogt, T. Gewohn, K. Bothe, C. Schinke, and R. Brendel, "Impact of using spectrally resolved ground albedo data for performance simulations of bifacial modules," in *Proc. 35th Eur. Photovolt. Sol. Energy Conf.*, 2018, pp. 1011–1016.

[57] C. Jardine, R. Gottschalg, T. Betts, and D. Infield, "Influence of spectral effects on the performance of multijunction amorphous silicon cells," to be published, Jan. 2002.

[58] S. Williams, T. Betts, T. Helf, R. Gottschalg, H. Beyer, and D. Infield, "Modelling long-term module performance based on realistic reporting conditions with consideration to spectral effects," vol. 2, 1908–1911 Vol.2, 2003.

[59] P. M. Rodrigo, E. F. Fernández, F. M. Almonacid, and P. J. Pérez-Higueras, "Quantification of the spectral coupling of atmosphere and photovoltaic system performance: Indexes, methods and impact on energy harvesting," *Solar Energy Materials and Solar Cells*, vol. 163, pp. 73–90, 2017, ISSN: 0927-0248. DOI: https://doi.org/10.1016/j.solmat.2017.01.018. [Online]. Available: https://www.sciencedirect.com/science/article/pii/S0927024817300193.

[60] D. L. King, J. A. Kratochvil, and W. E. Boyson, "Measuring solar spectral and angle-of-incidence effects on photovoltaic modules and solar irradiance sensors," Nov. 1997. [Online]. Available: https://www.osti.gov/biblio/548689.

5

[61] A. Fanney, B. Dougherty, and M. Davis, "Short-term characterization of building integrated photovoltaic panels," en, no. 125, 2003. [Online]. Available: https://tsapps.nist.gov/publication/get_pdf.cfm?pub_id=861066.

[62] J. A. Kratochvil, W. E. Boyson, and D. L. King, "Photovoltaic array performance model," Sandia National Laboratories, New Mexico, Tech. Rep., 2004. [Online]. Available: http://dx.doi.org/10.2172/919131.

[63] T. C. R. Russell, R. Saive, A. Augusto, S. G. Bowden, and H. A. Atwater, "The influence of spectral albedo on bifacial solar cells: A theoretical and experimental study," *IEEE Journal of Photovoltaics*, vol. 7, no. 6, pp. 1611–1618, 2017. DOI: 10.1109/JPHOTOV.2017.2756068.

[64] A. Smets, K. Jäger, O. Isabella, R. van Swaaij, and M. Zeman, *Solar Energy: The physics and engineering of photovoltaic conversion, technologies and systems*, English. UIT Cambridge Limited, 2016, ISBN: 978-1-906860-32-5.

[65] E. Skoplaki and J. Palyvos, "On the temperature dependence of photovoltaic module electrical performance: A review of efficiency/power correlations," *Solar Energy*, vol. 83, no. 5, pp. 614–624, 2009, ISSN: 0038-092X. DOI: https://doi.org/10.1016/j.solener.2008.10.008. [Online]. Available: https://www.sciencedirect.com/science/article/pii/S0038092X08002788.

[66] M. Lamers, E. Özkalay, R. Gali, *et al.*, "Temperature effects of bifacial modules: Hotter or cooler?" *Solar Energy Materials and Solar Cells*, vol. 185, pp. 192–197, 2018, ISSN: 0927-0248. DOI: https://doi.org/10.1016/j.solmat.2018.05.033. [Online]. Available: https://www.sciencedirect.com/science/article/pii/S0927024818302605.

[67] C. Z. Zhou, P. J. Verlinden, R. A. Crane, R. M. Swanson, and R. A. Sinton, "21.9% efficient silicon bifacial solar cells," in *Conference Record of the Twenty Sixth IEEE Photovoltaic Specialists Conference - 1997*, Anaheim, CA, USA, 1997, pp. 287–290. DOI: 10.1109/PVSC.1997.654085.

[68] M. K. Fuentes, "A simplified thermal model for flat-plate photovoltaic arrays," May 1987. [Online]. Available: https://www.osti.gov/biblio/6802914.

[69] P. Trinuruk, C. Sorapipatana, and D. Chenvidhya, "Estimating operating cell temperature of bipv modules in thailand," *Renewable Energy*, vol. 34, no. 11, pp. 2515–2523, 2009, ISSN: 0960-1481. DOI: https://doi.org/10.1016/j.renene.2009.02.027. [Online]. Available: https://www.sciencedirect.com/science/article/pii/S0960148109000962.

[70] D. Faiman, "Assessing the outdoor operating temperature of photovoltaic modules," *Progress in Photovoltaics: Research and Applications*, vol. 16, no. 4, pp. 307–315, 2008. DOI: https://doi.org/10.1002/pip.813. eprint: https://onlinelibrary.wiley.com/doi/pdf/10.1002/pip.813. [Online]. Available: https://onlinelibrary.wiley.com/doi/abs/10.1002/pip.813.

[71] G. J. Janssen, B. B. Van Aken, A. J. Carr, and A. A. Mewe, "Outdoor performance of bifacial modules by measurements and modelling," *Energy Procedia*, vol. 77, pp. 364–373, 2015, 5th International Conference on Silicon Photovoltaics, SiliconPV 2015, ISSN: 1876-6102. DOI: https://doi.org/10.1016/j.egypro.2015.07.051. [Online]. Available: https://www.sciencedirect.com/science/article/pii/S187661021500819X.

[72] J. A. Duffie and W. A. Beckman, *Solar Energy Thermal Processes*, 3rd. John Wiley & Sons Inc, 2006.

[73] M. T. Patel, R. A. Vijayan, R. Asadpour, M. Varadharajaperumal, M. R. Khan, and M. A. Alam, "Temperature-dependent energy gain of bifacial pv farms: A global perspective," *Applied Energy*, vol. 276, p. 115 405, 2020, ISSN: 0306-2619. DOI: https://doi.org/10.1016/j.apenergy.2020.115405. [Online]. Available: https://www.sciencedirect.com/science/article/pii/S030626192030917X.

[74] W. Gu, T. Ma, M. Li, L. Shen, and Y. Zhang, "A coupled optical-electrical-thermal model of the bifacial photovoltaic module," *Applied Energy*, vol. 258, p. 114 075, 2020, ISSN: 0306-2619. DOI: https://doi.org/10.1016/j.apenergy.2019.114075. [Online]. Available: https://www.sciencedirect.com/science/article/pii/S0306261919317623.

[75] G. Notton, C. Cristofari, M. Mattei, and P. Poggi, "Modelling of a double-glass photovoltaic module using finite differences," *Applied Thermal Engineering*, vol. 25, no. 17, pp. 2854–2877, 2005, ISSN: 1359-4311. DOI: https://doi.org/10.1016/j.applthermaleng.2005.02.008. [Online]. Available: https://www.sciencedirect.com/science/article/pii/S135943110500075X.

[76] M. T. Patel, M. S. Ahmed, H. Imran, N. Z. Butt, M. R. Khan, and M. A. Alam, "Global analysis of next-generation utility-scale pv: Tracking bifacial solar farms," *Applied Energy*, vol. 290, p. 116 478, 2021, ISSN: 0306-2619. DOI: https://doi.org/10.1016/j.apenergy.2021.116478. [Online]. Available: https://www.sciencedirect.com/science/article/pii/S0306261921000428.

[77] R. Perez, R. Seals, P. Ineichen, R. Stewart, and D. Menicucci, "A new simplified version of the perez diffuse irradiance model for tilted surfaces," *Solar Energy*, vol. 39, no. 3, pp. 221–231, 1987, ISSN: 0038-092X. DOI: https://doi.org/10.1016/S0038-092X(87)80031-2. [Online]. Available: https://www.sciencedirect.com/science/article/pii/S0038092X87800312.

[78] Sandia National Laboratories, *Perez Sky Diffuse Model*, https://pvpmc.sandia.gov/modeling-steps/1-weather-design-inputs/plane-of-array-poa-irradiance/calculating-poa-irradiance/po sky-diffuse/perez-sky-diffuse-model/, Accessed on April 13, 2023, 2023.

[79] N. Martin and J. Ruiz, "Calculation of the pv modules angular losses under field conditions by means of an analytical model," *Solar Energy Materials and Solar Cells*, vol. 70, no. 1, pp. 25–38, 2001, ISSN: 0927-0248. DOI: https://doi.org/10.1016/S0927-0248(00)00408-6. [Online]. Available: https://www.sciencedirect.com/science/article/pii/S0927024800004086.

[80] M. A. Green, *Solar cells: operating principles, technology, and system applications*. Jan. 1982. [Online]. Available: https://www.osti.gov/biblio/6051511.

[81] N. Ekins-Daukes and M. Kay, "Brighten the dark skies," *Nature Energy*, vol. 4, p. 1, Jul. 2019. DOI: 10.1038/s41560-019-0440-0.

[82] PVMD group, TU Delft, *Database for global hourly irradiance spectra with 1°x1° resolution*, 2023.

[83] J. Carolus, J. A. Tsanakas, A. van der Heide, E. Voroshazi, W. De Ceuninck, and M. Daenen, "Physics of potential-induced degradation in bifacial p-perc solar cells," *Solar Energy Materials and Solar Cells*, vol. 200, p. 109 950, 2019, ISSN: 0927-0248. DOI: https://doi.org/10.1016/j.solmat.2019.109950. [Online]. Available: https://www.sciencedirect.com/science/article/pii/S092702481930279X.

[84] S. A. Pelaez, C. Deline, P. Greenberg, J. S. Stein, and R. K. Kostuk, "Model and validation of single-axis tracking with bifacial pv," *IEEE Journal of Photovoltaics*, vol. 9, no. 3, pp. 715–721, 2019. DOI: 10.1109/JPHOTOV.2019.2892872.

[85] C. D. Rodríguez-Gallegos, O. Gandhi, S. K. Panda, and T. Reindl, "On the pv tracker performance: Tracking the sun versus tracking the best orientation," *IEEE Journal of Photovoltaics*, vol. 10, no. 5, pp. 1474–1480, 2020. DOI: 10.1109/JPHOTOV.2020.3006994.

[86] D. Berrian, J. Libal, M. Klenk, H. Nussbaumer, and R. Kopecek, "Performance of bifacial pv arrays with fixed tilt and horizontal single-axis tracking: Comparison of simulated and measured data," *IEEE Journal of Photovoltaics*, vol. 9, no. 6, pp. 1583–1589, 2019. DOI: 10.1109/JPHOTOV.2019.2924394.

[87] C. D. Rodríguez-Gallegos, H. Liu, O. Gandhi, *et al.*, "Techno-economic performance modelling of bifacial and tracking pv systems worldwide," pp. 0406–0409, 2021. DOI: 10.1109/PVSC43889.2021.9518852.

[88] E. Lorenzo, "On the historical origins of bifacial pv modelling," *Solar Energy*, vol. 218, pp. 587–595, 2021, ISSN: 0038-092X. DOI: https://doi.org/10.1016/j.solener.2021.03.006. [Online]. Available: https://www.sciencedirect.com/science/article/pii/S0038092X21001869.

[89] D. Chudinzow, J. Haas, G. Díaz-Ferrán, S. Moreno-Leiva, and L. Eltrop, "Simulating the energy yield of a bifacial photovoltaic power plant," *Solar Energy*, vol. 183, pp. 812–822, 2019, ISSN: 0038-092X. DOI: https://doi.org/10.1016/j.solener.2019.03.071. [Online]. Available: https://www.sciencedirect.com/science/article/pii/S0038092X19302993.

[90] K. R. McIntosh, M. D. Abbott, G. Loomis, *et al.*, "Irradiance on the upper and lower modules of a two-high bifacial tracking system," pp. 1916–1923, 2020. DOI: 10.1109/PVSC45281.2020.9300838.

[91] J. E. Castillo-Aguilella and P. S. Hauser, "Bifacial photovoltaic module best-fit annual energy yield model with azimuthal correction," pp. 3109–3112, 2016. DOI: 10.1109/PVSC.2016.7750238.

[92] I. Shoukry, J. Libal, R. Kopecek, E. Wefringhaus, and J. Werner, "Modelling of bifacial gain for stand-alone and in-field installed bifacial pv modules," *Energy Procedia*, vol. 92, pp. 600–608, 2016, Proceedings of the 6th International Conference on Crystalline Silicon Photovoltaics (SiliconPV 2016), ISSN: 1876-6102. DOI: https://doi.org/10.1016/j.egypro.2016.07.025. [Online]. Available: https://www.sciencedirect.com/science/article/pii/S1876610216304520.

[93] A. Asgharzadeh, T. Lubenow, J. Sink, *et al.*, "Analysis of the impact of installation parameters and system size on bifacial gain and energy yield of pv systems," pp. 3333–3338, 2017. DOI: 10.1109/PVSC.2017.8366690.

[94] U. A. Yusufoglu, T. H. Lee, T. M. Pletzer, *et al.*, "Simulation of energy production by bifacial modules with revision of ground reflection," *Energy Procedia*, vol. 55, pp. 389–395, 2014, Proceedings of the 4th International Conference on Crystalline Silicon Photovoltaics (SiliconPV 2014), ISSN: 1876-6102. DOI: https://doi.org/10.1016/j.egypro.2014.08.111. [Online]. Available: https://www.sciencedirect.com/science/article/pii/S1876610214013368.

[95] C. W. Hansen, R. Gooding, N. Guay, *et al.*, "A detailed model of rear-side irradiance for bifacial pv modules," pp. 1543–1548, 2017. DOI: 10.1109/PVSC.2017.8366707.

[96] L. Kreinin, A. Karsenty, D. Grobgeld, and N. Eisenberg, "Pv systems based on bifacial modules: Performance simulation vs. design factors," pp. 2688–2691, 2016. DOI: 10.1109/PVSC.2016.7750138.

[97] Z. Zengwei, Z. Zhen, J. Yongfeng, L. Haolin, and Z. Shengcheng, "Performance analysis on bifacial pv panels with inclined and horizontal east–west sun trackers," *IEEE Journal of Photovoltaics*, vol. 9, no. 3, pp. 636–642, 2019. DOI: 10.1109/JPHOTOV.2019.2899472.

[98] G. Janssen, R. Gali, K. de Groot, A. Carr, B. Van Aken, and I. Romijn, "Impact of inhomogeneous irradiance at the rear of bifacial panels on modelled energy yield," Oct. 2018. DOI: 10.4229/EUPVSEC20172017-5BV.4.31.

A

APPENDIX A

A.1. LITERATURE REVIEW ON EXISTING BIFACIAL PV MODELS

This appendix summarizes the main characteristics of the bifacial PV models adopted by the different studies analyzed in this work during the literature review phase.

Table A.1: Classification of the models adopted by the studies analyzed during the literature review. It includes the number of locations considered by each paper and the main modelling characteristics

Ref.	Objective	Locations	Approach (VF/RT)	Non-uniformity of rear irradiance	Spectral impact
[76]	Calculation of LCOE, energy yield and energy gain of different configurations (including tracking)	Global	2D VF	Neglected	Neglected
[84]	Comparison model vs performance data for 1T bifacial systems	2 locations (USA)	2D VF and RT	Considered	Neglected
[85]	Comparison between different tracking strategies	4 locations worldwide	2D VF	Neglected	Neglected
[86]	Comparison VF and RT models for energy yield and bifacial gain calculation	1 location (Chile)	VF and RT	Neglected	Neglected
[87]	LCOE calculation for different fixed-tilt and various tracking systems	Global	2D VF	Neglected	Neglected
[4]	LCOE calculation (including tracking configuration)	Global	2D VF	Neglected	Considered (corrective factor)
[11]	Find optimal angles installation conditions	Global	2D VF	Neglected	Considered (corrective factor)
[21]	Find optimal angles installation conditions	Global	2D VF	Neglected	Neglected
[20]	Review the main models available in literature	N.A.	VF and RT	Considered	Neglected
[88]	Historical overview	1 location (Spain)	3D VF	Neglected	Neglected
[35]	Create a 3D view factor model	N.A.	3D VF	Considered	Neglected

Continued on next page

A

Table A.1 – continued from previous page

Ref.	Objective	Locations	Approach (VF/RT)	Non-uniformity of rear irradiance	Spectral impact
[52]	Energy yield and non-uniformity of rear irradiance modelling and estimation	1 location (Spain)	2D VF	Considered	Partially considered
[25]	LCOE calculation	Global	2D VF	Neglected	Neglected
[73]	Estimate the temperature influence in LCOE calculation	Global	2D VF	Neglected	Neglected
[89]	Calculate bifacial gain and the effect of neglecting shadows on ground	1 location (Chile)	3D VF	Neglected	Neglected
[31]	Comparison between vertical bifacial and monofacial PV	Global	2D VF	Neglected	Neglected
[9]	Analyze the influence of using spectral data	3 location worldwide	2D VF	Neglected	Considered
[54]	Analyze the influence of using spectral data	1 location (Denmark)	2D VF	Considered	Considered
[55]	Investigate seasonal change in albedo	1 location (Denmark)	2D VF	Considered	Considered
[28]	Techno-economical analysis on the optimal installation parameters	1 location (Serbia)	2D VF	Considered	Neglected
[20]	Assess the impact of partial shading	1 location (India)	RT	Considered	Neglected
[74]	Evaluate the accuracy of the proposed model	2 locations (China)	2D VF	Neglected	Neglected
[36]	Understand the incident angle effect	Indoor simulation	3D VF and RT	Neglected	Neglected
[5]	Model the rear irradiance of bifacial PV modules	1 location (USA)	2D VF	Neglected	Neglected
[33]	Evaluate the performance of ground sculpting vertical PV	Global	2D VF and radiosity method	Neglected	Neglected
[22]	Calculate bifacial gain	2 locations worldwide	VF	Considered	Considered (corrective factor)
[90]	Determine the distribution of the irradiance on the module	1 location (Michigan)	2D VF and RT	Considered	Neglected
[71]	Calculate energy yield and bifacial gain	1 location (Netherlands)	VF	Neglected	Neglected
[48]	Develop an empirical model for bifacial PV	1 location (USA)	Empirical	Neglected	Neglected
[91]	Include azimuth corrections in the empirical model	1 location (USA)	Empirical	Neglected	Neglected
[92]	Calculate bifacial gain	2 locations worldwide	VF	Considered	Neglected
[93]	Impact of considering stand-alone vs farm on energy yield and bifacial gain	1 location (USA)	RT	Considered	Neglected
[94]	Calculate bifacial gain and optimal tilt	2 locations worldwide	VF	Neglected	Neglected
[14]	Calculate energy yield of vertical modules	1 location (Netherlands)	VF	Considered	Neglected
[27]	Calculate energy yield and bifacial gain	1 location (Germany)	VF	Neglected	Neglected

Continued on next page

Table A.1 – continued from previous page

Ref.	Objective	Locations	Approach (VF/RT)	Non-uniformity of rear irradiance	Spectral impact
[29]	Comparison of the irradiance incident on vertical and tilted PV farms	1 location (Israel)	2D VF	Neglected	Neglected
[95]	Test the accuracy of rear-irradiance models	1 location (USA)	3D VF	Considered	Neglected
[34]	Calculate energy yield, bifacial gain and optimal panel period	1 location (USA)	2D VF	Considered	Neglected
[96]	Calculate bifacial gain in relation to albedo and elevation	2 locations worldwide	N.A.	Neglected	Neglected
[97]	Investigate the performance of two different types of tracking	3 locations (China)	3D VF	Neglected	Neglected
[24]	Investigate the impact of time-varying albedo	Global	2D VF	Neglected	Neglected
[45]	Comparison between VF and RT models	1 location (Germany)	2D VF and RT	Considered	Neglected
[49]	Investigate the accuracy of 2D VF models	1 location (USA)	2D VF	Considered	Neglected
[26]	Bayesian optimization of tilt and module-to-module distance by minimizing the LCOE	4 locations worldwide	2D VF	Considered	Neglected
[43]	Define a standard for rear side irradiance at STC	N.A.	RT	Considered	Neglected
[51]	Calculate the mismatch losses due to non-uniformity of rear irradiance	N.A.	2D and RT	Considered	Neglected
[98]	Investigate the dependence of non-uniformity of rear irradiance on various parameters	1 location (Netherlands)	VF	Considered	Neglected

B

APPENDIX B

B.1. ADDITIONAL EQUATIONS FOR THE OPTICAL MODEL

B.1.1. EQUATIONS USED IN THE PEREZ MODEL

The following coefficients are used in the equations 3.3, 3.2, 3.3 to calculate the different components of diffuse irradiance [77], [78]. θ_z, E_a, AM_a indicate the solar zenith angle, the extraterrestrial radiation and the absolute air mass, respectively.

$$F_1 = \max\left[0, \left(f_{11} + f_{12} \cdot \Delta + f_{13} \cdot \frac{\pi\theta_z}{180°}\right)\right] \tag{B.1}$$

$$F_2 = f_{21} + f_{22} \cdot \Delta + f_{23} \cdot \frac{\pi\theta_z}{180°} \tag{B.2}$$

$$\Delta = \frac{DHI \cdot AM_a}{E_a} \tag{B.3}$$

The values of the coefficients f_{ij} depends on the sky clearness ϵ, which is calculated in equation B.4. In particular, they can be extracted from a table available in [78]. The constant k is equal to $5.5.35 \cdot 10^{-6}$ when using angles in degrees.

$$\epsilon = \frac{\frac{DHI+DNI}{DHI} + k \cdot \theta_z^3}{1 + k \cdot \theta_z^3} \tag{B.4}$$

B.1.2. EQUATIONS FOR THE SKY VIEW FACTOR OF GROUND'S SEGMENTS

The following equations have been used to calculate the angles depicted in figure 3.5 and used to determine the sky view factor as explained in equation 3.8.

$$\gamma_1 = \max\left(\arctan\left(-\frac{h_2 - \frac{l}{2}\sin(\theta_2)}{-y_{m,2} - \frac{l}{2}\cos(\theta_2)}\right), \arctan\left(-\frac{h_2 + \frac{l}{2}\sin(\theta_2)}{-y_{m,2} + \frac{l}{2}\cos(\theta_2)}\right)\right) \tag{B.5}$$

$$\gamma_2 = \min\left(\arctan\left(-\frac{h_1 - \frac{l}{2}\sin(\theta_1)}{-y_{m,1} - \frac{l}{2}\cos(\theta_1)}\right), \arctan\left(-\frac{h_1 + \frac{l}{2}\sin(\theta_1)}{-y_{m,1} + \frac{l}{2}\cos(\theta_1)}\right)\right) \tag{B.6}$$

$$\gamma_3 = \max\left(\arctan\left(-\frac{h_1 - \frac{l}{2}\sin(\theta_1)}{-y_{m,1} - \frac{l}{2}\cos(\theta_1)}\right), \arctan\left(-\frac{h_1 + \frac{l}{2}\sin(\theta_1)}{-y_{m,1} + \frac{l}{2}\cos(\theta_1)}\right)\right) \tag{B.7}$$

$$\gamma_4 = \min\left(\arctan\left(-\frac{h_3 - \frac{l}{2}\sin(\theta_3)}{y_{m,3} - \frac{l}{2}\cos(\theta_3)}\right), \arctan\left(-\frac{h_3 + \frac{l}{2}\sin(\theta_3)}{y_{m,3} + \frac{l}{2}\cos(\theta_3)}\right)\right) \tag{B.8}$$

$$\gamma_5 = \max\left(\arctan\left(-\frac{h_3 - \frac{l}{2}\sin(\theta_3)}{y_{m,3} - \frac{l}{2}\cos(\theta_3)}\right), \arctan\left(-\frac{h_3 + \frac{l}{2}\sin(\theta_3)}{y_{m,3} + \frac{l}{2}\cos(\theta_3)}\right)\right) \tag{B.9}$$

$$\gamma_6 = \min\left(\arctan\left(-\frac{h_4 - \frac{l}{2}\sin(\theta_4)}{y_{m,4} - \frac{l}{2}\cos(\theta_4)}\right), \arctan\left(-\frac{h_4 + \frac{l}{2}\sin(\theta_4)}{y_{m,4} + \frac{l}{2}\cos(\theta_4)}\right)\right) \tag{B.10}$$

B.1.3. EQUATIONS FOR THE FIELD OF VIEW OF THE SOLAR CELLS

The following equations have been used to calculate the angles highlighted in figure 3.6 and 3.7, which determine the field of view of the solar cells.

$$\gamma_{1,r} = \max\left(0\,,\ \frac{\pi}{2} - \theta_2 - \arctan\left(\frac{d_2 - \frac{l}{2}\cos(\theta_2) + (x - \frac{l}{2} + \frac{c}{2})\cos(\theta_1)}{h_1 - h_2 - \frac{l}{2}\sin(\theta_2) + (x - \frac{l}{2} + \frac{c}{2})\sin(\theta_1)}\right)\right) \tag{B.11}$$

$$\gamma_{2,r} = \max\left(0\,,\ \frac{\pi}{2} - \theta_2 - \arctan\left(\frac{d_2 + \frac{l}{2}\cos(\theta_2) + (x - \frac{l}{2} + \frac{c}{2})\cos(\theta_1)}{h_1 - h_2 + \frac{l}{2}\sin(\theta_2) + (x - \frac{l}{2} + \frac{c}{2})\sin(\theta_1)}\right)\right) \tag{B.12}$$

$$\gamma_{3,r} = \min\left(\pi\,,\ \frac{\pi}{2} - \theta_3 + \arctan\left(\frac{d_3 - \frac{l}{2}\cos(\theta_3) + (x - \frac{l}{2} + \frac{c}{2})\cos(\theta_1)}{h_1 - h_3 - \frac{l}{2}\sin(\theta_3) + (x - \frac{l}{2} + \frac{c}{2})\sin(\theta_1)}\right)\right) \tag{B.13}$$

$$\gamma_{4,r} = \min\left(\pi\,,\ \frac{\pi}{2} - \theta_3 + \arctan\left(\frac{d_3 + \frac{l}{2}\cos(\theta_3) + (x - \frac{l}{2} + \frac{c}{2})\cos(\theta_1)}{h_1 - h_3 + \frac{l}{2}\sin(\theta_3) + (x - \frac{l}{2} + \frac{c}{2})\sin(\theta_1)}\right)\right) \tag{B.14}$$

$$\gamma_{1,f} = \max\left(0\,,\ -\frac{\pi}{2} + \theta_2 + \arctan\left(\frac{d_2 + \frac{l}{2}\cos(\theta_2) + (x - \frac{l}{2} + \frac{c}{2})\cos(\theta_1)}{h_1 - h_2 + \frac{l}{2}\sin(\theta_2) + (x - \frac{l}{2} + \frac{c}{2})\sin(\theta_1)}\right)\right) \tag{B.15}$$

$$\gamma_{2,f} = \max\left(0\,,\ -\frac{\pi}{2} + \theta_2 + \arctan\left(\frac{d_2 - \frac{l}{2}\cos(\theta_2) + (x - \frac{l}{2} + \frac{c}{2})\cos(\theta_1)}{h_1 - h_2 - \frac{l}{2}\sin(\theta_2) + (x - \frac{l}{2} + \frac{c}{2})\sin(\theta_1)}\right)\right) \tag{B.16}$$

$$\gamma_{3,f} = \min\left(\pi\ ,\ 2\pi - \frac{\pi}{2} + \theta_3 - \arctan\left(\frac{d_3 - \frac{l}{2}\cos(\theta_3) + (x - \frac{l}{2} + \frac{c}{2})\cos(\theta_1)}{h_1 - h_3 - \frac{l}{2}\sin(\theta_3) + (x - \frac{l}{2} + \frac{c}{2})\sin(\theta_1)}\right)\right) \tag{B.17}$$

$$\gamma_{4,f} = \min\left(\pi\ ,\ 2\pi - \frac{\pi}{2} + \theta_3 - \arctan\left(\frac{d_3 + \frac{l}{2}\cos(\theta_3) + (x - \frac{l}{2} + \frac{c}{2})\cos(\theta_1)}{h_1 - h_3 + \frac{l}{2}\sin(\theta_3) + (x - \frac{l}{2} + \frac{c}{2})\sin(\theta_1)}\right)\right) \tag{B.18}$$

C

APPENDIX C

C.1. VALIDATION OF THE MODEL: ADDITIONAL RESULTS

The following tables contain daily MBD and RMSE values calculated for each of the days selected for the validation, both in absolute and relative terms.

Table C.1: Mean bias deviation (MBD) expressed in W/m^2 between modelled and measured data for the days selected for the validation.

Day	MBD sensor 1 (bottom) [W/m^2]	MBD sensor 2 [W/m^2]	MBD sensor 3 [W/m^2]	MBD sensor 4 [W/m^2]	MBD sensor 5 [W/m^2]	MBD sensor 6 (top) [W/m^2]
28 July 2020 15.30-18.15	-5.43	-8.17	-8.24	-4.98	-1.78	1.14
29 July 2020 10.00-18.00	-4.15	-13.43	-15.12	-12.60	-9.04	-6.02
30 July 2020 11.00-18.00	-7.68	-23.89	-25.64	-24.77	-21.38	-20.48
31 July 2020 11.30-15.30	8.47	0.44	-4.83	-6.37	-6.29	-5.54
1 August 2020 10.00-18.00	-1.98	-2.21	-2.86	-2.25	-1.21	0.78
2 August 2020 10.00-18.00	-1.71	-2.28	-3.02	-2.22	-1.02	0.97
3 August 2020 10.00-18.00	0.42	-0.08	-0.65	-0.01	0.81	2.44
4 August 2020 10.00-18.00	-3.80	-3.50	-4.81	-3.90	-2.26	2.87
1 Sep 2020 14.00-18.00	-10.77	-8.86	-8.43	-5.91	-2.34	4.38
6 Sep 2020 9.00-19.00	-1.38	0.70	3.52	8.29	14.35	23.93
7 Sep 2020 12.30-19.00	-6.09	-3.22	0.45	5.88	13.91	24.90
13 Sep 2020 9.00-19.00	4.07	5.86	5.39	6.85	9.11	16.85

Table C.2: Mean bias deviation (MBD) expressed in % between modelled and measured data for the days selected for the validation.

Day	MBD sensor 1 (bottom) [%]	MBD sensor 2 [%]	MBD sensor 3 [%]	MBD sensor 4 [%]	MBD sensor 5 [%]	MBD sensor 6 (top) [%]
28 July 2020 15.30-18.15	-8.21	-13.51	-13.56	-7.90	-2.70	1.64
29 July 2020 10.00-18.00	-3.89	-14.51	-16.87	-13.47	-9.06	-5.55
30 July 2020 11.00-18.00	-4.87	-19.54	-23.97	-23.00	-18.33	-15.39
31 July 2020 11.30-15.30	22.42	1.43	-15.66	-19.11	-16.69	-12.83
1 August 2020 10.00-18.00	-5.48	-7.54	-9.95	-7.34	-3.65	2.20
2 August 2020 10.00-18.00	-3.39	-5.78	-8.03	-5.59	-2.34	2.02
3 August 2020 10.00-18.00	3.37	-0.74	-5.30	-0.09	5.80	17.36
4 August 2020 10.00-18.00	-6.04	-6.83	-9.56	-7.30	-3.94	4.92
1 Sep 2020 14.00-18.00	-25.13	-21.16	-19.65	-13.88	-5.78	12.37
6 Sep 2020 9.00-19.00	-1.60	0.97	5.51	13.69	24.83	45.87
7 Sep 2020 12.30-19.00	-4.98	-3.22	0.51	7.23	18.19	35.66
13 Sep 2020 9.00-19.00	9.16	15.37	14.47	18.08	23.64	49.01

Table C.3: Root mean square error (RMSE) expressed in W/m^2 between modelled and measured data for the days selected for the validation.

Day	RMSE sensor 1 (bottom) [W/m^2]	RMSE sensor 2 [W/m^2]	RMSE sensor 3 [W/m^2]	RMSE sensor 4 [W/m^2]	RMSE sensor 5 [W/m^2]	RMSE sensor 6 (top) [W/m^2]
28 July 2020 15.30-18.15	5.99	8.93	9.13	6.51	4.53	4.28
29 July 2020 10.00-18.00	12.04	17.22	18.02	16.29	13.94	13.44
30 July 2020 11.00-18.00	11.99	25.28	26.56	25.77	22.44	21.84
31 July 2020 11.30-15.30	8.62	0.94	4.85	6.39	6.30	5.56
1 August 2020 10.00-18.00	4.61	4.35	4.46	4.63	4.41	4.99
2 August 2020 10.00-18.00	6.96	5.76	5.70	6.04	5.91	6.71
3 August 2020 10.00-18.00	2.02	1.78	2.17	2.71	3.25	4.44
4 August 2020 10.00-18.00	5.08	4.61	5.98	5.53	4.99	5.45
1 Sep 2020 14.00-18.00	11.13	9.31	8.90	6.57	3.91	5.93
6 Sep 2020 9.00-19.00	21.03	16.65	14.81	16.52	20.21	28.32
7 Sep 2020 12.30-19.00	9.61	8.23	7.97	10.34	16.36	27.02
13 Sep 2020 9.00-19.00	5.22	6.67	6.24	7.67	9.88	17.96

Table C.4: Root mean square error (RMSE) expressed in % between modelled and measured data for the days selected for the validation.

Day	RMSE sensor 1 (bottom) [%]	RMSE sensor 2 [%]	RMSE sensor 3 [%]	RMSE sensor 4 [%]	RMSE sensor 5 [%]	RMSE sensor 6 (top) [%]
28 July 2020 15.30-18.15	9.07	14.76	15.04	10.31	6.89	6.19
29 July 2020 10.00-18.00	11.28	18.60	20.10	17.42	13.96	12.39
30 July 2020 11.00-18.00	7.60	20.69	24.83	23.93	19.24	16.41
31 July 2020 11.30-15.30	22.83	3.07	15.74	19.15	16.73	12.87
1 August 2020 10.00-18.00	12.78	14.82	15.51	15.11	13.29	14.04
2 August 2020 10.00-18.00	13.79	14.56	15.14	15.20	13.57	14.02
3 August 2020 10.00-18.00	16.36	15.42	17.55	20.52	23.32	31.59
4 August 2020 10.00-18.00	8.06	9.00	11.88	10.37	8.69	9.32
1 Sep 2020 14.00-18.00	25.98	22.22	20.74	15.44	9.64	16.75
6 Sep 2020 9.00-19.00	24.47	23.26	23.19	27.27	34.98	54.27
7 Sep 2020 12.30-19.00	7.87	8.25	9.16	12.71	21.40	38.68
13 Sep 2020 9.00-19.00	11.75	17.52	16.75	20.23	25.65	52.24

D

APPENDIX D

D.1. INFLUENCE OF DESIGN PARAMETERS ON GNU: ADDITIONAL VISUALIZATIONS

The analysis concerning the influence of the design parameters, namely θ, d and h, on the GNU value is extended to multiple locations to verify the trends presented in subsection 4.3.3. The results are shown in the figures D.1-D.5, confirming the behaviour observed for the Utrecht case.

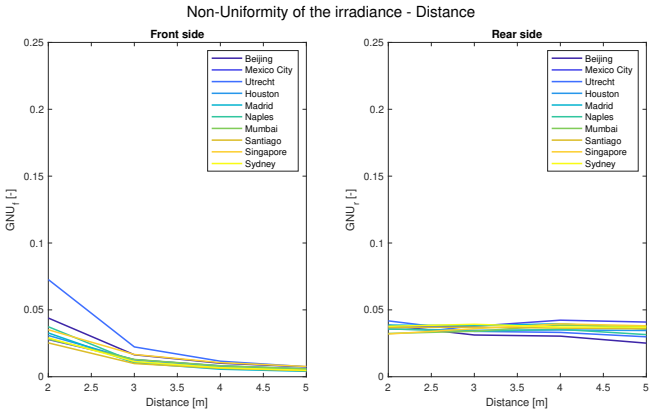

Figure D.1: Influence of the distance on the weighted average GNU for an optimally-tilted PV farm simulated in multiple locations. The results are for $h = 1.5\,m$ and $\theta = 30°$.

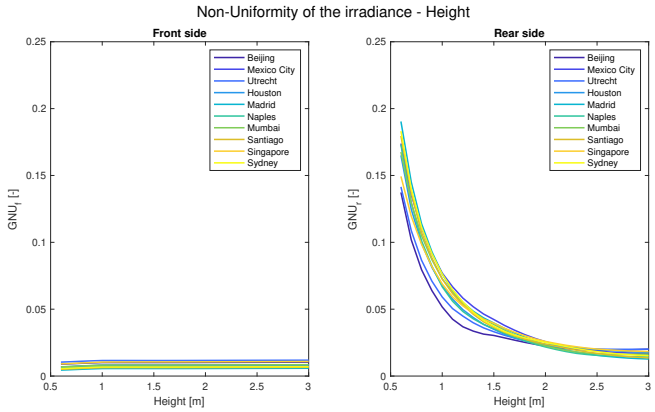

Figure D.2: Influence of the height on the weighted average GNU for an optimally-tilted PV farm simulated in multiple locations. The results are for $d = 4\,m$ and $\theta = 30°$.

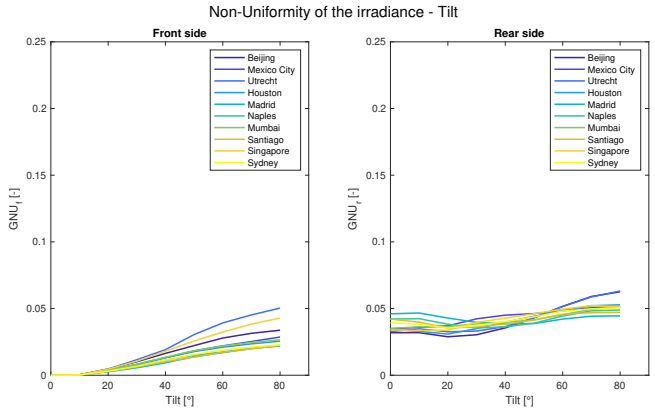

Figure D.3: Influence of the tilt on the weighted average GNU for an optimally-tilted PV farm simulated in multiple locations. The results are for $d = 4\,m$ and $h = 1.5\,m$.

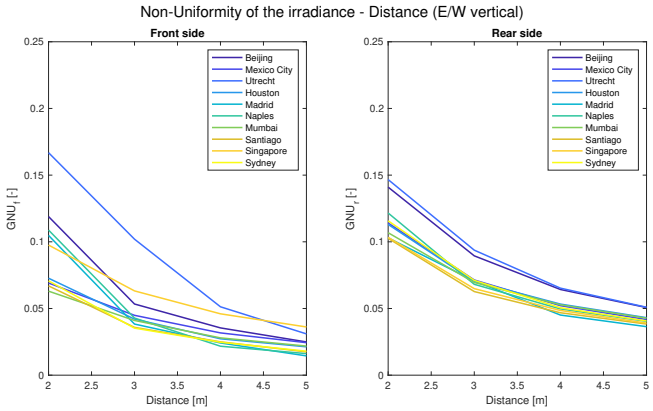

Figure D.4: Influence of the distance on the weighted average GNU for a vertical PV farm simulated in multiple locations. The results are for $h = 1.5\,m$.

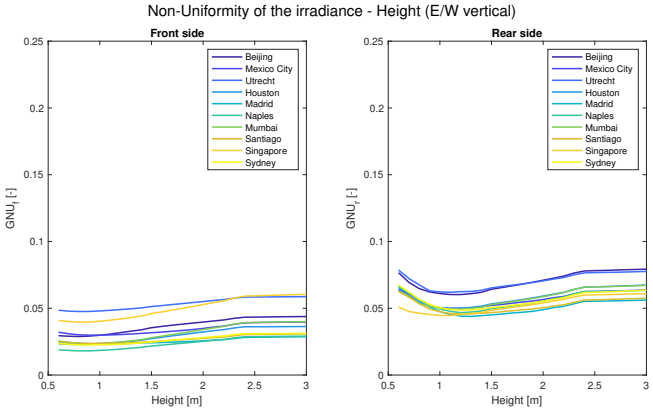

Figure D.5: Influence of the height on the weighted average GNU for a vertical PV farm simulated in multiple locations. The results are for $d = 4\,m$.

E

APPENDIX E

E.1. GLOBAL MAPS: VERTICAL VS OPTIMAL TILT CONFIGURATION

This appendix includes additional visualizations concerning the minimum price ratio required to achieve a revenues' gain while using vertical PV modules instead of the optimally-tilted counterpart.

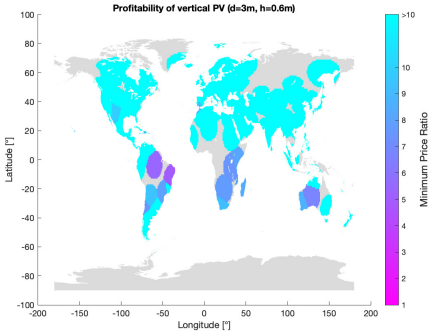

(a) Design parameters: $d = 3\,m$, $h = 0.6\,m$

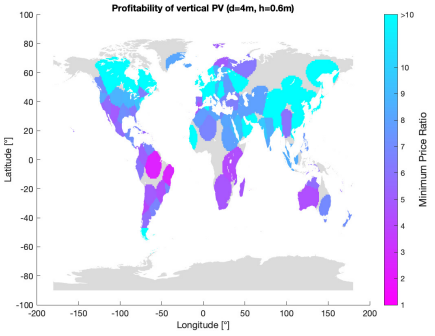

(b) Design parameters: $d = 4\,m$, $h = 0.6\,m$

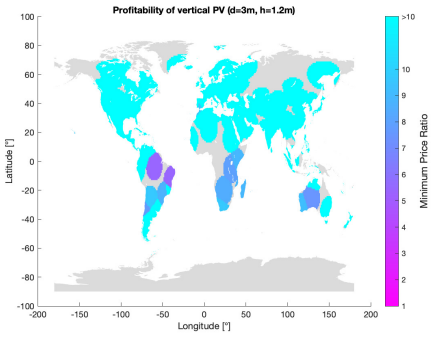

(c) Design parameters: $d = 3\,m$, $h = 1.2\,m$

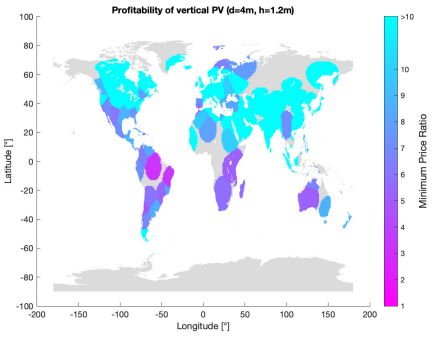

(d) Design parameters: $d = 4\,m$, $h = 1.2\,m$

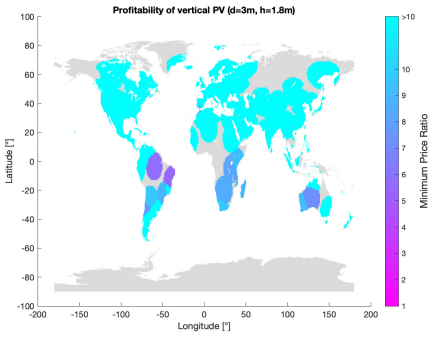

(e) Design parameters: $d = 3\,m$, $h = 1.8\,m$

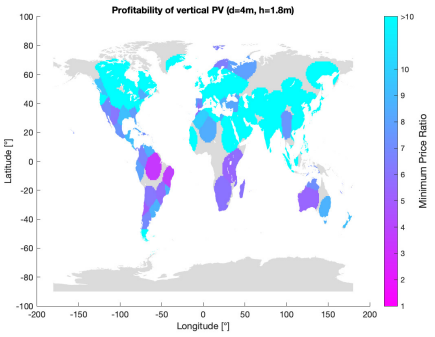

(f) Design parameters: $d = 4\,m$, $h = 1.8\,m$

Figure E.1: Global map of the minimum price ratio for which vertical modules are more profitable than the tilted counterpart. The other variables are set as follows: $p_{min} = 100€/MWh$, $n_{vert} = 1$, $n_{max,power} = 1$

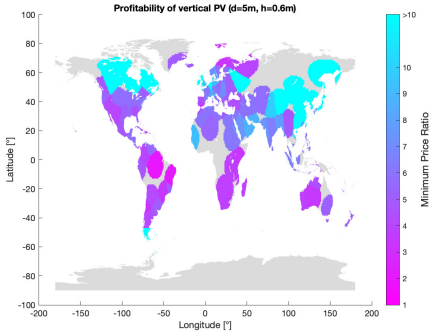

(a) Design parameters: $d = 5\,m$, $h = 0.6\,m$

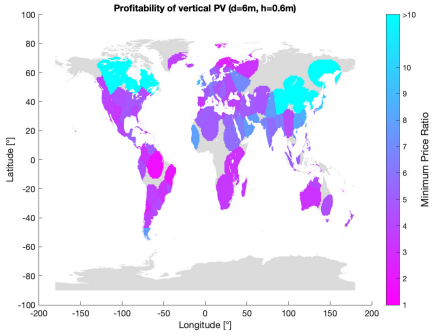

(b) Design parameters: $d = 6\,m$, $h = 0.6\,m$

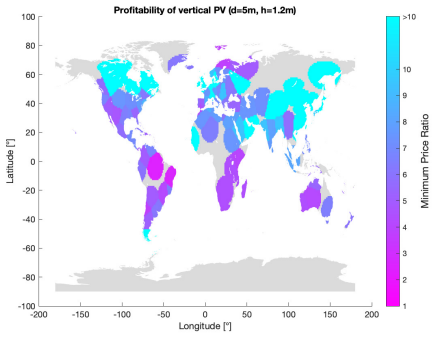

(c) Design parameters: $d = 5\,m$, $h = 1.2\,m$

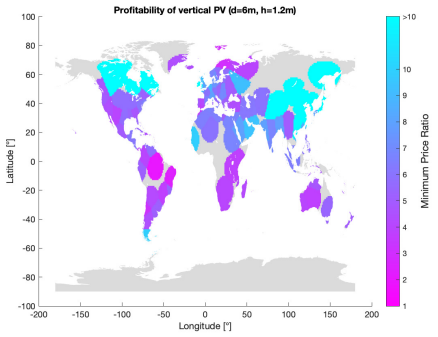

(d) Design parameters: $d = 6\,m$, $h = 1.2\,m$

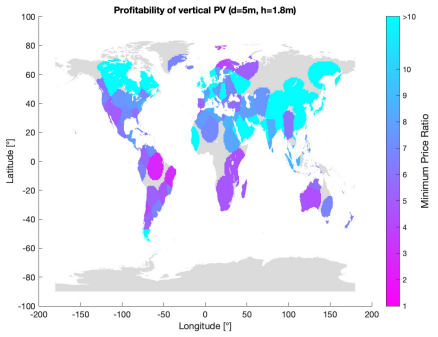

(e) Design parameters: $d = 5\,m$, $h = 1.8\,m$

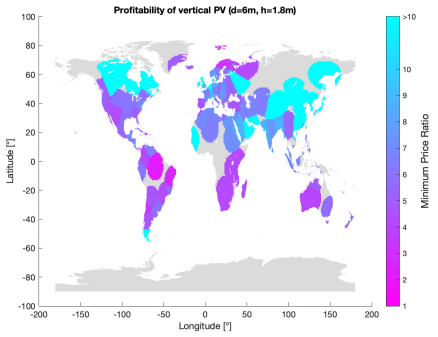

(f) Design parameters: $d = 6\,m$, $h = 1.8\,m$

Figure E.2: Global map of the minimum price ratio for which vertical modules are more profitable than the tilted counterpart. The other variables are set as follows: $p_{min} = 100€/MWh$, $n_{vert} = 1$, $n_{max,power} = 1$

F

APPENDIX F

F.1. SCIENTIFIC PAPER

This section contains a draft version of a scientific paper that summarizes the research performed during this thesis.

Modelling and Optimization of Bifacial PV Farms: Potential of E/W vertical configuration

Matteo Baricchio, PVMD Group, Delft University of Technology, Delft, the Netherlands
Hesan Ziar, PVMD Group, Delft University of Technology, Delft, the Netherlands
Marc Korevaar, Kipp&Zonen, Delft, the Netherlands
Pavel Babal, Kipp&Zonen, Delft, the Netherlands

***Abstract*—The profitability of E/W vertical bifacial PV farm with respect to the conventional N/S tilted configuration is studied in this work through a global analysis. A model based on 2D view factor concept is developed to estimate the power generated by a large scale farm. Non-uniformity of the incident irradiance and spectral impact are considered by adopting a multi-dimensional matrix approach. The model is validated in collaboration with the company *Kipp & Zonen*, focusing on the broadband rear irradiance and its non-uniformity. Specifically, the mean bias deviation and the RMSE calculated between modelled and measured data amount to $-1.29\,W/m^2$ (-2.22%) and $12.65\,W/m^2$ (21.69%), respectively. The validation highlights lower accuracy in case of higher tilt values, especially during clear days and at the edge of the modules, concluding that the error is proportional to the amount of unshaded ground seen by a cell, in alignment with the limitations of the view factor concept. Electricity prices are modelled by assuming daily U-shaped curves with minimum noon values, identifying different market conditions by the ratio between morning/evening and noon prices. Higher profitability of E/W vertical with respect to N/S tilted configuration is studied by calculating the minimum price ratio required to achieve such condition. These results are presented through global maps due to their strong dependence on the specific location and they are analyzed in relation to curtailment strategies, hybrid configurations, design parameters and market conditions. Among these variables, the row-to-row distance is found to have the highest impact on the decision concerning the optimal configuration since higher values are more beneficial for vertical modules, increasing their profitability with respect the tilted case. The locations characterized by a low diffuse fraction are recommended to install vertical PV farms.**

I. Introduction

SOLAR photovoltaic (PV) has seen the most rapid growth in the period from 2010 to 2022 among the renewable energy sources, reaching a global cumulative installed capacity of $1047\,GW$ at the end of 2022 [1]. Currently, bifacial PV modules represents only 30% of the market share, but this value will rise up to 70% in the next 10 years according to the estimations [2]. The peculiarity of bifacial PV modules consists in their property of absorbing the irradiance incident on both the front and the rear side. This can lead to an increase in the generated power up to 30% [3], which increases the energy density of such technology in comparison with monofacial case. On the other hand, the extra energy provided by the bifacial solar cells involves some additional investment costs. In the recent years, a significant decrease in these costs has made bifacial PV competitive in terms of levelized cost of energy worldwide [4].

Models that are able to predict the power generated by bifacial PV modules are required to determine the potential and the applicability of this technology. These can be divided into optical and thermo-electrical sub-models. The latter submodel relies on conventional concepts, widely adopted for monofacial PV modelling. In contrast, the former submodel adds complexity due to the presence of rear irradiance, resulting from multiple reflections and generating a non-uniform incident profile. In the recent years, different optical models have been developed to estimate the irradiance incident on bifacial PV modules. Various approaches have been explored for this purpose and they can be divided into two categories, depending whether they are based on the concept of view factor or ray-tracing. Inherited by heat transfer theory, view factor method is widely adopted in the literature due to the low computational time [5] and it is based on the assumption of isotropic scattering of the reflected rays [6]. Conversely, ray-tracing software like RADIANCE [7] are based on individual sunrays simulations, increasing the accuracy of the results as well as the time needed to compute the simulations [5]. Irrespective of the approach, there are other aspects that can be integrated in the models depending on trade-off between accuracy and computational resources required. These include the non-uniformity of the rear irradiance [8], the spectral impact of the incident radiation [9] and the influence of the mounting structure [10].

Bifacial PV models are adopted to simulate large PV farm operation, optimizing design parameters such as tilt, orientation, elevation, and row-to-row distance. Various studies explore different configurations, including vertically-mounted systems [4], [11]. Vertical modules are installed in the East/West (E/W) orientation to exploit morning and evening sun irradiation, exhibiting a two-peaks power curve with a minimum at noon, unlike conventional North/South (N/S) orientation of tilted modules that leads to a maximum in power production around midday [3]. Despite the generally lower energy yield of the E/W vertical configuration compared to the N/S tilted counterpart, this arrangement offers two main advantages that increase its appeal in the market. First, the physical mounting structure allows for versatile integration of the modules in various applications, such as agrivoltaics [12], [13] and noise barriers [14]. Second, the

shape of the power curve provides several benefits, including improved demand-supply matching, reduced storage capacity requirements [15], and mitigation of the duck-curve problem [16]. Additionally, the similarity between the generated power's daily profile and electricity day-ahead market prices can lead to increased revenues. Specifically, a two-peaks power curve is favoured by scenarios where a substantial price gap between morning/evening and noon prices is present, as observed when solar energy constitutes a significant portion of a country's electricity mix [17].

The aim of this study is to develop a model to estimate the power generated by a bifacial PV farm, in order to investigate the potential of E/W vertical configuration in terms of market revenues. This paper is structured as follows. In section II an overview of the models adopted in previous studies to simulate the operation of bifacial modules is outlined. The opto-thermo-electrical and the electricity market models developed for this analysis are explained in sections III and IV, respectively. Subsequently, section V describes the experimental validation of the optical model. Lastly, the results are discussed in section VI whereas the conclusions are included in section VII.

II. Literature review on bifacial PV models

A. Metrics of bifacial PV

Th comparison between different bifacial PV installations is based on various metrics that consider diverse aspects of this technology and its operation. The bifaciality property of the solar cells is assessed using the bifaciality factor (ϕ_{Bi}), namely the ratio between the power generated by the rear side and by the front side under standard test conditions (STC). The values usually range from 60% to 90% in commercial applications [6] whereas ϕ_{Bi} up to 92% and 95% are obtained for Silicon Heterojunction and n-PERT solar cells, respectively [18]. The surplus of energy generated by bifacial modules with respect to the monofacial is quantified by the bifacial gain (BG), which depends on the geographic location as well as the design parameters. Such aspects influence also the levelized cost of electricity ($LCOE$), adopted to compare the cost-effectiveness of different PV technologies [11]. In relation to the electricity market, the value factor (VF) quantifies the ability to capture higher electricity prices by a power plant, determining the benefits of the daily shape of various configurations' power curve [19].

B. View factor vs Ray-tracing

The view factor concept is adopted to estimate the radiation incident on different surfaces and it defined as shown in 1. The analytical solution of the integral included in the equation can be obtained only for limited cases hence numerical methods or approximation are utilized, including Nusselt unit spheres approach [20], Monte Carlo simulations [21] and Hottel's cross string rule [22]. This last methods is based on a 2D approximation and it is widely adopted in the field of PV modelling due to its low computational time achieved by neglecting the edge effects [6], i.e. the increase of the irradiation received by the modules at the edge of the row due to the presence of less obstacles. However, the impact of the approximation is limited in case of large-scale PV farms, for which the infinite rows' assumption leads to minimal errors.

$$F_{A_1 \to A_1} = \frac{1}{A_1} \iint_{A_1 A_2} \frac{\cos\theta_1 \cos\theta_2}{\pi s^2} dA_1 \, dA_2 \tag{1}$$

Ray-tracing consists in the simulation of individual rays' path to obtain a an illumination mapping through a rendering process. RADIANCE [7] is a widely used open-source software adopted for PV modelling purposes [23] and NREL recently released the version bifacial_radiance [24] specifically for bifacial PV applications. It enables the modelling of 3D complex environments, capturing the edge effects, the influence of the racking system and the non-uniformity on the spatial dimension [25], increasing the accuracy in comparison to view factor techniques. However, such method requires a computational time up to $10^4 - 10^5$ higher with respect to 2D view factor methods [25].

C. Non-uniformity of rear irradiance

One of the main drawbacks in bifacial PV technology is the non-uniformity of the irradiance incident on the rear side of the module, which causes mismatch losses (MM_{loss}) up to 1.5% on the annual energy yield [26]. Such non-uniformity arises from multiple causes, e.g. inconstant field of view of PV cells to the different elements, alternating shaded/unshaded patterns, presence of the mounting structure, and heterogeneity of the ground. Various metrics have been introduced to quantify its magnitude, including GNU, defined as shown in equation 2 [27].

$$GNU = \frac{G_{max} - G_{min}}{G_{max} + G_{min}} \tag{2}$$

To take into account the effect of the non-uniformity, the spatial resolution of the irradiance is often increased from module to cell level in multiple studies. Alternatively, empirical relations to estimate MM_{loss} have been developed by Raina and Sinha [8] based on GNU obtaining $R^2 = 98.1\%$ whereas an accuracy up to $R^2 = 0.995$ is achieved by Deline et al. [26] considering the mean standard deviation and the mean absolute difference of rear irradiance distribution.

D. Spectral influence

Solar cells are spectrally-sensitive devices, hence the power generated is dependent on the the spectrum of the incoming radiation. The spectrum of ground-reflected irradiance, dominant among the rear side components, is dependent on the specific ground type, increasing the complexity of spectral impact in case of bifacial modules [9]. Therefore, several studies recommend to consider the spectral effect while developing bifacial PV models [9], [28]–[30] since the use of a constant scalar albedo could lead to relative errors in bifacial gain calculations up to 19.5% [30]. Even though the spectral impact is often neglected in the existing bifacial models, different approaches have been developed to tackle this issue, ranging from using of spectral data to including corrective coefficients [11].

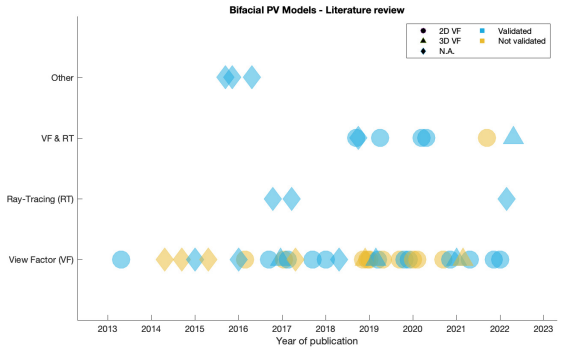

Fig. 1. Classification of the models used in the studies analyzed for this literature review depending on the approach that has been used [4]–[6], [8], [9], [11], [14], [18], [23], [26]–[29], [31]–[64]

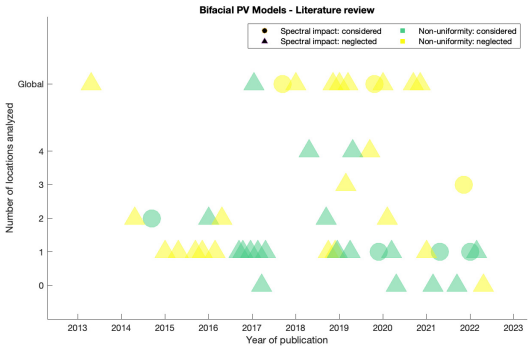

Fig. 2. Classification of the models used in the studies analyzed for this literature review concerning the non-uniformity of the rear irradiance and the spectral impact [4]–[6], [8], [9], [11], [14], [18], [23], [26]–[29], [31]–[64]

E. Classification of optical models

Aiming to select the proper model's features for the objective of this research, the optical bifacial models adopted in 47 different studies have been reviewed. First, a distinction between view factor and ray-tracing approach is displayed in figure 1, where a majority of the former method is highlighted. However, studies where the two techniques are compared are also present even though the simulations are limited to few specific cases. Second, this study investigates the incorporation of considerations related to the non-uniformity of rear irradiance and the spectral impact within the existing models. The results are depicted in figure 2, observing that these features are often neglected when the geographical scale of the simulation is extended to multiple locations.

F. Thermo-electrical models

As mentioned in I, limited cnahges are present concerning thermo-electrical submodels between bifacial and monofacial PV hence an extensive literature is available concerning these aspects. Depending on the requirements in terms of accuracy and computational resources, various models are adopted to estimate the cells' temperature. These include INOCT [65], Sandia [66], Faiman [67], Janssen [48] models or other alternatives which require a large number of parameters and/or intensive computational resources, e.g. fluid-dynamics

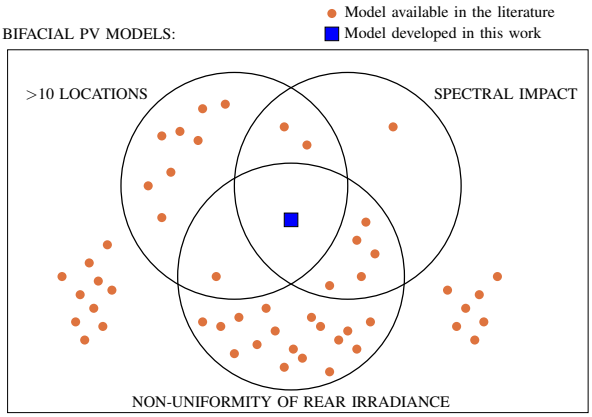

Fig. 3. Venn diagram of the bifacial PV models available in literature [4]–[6], [8], [9], [11], [14], [18], [23], [26]–[29], [31]–[64]

models [68]. The same requirements determine the electrical submodel, which range from constant efficiency expressions [11] to 1-diode approximation.

G. Characteristics of the model developed in this study

Considering the objective of this study, a low computational time represents the main requirement due the global scale involved hence a 2D view factor approach is selected. In contrast to previous global analysis on bifacial PV, this work aims to take into account the effect of the non-uniformity of rear irradiance and the spectral influence, considered crucial aspects to ensure sufficient accuracy. In conclusion, the features of this model are highlighted in figure 3 in comparison to the existing alternatives found in the literature.

III. Bifacial PV farm model

A. Structure of the optical submodel

The optical submodel calculates the irradiance incident on the bifacial PV modules receiving as input meteorological conditions, farm's design parameters and modules' specifications. It is based on view factor concept while adopting the 2D "large-farm" assumption, which entails infinite rows' length. The non-uniformity of the irradiance and the spectral impact are considered by using a four-dimensional matrix as base unit to perform annual farm simulation. The first and the second dimensions represent spatial irradiance distributions along farm's rows and modules' cells, respectively, whereas the third and fourth refers to the time and spectrum's wavelength. Therefore, high computational performance is achieved by replacing prolonged iterations with matrices operations. However, this increases the complexity of the algorithm, involving matrices up to the sixth dimension and continuous decoupling of sub-problems to avoid excessive computational heaviness. Additionally, the matrix structure allows to assign different design parameters for each modules' row, enabling to test unconventional configurations. In summary, using this method the irradiance is calculated for every wavelength of the spectrum on cell level while limiting the increase in

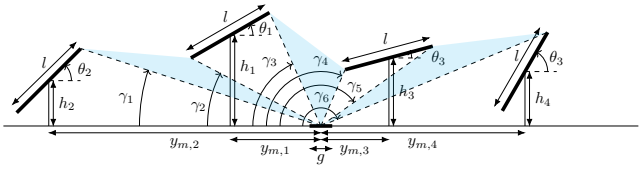

Fig. 4. Sky view factor of a ground segment. The possibility of unconventional farm's configurations is highlighted in the image.

computational time.

The total irradiance incident on front and rear solar cells is determined by three different components, discussed in the next subsections:

- Sky irradiance (I_{sky})
- Ground-reflected irradiance (I_{ground})
- Irradiance reflected by neighbouring modules (I_{mod})

B. Irradiance decomposition

Perez Sky Diffuse model [69] is used to decompose the DHI into circumsolar ($I_{dif,circ}$), isotropic ($I_{dif,iso}$) and horizon ($I_{dif,hor}$) diffuse components. These are used to estimate the direct and diffuse contribution to the irradiance incident on the PV cells.

C. Ground segmentation

The pattern created by shadows projected by the modules on the ground is calculated, obtaining a series of unshaded and shaded segments that depend on the sun's position and the design parameters. To estimate the irradiance incident on the ground, its sky view factor has to be calculated, which is a continuous function of the spatial coordinate hence requiring a ground segmentation. Therefore, the ground sky view factor (SVF_g) is calculated for each ground segment, whose length influences the accuracy of the model. The calculation of SVF_g is limited to the angular sectors between the nearest four modules to each segments, as shown in equation 3 and depicted in figure 4.

$$SVF_g = \sum_{i=1}^{3} \frac{\cos(\gamma_{2i-1}) - \cos(\gamma_{2i})}{2} \tag{3}$$

Whereas SVF_g determines the amount of diffuse irradiance reaching a ground segment, a_g quantifies the fraction of direct component and it is defined as follows, where AOI_g indicates the angle of incidence.

$$a_g = \begin{cases} 0 & \text{if segment is shaded} \\ \max\left(0, \cos(AOI_g)\right) & \text{if segment is unshaded} \end{cases} \tag{4}$$

D. Field of view

To calculate the influence of each of the surrounding element, the field of view of each solar cell is determined, namely the 180° view is divided into angular sectors associated to sky, ground and neighbouring modules, respectively. This is applied for both front and rear cells and an example for the latter case is depicted in figure 5.

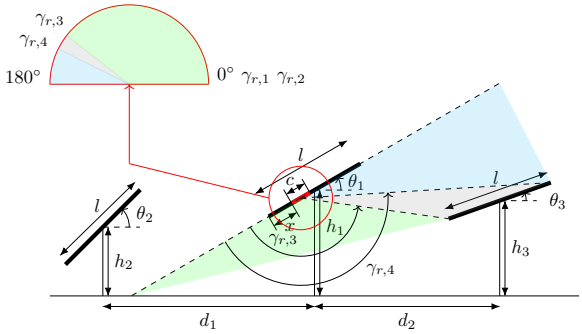

Fig. 5. Field of view: example of a rear cell

E. Sky irradiance

The sky irradiance is calculated according to the equation 5, where both direct and diffuse contribution are included.

$$\begin{aligned} I_{sky} = a_{\text{sky}} \cdot f_{AOI,dir} \cdot (DNI + I_{dif,circ}) + \\ + \ SVF \cdot f_{AOI,dif} \cdot I_{dif,iso} \end{aligned} \tag{5}$$

Only unshaded cells receive direct irradiance and such condition is satisfied when the 2D projection of the sunrays' angle of incidence (AOI_{2d}) on the plane of interest is within the sky sector identified in the field of view of the specific cell. The shaded/unshaded condition is included through the factor a_{sky}, defined in equation 6, where AOI indicates the angle of incidence with respect to the cells' normal direction.

$$a_{sky} = \begin{cases} \cos(AOI) & \text{if the cell is unshaded} \\ 0 & \text{if the cell is shaded} \end{cases} \tag{6}$$

Diffuse sky component depends on the sky view factor (SVF), which is calculated as shown in equation 7, where γ_{sky_1} and $\gamma_{sky,2}$ indicate the angles that define the sky angular sector identified in the field of view.

$$SVF = \frac{\cos(\gamma_{sky,1}) - \cos(\gamma_{sky,2})}{2} \tag{7}$$

Lastly, $f_{AOI,dir}$ and $f_{AOI,dif}$ are the AOI correction factors based on the theory of Martin and Ruiz [70]. Whereas the former is determined by the AOI, for the latter the average between the values of a one-degree-resolution series of angles within the extremes of the angular sector is adopted.

F. Ground-reflected irradiance

The contribution to the ground-reflected irradiance is limited to segments seen by a cell, appointed as "active" in this study, as highlighted in figure 6. This status depends on the field of view, i.e. segments are considered active when they are entirely enclosed in the projection of the ground angular sector.

The ground-reflected irradiance is calculated according to equation 8. f_{AOI} is the AOI corrective factor determined similarly to the sky direct component whereas ρ indicates the albedo, for which both scalar and spectral values are supported. Lastly, the expression 9 adopted for the view factor

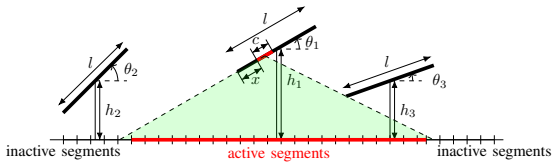

Fig. 6. Example of ground active segments for a rear cell

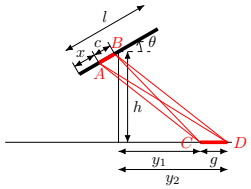

Fig. 7. View factor between a cell and a ground segment

between a solar cell and a ground segment ($VF_{c\to g}$) is based on Hottel's cross string rule, where the nomenclature refers to the figure 7.

$$I_{ground} = \rho \cdot \sum_{\substack{\text{active}\\ \text{segments}}} f_{AOI} \cdot VF_{c\to g} \cdot \cdot (a_g \cdot (DNI + I_{dif,circ}) + SVF_g \cdot I_{dif,iso}) \quad (8)$$

$$VF_{c\to g} = \frac{BC - AC + AD - BD}{2 \cdot c} \quad (9)$$

G. Irradiance reflected by neighbouring modules

The irradiance component consisting of neighbouring modules' reflections is calculated as illustrated in equation 10. This is proportional to the irradiance incident on such modules, wherein an average spatial value is considered. $VF_{c\to m}$ is the view factor between the cell and the neighbouring module, based on the field of view, similarly to $VF_{c\to g}$. r indicates the reflectivity of the modules whereas f_{AOI} is computed analogously to the sky diffuse irradiance.

$$I_{mod} = r \cdot VF_{c\to m} \cdot f_{AOI} \cdot I_{incident\ neigh\ mod} \quad (10)$$

H. Thermo-electrical submodel

The choice of the thermal model to predict cells' temperature (T_{cell}) is based on two criteria, namely the availability of data for the analyzed locations and the computational time restrictions. These reasons lead to adopt the INOCT model, considering rack mounted modules.

Concerning the electrical model, preliminary tests adopting 1-diode approximation have failed the computational time requirements due to the global-scale of the analysis hence a fill factor approximation introduced by Green [71] is adopted. Equations 11-14 are implemented to estimate the short-circuit current and the open-circuit voltage of every cell, where front and rear sides are modelled as a parallel circuit. Specifically, two different EQE curves are adopted to distinguish front and rear cells.

$$J_{sc,front} = \frac{q}{hc} \cdot (1 + k_{J_{sc}} \cdot (T_{cell} - 25°C)) \cdot \cdot \int_{\lambda_1}^{\lambda_2} I_{front}(\lambda) \cdot EQE_{front}(\lambda)\, d\lambda \quad (11)$$

$$J_{sc,rear} = \frac{q}{hc} \cdot (1 + k_{J_{sc}} \cdot (T_{cell} - 25°C)) \cdot \cdot \int_{\lambda_1}^{\lambda_2} I_{rear}(\lambda) \cdot EQE_{rear}(\lambda)\, d\lambda \quad (12)$$

$$J_{sc} = J_{sc,front} + J_{sc,rear} \quad (13)$$

$$V_{oc} = \left[\frac{V_{oc,specs}}{N_s} + \frac{nk \cdot (T_{cell} + 273\,K)}{q} \cdot \log\left(\frac{G_{tot}}{G_{STC}}\right)\right] \cdot (1 + k_{V_{oc}} \cdot (T_{cell} - 25°C)) \quad (14)$$

Green approximation is based on the relations 15 and 16, where the constant c_{ff} is tuned by minimizing the error with respect to the 1-diode model. For this study, this value is set equal to 200, limiting the error in the annual energy yield up to 0.7%. The relatively high magnitude is caused by the neglect of the cells' interconnection losses and the logarithmic nature of the relation.

$$FF = \frac{v_{oc} - \log(v_{oc} + c_{ff})}{v_{oc} + 1} \quad (15)$$

$$v_{oc} = \frac{qV_{oc}}{k(T_{cell} + 273\,K)} \quad (16)$$

IV. Electricity Market Model

Analyzing few selected European countries, a negative correlation between electricity prices and sun's altitude (a_s) is observed, i.e. price values are minimal during noon. Moreover, an increase (in absolute value) of the correlation has been registered in 2022 with respect to 2018 [17], proving the sensitivity on the PV installed capacity. This is illustrated in figure 8. To enable the simulation of different market scenarios, electricity prices are modelled depending on a_s, creating an annual price curve for each location. Specifically, five different parameters are used to determine the shape of the price timeseries:

- Price ratio (p_{ratio})
- Minimum price (p_{min})
- Minimum a_s ($a_{s,min}$)
- Maximum a_s ($a_{s,max}$)
- Shape factor (f_{shape})

The resolution of the price curve depends on the a_s input array and the price values oscillates between the minimum "noon price" (p_{min}) and the maximum "morning/ evening price" calculated as $p_{min} \cdot p_{ratio}$. $a_{s,min}$, $a_{s,max}$ and f_{shape} define the transition between these prices, i.e. a_s values that satisfy the condition $a_s < a_{s,min}$ are associated to the

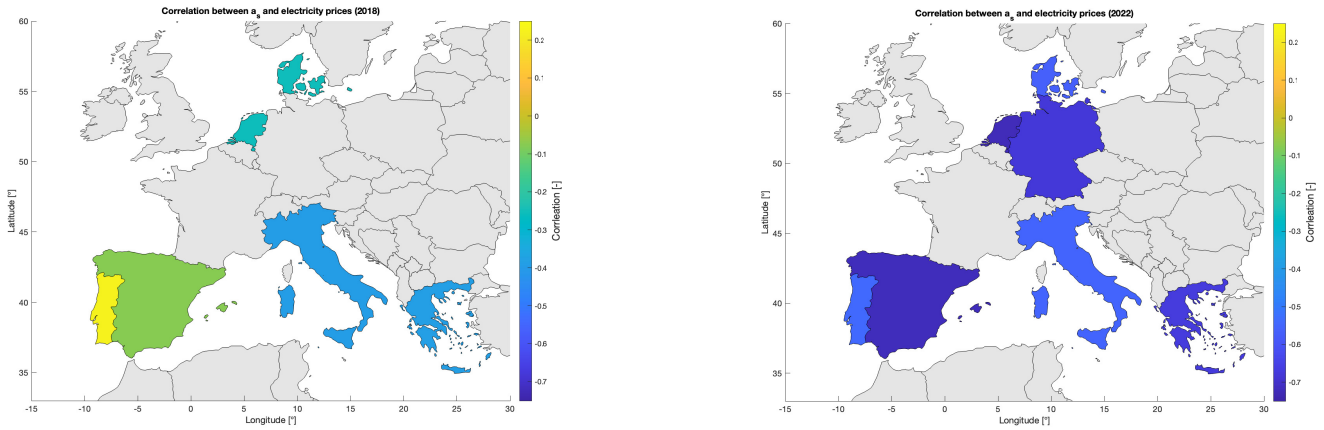

Fig. 8. Correlation between electricity prices and a_s of few selected countries in Europe, referring to 2018 (a) and 2022 (b), respectively

TABLE I
CONSTANT TUNED VALUES OF $a_{s,min}$, $a_{s,max}$, f_{shape}

Parameter	Value
$a_{s,min}$	$5.4°$
$a_{s,max}$	$32.5°$
f_{shape}	4

maximum price whereas the minimum price is assigned to a_s values such that $a_s > a_{s,max}$. Lastly, f_{shape} is an integer number that determines the presence of intermediate prices between the maximum and the minimum values since it is defined as the number of possible values that can be assumed by the price curve, e.g. $f_{shape} = 2$ leads to a rectangular curve. Moreover, a seasonal effect is intrinsic in this method due to the a_s dependence, e.g. higher prices are obtained during the winter period due to lower average a_s values in the Northern hemisphere. These five parameters are tuned using real electricity prices of 8 European countries registered during 2018 and 2022, i.e. 16 cases in total. Minimizing RMSE on daily basis, 365 values of p_{ratio}, $p_{min}a_{s,min}$, $a_{s,max}$ and f_{shape} are found for each case. Definitive values are obtained through two averaging processes. First, for each specific case yearly average values are assumed to be representative for the entire year. Second, average values among the 16 different cases are calculated to generalize the results on a global scale. Whereas different values of p_{ratio} and p_{min} are tested to simulate various market conditions, $a_{s,min}$, $a_{s,max}$ and f_{shape} are kept constant during this study and their values are included in table I. The process of electricity prices' modelling is summarised in figure 9.

V. VALIDATION OF THE MODEL

The validation of the model is limited to the estimation of the rear irradiance incident on different positions along the modules' length. Other features are neglected in this validation process due to their wide use for monofacial modules in the recent years [5]. This validation has been conducted in

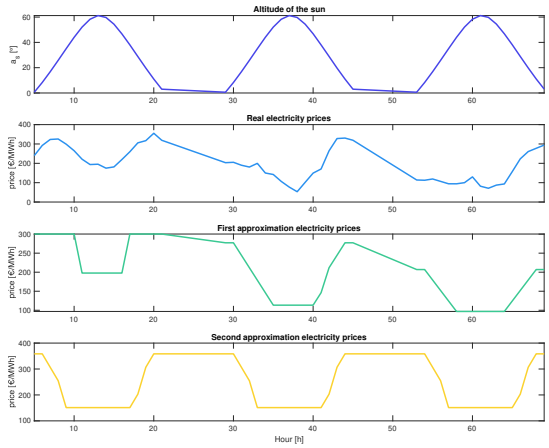

Fig. 9. Main steps in the modelling of the electricity prices: correlation between a_s and prices, first approximation on daily basis, second approximation on annual basis. This example refers to the period 16-18 June 2022 of the Netherlands.

collaboration with the company *Kipp & Zonen* which has performed a series of measurements using their sensors.

A. Experimental setup and Data processing

The measurements took place in Delft $(52.0°N, 4.4°E)$ between July and September 2020. The experimental setup consists in three bifacial PV modules equipped with six pyranometers on the rear side, as depicted in figure 10. Additional structures and monofacial modules have been placed next to the bifacial modules to simulate the farm environment. Data gathered during 12 different days have been selected for this analysis and both the tilt and the ground type have been varied to test the performance of the model under diverse installation conditions. These information are specified in the Appendix B. Front irradiance has been measured as well in order to quantify the impact of the rear

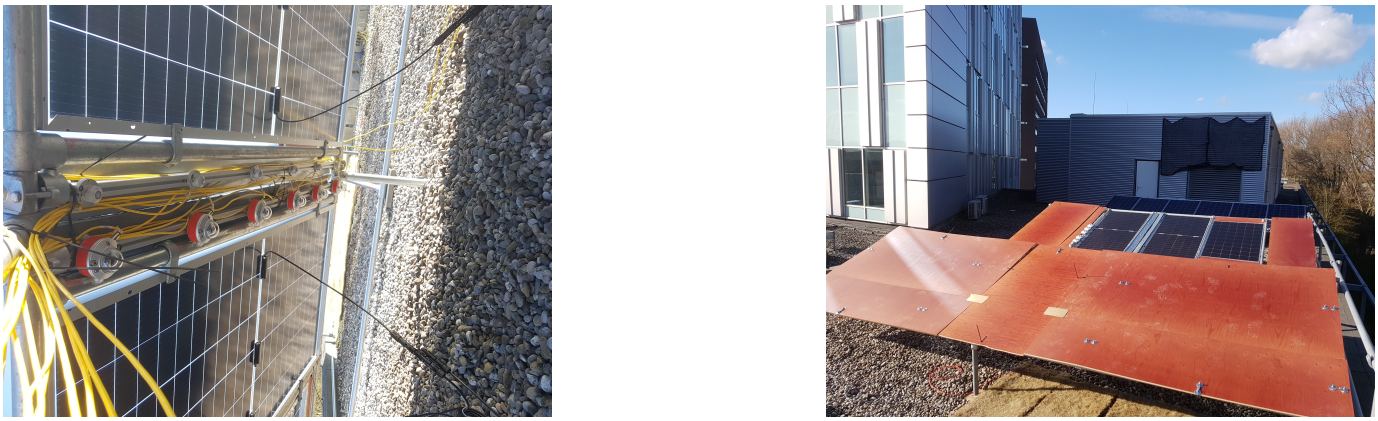

(a) (b)

Fig. 10. Experimental setup provided by the company *Kipp & Zonen*

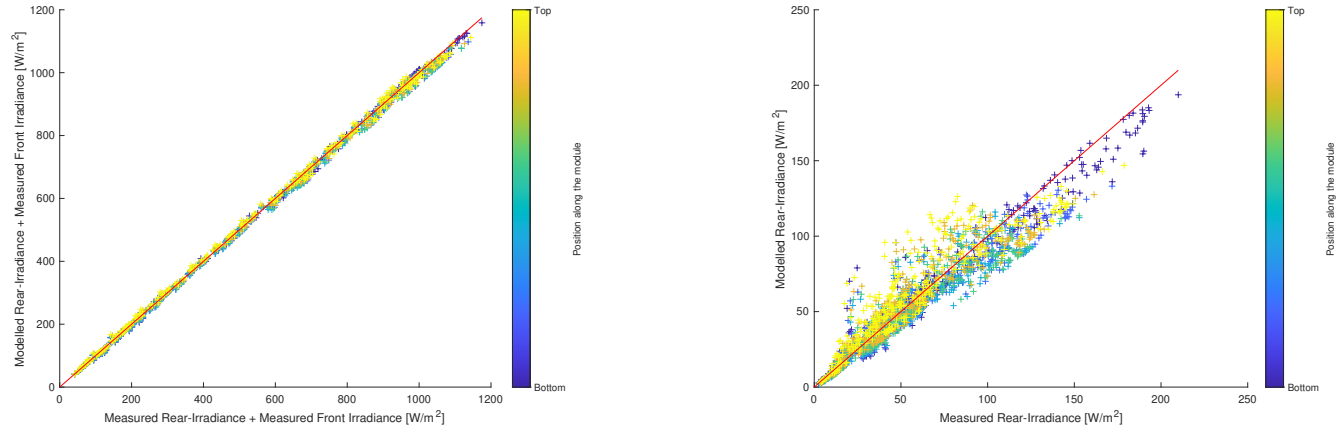

(a) (b)

Fig. 11. Validation results: Comparison between modelled and measured data, considering both the total irradiance values, i.e. front+rear (a) and only the rear component (b)

component's deviations on the total value. A 15-minutes resolution is adopted to mitigate the slight time misalignment between the sensors hence a time-averaging process has been accomplished to match the time resolution of the different signals, in accordance to the approach of Marion et al. [5].

B. Results of the experimental validation

Modelled and measured data are compared by calculating the roor mean square error (RMSE) and the mean bias deviation (MBD), which amount to $-1.29\,W/m^2$ (-2.22%) and $12.65\,W/m^2$ (21.69%), respectively. These values refer to the overall comparison and are consistent with findings of previous studies based on view factor models [5]. The outcome of the validation is depicted in figure 11, where it can be observed that the errors in the estimation of the rear irradiance are minimal in case the front side component is added. Additional results are included in the Appendix B.

Further analysis are performed to investigate the conditions and the parameters that mostly affect the model's ability to predict the incident irradiance, as highlighted in figure 12. First, a slight trend with respect to the hour of the day can be observed, where higher errors are obtained during morning and evening periods. Such behaviour is probably caused by the higher influence of the surrounding structure when the sun's altitude approaches zero. An evident trend concerns the tilt values, i.e. high tilts lead to an overestimation of the irradiance whereas an underestimation is registered in case of low values. In general, it is observed that higher tilt values also cause larger errors on the estimation. Such behaviour can be explained by taking into account the limitations of the view factor approach, which assumes a diffuse reflection of the incident light. Therefore, the largest errors occur in case of higher tilts, for which a larger portion of unshaded ground is visible by the rear cells, confirming that the hypothesis of diffuse surfaces is evidently inadequate for these ground segments. Such statement is also proved by observing that larger errors occur at the edge of the modules, which have a

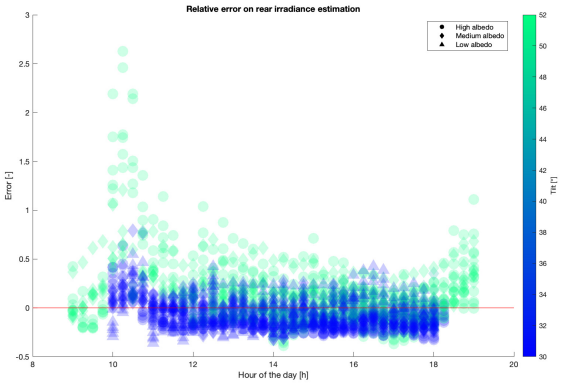

Fig. 12. Relative error on the rear irradiance estimation with respect to the hour of the day for different tilt and albedo vales.

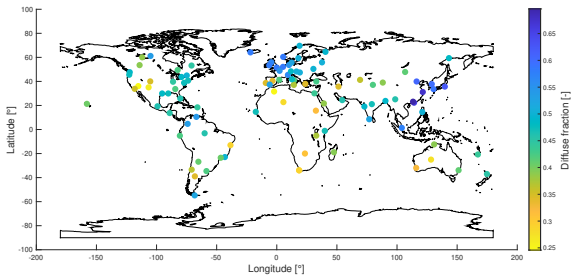

Fig. 13. Global map of the 102 locations analyzed in this study. GHI-weighted average value of diffuse fraction is included for each location.

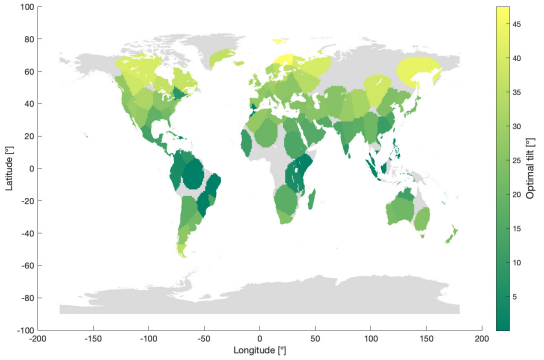

Fig. 14. Optimal tilt for bifacial PV modules obtained from the simulation over 102 locations, where d and h have been set to $3\,m$ and $1.5\,m$, respectively.

wider view on unshaded ground during clear sky conditions. Conversely, clear trends are not found in relation to the albedo, probably due to the lack of variety of measurements with respect to such feature. Lastly, the error in the estimation of GNU is also investigated, resulting in underestimation of the non-uniformity for high tilt values and overestimation in case of lower values.

VI. Results and Discussion

A. Simulations' input data

102 locations are selected for this study and their hourly data are downloaded from the software METEONORM concerning DNI (broadband), DHI (broadband), a_s, A_s, p, T_{amb} for a total duration of one year. These locations are highlighted in figure 13 along with the correspondent GHI-weighted average of diffuse fraction, assumed to be representative for the whole year. This is appointed as diffuse fraction in this analysis, unless otherwise specified. Spectral DNI and DHI curves are reconstructed from the broadband values using normalized irradiance-weighted average spectrum for both components [72], enabling the decoupling between spectral and temporal dimension hence reducing the computational time. Light soil is adopted as ground type for the simulations, whose albedo spectral curve is obtained through the software SMARTS. Two different EQE curves for front and rear side of the modules are taken from the work of Carolus et al. [73]. Therefore, ϕ_{Bi} is calculated as shown in equation 17 and it is equal to 65.14% in this case. Detailed specifications of the modules considered in this work are included in the Appendix C. Lastly, ground segments' length is set to $0.2\,m$ in order to limit to 0.15% the error on the annual energy yield caused by segments' resolution.

$$\phi_{Bi} = \frac{J_{sc,rear}}{J_{sc,front}} = \frac{\int_{\lambda_1}^{\lambda_2} EQE_{rear}(\lambda)}{\int_{\lambda_1}^{\lambda_2} EQE_{front}(\lambda)} \tag{17}$$

B. PV farm configurations

As introduced in section I, the performance of two different farm configurations are compared in this study, namely N/S tilted and E/W vertical modules. Specifically, the tilt of the former configuration is chosen by maximizing the annual energy yield for each location and it is appointed as optimal tilt (θ_{opt}). Unlike monofacial PV modules, θ_{opt} is highly sensitive on the installation conditions, in accordance with previous studies analyzed in section II. In general, θ_{opt} is directly proportional to the row-to-row distance (d) whereas an opposite trend is obtained for the elevation of the modules (h). For simplicity, the optimal tilt values adopted for this study refer to the condition $d = 3\,m$ and $h = 1.5\,m$ since the impact of the design parameters decreases above such limit. Worldwide results are depicted in figure 14.

C. Effect of design parameters on the energy yield

The impact of the design parameters differ depending on the farm configurations. This is observed by analyzing the derivative of the energy yield with respect to row-to-row distance ($\frac{\partial EY}{\partial d}$) and modules' height ($\frac{\partial EY}{\partial h}$). This is expressed as percentage of increase in the energy yield value for an increment of distance/height by $1\,m$.

Figure 15 shows that $\frac{\partial EY}{\partial d}$ is always positive for both cases and the decreasing trend implies a saturation behaviour, i.e. an increase of d leads to limited improvements in

terms of energy yield after a certain limit. However, higher values of $\frac{\partial EY}{\partial d}$ are registered for the vertical configuration, highlighting that d has more impact in case a vertical PV farm is considered. Even though it cannot be detected from figure 15, such results are sensitive to h as well, highlighting a strong inter-dependence between these design parameters. Specifically, $\frac{\partial EY}{\partial d}$ is directly proportional to h hence the benefits of larger d values are greater in case of high modules' elevation. Lastly, figure 15 confirms that these general trends are valid for all the locations investigated in this study, identified using the diffuse fraction. However, the exact magnitude of the derivative is location dependent and a correlation with respect to the diffuse fraction is not found.

$\frac{\partial EY}{\partial h}$ is analyzed in figure 16, where a saturation behaviour similar to the previous case can be detected for both configurations. In contrast to the distance's influence, negative values of $\frac{\partial EY}{\partial h}$ are registered after a certain h value in this case, highlighting the presence of an optimal height (h_{opt}) that maximizes the energy yield. Once such value is reached, a further increase in h leads to minimal penalization in the energy yield hence the optimal height can be appointed as a saturation limit as well. Moreover, h_{opt} depends not only on the farm configuration but also on the row-to-row distance and the specific location. In general, higher values of h_{opt} are obtained for tilted modules with respect to the vertical counterpart. Moreover, in the former case h_{opt} is proportional to d value whereas in the latter such trend is not evident.

In summary, increasing the row-to-row distance of a bifacial PV farm is beneficial for the energy yield irrespective of the configuration whereas an optimal height value that maximizes the energy yield can calculated depending on the location and the other design parameters. This is the result of the influence of d and h on individual aspects that affect the energy yield calculation, including ground SVF, unshaded ground fraction, mutual shading and non-uniformity of rear irradiance. Such relations are outlined in table II.

TABLE II
INFLUENCE OF d AND h: WHETHER HIGH, LOW OR OPTIMAL VALUES ARE BENEFICIAL FOR THE ENERGY YIELD CONCERNING DIFFERENT ASPECT.

	Ground SVF	Unshaded ground fraction	Mutual shading	GNU
Distance	High	High	High	High
Height	Low	High	No influence	Optimal

D. Economic potential of E/W vertical configuration

The profitability of the of E/W vertical with respect to N/S tilted configuration is studied in relation to six different variables:

1) Max power fraction ($n_{max,power}$), which provides details about a possible curtailment strategy and it is defined as the ratio between the maximum power allowed and the nominal power of the power plant.
2) Ratio vertical/total modules (n_{vert}), which consider the possibility of "hybrid" PV farms where part of the modules are E/W vertical whereas the remaining are N/S tilted. It is expressed as the ratio between the number of vertical modules among the total.
3) Row-to-row distance (d)
4) Elevation of the modules (h)
5) Minimum noon price (p_{min})
6) Price ratio (p_{ratio})

The economic potential of vertical modules is quantified by the revenues' gain (R_{gain}) obtained while adopting the E/W vertical configuration instead of the N/S tilted counterpart, as shown in equation 18. Specifically, a positive R_{gain} indicates that the E/W vertical is more profitable than the N/S tilted configuration under the specified conditions.

$$R_{gain} = \frac{R_{\text{new configuration}} - R_{\text{optimal tilt}}}{R_{\text{optimal tilt}}} \cdot 100\% \qquad (18)$$

A preliminary assessment of the economic potential of the vertical configuration is performed by identifying the combination of $n_{max,power}$ and n_{vert} that achieve a positive revenues' gain ($R_{gain} > 0\%$). The results are visualized through contour plots, as illustrated in figures 17, 18 and 19, which report the examples of Utrecht and Madrid. The graphs are characterized by n_{vert} on the x-axis and $n_{max,power}$ on the y-axis whereas the contour lines refer to the energy yield and the R_{gain} depending on the color scale. The main focus of these graphs is to study the presence of "gain regions", i.e. areas in the graph where the condition $R_{gain} > 0\%$ is satisfied. Specifically, figures 18 and 19 show the enlargement of the gain regions when d and p_{ratio} are increased, proving the high sensitivity of E/W vertical modules' profitability on these parameters. Overall, in the conditions shown in these examples vertical or hybrid PV farms appear to be favourable only in case a low $n_{max,power}$ is considered, which it is not realistic due to the excessive energy curtailed.

To extend the analysis on a global perspective, the focus is shifted to the following question: *What is the minimum price ratio (p_{ratio}) required to achieve higher revenues using E/W vertical instead of N/S tilted PV modules ($R_{gain} > 0$)?* An answer is provided by using scatter plots characterized by p_{ratio} on the y-axis and the examined feature on the x-axis, i.e. $n_{max,power}$, n_{vert}, d or h. The size of each data point is proportional to the number of the locations that satisfy the condition $R_{gain} > 0$ for a specific p_{ratio} and feature's value. Moreover, a color scale is used to identify the diffuse fraction (weighted-averaged yearly value) of each location. In case a data point represents more than one location, i.e. is larger in size, the color refers to the average diffuse fraction of these locations. Price ratios between 1 and 10 are considered in the analysis. Furthermore, the dots correspondent to the maximum value on the y-axis indicate the locations for which the condition $R_{gain} > 0\%$ is never achieved for these p_{ratio} values. In simple terms, the larger the size of the dots at the bottom of the graphs, the higher is the profitability of the vertical/hybrid farm with respect to the conventional tilted configuration.

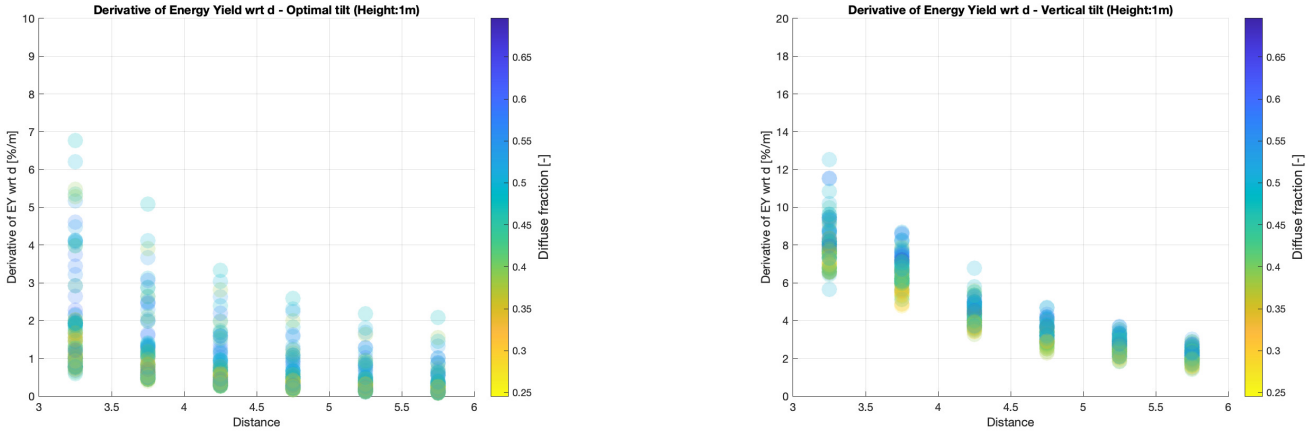

(a) (b)

Fig. 15. Derivative of the energy yield with respect to the row-to-row distance ($\frac{\partial EY}{\partial d}$). Values of the 102 different locations are presented for each value of d using the diffuse fraction color scale and for both tilted (a) and vertical (b) configuration. A height of $1\,m$ is considered.

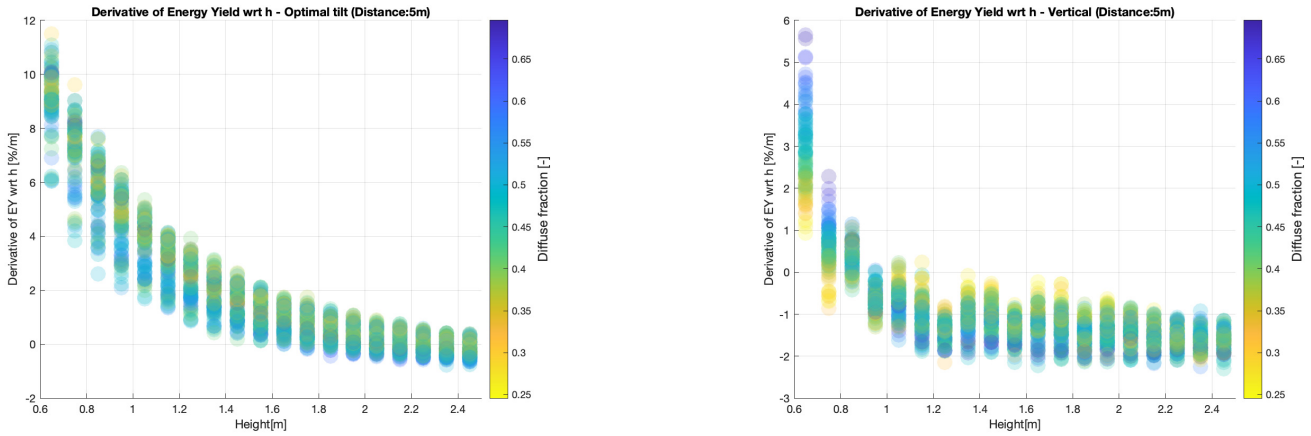

(a) (b)

Fig. 16. Derivative of the energy yield with respect to the height ($\frac{\partial EY}{\partial h}$). Values of the 102 different locations are presented for each value of h using the diffuse fraction color scale and for both tilted (a) and vertical (b) configuration. A distance of $5\,m$ is considered.

First, the influence of $n_{max,power}$ is depicted in figure 20, where both vertical and hybrid farms are considered, namely $n_{vert} = 1$ and variable n_{vert}, i.e. the value n_{vert} is chosen in order to maximize R_{gain}. It can be observed that the profitability of the vertical configuration increases as the $n_{max,power}$ value decreases, as expected. However, such trend is only evident for $n_{max,power} < 0.7$ which entails significant power losses due to curtailment. Moreover, it is evident that hybrid PV farms are beneficial only for low $n_{max,power}$ values. This is confirmed also by figure 21, where the influence of n_{vert} is investigated for different curtailment strategies, highlighting that no effect can be detected in case $n_{max,power} = 1$.

The same trend between the energy yield and the design parameters d and h is observed for the revenues, namely the highest revenues are obtained for larger d and optimal h values. Specifically, the influence of p_{ratio} and p_{min} is found to be minimal, i.e. less relevant than the inter-dependence of the design parameters. Figure 22 shows that larger d values increase the number of locations where E/W vertical modules are more profitable than N/S tilted configuration, proving the higher sensitivity on d of vertical installations. On the other hand, small h values seem to be beneficial for the profitability of the E/W vertical configuration, since lower h_{opt} and minor impact of h on the energy yield are observed for the vertical case. In general, the impact of h is limited with respect to d concerning the comparison between the two configurations.

With the exception of negative values, for which vertical configurations are always preferable, p_{min} does not affect the values of R_{gain}. This is caused by R_{gain} definition since it is expressed in relative terms, as demonstrated in the Appendix D. Lastly, table III summarizes the results outlined in the previous paragraphs.

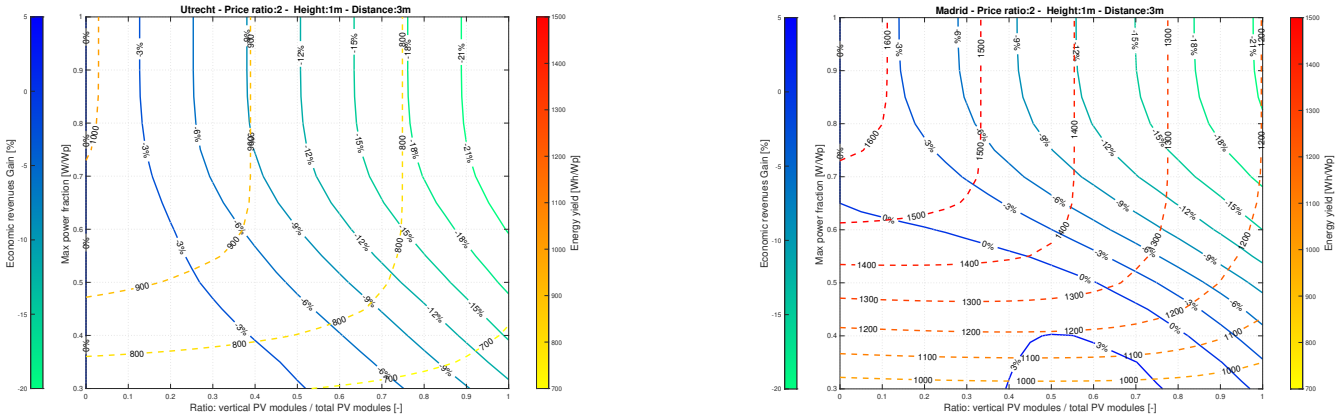

(a) (b)

Fig. 17. Contour plots that show the energy yield and the revenues' gain for different $n_{max,power}$ and n_{vert} values. The examples of Utrecht (a) and Madrid (b) are presented. The other variables are set as follows: $d = 3\,m$, $h = 1\,m$, $p_{min} = 200\,€/MWh$, $p_{ratio} = 2$

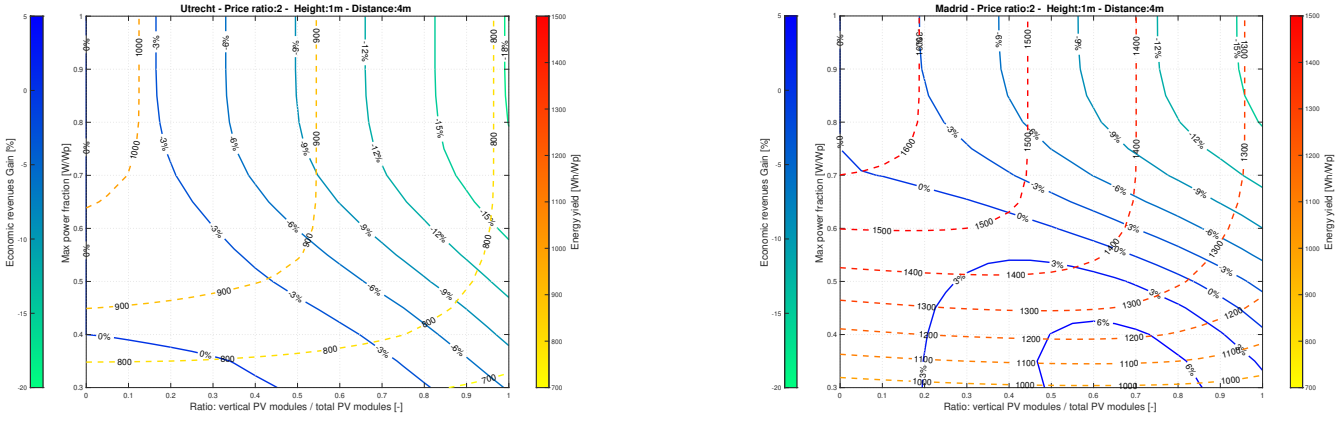

(a) (b)

Fig. 18. Contour plots that show the energy yield and the revenues' gain for different $n_{max,power}$ and n_{vert} values. The examples of Utrecht (b) and Madrid (b) are presented. The other variables are set as follows: $d = 4\,m$, $h = 1\,m$, $p_{min} = 200\,€/MWh$, $p_{ratio} = 2$

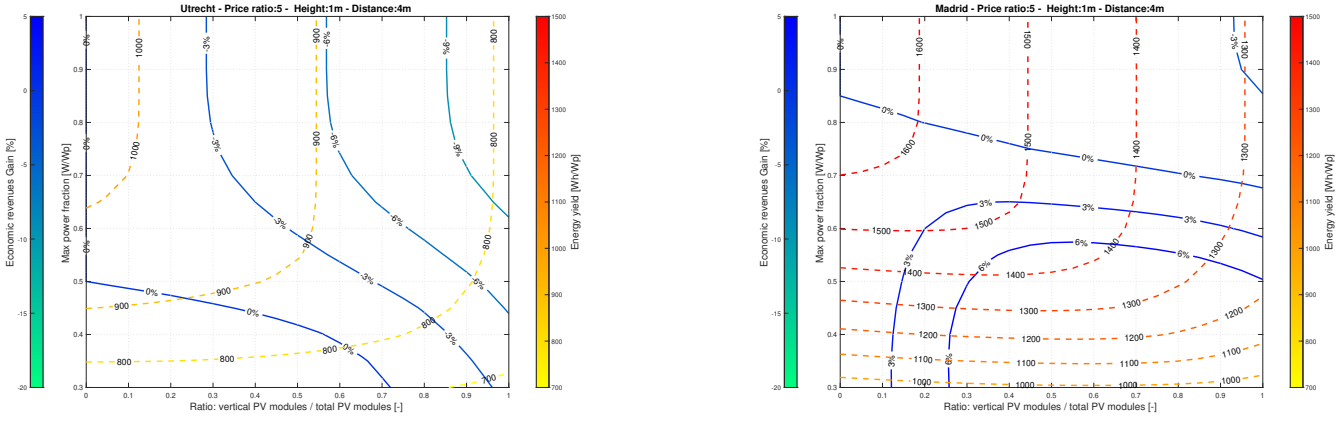

(a) (b)

Fig. 19. Contour plots that show the energy yield and the revenues' gain for different $n_{max,power}$ and n_{vert} values. The examples of Utrecht (a) and Madrid (b) are presented. The other variables are set as follows: $d = 4\,m$, $h = 1\,m$, $p_{min} = 200\,€/MWh$, $p_{ratio} = 5$

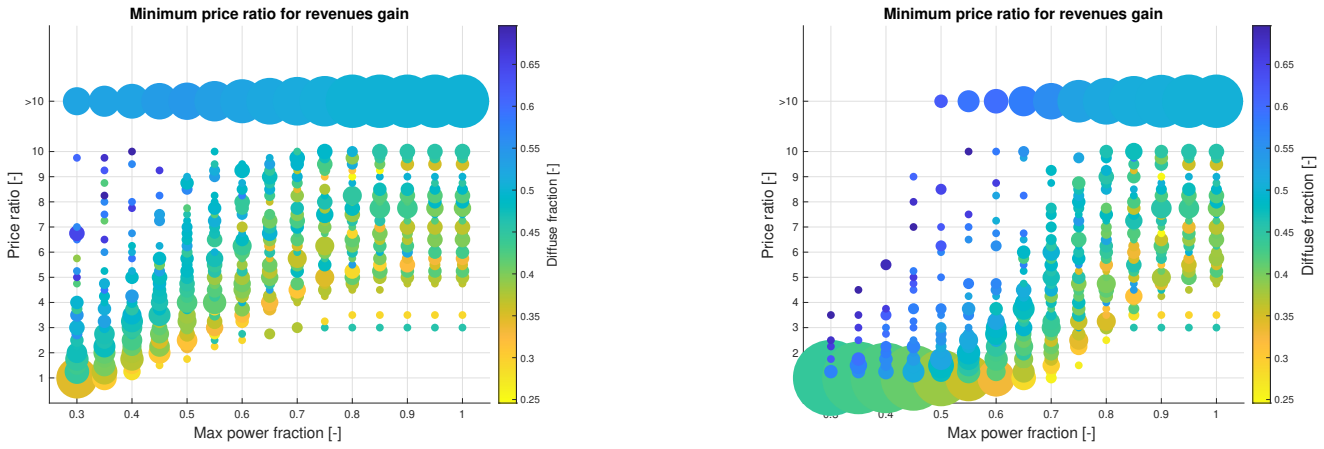

Fig. 20. Influence of $n_{max,power}$ on the minimum price ratio required to achieve $R_{gain} > 0\%$, where both $n_{vert} = 1$ (a) and $n_{vert} = var$ (b) are considered. The other variables are set as follows: $d = 4\,m$, $h = 1\,m$, $p_{min} = 100\,€/MWh$

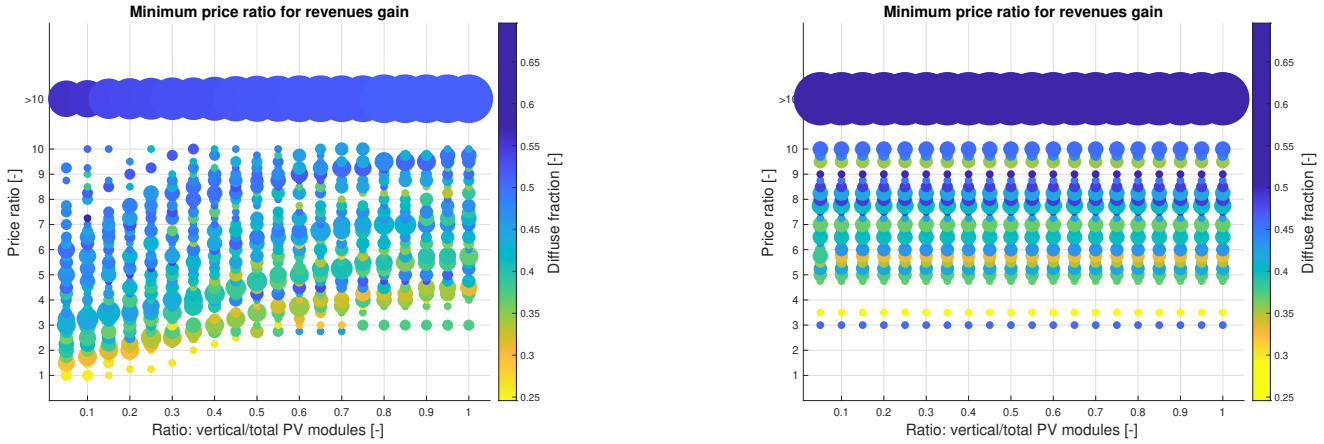

Fig. 21. Influence of n_{vert} on the minimum price ratio required to achieve $R_{gain} > 0\%$, where both $n_{max,power} = 0.7$ (a) and $n_{max,power} = 1$ (b) are considered. The other variables are set as follows: $d = 4\,m$, $h = 1\,m$, $p_{min} = 100\,€/MWh$

An example of global visualization is depicted in figure 23, where the minimum p_{ratio} required to satisfy the condition $R_{gain} > 0\%$ is highlighted. Even though the spatial diversification of the results suggests that the profitability of vertical modules is strictly dependent on the local climate, a slight trend can be recognized with the diffuse fraction. Specifically, locations characterized by a low diffuse fraction are favourable for E/W vertical configuration. This is proved by analyzing the correlation between the diffuse fraction representative of each location and R_{gain}. The results illustrated in 24 show that negative correlation is obtained whereas its magnitude depends on the design parameters and the market conditions. Moreover, such correlation increases (in absolute value) up to -0.7 when only morning/evening hours are considered.

VII. Conclusions

The aim of this study was to investigate the potential of E/W vertical bifacial PV farms in terms of market revenues. Specifically, this configuration is compared with the conventional N/S tilted counterpart and the analysis is extended to a global scale. This is achieved through the development of a bifacial PV model that estimates the power generated by a large-scale farm. An extensive literature review has been performed to understand the features and the limitations of the existing models used for bifacial PV modules, concluding that 2D view factor method represents the only feasible solution when multiple locations are simulated. A multi-dimensional matrix approach has been adopted to include the effect of the non-uniformity of the incident irradiance without affecting the computational time of the simulations. Moreover, such model enables the simulation of farms characterized by unconventional configurations since the design parameters can be set at each row instead of for the entire farm.

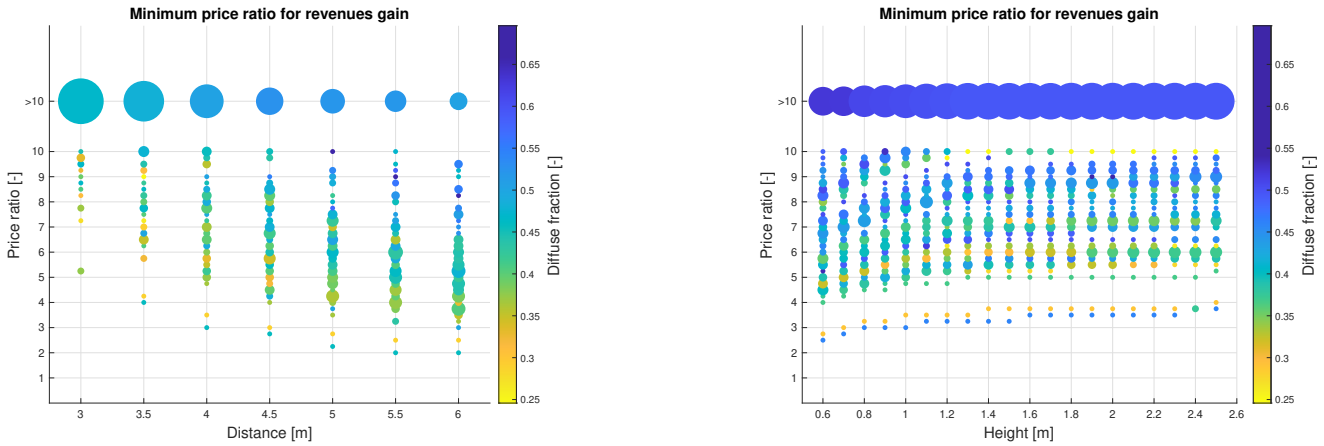

(a) (b)

Fig. 22. Influence of d (a) and h (b) on the minimum price ratio required to achieve $R_{gain} > 0\%$. The other variables are set as follows: $h = 1\,m$ (a) $d = 4\,m$ (b), $p_{min} = 100\,€/MWh$, $n_{vert} = 1$, $n_{max,power} = 1$

TABLE III
INFLUENCE OF DIFFERENT VARIABLES ON THE MINIMUM p_{ratio} REQUIRED TO SATISFY THE CONDITION $R_{gain} > 0\%$

Variable	Influence
$n_{max,power}$	The influence is significant only in case of low $n_{max,power}$ values, which are not considered relevant for large-scale PV farms.
n_{vert}	Hybrid PV farms are favourable only in case of low $n_{max,power}$, hence they are not relevant for this study.
d	Large d values increase the profitability of the vertical configuration over the tilted modules.
h	h values have a limited impact on the revenues, but lower values increase the profitability of vertical modules with respect to the tilted counterpart.
p_{min}	Only the sign of the minimum price is relevant to decide the optimal configuration and vertical modules are always preferred in case of a negative p_{min}.

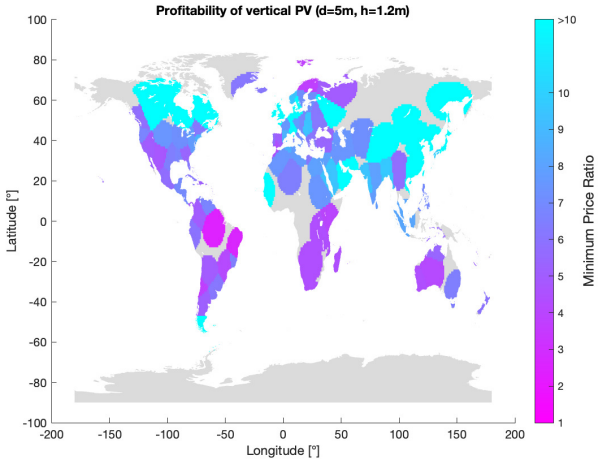

Fig. 23. Global map for the minimum price ratio for which vertical modules are more profitable than tilted ones. The relevant variables are set as follows: $d = 5\,m$, $h = 1.2\,m$, $p_{min} = 100\,€/MWh$, $n_{vert} = 1$, $n_{max,power} = 1$

The model has been validated in collaboration with the company *Kipp & Zonen*, testing different tilt values and ground types. The validation is limited to the irradiance incident on the rear side of the modules along six different positions, since the submodels adopted to predict the front irradiance and to estimate the electrical power are inherited from the monofacial technologies. Overall, MBD and RMSE between modelled and measured data amount to $-1.29\,W/m^2$ (-2.22%) and $12.65\,W/m^2$ (21.69%), respectively. Specifically, it has been observed that the design parameter that mostly affect the ability to predict the irradiance is the tilt and the error increases as the amount of unshaded ground seen by the specific cell increases, namely for high tilt values and at the edges of the modules. These results have confirmed the limitations of the view factor theory, which assumes all surfaces to be diffuse emitters.

Various market scenarios and installation conditions have been tested to determine their influence in the choice of the optimal configuration in terms of market revenues. The following conclusions have been drawn:

1) The profitability of E/W vertical over the N/S tilted configuration is dependent on the design parameters, the curtailment strategy, the fraction of vertical modules in case of hybrid farms, the electricity market conditions and the specific location of the PV farm.
2) The influence of the curtailment strategy is limited to the cases when the maximum power allowed is lower than 70% of the nominal power ($n_{max,power} < 0.7$).
3) Hybrid PV farms which combine both configurations are beneficial only in case of heavy curtailment strategies, namely $n_{max,power} < 0.7$, otherwise either completely vertical or entirely tilted farms have to be preferred depending on the other parameters.
4) Assuming an electricity price curve with a minimum around noon, the only market variable that affects the choice of the optimal configuration is the ratio between morning/evening and noon price. Therefore, the mag-

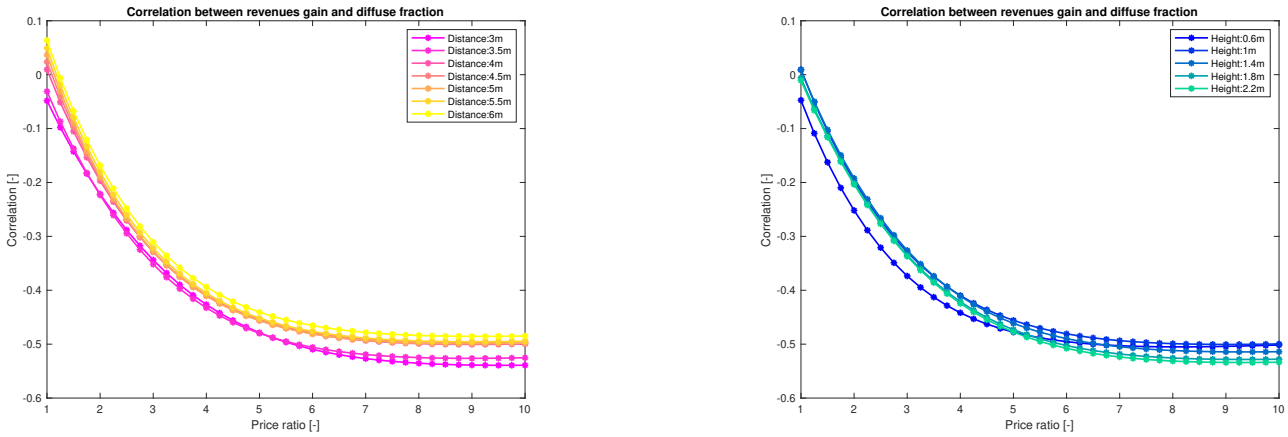

Fig. 24. Correlation between the diffuse fraction (GHI-weighted average) and R_{gain}. The influence of d, h and p_{ratio} is highlighted. Unless specified in the legend, the other variables are set as follows: $d = 4\,m$, $h = 1\,m$, $n_{vert} = 1$, $n_{max,power} = 1$

nitude of the prices is not relevant in such decision whereas a minimum price ratio that guarantees higher profitability for vertical over tilted modules can be identified depending on the specific location and the other parameters.

5) Larger row-to-row distance values increase the energy yield and the revenues of both vertical and tilted PV farms up to a saturation value. However, the impact of this parameter is higher for the former case hence an increase in the row-to-row distance fosters the profitability of E/W vertical over N/S tilted configurations.
6) An optimal height that maximizes the energy yield and revenues can be calculated for vertical and tilted PV modules. Such value is lower for the former configuration and depends on the specific location as well as the row-to-row distance. However, its impact on the decision of the optimal configuration is less relevant than the other parameters.
7) There is a negative correlation between the revenues gain of vertical over tilted PV farms and the GHI-weighted average diffuse fraction of the locations. Such correlation increases (in absolute value) when only mornings and evenings are considered, meaning that vertical PV farms are favourable in locations characterized by a low diffuse fraction during morning and evening hours.

The exhaustiveness of this work is constrained by the computational resources and data available, preventing further investigation on the topic. The following guidelines aim to outline possible research pathways concerning this field.

1) Even though the main limitations are intrinsic to the view factor concept, the use of corrective coefficients to include the effect of the mounting structure could be considered, in order to increase the accuracy of the rear irradiance estimation.
2) To further improve the computational speed of the algorithm, the necessity of extending the dimensions of problem to consider effects like non-uniformity of the irradiance could be replaced by empirical coefficients. Their dependence on design and meteorological parameters could be investigated through machine learning techniques. Such improvements would enable application of methods that are computationally more intense, e.g. genetic algorithms to optimize farms on row's level.
3) The influence of different ground types and the bifaciality factor should be studied to complete the sensitivity analysis performed in this study.
4) Coupling with storage technologies should be considered to provide a wide overview of the profitability of E/W vertical configuration.

REFERENCES

[1] IRENA, "World energy transitions outlook 2023: 1.5°c pathway," International Renewable Energy Agency, Abu Dhabi, Tech. Rep., 2023.
[2] M. Fischer, M. Woodhouse, P. Baliozian, and J. Trube, "International technology roadmap for photovoltaics (ITRPV) 14th edition: 2022 results," Tech. Rep., 2023. [Online]. Available: https://www.vdma.org/
[3] R. Kopecek and J. Libal, "Towards large-scale deployment of bifacial photovoltaics," *Nat Energy*, vol. 3, pp. 443–446, 2018. [Online]. Available: https://doi.org/10.1038/s41560-018-0178-0
[4] C. D. Rodríguez-Gallegos, H. Liu, O. Gandhi, J. P. Singh, V. Krishnamurthy, A. Kumar, J. S. Stein, S. Wang, L. Li, T. Reindl, and I. M. Peters, "Global techno-economic performance of bifacial and tracking photovoltaic systems," *Joule*, vol. 4, no. 7, pp. 1514–1541, 2020. [Online]. Available: https://www.sciencedirect.com/science/article/pii/S2542435120301884
[5] B. Marion, S. MacAlpine, C. Deline, A. Asgharzadeh, F. Toor, D. Riley, J. Stein, and C. Hansen, "A practical irradiance model for bifacial pv modules," *2017 IEEE 44th Photovoltaic Specialist Conference (PVSC)*, pp. 1537–1542, 2017.
[6] S. A. Pelaez, C. Deline, S. M. MacAlpine, B. Marion, J. S. Stein, and R. K. Kostuk, "Comparison of bifacial solar irradiance model predictions with field validation," *IEEE Journal of Photovoltaics*, vol. 9, no. 1, pp. 82–88, 2019.
[7] G. J. Ward, *The RADIANCE Lighting Simulation and Rendering System*. New York, NY, USA: Association for Computing Machinery, 1994. [Online]. Available: https://doi.org/10.1145/192161.192286
[8] G. Raina and S. Sinha, "A comprehensive assessment of electrical performance and mismatch losses in bifacial pv module under different front and rear side shading scenarios," *Energy Conversion and Management*, vol. 261, p. 115668, 2022. [Online]. Available: https://www.sciencedirect.com/science/article/pii/S0196890422004642

[9] E. Mouhib, P. M. Rodrigo, L. Micheli, E. F. Fernández, and F. Almonacid, "Quantifying the rear and front long-term spectral impact on bifacial photovoltaic modules," *Solar Energy*, vol. 247, pp. 202–213, 2022. [Online]. Available: https://www.sciencedirect.com/science/article/pii/S0038092X2200768X

[10] S. Ayala Pelaez, C. Deline, J. S. Stein, B. Marion, K. Anderson, and M. Muller, "Effect of torque-tube parameters on rear-irradiance and rear-shading loss for bifacial pv performance on single-axis tracking systems," *2020 IEEE 46th Photovoltaic Specialists Conference (PVSC)*, 10 2020. [Online]. Available: https://www.osti.gov/biblio/1726058

[11] C. D. Rodríguez-Gallegos, M. Bieri, O. Gandhi, J. P. Singh, T. Reindl, and S. Panda, "Monofacial vs bifacial si-based pv modules: Which one is more cost-effective?" *Solar Energy*, vol. 176, pp. 412–438, 2018. [Online]. Available: https://www.sciencedirect.com/science/article/pii/S0038092X18309915

[12] O. A. Katsikogiannis, H. Ziar, and O. Isabella, "Integration of bifacial photovoltaics in agrivoltaic systems: A synergistic design approach," *Applied Energy*, vol. 309, p. 118475, 2022. [Online]. Available: https://www.sciencedirect.com/science/article/pii/S0306261921016986

[13] H. Alam, M. A. Alam, and N. Z. Butt, "Techno economic modeling for agrivoltaics: Can agrivoltaics be more profitable than ground mounted pv?" *IEEE Journal of Photovoltaics*, vol. 13, no. 1, pp. 174–186, 2023.

[14] G. Faturrochman, M. de Jong, R. Santbergen, W. Folkerts, M. Zeman, and A. Smets, "Maximizing annual yield of bifacial photovoltaic noise barriers," *Solar Energy*, vol. 162, pp. 300–305, 2018. [Online]. Available: https://www.sciencedirect.com/science/article/pii/S0038092X1830001X

[15] S. Obara, D. Konno, Y. Utsugi, and J. Morel, "Analysis of output power and capacity reduction in electrical storage facilities by peak shift control of pv system with bifacial modules," *Applied Energy*, vol. 128, pp. 35–48, 2014. [Online]. Available: https://www.sciencedirect.com/science/article/pii/S0306261914004061

[16] R. Shigenobu, M. Ito, and H. Taoka, "Optimal design of bifacial pv system to mitigate duck-curve problem of power system with the uc problem," *Energy Reports*, vol. 7, pp. 7004–7014, 2021. [Online]. Available: https://www.sciencedirect.com/science/article/pii/S2352484721010775

[17] "ENTSO-E Transparency Platform," https://transparency.entsoe.eu/, accessed on May 15, 2023.

[18] G. Raina and S. Sinha, "A holistic review approach of design considerations, modelling, challenges and future applications for bifacial photovoltaics," *Energy Conversion and Management*, vol. 271, p. 116290, 2022. [Online]. Available: https://www.sciencedirect.com/science/article/pii/S0196890422010676

[19] D. Chudinzow, S. Nagel, J. Güsewell, and L. Eltrop, "Vertical bifacial photovoltaics – a complementary technology for the european electricity supply?" *Applied Energy*, vol. 264, p. 114782, 2020. [Online]. Available: https://www.sciencedirect.com/science/article/pii/S0306261920302944

[20] W. Nusselt, *Graphische Bestimmung der Winkelverhaltwisses beider Warmestrahlang*, 1928, vol. 72.

[21] M. Mirhosseini and A. Saboonchi, "View factor calculation using the monte carlo method for a 3d strip element to circular cylinder," *International Communications in Heat and Mass Transfer*, vol. 38, no. 6, pp. 821–826, 2011. [Online]. Available: https://www.sciencedirect.com/science/article/pii/S0735193311000674

[22] H. C. Hottel and A. F. Sarofin, *Radiative Transfer*. New York: McGraw Hill, 1967.

[23] C. Deline, S. MacAlpine, B. Marion, F. Toor, A. Asgharzadeh, and J. S. Stein, "Assessment of bifacial photovoltaic module power rating methodologies—inside and out," *IEEE Journal of Photovoltaics*, vol. 7, no. 2, pp. 575–580, 2017.

[24] S. A. Pelaez and C. Deline, "bifacial_radiance: a python package for modeling bifacial solar photovoltaic systems," *Journal of Open Source Software*, vol. 5, no. 50, p. 1865, 2020. [Online]. Available: https://doi.org/10.21105/joss.01865

[25] A. Asgharzadeh, M. A. Anoma, A. Hoffman, C. Chaudhari, S. Bapat, R. Perkins, D. Cohen, G. M. Kimball, D. Riley, F. Toor, and B. Bourne, "A benchmark and validation of bifacial pv irradiance models," *2019 IEEE 46th Photovoltaic Specialists Conference (PVSC)*, pp. 3281–3287, 2019.

[26] C. Deline, S. Ayala Pelaez, S. MacAlpine, and C. Olalla, "Estimating and parameterizing mismatch power loss in bifacial photovoltaic systems," *Progress in Photovoltaics: Research and Applications*, vol. 28, no. 7, pp. 691–703, 2020. [Online]. Available: https://onlinelibrary.wiley.com/doi/abs/10.1002/pip.3259

[27] J. Ledesma, R. Almeida, F. Martinez-Moreno, C. Rossa, J. Martín-Rueda, L. Narvarte, and E. Lorenzo, "A simulation model of the irradiation and energy yield of large bifacial photovoltaic plants," *Solar Energy*, vol. 206, pp. 522–538, 2020. [Online]. Available: https://www.sciencedirect.com/science/article/pii/S0038092X20306071

[28] N. Riedel-Lyngskær, M. Ribaconka, M. Pó, S. Thorsteinsson, A. Thorseth, C. Dam-Hansen, and M. L. Jakobsen, "Spectral albedo in bifacial photovoltaic modeling: What can be learned from onsite measurements?" *2021 IEEE 48th Photovoltaic Specialists Conference (PVSC)*, pp. 0942–0949, 2021.

[29] N. Riedel-Lyngskær, M. Ribaconka, M. Pó, A. Thorseth, S. Thorsteinsson, C. Dam-Hansen, and M. L. Jakobsen, "The effect of spectral albedo in bifacial photovoltaic performance," *Solar Energy*, vol. 231, pp. 921–935, 2022. [Online]. Available: https://www.sciencedirect.com/science/article/pii/S0038092X21010720

[30] M. R. Vogt, T. Gewohn, K. Bothe, C. Schinke, and R. Brendel, "Impact of using spectrally resolved ground albedo data for performance simulations of bifacial modules," in *Proc. 35th Eur. Photovolt. Sol. Energy Conf.*, 2018, pp. 1011–1016.

[31] M. T. Patel, M. S. Ahmed, H. Imran, N. Z. Butt, M. R. Khan, and M. A. Alam, "Global analysis of next-generation utility-scale pv: Tracking bifacial solar farms," *Applied Energy*, vol. 290, p. 116478, 2021. [Online]. Available: https://www.sciencedirect.com/science/article/pii/S0306261921000428

[32] D. Berrian, J. Libal, M. Klenk, H. Nussbaumer, and R. Kopecek, "Performance of bifacial pv arrays with fixed tilt and horizontal single-axis tracking: Comparison of simulated and measured data," *IEEE Journal of Photovoltaics*, vol. 9, no. 6, pp. 1583–1589, 2019.

[33] C. D. Rodríguez-Gallegos, H. Liu, O. Gandhi, J. P. Singh, V. Krishnamurthy, A. Kumar, J. S. Stein, L. Li, S. Wang, T. Reindl, and I. M. Peters, "Techno-economic performance modelling of bifacial and tracking pv systems worldwide," *2021 IEEE 48th Photovoltaic Specialists Conference (PVSC)*, pp. 0406–0409, 2021.

[34] C. D. Rodríguez-Gallegos, O. Gandhi, S. K. Panda, and T. Reindl, "On the pv tracker performance: Tracking the sun versus tracking the best orientation," *IEEE Journal of Photovoltaics*, vol. 10, no. 5, pp. 1474–1480, 2020.

[35] X. Sun, M. R. Khan, C. Deline, and M. A. Alam, "Optimization and performance of bifacial solar modules: A global perspective," *Applied Energy*, vol. 212, pp. 1601–1610, 2018. [Online]. Available: https://www.sciencedirect.com/science/article/pii/S0306261917317567

[36] E. Lorenzo, "On the historical origins of bifacial pv modelling," *Solar Energy*, vol. 218, pp. 587–595, 2021. [Online]. Available: https://www.sciencedirect.com/science/article/pii/S0038092X21001869

[37] M. Alam, M. S. Gul, and T. Muneer, "Ground view factor computation model for bifacial photovoltaic collector field: uniform and non-uniform surfaces," *Energy Reports*, vol. 7, pp. 9133–9149, 2021. [Online]. Available: https://www.sciencedirect.com/science/article/pii/S2352484721013457

[38] M. T. Patel, M. R. Khan, X. Sun, and M. A. Alam, "A worldwide cost-based design and optimization of tilted bifacial solar farms," *Applied Energy*, vol. 247, pp. 467–479, 2019. [Online]. Available: https://www.sciencedirect.com/science/article/pii/S0306261919305604

[39] M. T. Patel, R. A. Vijayan, R. Asadpour, M. Varadharajaperumal, M. R. Khan, and M. A. Alam, "Temperature-dependent energy gain of bifacial pv farms: A global perspective," *Applied Energy*, vol. 276, p. 115405, 2020. [Online]. Available: https://www.sciencedirect.com/science/article/pii/S030626192030917X

[40] D. Chudinzow, J. Haas, G. Díaz-Ferrán, S. Moreno-Leiva, and L. Eltrop, "Simulating the energy yield of a bifacial photovoltaic power plant," *Solar Energy*, vol. 183, pp. 812–822, 2019. [Online]. Available: https://www.sciencedirect.com/science/article/pii/S0038092X19302993

[41] S. Guo, T. M. Walsh, and M. Peters, "Vertically mounted bifacial photovoltaic modules: A global analysis," *Energy*, vol. 61, pp. 447–454, 2013. [Online]. Available: https://www.sciencedirect.com/science/article/pii/S0360544213007275

[42] V. Durković and Željko Durišić, "Extended model for irradiation suitable for large bifacial pv power plants," *Solar Energy*, vol. 191, pp. 272–290, 2019. [Online]. Available: https://www.sciencedirect.com/science/article/pii/S0038092X19308448

[43] W. Gu, T. Ma, M. Li, L. Shen, and Y. Zhang, "A coupled optical-electrical-thermal model of the bifacial photovoltaic module," *Applied Energy*, vol. 258, p. 114075, 2020. [Online]. Available: https://www.sciencedirect.com/science/article/pii/S0306261919317623

[44] Y. Zhang, J. Q. Gao, Y. Yu, Q. Shi, and Z. Liu, "Influence of incidence angle effects on the performance of bifacial photovoltaic modules considering rear-side reflection," *Solar Energy*, vol. 245, pp. 404–409, 2022. [Online]. Available: https://www.sciencedirect.com/science/article/pii/S0038092X22005771

[45] M. R. Khan, E. Sakr, X. Sun, P. Bermel, and M. A. Alam, "Ground sculpting to enhance energy yield of vertical bifacial solar farms," *Applied Energy*, vol. 241, pp. 592–598, 2019. [Online]. Available: https://www.sciencedirect.com/science/article/pii/S0306261919301278

[46] U. A. Yusufoglu, T. M. Pletzer, L. J. Koduvelikulathu, C. Comparotto, R. Kopecek, and H. Kurz, "Analysis of the annual performance of bifacial modules and optimization methods," *IEEE Journal of Photovoltaics*, vol. 5, no. 1, pp. 320–328, 2015.

[47] K. R. McIntosh, M. D. Abbott, G. Loomis, B. A. Sudbury, A. Mayer, C. Zak, and J. Meydbrey, "Irradiance on the upper and lower modules of a two-high bifacial tracking system," *2020 47th IEEE Photovoltaic Specialists Conference (PVSC)*, pp. 1916–1923, 2020.

[48] G. J. Janssen, B. B. Van Aken, A. J. Carr, and A. A. Mewe, "Outdoor performance of bifacial modules by measurements and modelling," *Energy Procedia*, vol. 77, pp. 364–373, 2015, 5th International Conference on Silicon Photovoltaics, SiliconPV 2015. [Online]. Available: https://www.sciencedirect.com/science/article/pii/S187661021500819X

[49] J. E. Castillo-Aguilella and P. S. Hauser, "Multi-variable bifacial photovoltaic module test results and best-fit annual bifacial energy yield model," *IEEE Access*, vol. 4, pp. 498–506, 2016.

[50] ——, "Bifacial photovoltaic module best-fit annual energy yield model with azimuthal correction," *2016 IEEE 43rd Photovoltaic Specialists Conference (PVSC)*, pp. 3109–3112, 2016.

[51] I. Shoukry, J. Libal, R. Kopecek, E. Wefringhaus, and J. Werner, "Modelling of bifacial gain for stand-alone and in-field installed bifacial pv modules," *Energy Procedia*, vol. 92, pp. 600–608, 2016, proceedings of the 6th International Conference on Crystalline Silicon Photovoltaics (SiliconPV 2016). [Online]. Available: https://www.sciencedirect.com/science/article/pii/S1876610216304520

[52] A. Asgharzadeh, T. Lubenow, J. Sink, B. Marion, C. Deline, C. Hansen, J. Stein, and F. Toor, "Analysis of the impact of installation parameters and system size on bifacial gain and energy yield of pv systems," *2017 IEEE 44th Photovoltaic Specialist Conference (PVSC)*, pp. 3333–3338, 2017.

[53] U. A. Yusufoglu, T. H. Lee, T. M. Pletzer, A. Halm, L. J. Koduvelikulathu, C. Comparotto, R. Kopecek, and H. Kurz, "Simulation of energy production by bifacial modules with revision of ground reflection," *Energy Procedia*, vol. 55, pp. 389–395, 2014, proceedings of the 4th International Conference on Crystalline Silicon Photovoltaics (SiliconPV 2014). [Online]. Available: https://www.sciencedirect.com/science/article/pii/S1876610214013368

[54] S. Wang, O. Wilkie, J. Lam, R. Steeman, W. Zhang, K. S. Khoo, S. C. Siong, and H. Rostan, "Bifacial photovoltaic systems energy yield modelling," *Energy Procedia*, vol. 77, pp. 428–433, 2015, 5th International Conference on Silicon Photovoltaics, SiliconPV 2015. [Online]. Available: https://www.sciencedirect.com/science/article/pii/S1876610215008280

[55] J. Appelbaum, "Bifacial photovoltaic panels field," *Renewable Energy*, vol. 85, pp. 338–343, 2016. [Online]. Available: https://www.sciencedirect.com/science/article/pii/S0960148115300732

[56] C. W. Hansen, R. Gooding, N. Guay, D. M. Riley, J. Kallickal, D. Ellibee, A. Asgharzadeh, B. Marion, F. Toor, and J. S. Stein, "A detailed model of rear-side irradiance for bifacial pv modules," *2017 IEEE 44th Photovoltaic Specialist Conference (PVSC)*, pp. 1543–1548, 2017.

[57] M. R. Khan, A. Hanna, X. Sun, and M. A. Alam, "Vertical bifacial solar farms: Physics, design, and global optimization," *Applied Energy*, vol. 206, pp. 240–248, 2017. [Online]. Available: https://www.sciencedirect.com/science/article/pii/S0306261917310589

[58] L. Kreinin, A. Karsenty, D. Grobgeld, and N. Eisenberg, "Pv systems based on bifacial modules: Performance simulation vs. design factors," *2016 IEEE 43rd Photovoltaic Specialists Conference (PVSC)*, pp. 2688–2691, 2016.

[59] Z. Zengwei, Z. Zhen, J. Yongfeng, L. Haolin, and Z. Shengcheng, "Performance analysis on bifacial pv panels with inclined and horizontal east–west sun trackers," *IEEE Journal of Photovoltaics*, vol. 9, no. 3, pp. 636–642, 2019.

[60] M. T. Patel, M. Ryyan Khan, A. Alnuaimi, O. Albadwawwi, J. J. John, and M. A. Alam, "Implications of seasonal and spatial albedo variation on the energy output of bifacial solar farms: A global perspective," *2019 IEEE 46th Photovoltaic Specialists Conference (PVSC)*, pp. 2264–2267, 2019.

[61] D. Berrian and J. Libal, "A comparison of ray tracing and view factor simulations of locally resolved rear irradiance with the experimental values," *Progress in Photovoltaics: Research and Applications*, vol. 28, no. 6, pp. 609–620, 2020. [Online]. Available: https://onlinelibrary.wiley.com/doi/abs/10.1002/pip.3261

[62] M. A. Anoma, D. Jacob, B. C. Bourne, J. A. Scholl, D. M. Riley, and C. W. Hansen, "View factor model and validation for bifacial pv and diffuse shade on single-axis trackers," *2017 IEEE 44th Photovoltaic Specialist Conference (PVSC)*, pp. 1549–1554, 2017.

[63] P. Tillmann, K. Jäger, and C. Becker, "Minimising the levelised cost of electricity for bifacial solar panel arrays using bayesian optimisation," *Sustainable Energy Fuels*, vol. 4, pp. 254–264, 2020. [Online]. Available: http://dx.doi.org/10.1039/C9SE00750D

[64] G. Janssen, R. Gali, K. de Groot, A. Carr, B. Van Aken, and I. Romijn, "Impact of inhomogeneous irradiance at the rear of bifacial panels on modelled energy yield," *33rd European PV Solar EnergyConference and Exhibition (EU PVSEC)*, 10 2018.

[65] M. K. Fuentes, "A simplified thermal model for flat-plate photovoltaic arrays," 5 1987. [Online]. Available: https://www.osti.gov/biblio/6802914

[66] J. A. Kratochvil, W. E. Boyson, and D. L. King, "Photovoltaic array performance model," Sandia National Laboratories, New Mexico, Tech. Rep., 2004. [Online]. Available: http://dx.doi.org/10.2172/919131

[67] D. Faiman, "Assessing the outdoor operating temperature of photovoltaic modules," *Progress in Photovoltaics: Research and Applications*, vol. 16, no. 4, pp. 307–315, 2008. [Online]. Available: https://onlinelibrary.wiley.com/doi/abs/10.1002/pip.813

[68] J. A. Duffie and W. A. Beckman, *Solar Energy Thermal Processes*, 3rd ed. John Wiley & Sons Inc, 2006.

[69] R. Perez, R. Seals, P. Ineichen, R. Stewart, and D. Menicucci, "A new simplified version of the perez diffuse irradiance model for tilted surfaces," *Solar Energy*, vol. 39, no. 3, pp. 221–231, 1987. [Online]. Available: https://www.sciencedirect.com/science/article/pii/S0038092X87800312

[70] N. Martin and J. Ruiz, "Calculation of the pv modules angular losses under field conditions by means of an analytical model," *Solar Energy Materials and Solar Cells*, vol. 70, no. 1, pp. 25–38, 2001. [Online]. Available: https://www.sciencedirect.com/science/article/pii/S0927024800004086

[71] M. A. Green, *Solar cells: operating principles, technology, and system applications*, 1 1982. [Online]. Available: https://www.osti.gov/biblio/6051511

[72] PVMD group, TU Delft, "Database for global hourly irradiance spectra with 1°x1° resolution," 2023.

[73] J. Carolus, J. A. Tsanakas, A. van der Heide, E. Voroshazi, W. De Ceuninck, and M. Daenen, "Physics of potential-induced degradation in bifacial p-perc solar cells," *Solar Energy Materials and Solar Cells*, vol. 200, p. 109950, 2019. [Online]. Available: https://www.sciencedirect.com/science/article/pii/S092702481930279X

APPENDIX A
ADDITIONAL EQUATIONS FOR BIFACIAL PV FARM MODEL

A. PV modules' shadows

Equations 19, 20 and 21 are adopted to calculate the shadow of the modules on the ground, as depicted in figure 25.

$$y_1 = \frac{h - \frac{l}{2}\sin(\theta)}{\tan(\phi_s)} - \frac{l}{2}\cos(\theta) \tag{19}$$

$$y_2 = \frac{h + \frac{l}{2}\sin(\theta)}{\tan(\phi_s)} + \frac{l}{2}\cos(\theta) \tag{20}$$

$$\phi_s = \max\left[0, \arctan\left(\frac{\tan(a_s)}{\cos(A_m - A_s)}\right)\right] \tag{21}$$

B. View factor between PV cell and ground segment

The expression 22-25 are used to calculate the length of the segments included in equation 9, referring to figure 7.

$$AC = \sqrt{\left(h + \left(x - \frac{l}{2}\right)\cdot\sin(\theta)\right)^2 + \left(y_1 - \left(x - \frac{l}{2}\right)\cdot\cos(\theta)\right)^2} \tag{22}$$

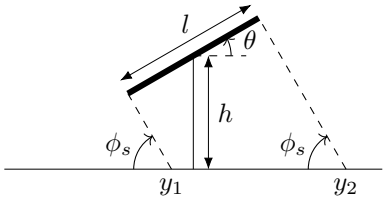

Fig. 25. Extremes of the shadow on the ground

$$AD = \sqrt{\left(h + \left(x - \frac{l}{2}\right) \cdot \sin(\theta)\right)^2 + \left(y_2 - \left(x - \frac{l}{2}\right) \cdot \cos(\theta)\right)^2} \quad (23)$$

$$BC = \sqrt{\left(h + \left(x - \frac{l}{2} + c\right) \cdot \sin(\theta)\right)^2 + \left(y_1 - \left(x - \frac{l}{2} + c\right) \cdot \cos(\theta)\right)^2} \quad (24)$$

$$BD = \sqrt{\left(h + \left(x - \frac{l}{2} + c\right) \cdot \sin(\theta)\right)^2 + \left(y_2 - \left(x - \frac{l}{2} + c\right) \cdot \cos(\theta)\right)^2} \quad (25)$$

C. View factor between PV cells and neighbouring modules

The view factor between PV cells and neighbouring modules ($VF_{c\to m}$) are calculated according to the expression 26, where the segments are obtained from the coordinates included in the equations 27-30, as illustrated in figure 26. Taking into account the possibility of unconventional configurations adds complexity to these equations. Specifically, symbols ξ_1 and ξ_2 indicate the angles between the lines that connect the extremes of the cell and the neighbouring modules and the vertical direction.

$$VF_{c\to m} = \frac{BC + AD - AC - BC}{2 \cdot c} \quad (26)$$

$$\begin{cases} x_a = (x - \frac{l}{2}) \cdot \cos(\theta_1) \\ y_a = h_1 + (x - \frac{l}{2}) \cdot \sin(\theta_1); \end{cases} \quad (27)$$

$$\begin{cases} x_b = (x - \frac{l}{2} + c) \cdot \cos(\theta_1) \\ y_b = h_1 + (x - \frac{l}{2} + c) \cdot \sin(\theta_1); \end{cases} \quad (28)$$

$$\begin{cases} x_c = \frac{-\tan(\xi_1 - \frac{\pi}{2}) \cdot x_a + y_a + \tan(\theta_2) \cdot d_2 - h_3}{\tan(\theta_2) - \tan(\xi_1 - \frac{\pi}{2})} \\ y_c = \tan(\theta_3) \cdot (x_c - d_2) + h_3 \end{cases} \quad (29)$$

$$\begin{cases} x_d = \frac{-\tan(\xi_2 - \frac{\pi}{2}) \cdot x_b + y_b + \tan(\theta_3) \cdot d_2 - h_3}{\tan(\theta_3) - \tan(\xi_2 - \frac{\pi}{2})} \\ y_d = \tan(\theta_3) \cdot (x_d - d_2) + h_3 \end{cases} \quad (30)$$

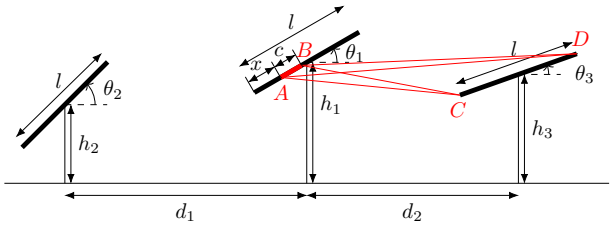

Fig. 26. View factor between a cell and the neighbouring module

D. Temperature of PV cells: INOCT model

Equations 31-35 are used to estimate the cells' temperature using INOCT model, where rack mounting installations are considered.

$$T_{INOCT} = T_{NOCT} - 3 \quad (31)$$

$$T_{cell} = T_{amb} + \frac{G_{tot}}{G_{NOCT}} \cdot (T_{INOCT} - 20°C) \quad (32)$$

$$G_{front} = \int_{\lambda_1}^{\lambda_2} [I_{front,sky}(\lambda) + I_{front,ground}(\lambda) + I_{front,mod}(\lambda)]\ d\lambda \quad (33)$$

$$G_{rear} = \int_{\lambda_1}^{\lambda_2} [I_{rear,sky}(\lambda) + I_{rear,ground}(\lambda) + I_{rear,mod}(\lambda)]\ d\lambda \quad (34)$$

$$G_{tot} = G_{front} + G_{rear} \quad (35)$$

APPENDIX B
EXPERIMENTAL VALIDATION: ADDITIONAL DATA

Tables IV, V, VI include the installation conditions and the detailed results of the validation process.

TABLE IV
DESIGN PARAMETERS USED FOR THE VALIDATION.

Design Parameter	Value
Length	$2.14\,m$
Orientation	$187°N$
Height (from the bottom extreme)	$0.5\,m$
Row-to-row distance	$4.3\,m - 4.8\,m - 5\,m$

TABLE V
TIME PERIODS SELECTED FOR THE MODEL'S VALIDATION AND THE CORRESPONDENT INSTALLATION CONDITIONS.

Time period	Weather	Ground type	Albedo	Tilt
28-7-2020 15.30-18.15	Cloudy	White fleece	0.53	30°
29-7-2020 10.00-18.00	Cloudy	White fleece	0.53	30°
30-7-2020 11.00-18.00	Sunny	White fleece	0.53	30°
31-7-2020 11.30-15.30	Sunny	Grass	0.13	30°
1-8-2020 10.00-18.00	Cloudy	Stones	0.19	30°
2-8-2020 10.00-18.00	Sunny	Stones	0.19	30°
3-8-2020 10.00-18.00	Rainy	Stones	0.15	30°
4-8-2020 10.00-18.00	Sunny	Stones	0.19	45°
1-9-2020 14.00-18.00	Cloudy	White fleece	0.50	52°
6-9-2020 9.00-19.00	N.A.	White fleece	0.45	52°
7-9-2020 12.30-19.00	Cloudy	White fleece	0.50	52°
13-9-2020 9.00-19.00	Sunny	Stones	0.18	52°

APPENDIX C
SPECIFICATION OF THE MODULES

Table VII summarizes the specifications of the modules adopted for the simulations.

TABLE VI
VALIDATION RESULTS: RMSE AND MBD BETWEEN MODELLED AND MEASURED DATA FOR THE SELECTED DAYS.

		Sensor 1 (bottom)		Sensor 2		Sensor 3		Sensor 4		Sensor 5		Sensor 6 (top)	
Day	Unit	RMSE	MBD	RMSE	MBD	RMSE	MBD	RMSE	MBD	RMSE	MBD	RMSE	MBD
28-7-2020	[W/m^2]	5.99	-5.43	8.93	-8.17	9.13	-8.24	6.51	-4.98	4.53	-1.78	4.28	1.14
	[%]	9.07	-8.21	14.76	-13.51	15.04	-13.56	10.31	-7.90	6.89	-2.70	6.19	1.64
29-7-2020	[W/m^2]	12.04	-4.15	17.22	-13.43	18.02	-15.12	16.29	-12.60	13.94	-9.04	13.44	-6.02
	[%]	11.28	-3.89	18.60	-14.51	20.10	-16.87	17.42	-13.47	13.96	-9.06	12.39	-5.55
30-7-2020	[W/m^2]	11.99	-7.68	25.28	-23.89	26.56	-25.64	25.77	-24.77	22.44	-21.38	21.84	-20.48
	[%]	7.60	-4.87	20.69	-19.54	24.83	-23.97	23.93	-23.00	19.24	-18.33	16.41	-15.39
31-7-2020	[W/m^2]	8.62	8.47	0.94	0.44	4.85	-4.83	6.39	-6.37	6.30	-6.29	5.56	-5.54
	[%]	22.83	22.42	3.07	1.43	15.74	-15.66	19.15	-19.11	16.73	-16.69	12.87	-12.83
1-8-2020	[W/m^2]	4.61	-1.98	4.35	-2.21	4.46	-2.86	4.63	-2.25	4.41	-1.21	4.99	0.78
	[%]	12.78	-5.48	14.82	-7.54	15.51	-9.95	15.11	-7.34	13.29	-3.65	14.04	2.20
2-8-2020	[W/m^2]	6.96	-1.71	5.76	-2.28	5.70	-3.02	6.04	-2.22	5.91	-1.02	6.71	0.97
	[%]	13.79	-3.39	14.56	-5.78	15.14	-8.03	15.20	-5.59	13.57	-2.34	14.02	2.02
3-8-2020	[W/m^2]	2.02	0.42	1.78	-0.08	2.17	-0.65	2.71	-0.01	3.25	0.81	4.44	2.44
	[%]	16.36	3.37	15.42	-0.74	17.55	-5.30	20.52	-0.09	23.32	5.80	31.59	17.36
4-8-2020	[W/m^2]	5.08	-3.80	4.61	-3.50	5.98	-4.81	5.53	-3.90	4.99	-2.26	5.45	2.87
	[%]	8.06	-6.04	9.00	-6.83	11.88	-9.56	10.37	-7.30	8.69	-3.94	9.32	4.92
1-9-2020	[W/m^2]	11.13	-10.77	9.31	-8.86	8.90	-8.43	6.57	-5.91	3.91	-2.34	5.93	4.38
	[%]	25.98	-25.13	22.22	-21.16	20.74	-19.65	15.44	-13.88	9.64	-5.78	16.75	12.37
6-9-2020	[W/m^2]	21.03	-1.38	16.65	0.70	14.81	3.52	16.52	8.29	20.21	14.35	28.32	23.93
	[%]	24.47	-1.60	23.26	0.97	23.19	5.51	27.27	13.69	34.98	24.83	54.27	45.87
7-9-2020	[W/m^2]	9.61	-6.09	8.23	-3.22	7.97	0.45	10.34	5.88	16.36	13.91	27.02	24.90
	[%]	7.87	-4.98	8.25	-3.22	9.16	0.51	12.71	7.23	21.40	18.19	38.68	35.66
13-9-2020	[W/m^2]	5.22	4.07	6.67	5.86	6.24	5.39	7.67	6.85	9.88	9.11	17.96	16.85
	[%]	11.75	9.16	17.52	15.37	16.75	14.47	20.23	18.08	25.65	23.64	52.24	49.01

TABLE VII
PV MODULES' SPECIFICATIONS ADOPTED IN THIS STUDY, BASED ON THE PRODUCT LG400N2T-A5.

Parameter	**Value**
Dimensions of the module ($w \cdot l$)	$2.064 \times 1.024\,m$
Cells configuration	6×12
Bypass diodes	3
Cell's length (c)	$0.1707m$
Rated power (P_{rated})	$440\,Wp$
Short-circuit current ($I_{sc,STC}$)	$11.24\,A$
Open-circuit voltage $V_{oc,STC}$	$49.7\,V$
Series-connected cells (N_s)	72
Parallel-connected cells (N_p)	1
NOCT Temperature (T_{NOCT})	$45°C$
Temperature coefficient for I_{sc} ($k_{I_{sc}}$)	$0.03\,\%/C$
Temperature coefficient for V_{oc} ($k_{V_{oc}}$)	$-0.27\,\%/C$
Ideality factor (n)	2
Reflectivity (r)	10%

APPENDIX D
INFLUENCE OF p_{min} ON THE PROFITABILITY OF E/W VERTICAL OVER N/S TILTED CONFIGURATION

The minimum price influences the revenues gain in absolute terms but has no impact when relative metrics are adopted, as explained through an example. Let's consider two different electricity price curves $e_1(t)$ and $e_2(t)$ modelled as described in section IV. Suppose that are characterized by the same price ratio ($p_{ratio,1} = p_{ratio,2}$) but two different (positive) minimum noon prices ($p_{min,1} \neq p_{min,2}$). According to their definition, the relation between $e_1(t)$ and $e_2(t)$ expressed in 36 is valid.

$$e_1(t) = \frac{p_{min,1}}{p_{min,2}} \cdot e_2(t) \tag{36}$$

The revenues of the vertical and the tilted configuration obtained for the market conditions described by $e_1(t)$ are indicated with $R_{v,1}$ and $R_{t,1}$. Similarly, $R_{v,2}$ and $R_{t,2}$ refer to $e_2(t)$ electricity price curve. The revenues' gain can be obtained as shown in 37 and 38, where $P_v(t)$ and $P_t(t)$ are the power curves of the vertical and tilted farm during the time period $[t_1, t_2]$.

$$R_{gain,1} = \frac{R_{v,1} - R_{t,1}}{R_{t,1}} = \frac{R_{v,1}}{R_{t,1}} - 1 = \frac{\int_{t_1}^{t_2} e_1(t) P_v(t) dt}{\int_{t_1}^{t_2} e_1(t) P_t(t) dt} - 1 \tag{37}$$

$$R_{gain,2} = \frac{R_{v,2} - R_{t,2}}{R_{t,2}} = \frac{R_{v,2}}{R_{t,2}} - 1 = \frac{\int_{t_1}^{t_2} e_2(t) P_v(t) dt}{\int_{t_1}^{t_2} e_2(t) P_t(t) dt} - 1 \tag{38}$$

Therefore, combining the relations 36, 37 and 38, the condition illustrated in equation 39 is derived, proving the validity of the statement concerning the impact of p_{min} on the results.

$$R_{gain,1} = \frac{\int_{t_1}^{t_2} e_1(t) P_v(t) dt}{\int_{t_1}^{t_2} e_1(t) P_t(t) dt} - 1 =$$
$$= \frac{\int_{t_1}^{t_2} \left[\frac{p_{min,1}}{p_{min,2}} \cdot e_2(t) \right] P_v(t) dt}{\int_{t_1}^{t_2} \left[\frac{p_{min,1}}{p_{min,2}} \cdot e_2(t) \right] P_t(t) dt} - 1 =$$
$$= \frac{\cancel{\frac{p_{min,1}}{p_{min,2}}} \cdot \int_{t_1}^{t_2} e_2(t) P_v(t) dt}{\cancel{\frac{p_{min,1}}{p_{min,2}}} \cdot \int_{t_1}^{t_2} e_2(t) P_t(t) dt} - 1 =$$
$$= \frac{\int_{t_1}^{t_2} e_2(t) P_v(t) dt}{\int_{t_1}^{t_2} e_2(t) P_t(t) dt} - 1 = R_{gain,2} \quad (39)$$

APPENDIX E
RESULTS: ADDITIONAL VISUALIZATIONS

Additional visualizations are included concerning global maps for the minimum price ratio required to achieve a revenues' gain while using vertical PV modules instead of the optimally-tilted counterpart. The various cases depicted in figure 27 refer to different design parameters.

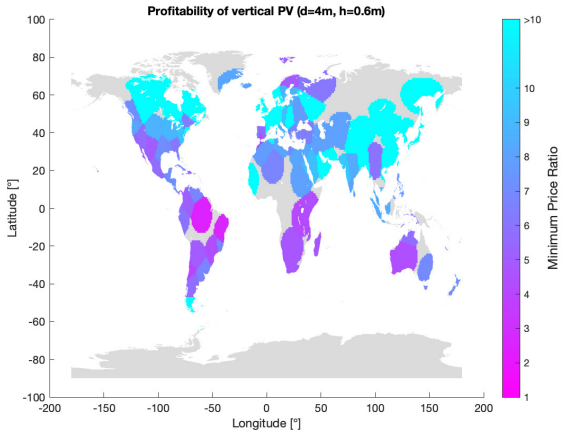

(a) Design parameters: $d = 4\,m$, $h = 0.6\,m$

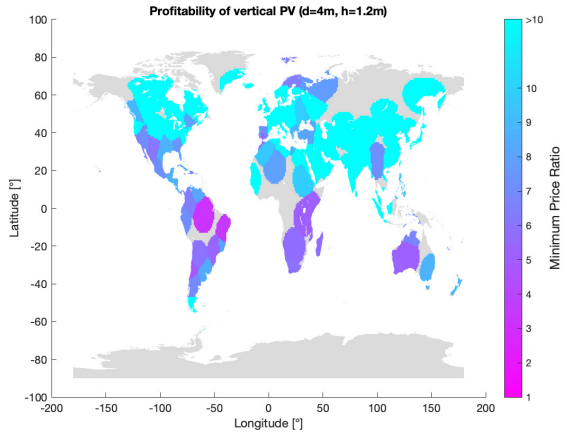

(b) Design parameters: $d = 4\,m$, $h = 1.2\,m$

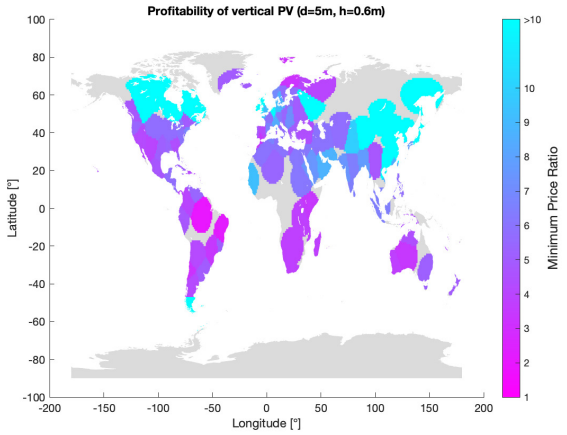

(c) Design parameters: $d = 5\,m$, $h = 0.6\,m$

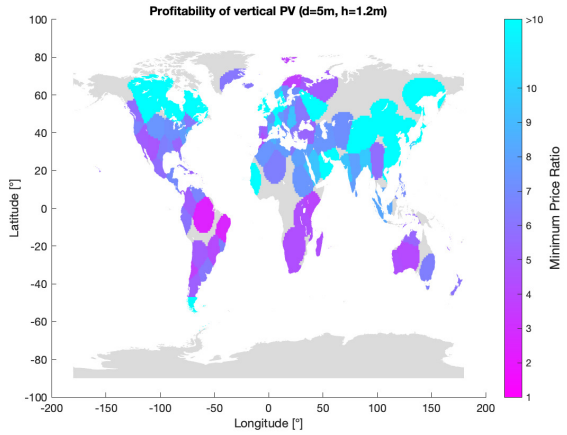

(d) Design parameters: $d = 5\,m$, $h = 1.2\,m$

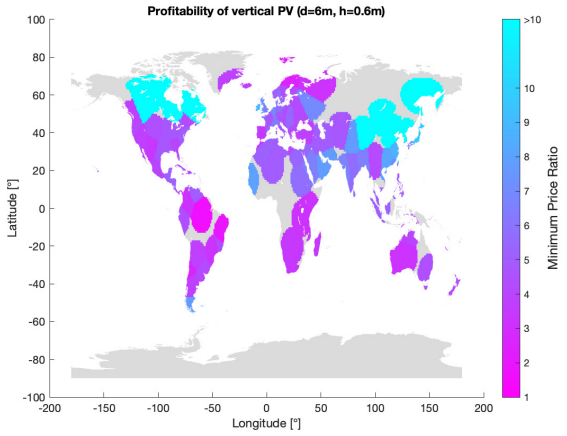

(e) Design parameters: $d = 6\,m$, $h = 0.6\,m$

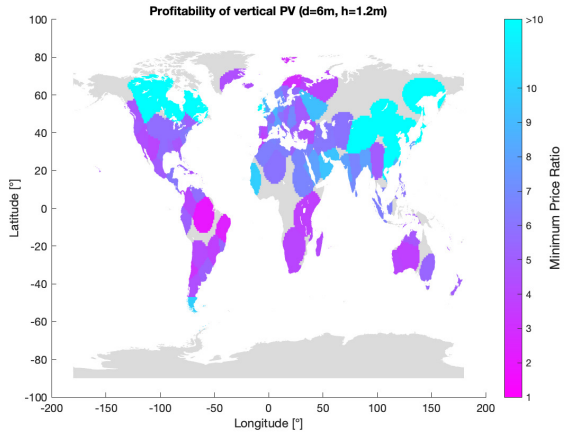

(f) Design parameters: $d = 6\,m$, $h = 1.2\,m$

Fig. 27. Global map for the minimum price ratio for which vertical modules are more profitable than tilted ones. The other variables are set as follows: $p_{min} = 100\,€/MWh$, $n_{vert} = 1$, $n_{max,power} = 1$